Fiber Nonlinearity Mitigation using Mid-span Spectral Inversion in Long-haul Coherent Optical OFDM Systems

A THESIS PRESENTED TO

THE DEPARTMENT OF THE ELECTRICAL AND COMPUTER SYSTEMS ENGINEERING

MONASH UNIVERSITY, CLAYTON, AUSTRALIA

IN FULFILMENT

OF THE REQUIREMENTS FOR THE PhD DEGREE

By

Mohammad Monir Morshed, MSc

March 2015

Copyright Notices

Notice 1

Notice 2

To my father

Statement of Originality

The work presented in this thesis is to the best of the author's knowledge original, except as acknowledged in the text. The material has not been submitted, either in whole or in part, for a degree at this or any other university.

Mohammad Monir Morshed

Abstract

Optical fiber communication systems have become the backbone of today's communication networks due to their enormous bandwidth, over several terahertz (THz), enabling capacities of 100 Tb/s and beyond. Almost all of world's long-haul internet traffic is carried by these optical backbone networks. Despite the fact that the internet bubble ended in the early 2000s, its traffic has been constantly increasing at an astounding rate of 75% per year. In addition to that, new emerging video-centric applications such as IPTV will continue to increase the demand on the underlying optical backbone networks.

As a result, ten to twenty years from now, optical networks will have to carry vastly increased amounts of data. However, recent research shows that fundamental limits in optical backbone networks are being approached. These limits are imposed by noise generated from inline amplifiers used to boost up the signal and the intrinsic nonlinearity of conventional standard single mode fiber (S-SMF). In order to meet long-term needs and challenges, therefore, research in wideband optical subsystems enabling high capacity long-haul transmission must be urgently pursued.

One approach to break through the current capacity limit is a combination of using advanced modulation formats like coherent optical Orthogonal Frequency Division Multiplexing (CO-OFDM) and fiber nonlinearity mitigation techniques. In OFDM, the orthogonal property of the sub-carriers allows formation of an almost rectangular spectrum, which increases spectral efficiency. However, at the high powers required for higher order modulation formats, the nonlinearity in the fiber causes nonlinear mixing between the subcarriers, restricting the maximum allowable power below nonlinear threshold, and hence constraining the total capacity and distance.

The PhD thesis proposed using mid-span spectral inversion (MSSI) that uses optical phase conjugation (OPC) module as shown in the figure below to mitigate the fiber nonlinearity in CO-OFDM systems.

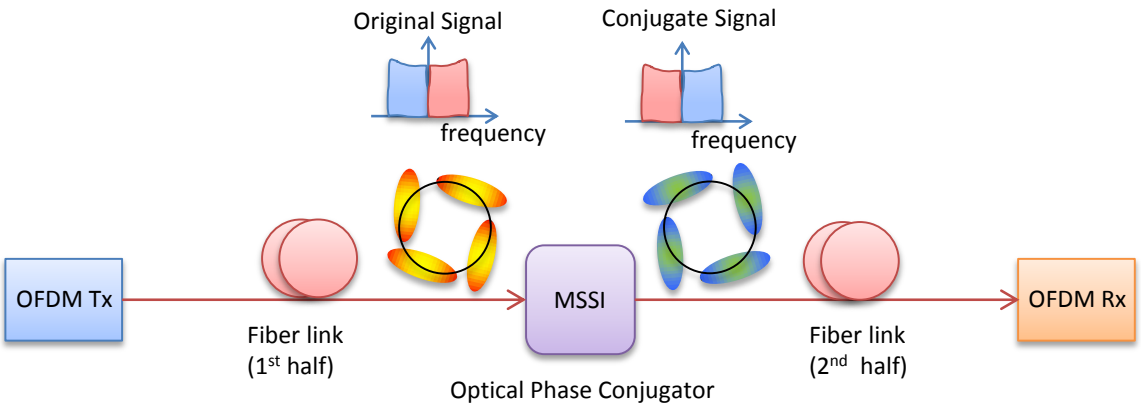

Figure: Schematic of using MSSI in CO-OFDM system.

Using MSSI, the spectrum of the first-half of the link (from the Tx to the OPC module) will be inverted by Four-Wave Mixing (FWM) of the OFDM signal with a pump wave. The spectrally inverted signal is then selected to pass through the second half of the link. Because the signal is spectrally inverted, the second half of the link should undo the dispersion and nonlinearity of the first half of the link.

During the project, a detailed analytical formalism to describe the performance of the OPC module has been developed. This aids the design and improvement of fundamental performance of OPC module. The first experimental demonstration of using MSSI in a coherent system has been made using dual polarization CO-OFDM systems carrying 1.21-Tb/s over 800 km. A design outline for optimum performance using MSSI has been developed. Two novel methods for improving the fundamental performance of MSSI have been proposed. The first method splits the nonlinear element into two parts, inserting a notch filter to remove the pump and then reinserting the pump into the second part of the nonlinear element. The second method uses a phase shift filter between the two nonlinear elements, to improve robustness in practical implementation. Both methods offer 1 dB of maximum signal quality improvement in a 10 × 80-km 4-QAM 224-Gb/s CO-OFDM system.

In summary, this work has demonstrated by simulation and experiments that MSSI offers benefits to coherent optical systems, including OFDM systems. It has developed analytical formalisms that identify the performance-limiting mechanisms in optical phase conjugators based on third order nonlinearity, and has introduced two methods of mitigating these mechanisms. MSSI fell from favour in the mid-2000s due to its complexity. However, after this successful demonstration of fiber nonlinearity compensation using MSSI in a coherent system, MSSI has now drawn considerable attention recently. Subsequently, there have been demonstrations of Raman-enhanced MSSI and multiple phase-conjugations based coherent systems at the 2014 conference on Optical Fiber Communications (OFC).

List of Author's Publications written during the project

International Journal Papers

1. L. B. Du, **M. Morshed**, and A. J. Lowery, "Fiber nonlinearity compensation for OFDM super-channels using optical phase conjugation," Opt. Express **20**, 19921-19927 (2012).
2. **M. Morshed**, L. B. Du, and A. J. Lowery, "Mid-span spectral inversion for coherent optical OFDM systems: Fundamental limits to performance," J. Lightwave Technol. **31**, 58-66 (2013).
3. **M. Morshed**, A. J. Lowery, and L. B. Du, "Improving performance of optical phase conjugation by splitting the nonlinear element," Opt. Express **21**, 4567-4577 (2013).
4. **M. Morshed**, L. B. Du, B. Foo, M. D. Pelusi, B. Corcoran, and A. J. Lowery, "Experimental demonstrations of dual polarization CO-OFDM using mid-span spectral inversion for nonlinearity compensation," Optics Express **22**, 10455-10466 (2014).

Referred Conference Proceedings

5. L. B. Du, **M. Morshed**, and A. J. Lowery, "604-Gb/s coherent optical OFDM over 800 km of S-SMF with mid-span spectral inversion," in *Opto-Electronics and Communications Conference* (Busan, 2012), pp. 3B2-3.
6. **M. Morshed**, L. B. Du, and A. J. Lowery, "Performance limitation of coherent optical OFDM systems with non-ideal optical phase conjugation," in *IEEE Photonics Conference (IPC)*(Burlingame, CA, 2012), pp. 394-395, TuU.
7. L. B. Du, J. Schroeder, **M. Morshed**, B. Eggleton, and A. J. Lowery, "Optical Inverse Fourier Transform Generated 11.2-Tbit/s No-Guard-Interval All-Optical OFDM Transmission," in *Optical Fiber Communication Conference/National Fiber Optic Engineers Conference 2013*(Optical Society of America, Anaheim, California, 2013), p. OW3B.5.
8. J. B. Schroeder, L. B. Du, **M. Morshed**, B. Eggleton, and A. J. Lowery, "Colorless Flexible Signal Generator for Elastic Networks and Rapid Prototyping," in *Optical Fiber Communication Conference/National Fiber Optic Engineers Conference* 2013(Optical Society of America, Anaheim, California, 2013), p. JW2A.44.
9. **M. Morshed**, L. B. Du, and A. J. Lowery, "Improving the performance of optical phase conjugator using a mid-way filter," in *CLEO-PR & OECC/PS*(Kyoto, Japan, 2013), pp. TuR4-3.
10. **M. Morshed**, L. B. Du, B. Foo, M. D. Pelusi, and A. J. Lowery, "Optical phase conjugation for nonlinearity compensation of 1.21-Tb/s pol-mux coherent optical OFDM," in *18th Opto-Electronics and Communications Conference*(Kyoto, Japan, 2013), pp. Post deadline, PD 3-4.
11. **M. Morshed**, A. J. Lowery, and L. B. Du, "Reducing Nonlinear Distortion in Optical Phase Conjugation using a Midway Phase-Shifting Filter," in *Optical Fiber Communication Conference*(Optical Society of America, San Francisco, California, 2014), p. W2A.56.
12. **M. Morshed**, B. Corcoran, and A. J. Lowery, "Improving Broad-band Mid-span Spectral Inversion Performance for Fiber Nonlinearity Compensation," in *Conference on Lasers and Electro-Optics (CLEO)*(San Jose, CA, USA, 2014), p. SW1J.8
13. **M. Morshed**, B. Corcoran, and A. J. Lowery, "Mid-span Spectral Inversion in Broad Band CO-OFDM Systems for Increased Transmission Distance," in *Optoelectronics and Communications Conference/ Australian Conference on Optical Fibre Technology (OECC/ACOFT)* (Melbourne, AUS, 2014), p. WE8B-2.
14. **M. Morshed**, B. Corcoran, L. B. Du, B. Foo, C. Zhu, and A. J. Lowery, "Carrier Phase Recovery Aided by Mid-Span Spectral Inversion in an N-WDM System," in *Optoelectronics and Communications Conferrence/Australian Conference on Optical Fibre Technology (OECC/ACOFT)* (Melbourne, AUS), p. TH11F-4.

Acknowledgements

This research project would not have been possible without the support of many people. First of all, I express my deep gratitude to my supervisor, Professor Arthur J. Lowery, for many things. To list a few, for offering me the opportunity to undertake a PhD with a very exciting topic, for encouraging me with his positive feedback all the time, for dragging me forward slowly but surely from where I was to where I should be in my research, and for sharing his immense knowledge in the area with me during this time. When I became stuck in my research, discussions with him gave me lots of new ideas that are the best treasures a student can ever get from his supervisor. I was lucky to have those abundantly from him during my discussions with him. Prof. Lowery was also very kind and sympathetic supervisor who had understanding of my personal situations as well. It is said that the good people are those who help others when asked, and the best of the people are those who help before being asked. Professor Arthur Lowery certainly falls into the latter category. I cannot imagine a better advisor and mentor for my PhD study.

Next, I would like to give my sincere thanks to Dr. Liang Bangyuan Du, with whom I had the best opportunity to work in the first two years and half of my PhD. He is a great expert in this area and an excellent individual. For example, among other things, he taught me the details of our test bed for optical fiber communication systems and helped me get started with VPItransmissionMaker. Besides these, his insight in this area was another thing that I benefited from whenever I discussed with him.

I thank also Dr. Jochen Schroeder and Dr. Mark Pelusi of Sydney University for letting me borrow their high power EDFA and WaveShapers that were crucial for the experimental demonstrations. Very special thanks go to Dr. Bill Corcoran for his helpful advice and cooperation during the last stage of this project. I also thank fellow PhD student Benjamin Foo for extending his helping hand to me during experiments.

I also thank my parents, brothers and sister for the support they have provided me throughout my entire life. I also acknowledge my wife and three loving kids Rayyan, Afnaan and Sameeha, who are blessings for me.

I am deeply grateful to Monash University for offering me an Australian Postgraduate Award APA) and Endeavour International Postgraduate Research Scholarship (IPRS), so I could travel to this beautiful country to pursue my PhD in Monash University. I also recognize that this research would not have been possible without the financial assistance of Australia Research Council Centre of Excellence for Ultrahigh bandwidth Devices for Optical Systems, CUDOS (Project number CE110001018). Finally, I would like to thank VPIphotonics.com for the use of VPItransmissionMaker.

Table of Contents

List of Figures

List of Tables

1 Introduction

1.1 Optical fibers in communication systems

Optical fibers, which are the core components of optical communication systems, offer the highest capacity of communications medium, making them the most cost-effective choice for data transmission today [1]. The history of commercial use of optical fiber communications took off when J.E. Goell of Bell laboratories reported an experiment of a 6.3-Mb/s optical signal repeater [2], targeting digital communication with newly developed low-loss optical fiber [3] in 1973. In the same year, White and Chin reported successful demonstration of a 100-Mb/s fiber communication system [4]. In these pioneering early experiments, the transmitters used direct modulation of a light-emitting diode; while the receiver consisted of PIN diodes and avalanche detectors [5]. Since then, after more than 40 years of development, optical channels with capacities as high as 100 Tb/s have been demonstrated successfully by several research groups [6, 7]. Thanks to these phenomenal developments, communications operators can still manage the data-traffic, despite the fact that demand for data transmission has increased exponentially [8] since the late 1980s, when the internet was developed and World Wide Web (WWW) was launched.

Figure 1.1 illustrates the architecture of today's telecommunication network. As shown, the network is divided in the core, the metropolitan and the access network.

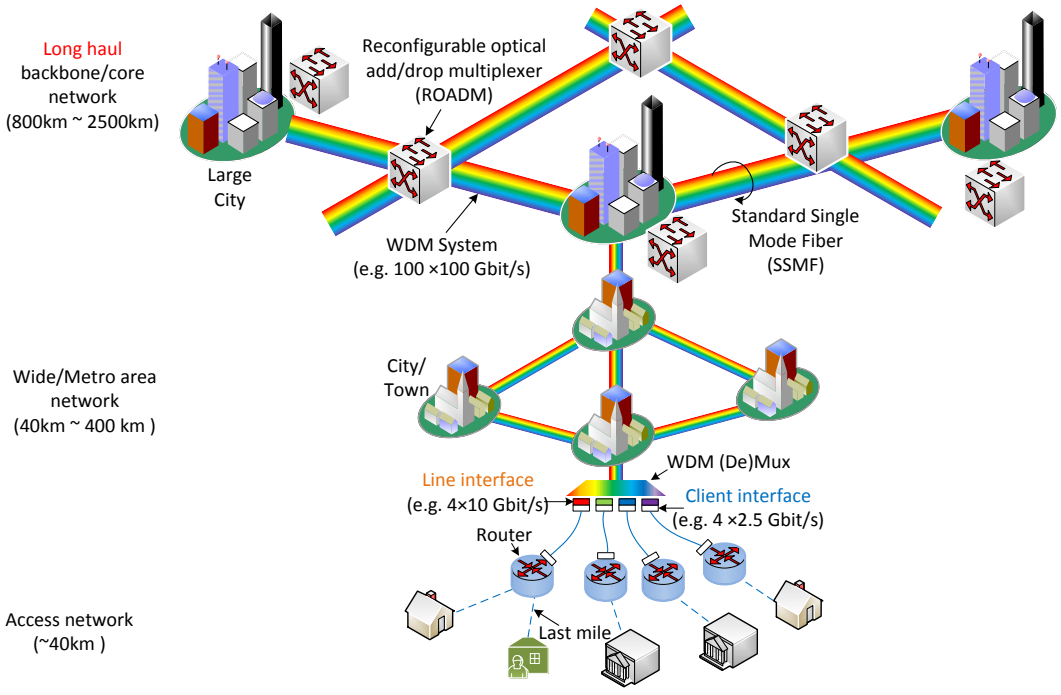

Figure 1-1: Simplified illustration of modern telecommunication network.

In the access network, which is typically less than 40 km in reach, client data are routed to be put into a transport layer via a client interface. The client interface may perform traffic aggregation, switching etc. before delivering its payload to the wide/metro area network. The connection to the end user, usually referred to as the 'last mile' is mostly co-axial cable or twisted pair copper wire. As the bandwidth of these connections is limited, especially when the distance from the local exchange node to the end user is long, this may be a cause of traffic bottlenecks. "Fiber-to-the-Home (FTTH)" can be used to overcome this bottleneck.

Several access networks are connected to the wide/metropolitan area network (WAN/MAN). The typical transmission reach of such networks spans from 40~400 km. The line interface multiplexes the data coming from access network into fixed segments spacing 50 GHz or 100 GHz centred on the International Telecommunication Union (ITU) frequency grid. This forms a so-called wavelength division multiplex (WDM) system.

Large cities around the world are connected by the core or backbone network, which typically ranges between 800 km~2500 km. This reach is also known as 'long haul' to distinguish it from 'ultra-long-haul' that ranges between 2000 km~6000 km. The backbone or core network can be considered as the 'photonic highway' of communication systems where large amounts of traffic are transmitted over long distances, with more than 100 WDM channels travelling in a single fiber. Reconfigurable add/drop multiplexers (ROADM) optically filter a frequency band that can be directed to any fiber, and thus control the WDM traffic in a fixed ITU spectrum grid. Recently, the ROADM function is evolving from a fixed segmentation to a user definable segmentation (referred to as 'flexigrid') in order to make more efficient use of the available WDM spectrum. Standard single mode fiber (SSMF), made from silica glass, are used in core network. These fibers have extremely low attenuation (0.2dB/km@1550 nm) allowing transmission up to 100 km before amplification is usually provided by erbium doped fiber amplifiers (EDFA). Furthermore, the optical bandwidth of such a fiber is extremely high. In the low-loss window of 1530-1565 nm (also referred as C-band or Conventional band) and 1565-1625 nm (also referred as L-band or Long band) alone, the total usable bandwidth is more than 10 THz.

1.2 Key enabling technologies in optical communication systems

The recent progress of the optical communication systems has been based upon development of several key enabling technologies over last decades [8]. These are:

1) 0.8 μm laser sources and multimode fibers in the early 1980s;
2) 1.3 μm lasers and single mode fibers in the mid-1980s;
3) 1.5 μm laser sources and dispersion shifted fiber (DSF) in the early 1990s;

4) Optically amplified transmission with erbium-doped fiber amplifiers (EDFA) in the mid-1990s;
5) Introduction of wavelength division multiplexing (WDM) in the late 1990s.
6) Coherent transmission and later developments.

Especially worth a mention is the development of EDFA, which coincidentally works best in the wavelength range for lowest fiber loss, 1530 nm to 1565 nm. The introduction of EDFA also paved the way for several complementary technologies; like WDM systems and electronic signal processing. While WDM systems help leverage the gain bandwidth of EDFAs, the electronic signal processing incorporated in the early 2000s in the form of forward error correction (FEC), compensates signal-to-noise (SNR) degradation due to EDFA noise [8].

Another major breakthrough in recent years is the reappearance of coherent transmission in the mid-2000s [9], which converts all the parameters; *i.e.*, amplitude, phase, frequency and state of polarization (SOP) of an optical field into the electrical domain. This enables efficient utilization of these parameters to be modulated and demodulated for high capacity long haul transmission. Especially, the ability of phase detection allows quadrature modulation to be detected which helps improve the receiver sensitivity compared with intensity modulation direct detection (IMDD) system. Also, any kind of multilevel modulation format such as *M*-ary quadrature amplitude modulation (*M*-QAM) can be introduced into optical communication system by using combined phase and amplitude modulation [10]. This helps increase the spectral efficiency (SE) by *M* times compared with SE limit of 1 bit/s/Hz/polarization of a binary modulation format.

The research in coherent transmission first took place in the early 1980s [11-16]. The main research focus at that time was using a homodyne receiver with optical phase locked loop (OPLL). However, stringent requirement on laser line width, alignment of state of polarization (SOP) of signal and local oscillator (LO) rendered it impossible to be a commercial product at that time [17]. Another disadvantage was that it required compensation for most or all impairments coming from linewidth, chromatic dispersion (CD), polarization mode dispersion (PMD) before any error signal could be extracted for using in the OPLL. Unfortunately, the analog-to-digital converter (ADC) at that time was not fast enough to enable this processing to be performed in the digital domain [18]. Fortunately, the developments of sophisticated laser sources with linewidths less than few hundred kHz [19] and faster ADCs in the recent years have enabled the implementation of digital signal processing (DSP) based compensation of the above mentioned impairments, which allows free running signal and LO lasers for today's coherent receivers [20-22].

1.2.1 Progress in the last decade

Table 1-1 summarizes the major experimental results demonstrated in research labs to show the progress in capacity (Tb/s) and spectral efficiency (bit/s/Hz) since 2001. These results are collected mainly from two of the world's most prestigious conferences in this research area: Optical Fiber Communication Conference (OFC) and European Conference on Optical Communication (ECOC).

Table 1-1: Pioneering experiments in the last decade

Year	Author	Capacity [Tb/s]	SE [bit/s/Hz]	Distance [km]	Detection	Modulation Format	Ref
2001	G. Vareille *et al.*	3	0.46	7380	Direct	NRZ	[23]
2002	G. Charlet *et al.*	6.4	0.8	2100	Balanced	Duobinary	[24]
2003	B. Zhu *et al.*	6.4	0.8	3200	Balanced	CSRZ-DPSK	[25]
2003	G. Charlet *et al.*	6.3	0.8	2700	Balanced	Duobinary	[26]
2004	G. Charlet *et al.*	6	0.8	6120	Balanced	DPSK	[27]
2005	G. Charlet *et al.*	6.5	0.8	4080	Balanced	RZ-DQPSK	[28]
2006	A. Sano *et al.*	14	2	160	Balanced	PDM-CSRZ-DQPSK	[29]
2006	A.Gnauck *et al.*	12.3	3.2	240	Balanced	PDM RZ-DQPSK	[30]
2007	A. Sano *et al.*	20.4	2	240	Balanced	PDM-CSRZ-DQPSK	[31]
2007	A.Gnauck *et al.*	25.6	3.2	240	Balanced	PDM-RZ-DQPSK	[32]
2008	A. Sano *et al.*	13.4	2	3600	Coherent	PDM QPSK OFDM	[33]
2008	J. Yu *et al.*	17	4.2	662	Coherent	PDM RZ-8PSK	[34]
2008	G. Charlet *et al.*	16.4	2	2550	Coherent	PDM QPSK	[35]
2009	X. Zhou *et al.*	32	4.1	580	Coherent	PDM RZ 8-QAM	[36]
2010	A. Sano *et al.*	69.1	6.4	240	Coherent	PDM 16-QAM	[37]
2010	X. Zhou *et al.*	64	8	320	Coherent	PDM 64-QAM	[38]
2011	D. Qian *et al.*	101.7	11	165	Coherent	DP128-QAM OFDM	[6]
2012	A.Sano *et al.*	102.3	9.1	340	Coherent	PDM 64-QAM	[7]
2013	T.J.Xia *et al.*	54	6.7	634	Coherent	PDM 16-QAM	[39]

Figure 1-2 plots the progress in spectral efficiency and capacity since 2001 from the above Table 1-1. The figure also shows the modulation formats used in those pioneering experiments to outline the evolution in optical transmitters and receivers in the last decade. The empty triangular markers show the spectral efficiency (bit/s/Hz), which is defined as the ratio of total transmission rate to signal optical bandwidth. The filled square markers show the total transmission capacity (Tb/s). Three colours indicate three types of detection scheme: direct detection (Δ & ■), balanced detection (Δ & ■) and coherent detection (Δ & ■).

Direct detection (DD) receiver uses a simple photo detector to down convert the optical signal to electrical domain. The receiver is simple, however, with direct detection receiver and non-return to

zero (NRZ) modulation format prior to 2002, spectral efficiency higher than 0.46 (bit/s/Hz) [23] could not be achieved. Therefore, total transmission capacity was clamped to about 3 Tb/s using full C+L band optical bandwidth. Then in early 2000s, balanced receivers using delay line interferometer to cancel the common noise and allowing differential phase shift keying (DPSK) increased the spectral efficiency up to 0.8 (bit/s/Hz) [24, 25, 40]. This detection scheme also improved the receiver optical signal to noise ratio (OSNR) sensitivity by about 3 dB. Fiber transmission capacity, therefore, were doubled to more than 6 Tb/s and were plateaued for a while until mid-2000s, when polarization multiplexing (Pol. Mux.) and differential quadrature phase shift keying (DQPSK) further increased the spectral efficiency by four times to 3.2 (bit/s/Hz) [30]. The highest transmission capacity reported around this time was 25.6 Tb/s [32]. In the same time around, research in coherent detection became vibrant again [9], thanks to the newly developed high speed ADC and more sophisticated lasers. Higher-order QAM was enabled by coherent detection, as it preserves all the information in amplitude, phase as well as state of polarization. After that a seamless progression of breakthroughs followed, extending spectral efficiency, capacity and distance in fiber-optics systems. Spectral efficiencies as high as 15 bits/s/Hz have been achieved recently using 1024-QAM and coherent detection in a single mode fiber [41].

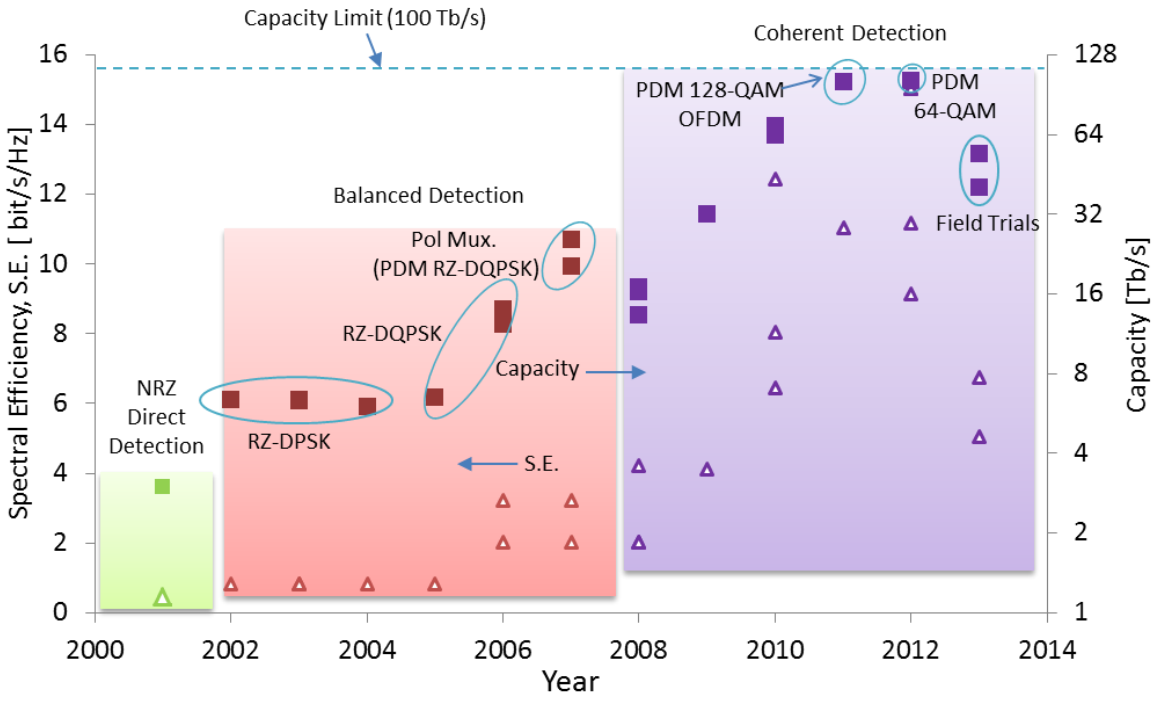

Figure 1-2: Recent progress in lightwave systems.

1.2.2 Emergence of OFDM for optical communications

With the growing demand of higher spectral efficiency in the late-2000s and a modulation format increasingly more suitable for flexible network design, orthogonal frequency division multiplexing

(OFDM) emerged as an attractive candidate in the same time. OFDM is a multi-carrier transmission technique where a data is transmitted with many lower-rate subcarrier tones which are orthogonal to each other [42]. It has been incorporated into wireless network standards (802.11a/g WiFi, HiperLAN2, 802.16 WiMAX) and digital audio and video broadcasting (DAB and DVB-T) in Europe, Asia, Australia, and other parts of the world [43, 44]. The two competing fourth-generation (4G) mobile network standards, (WiMAX, or IEEE 802.16) and Long-Term Evolution (LTE), both have adopted OFDM as the core of their physical interface [44]. Despite all its triumphs in mobile communications, it was only in 2006 that it arrived in long-haul optical communication systems. The first report aimed at simple realization based on low-cost optical components, which later came to be known as direct-detection Optical OFDM (DDO-OFDM) [45]. The other report aimed to achieve high spectral efficiency and receiver sensitivity, which now is known as coherent optical OFDM (CO-OFDM) systems [46]. In 2007, the first CO-OFDM and DDO-OFDM was experimentally reported with line rate of 8 Gb/s and 20Gb/s respectively [47, 48]. Since then, the interest in optical OFDM has increased significantly. In the last few years, the transmission capacity using OFDM continued to grow about ten times per year. In 2011, 101.7 Tb/s using polarization division multiplexed (PDM) 128-QAM CO-OFDM was demonstrated [6]. Table 1-2 shows the development of optical OFDM in recent times. In the OFC 2014, a field trial with a record-high spectral efficiency of 11.0 [b/s/Hz] was demonstrated using PDM-OFDM-256-Interative-Polar-Modulation signals over a commercially deployed legacy WDM system [49].

Table 1-2: Progress of optical OFDM in long haul fiber systems

Year	Author	Comments	Ref
	Lowery *et al.*	First proposal of DDO-OFDM	[45]
2006	Shieh *et al.*	First report on CO-OFDM	[46]
	Djordjevic *et al.*	Another report on DDO-OFDM	[50]
2007	Shieh *et al.*	First experimental demonstration of CO-OFDM, 8 Gb/s, 1000 km.	[47]
	Schmidt *et al.*	First experimental demonstration of DDO-OFDM, 20 Gb/s, 320km.	[48]
	Yang *et al.*	First 107 Gb/s CO-OFDM reception.	[51]
2008	Jansen *et al.*	First PDM-OFDM transmission, 1000km SSMF	[52]
	Yamada *et al.*	Tb/s DWDM OFDM with no-guard-interval over 2100km SSMF.	[53]
	Ma *et al.*	1 Tb/s single channel transmission over 600 km.	[54]
2009	Dischler *et al.*	1.2 Tb/s single channel transmission over 400 km.	[55]
	Chandrasekhar *et al.*	1.2 Tb/s no-guard-interval CO-OFDM over 7200 km of LEAF.	[56]
2010	Hillerkuss *et al.*	10.8 Tb/s data generated and decoded with real time optical FFT	[57]
2011	Hillerkuss *et al.*	26 Tb/s super-channel with all optical FFT over 50 km	[58]
	Qian *et al.*	101.7 Tb/s PDM-128-QAM-OFDM transmission over 165 km	[6]
2012	X. Liu *et al.*	PDM-OFDM with 256-Iterative-polar-Modulation, SE 11.15 [b/s/Hz]	[59]
2013	Du *et al.*	Flexible software-programmable 11.2 Tb/s all optical OFDM over 400 km	[60]
2014	Chandrasekhar *et al.*	Field trial of record 11 [b/s/Hz] PDM-OFDM-256-IPM signals over 495.2 km	[49]

1.3 Nonlinear Shannon limit

Despite its excellent properties, like extremely high bandwidth and low loss; optical fiber has its own unique set of problems, namely fiber nonlinearity, which does not exist in the wireless systems. The impact of fiber nonlinearities in terms of transmission capacity has been recently addressed [61-63]. It was found that in contrast to linear channels where transmission capacity could be increased indefinitely by using higher launch powers with higher-order modulation formats, the capacity of a nonlinear channel does not grow indefinitely and has a maximum value [61-63]. This is called the "nonlinear Shannon limit". The launch power where the capacity reaches its maximum is referred as nonlinear threshold (NLT) power, beyond which transmission capacity decreases again. Thus fiber nonlinearities restrict the launch power below this optimum power. Figure 1-3 shows nonlinear

Shannon limit calculated using Equations (2) and (3) from [61]. The figure shows that in the linear regime, the spectral efficiency increases as the logarithm of the launch power. However, fiber nonlinearity introduces an upper bound to the spectral efficiency, thus limiting the capacity in real fiber optic communications systems.

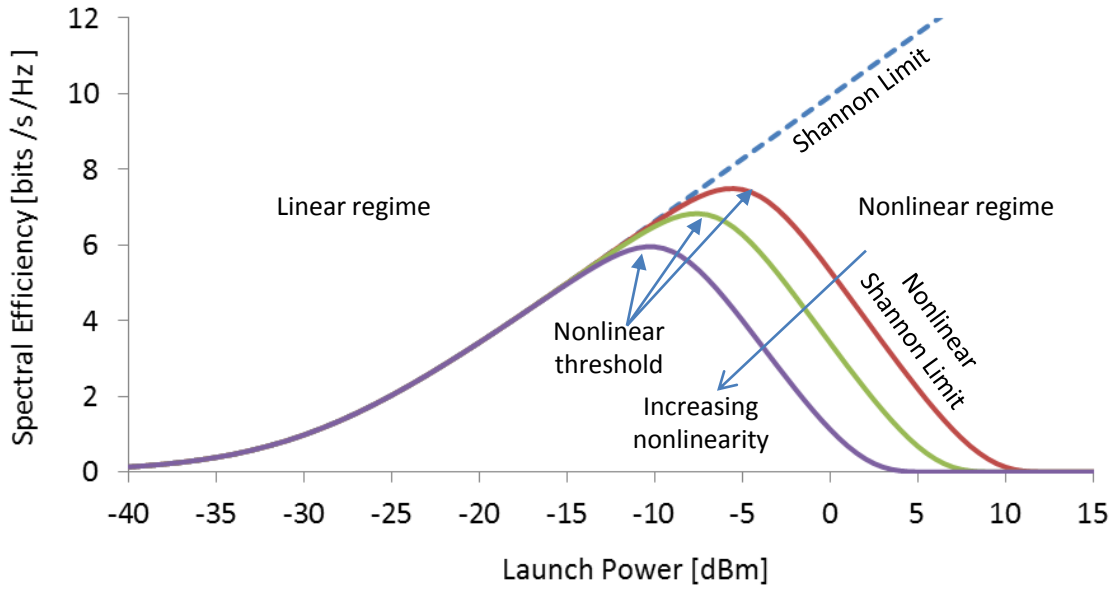

Figure 1-3: Nonlinear Shannon limit in an optical fiber channel. (Signal bandwidth = 40 GHz, Number of channels=100, Dispersion=20 ps/nm/km, nonlinear coefficient, γ=0 $W^{-1}.km^{-1}$ (▪▪▪), 5 $W^{-1}.km^{-1}$ (—), 10 $W^{-1}.km^{-1}$ (—), 25 $W^{-1}.km^{-1}$ (—)).

In addition to limiting the capacity, fiber nonlinearities also restrict the transmission distance for any high capacity long haul system. In fact, fiber nonlinearity is the major limiting factor today for any such system. Additionally, optical OFDM suffers from a well-known problem, namely high peak-to-average power ratio (PAPR) [64-66] which could add to fiber nonlinearity and thus degrade performance if not compensated.

It is for these reasons that although recent experiments have achieved capacities that are close to theoretical limit in a single mode fiber using full $C+L$ band, transmission distances were not more than mere 165 km in a standard single mode fiber (S-SMF).

Figure 1-4 shows the recent development of transmission distance against spectral efficiency collected from the Table 1-1. Three types of detection methods are also shown in ■ (Direct detection), ● (Balanced detection) and ▲ (Coherent detection). Arrow ‘a’ shows the leap in SE achieved by employing balanced detections compared with direct detections. Arrow ‘b’ shows the doubling of SE by using polarization division multiplexing (PDM). Arrows indicated by ‘c’ show the improvement in SE due to coherent detections compared with balanced detections. This was possible because of *M*-ary

modulations like 16-QAM were made possible by employing coherent detection. The arrow indicated by 'd' shows further increase in SE achieved by even higher order modulations like 1024-QAM, although at the expense of shorter transmission distances.

Figure 1-4 also shows that for transmission distance less than few hundreds km, SE as high as 15 could be achieved. However, as the transmission distance increases beyond 2500 km, SE higher than 2 bits/s/Hz are not achieved using S-SMF even with coherent receivers. Using large effective area fiber (LEAF), capacity-distance product indicator, $C \times D$ for long haul system has been extended by about three times, as indicated by arrow 'e'. However, any change in deployed fibers would require huge costs in system deployment and operation (CAPEX/OPEX). Scaling up existing system performance so that it can carry high capacity data over long distance is a realistic solution to current problem.

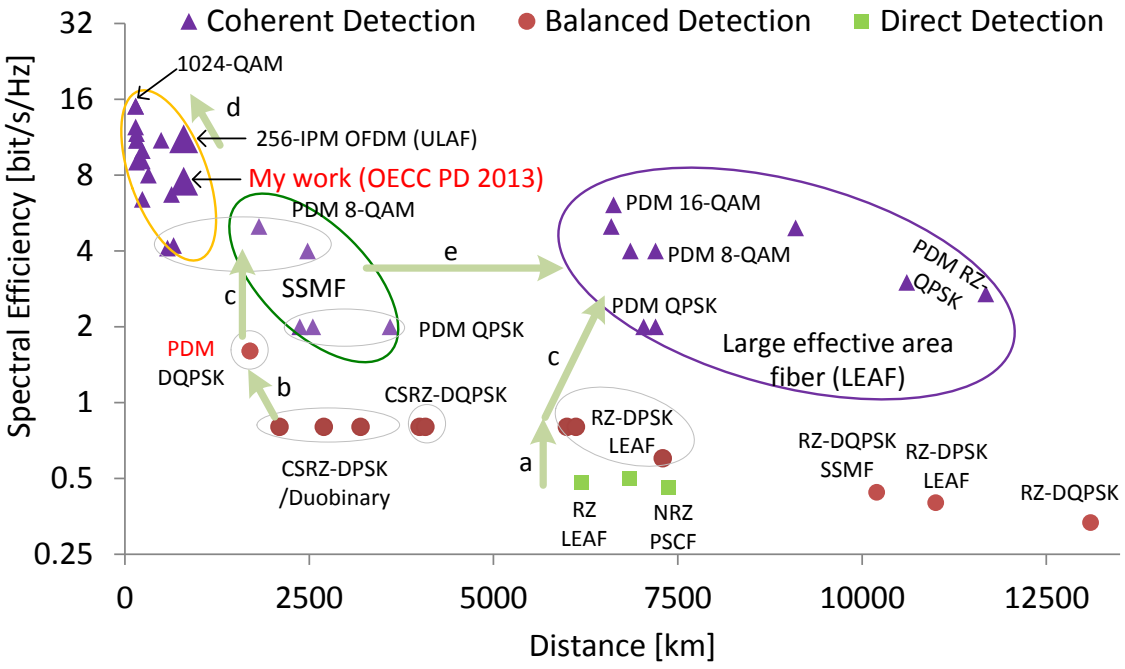

Figure 1-4: Recent development of transmission distance vs spectral efficiency.

1.4 Fiber nonlinearity mitigation

One realistic and cost effective way to scale up the system performance is mitigating the effects of fiber nonlinearity in systems. Theoretical studies have suggested that the transmission performance can be significantly improved if ideal fiber nonlinearity mitigation techniques are used, such as digital back propagation (DBP) [67, 68]. However, the high computational complexity of DBP means that achieving ideal fiber nonlinearity compensation is impractical in a link using wavelength division multiplexing (WDM) [69]. Less computationally intensive SPM [64, 70] and XPM [71] compensation

methods using digital signal processing (DSP) have been proposed. However, these methods are less effective for links without dispersion compensation, therefore are less desirable for greenfield deployments. More details of fiber nonlinearity mitigation methods will be discussed in Chapter 2.

1.4.1 Mid-span spectral inversion (MSSI) for nonlinearity mitigation

Another interesting method to compensate fiber nonlinear effect is by using optical phase conjugation (OPC) in the middle of the link, a scheme known as mid-span spectral inversion (MSSI). First proposed by Yariv *et al*. [72] for channel dispersion compensation; Pepper *et al*. [73] later extended it to show that OPC can also compensate nonlinear phase distortion. Since then, various groups have used mid-span spectral inversion (MSSI) employing OPC near the middle of the link to compensate fiber nonlinearity [74-79]. In a MSSI link, the phase of the signals is conjugated and the spectrum is inverted at the middle of the link. The signal which has accumulated phase distortions from the first part of the link due to fiber nonlinearity now has opposite phase in the second part of the link. As a result, the effects in the second part of the link after the OPC cancel out the impairments of the first part.

Although MSSI has been studied for non-coherent systems [76-78], it had not been experimentally demonstrated for any coherent optical system yet. Our group has recently performed the first experimental demonstration of using MSSI for a single polarization CO-OFDM system to compensate fiber nonlinearity in an OFDM super-channel [80, 81]. The advantage of using MSSI is that it is scalable for WDM systems because multiple wavelengths can be spectrally inverted simultaneously using a single optical phase conjugation (OPC) module [79]. It is also modulation format independent [79]. Although MSSI fell from favour after mid-2000s, due to its complexity, because systems are approaching the nonlinear Shannon limit [62, 63] and require higher OSNRs to support higher order modulation formats, MSSI may again become a useful technology in optical systems. Therefore, I have investigated using mid-span spectral inversion (MSSI) for nonlinearity compensation in CO-OFDM systems.

1.5 Goals of the research

The thesis proposes using MSSI of third order nonlinearity based optical phase conjugation (OPC) to mitigate fiber nonlinearities in CO-OFDM systems. Because the signal is spectrally inverted after the first half of the link, the second half of the link should undo all the dispersion effects and major nonlinearities of the first half. However, since only limited works have been reported so far on using MSSI for any coherent system and especially for CO-OFDM systems [82, 83], there are many theoretical and practical aspects that need to be addressed in order to discuss its possible potential for future application on optical communications, if any. The main challenges are:

- Since OFDM signals consist of many closely spaced subcarriers, it is expected that using third order nonlinearity for optical phase conjugation (OPC) in MSSI will generate thousands of FWM tones, both in and out of the conjugated signal band. It is not clear quantitatively whether these third order mixing products falling over the conjugated signal will render MSSI using third order nonlinearity based OPC unsuitable for any CO-OFDM systems.
- It is possible that the pump will also get distorted because many nonlinear products generated around it due to third order mixing. It is not clear quantitatively how many of these products cause pump degradation, and hence degrade the OPC performance.
- The OPC conversion efficiency of the third order nonlinearity based OPC will be limited by pump power. The higher the pump powers the higher the OPC conversion efficiency is. However, stimulated Brillouin scattering (SBS) will restrict the pump power into the highly nonlinear fiber (HNLF). This might put a limit on the practical OPC conversion efficiency, which in turn will lead to increase OSNR penalty due to MSSI. It is also not clear how much total insertion loss due to MSSI can be allowed in order to gain benefit from its use in any practical systems.
- Finally, the OPC conversion efficiency will vary among its conversion bandwidth due to relatively rapid walk-off for closely-spaced OFDM subcarriers with even small amount of dispersion in the HNLF. Therefore, chromatic dispersion of the HNLF will need to be as small as possible. It is not clear whether currently commercially available HNLF with non-zero chromatic dispersion will support large bandwidth OPC for using with CO-OFDM systems.

The motivation of this PhD thesis is to address these unknown issues to clarify the possibility of using third-order based OPC for CO-OFDM systems. Specifically, therefore, the motivations of this thesis are:

- Survey the current state-of-the art in optical fiber communications and existing methods for mitigating fiber nonlinearities.
- Develop analytical formalisms to quantify the performance penalty and limitations due to undesired FWM products falling over the conjugated signal.
- Analyse the OSNR penalty introduced due to MSSI, and thus outline the system that can benefit from using MSSI for nonlinearity mitigation.
- Experimentally demonstrate using MSSI with CO-OFDM for fiber nonlinearity mitigation.
- Outline the design considerations for CO-OFDM systems that use MSSI for fiber nonlinearity mitigation.
- Investigate novel OPC methods to improve system performance using MSSI.

1.6 Original contributions in this thesis

The following original contributions have been derived from this thesis:

1. Development of an analytical formalism to predict the ultimate back-to-back performance of a CO-OFDM system using OPC in MSSI based on third order nonlinearity [84, 85]. It has been identified that two major two-step nonlinear mixing products limit the performance of such a system. This is a unique contribution of this thesis which can be further leveraged to any investigation of fundamental performance improvement, and even be used to calculate the optimum launch power of an OPC module in a given system.
2. First experimental demonstration of using MSSI in a coherent optical communication system for combating fiber nonlinearities [80, 81].
3. First experimental demonstrations of using MSSI in dual-polarization CO-OFDM system [86]. This is, to the best of our knowledge, first for dual-polarization for any coherent communication system.
4. Using the insight gained from a new analytical model, two novel methods to improve the fundamental performance of optical phase conjugation based on third order nonlinearity have been proposed. The first method is splitting the highly nonlinear fiber into two parts and inserting a notch filter between them to clean the pump [87, 88].
5. The second method that has been proposed for improving the fundamental OPC performance is using a phase-shifted all pass filter, to reduce the complexity of the first method. This method improves the performance significantly with lower complexity.
6. Finally, based on the analytical model, optimization of the OPC module for a conventional way of single stage OPC has been investigated.

All these original contributions have generated four highly ranked international journal papers and ten international prestigious conference papers. These outcomes of the PhD thesis have not only impact on the theoretical and experimental understanding of MSSI in CO-OFDM systems, but it has also helped reignite the interest in this research area, and has been cited in papers from Bell Laboratories [89], Coriant R&D, Munich, Germany [90] and Aston University, Birmingham, UK [91].

1.7 Thesis outline

Figure 1-5 shows the thesis outline. The blocks of the outline are briefly introduced below.

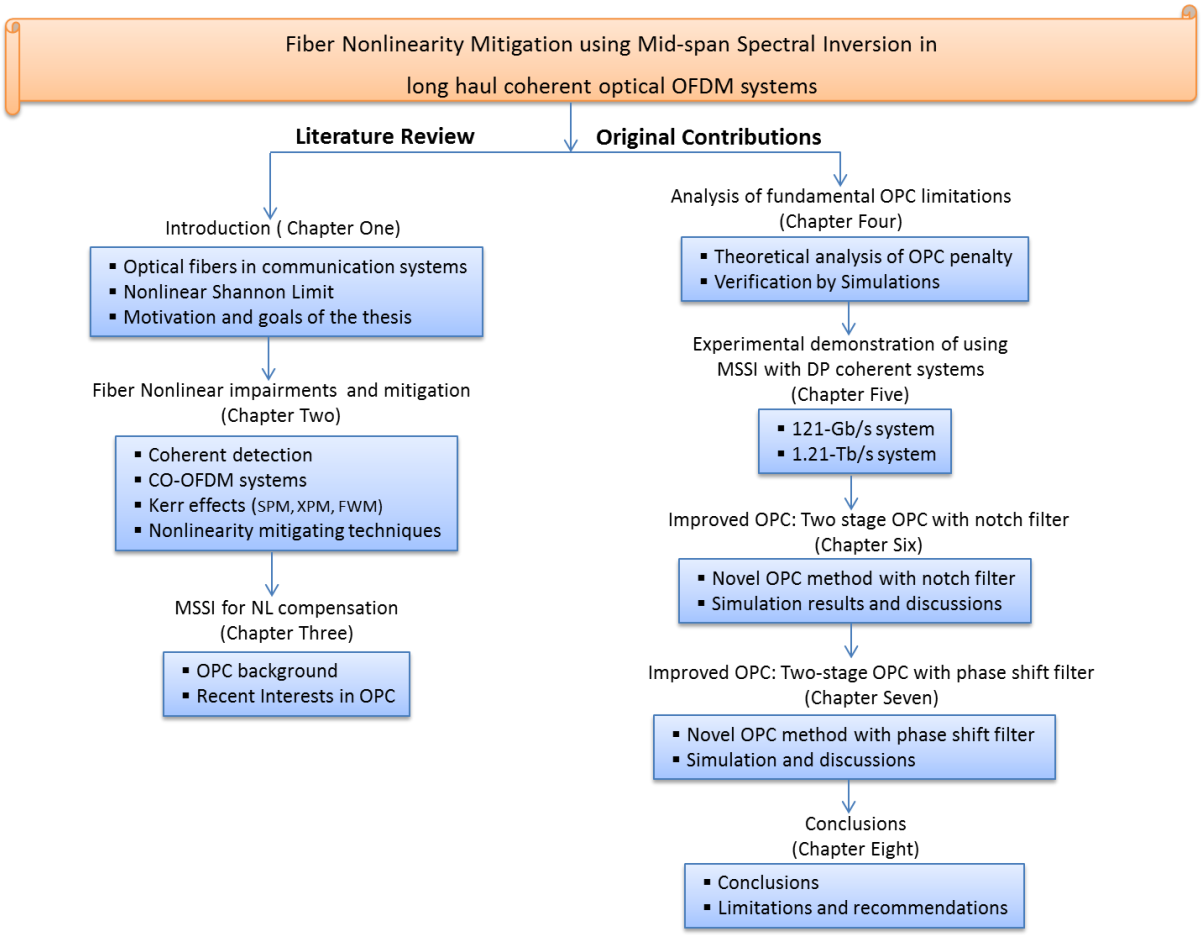

Figure 1-5: Thesis outline.

Chapter 1- Introduction

An introduction to current telecommunication network, brief history of optical communication system, its recent progress, key enabling technologies, nonlinear Shannon limit, Research goals, original contributions in this thesis are presented in this chapter. These are followed by outline of the thesis.

Chapter 2- Fiber nonlinear impairments and their mitigation

As this research aims to mitigate fiber nonlinear effects in CO-OFDM systems, brief discussions of coherent detection, polarization division multiplexing and OFDM principles have been presented first in this chapter. These are followed by theoretical introductions of various fiber nonlinear effects, like self-phase modulation (SPM), cross-phase modulation (XPM) and four-wave mixing (FWM). Discussions of fiber nonlinearities in CO-OFDM systems follow. Finally, various existing methods

for nonlinearity compensations in CO-OFDM systems are presented and their performances are compared.

Chapter 3- MSSI for optical nonlinearity mitigation

Fundamental principles of MSSI using optical phase conjugation (OPC), its mechanisms for nonlinearity compensation, and required systems conditions are discussed. These are followed by discussions of using MSSI in practical systems and its performance limitations due to asymmetrical link properties. Various techniques to mitigate this effect of asymmetrical link properties are presented. Finally recent growing interest in OPC is presented.

Chapter 4- Analysis of fundamental performance limitations of OPC

A detailed description of theoretical analysis for fundamental performance limitations using MSSI with CO-OFDM systems is presented. Based on simple FWM mixing analysis method, I found two types of two-stage nonlinear mixing products along with the ASE that inherently limit the OPC performance based on third order nonlinearities. Back-to-back system performance when using MSSI with CO-OFDM systems is also derived, which shows excellent agreement with simulations results. This chapter is the first of the original contributions derived from this PhD thesis.

Chapter 5-Experimental demonstrations of MSSI in dual polarization CO-OFDM systems

First experimental demonstrations of MSSI for dual-polarization (DP) CO-OFDM systems are presented in this chapter. The results are the first for any DP coherent systems which uses MSSI for nonlinearities mitigation. Benefits of using MSSI in terms of increased maximum viable powers are confirmed for 121-Gb/s and 1.2-Tb/s DP CO-OFDM systems comprising 10×80-km S-SMF links. Following the experimental demonstrations, simulation results have been presented, which show that these higher viable launch powers help achieve more than 70% increase in overall transmission distances with fixed span lengths.

Chapter 6-Improving the OPC performance: Two-stage OPC with notch filter

Based on the theoretical analysis presented in Chapter Four, in this chapter a novel method using two-stage OPC with a notch filter is investigated to reduce fundamental performance limitations of optical phase conjugation. Working principle and the results of the two-stage OPC with notch filter is presented. These show about 3 dB back-to-back performance improvement compared with systems using conventional OPC module. System performance at optimum launch power showing improvement of 1 dB in a 10×80-km km 4-QAM 224-Gb/s CO-OFDM systems is presented.

Chapter 7-Improving the OPC performance: Two-stage OPC with phase-shift filter

In this chapter, a practically implementable method of two-stage OPC module, using a phase-shifted all pass filter is presented. The results show about 3.6 dB back-to-back performance improvement compared with systems using conventional OPC module. Transmission system performance improvement of 1.2 dB at optimum launch power in a 10×80-km km 4-QAM 224-Gb/s CO-OFDM systems is presented. The effects of insertion loss of the filter, amplifier noise figures and XPM attenuation mechanisms are presented.

Chapter 8-Conclusions

The background of the research, the goal of the thesis, methodologies used to achieve these goals, and the results obtained in the different chapters are summarized in this chapter. Performance of MSSI for nonlinearity mitigation is compared with other existing methods. Limitations of using MSSI and recommendations for system considerations are discussed. The chapter ends with recommendations for future research.

2 CO-OFDM systems and Fiber Nonlinearities

This chapter introduces principles of coherent detection and CO-OFDM systems. These will be followed by fundamentals of various fiber nonlinear impairments due to the Kerr effect, which are the major limiting factors for any long-haul fiber-optic transmission systems, especially for CO-OFDM systems.

2.1 Coherent systems

In this section, the principle of coherent detection will be presented to show how it preserves the full information on the optical complex amplitude, i.e. the amplitude, the phase, frequency and the state of polarization (SOP) into electrical domain.

The fundamental concept of coherent detection is mixing the electric field of modulated signal light with the continuous-wave local oscillator (LO). This is achieved by using a coupler and a pair of photo-didoes configured as a balanced detector. The coupler adds 180° phase shift to either the signal field or the LO field between the two output ports. Figure 2-1 shows the schematic of a simple coherent optical receiver.

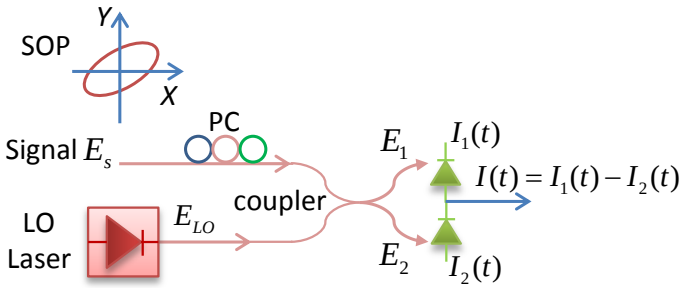

Figure 2-1: Block diagram of a balanced coherent receiver.

The optical Signal field E_s and local oscillator E_{LO} can be expressed as [10]:

$$E_s(t) = A_s(t)\exp\left(j\left(\omega_s t + \theta_s(t)\right)\right) \tag{2.1}$$

$$E_{LO}(t) = A_{LO}(t)\exp\left(j\left(\omega_{LO} t + \theta_{LO}(t)\right)\right) \tag{2.2}$$

where $A_s(t)$ is the slowly varying complex envelope of the signal, ω_s is the angular frequency of the signal, $\theta_s(t)$ is modulated signal phase, $A_{LO}(t)$ is the slowly varying complex envelope of the LO, ω_{LO} is the angular frequency of the LO, and $\theta_{LO}(t)$ is LO phase.

The SOP of the signal is adjusted by using a polarization controller (PC) to align with that of the LO light. The output electric fields of the coupler are then given by:

$$E_1 = \frac{1}{\sqrt{2}}\left(E_s + E_{LO}\right) \tag{2.3}$$

$$E_2 = \frac{1}{\sqrt{2}}\left(E_s - E_{LO}\right) \tag{2.4}$$

Upon square detection from each of the photo-diode and using Equations (2.1) and (2.2) into Equations (2.3) and (2.4), the output photo-currents can be obtained as [10]:

$$I_1(t) = \frac{R}{4}\left[P_s + P_{LO} + 2\sqrt{P_s P_{LO}}\cos(\omega_{IF} + \theta_s(t) - \theta_{LO}(t))\right] \tag{2.5}$$

$$I_2(t) = \frac{R}{4}\left[P_s + P_{LO} - 2\sqrt{P_s P_{LO}}\cos(\omega_{IF} + \theta_s(t) - \theta_{LO}(t))\right] \tag{2.6}$$

where R is the responsitivity of the photo diode, $P_s = |A_s|^2$ is the power of signal, $P_{LO} = |A_{LO}|^2$ is the power of the LO and $\omega_{IF} = \omega_s - \omega_{LO}$ is intermediate frequency. Balanced detection is usually adopted into the coherent receiver to suppress the DC component and double the signal photocurrent. The output of the balanced detector is given by:

$$I(t) = I_1(t) - I_2(t) = R\sqrt{P_s P_{LO}}\cos(\omega_{IF}t + \theta_s(t) - \theta_{LO}(t)) \tag{2.7}$$

For homodyne detection, ω_{IF} becomes zero. When $|\omega_{IF}| \gg \omega_b / 2$, with ω_b being the modulation bandwidth of the optical signal, it is referred to as heterodyne detection.

2.1.1 Phase diversity coherent receiver

By using a second homodyne receiver whose LO phase is shifted by 90° both the I and the *Q* components of the signal can be detected. This function is achieved by a 90° optical hybrid shown in Fig. 2-2.

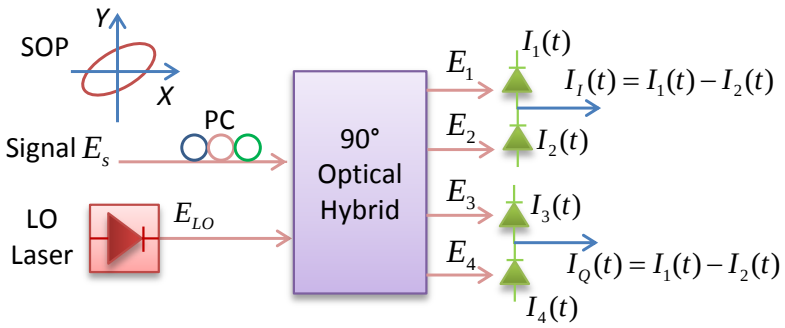

Figure 2-2: Block diagram of a phase diversity coherent detection.

The transfer matrix of the 90° optical hybrid is given as [10]:

$$T_{90^0\,hybrid} = \frac{1}{2}.\begin{bmatrix} 1 & 1 \\ 1 & -1 \\ 1 & j \\ 1 & -j \end{bmatrix} \tag{2.8}$$

This gives the input-output relation of the 90 °optical hybrid as:

$$\begin{bmatrix} E_1 \\ E_2 \\ E_3 \\ E_4 \end{bmatrix} = \frac{1}{2}.\begin{bmatrix} 1 & 1 \\ 1 & -1 \\ 1 & j \\ 1 & -j \end{bmatrix}.\begin{bmatrix} E_s \\ E_{LO} \end{bmatrix} \tag{2.9}$$

Following Equation (2.7), the outputs from balanced photodetectors are given as:

$$I_I(t) = I_1(t) - I_2(t) = R\sqrt{P_s P_{LO}}\cos(\theta_s(t) - \theta_{LO}(t)) \tag{2.10}$$

$$I_Q(t) = I_3(t) - I_4(t) = R\sqrt{P_s P_{LO}}\sin(\theta_s(t) - \theta_{LO}(t)) \tag{2.11}$$

The complex amplitude of the signal can be found by using the Equations (2.10) and (2.11) as:

$$I_c(t) = I_I(t) + jI_Q(t) = R\sqrt{P_s P_{LO}}\exp(j(\theta_s(t) + \theta_n(t))) \tag{2.12}$$

where $\theta_n(t)$ is the total phase noise including phase noise from both carrier and LO lasers arising from their finite linewidth as well as phase noise developed during transmission.

2.1.2 Polarization diversity coherent receiver

The polarization diversity receiver which detects two independent signals transmitted using two orthogonal polarizations in a single mode fiber is shown in Fig. 2-3. In this type of coherent receiver, two phase-diversity homodyne receivers are combined using two polarization beam splitters (PBS). The PBSs split both the signal and LO into two orthogonal polarizations.

The x- and y-polarization components of the signal after the PBS can be written as [10]:

$$\begin{bmatrix} E_{s,x} \\ E_{s,y} \end{bmatrix} = \begin{bmatrix} \sqrt{\alpha} A_s e^{j\delta} \\ \sqrt{1-\alpha} A_s \end{bmatrix} \exp(j\omega_s t) \tag{2.13}$$

where α is the power ratio of the two polarization components and δ is the phase difference between them. These parameters are time varying and are dependent of the birefringence of the fiber. In contrast, equal power of x- and y-polarization components are obtained from a 45° the linearly polarized LO and are given as:

$$\begin{bmatrix} E_{LO,x} \\ E_{LO,y} \end{bmatrix} = \frac{1}{\sqrt{2}} \begin{bmatrix} A_{LO} \\ A_{LO} \end{bmatrix} \exp(j\omega_{LO} t) \tag{2.14}$$

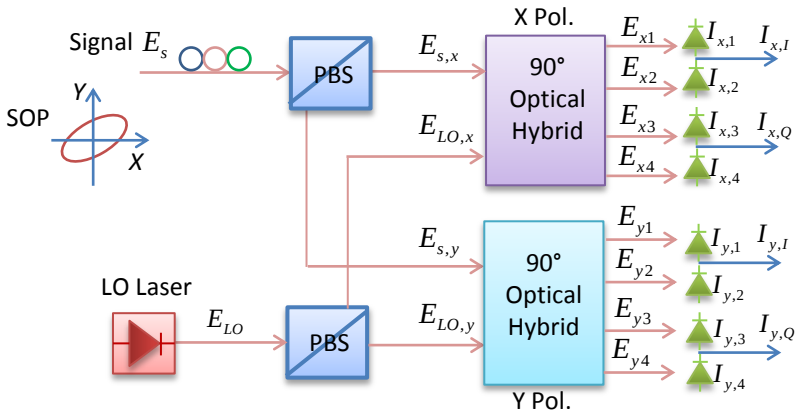

Figure 2-3: Block diagram of polarization/phase diversity coherent detection.

Using Equations (2.9), (2.13) and (2.14), the electric fields generated at the outputs of the two 90° optical hybrids can be obtained as:

$$E_{x1,2} = \frac{1}{2}\left(E_{sx} \pm \frac{1}{\sqrt{2}} E_{LO} \right) \tag{2.15}$$

$$E_{x3,4} = \frac{1}{2}\left(E_{sx} \pm \frac{j}{\sqrt{2}} E_{LO} \right) \tag{2.16}$$

$$E_{y1,2} = \frac{1}{2}\left(E_{sy} \pm \frac{1}{\sqrt{2}} E_{LO} \right) \tag{2.17}$$

$$E_{y3,4} = \frac{1}{2}\left(E_{sy} \pm \frac{j}{\sqrt{2}} E_{LO} \right) \tag{2.18}$$

where $E_{LO} = E_{LO,x} = E_{LO,y}$. Following the same process as of Equations (2.10) and (2.11), output photocurrents are then given as:

$$I_{x,I}(t) = R\sqrt{\frac{\alpha P_s P_{LO}}{2}} \cos(\theta_s(t) - \theta_{LO}(t) + \delta) \tag{2.19}$$

$$I_{x,Q}(t) = R\sqrt{\frac{\alpha P_s P_{LO}}{2}} \sin(\theta_s(t) - \theta_{LO}(t) + \delta) \tag{2.20}$$

$$I_{y,I}(t) = R\sqrt{\frac{(1-\alpha) P_s P_{LO}}{2}} \cos(\theta_s(t) - \theta_{LO}(t)) \tag{2.21}$$

$$I_{y,Q}(t) = R\sqrt{\frac{(1-\alpha) P_s P_{LO}}{2}} \sin(\theta_s(t) - \theta_{LO}(t)) \tag{2.22}$$

The complex amplitudes of the two polarization components can be restored by using the above four equations as:

$$I_{xc}(t) = I_{x,I}(t) + jI_{x,Q}(t) \tag{2.23}$$

$$I_{yc}(t) = I_{y,I}(t) + jI_{y,Q}(t) \tag{2.24}$$

These equations show that the polarization diversity receiver can separately detect the complex amplitudes of the two polarization components.

2.1.3 Digital coherent receiver

A combination of coherent detection and digital signal processing produces a digital coherent optical receiver, which has produced record transmission results, such as maximum capacity [7], maximum capacity distance product [92, 93], and maximum spectral efficiency [94]. Not only can digital

coherent receivers allow for more robust transmission, but due to the presence of a local oscillator, the receiver is inherently flexible in frequency selectivity, permitting new network architectures [95].

Figure 2-4 shows a schematic of a digital coherent receiver. Following the inphase and quadrature component detection of optical field, the corresponding photo-currents are sampled by analog-to-digital converters (ADC). Subsequently, the sampled data are processed by digital signal processing (DSP) blocks to decode the transmitted data. As shown in Fig. 2-4, the standard DSP processing blocks for a single carrier system consists of resampling and IQ imbalance compensation, CD compensation, MIMO channel equalization, carrier recovery, demodulation and BER estimation [95].

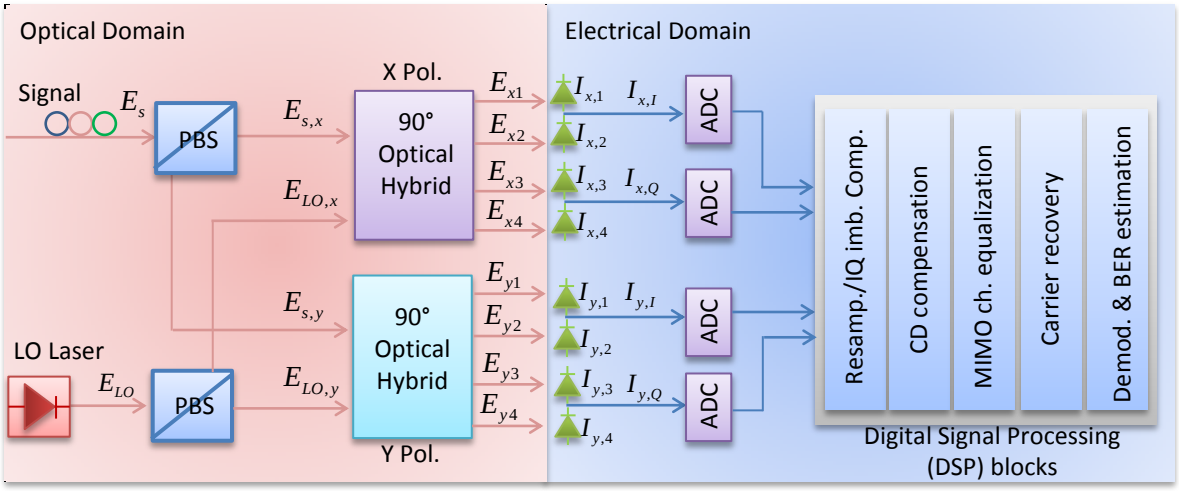

Figure 2-4: Configuration of a digital coherent receiver.

2.2 CO-OFDM systems

OFDM is a special class of multi-carrier modulation (MCM), which, instead of transmitting data using a single carrier, transmits in parallel on a number of different subcarriers. As a result the symbol period is much longer than for a single carrier system with the same total data rate. Since the symbol period is longer, inter-symbol interference (ISI) affects at most one symbol. Therefore, equalization is simplified [96]. The key distinction of OFDM from conventional multicarrier system is the use of orthogonality in OFDM subcarriers (SC). This is achieved digitally using an inverse fast Fourier transform (IFFT). This enables the generation of orthogonal subcarriers for OFDM in precise and computationally efficient way.

Figure 2-5(a) shows a schematic of seven orthogonal subcarriers with frequency spacing of Δf . It shows that although the spectra of individual subcarriers overlap, since they are orthogonal, the subcarriers can be demodulated without inter-carrier interference (ICI). Figure 2-5(b) shows the waveforms in time domain. The subcarriers are mathematically orthogonal to each other over one

OFDM symbol period T_s. The frequency spacing is given by the inverse of the symbol rate, i.e. $\Delta f = \frac{1}{T_s}$. OFDM waveform is obtained by the summation of all the subcarrier-waveforms, as shown in Fig. 2-5(b). Fig. 2-5(b) also shows the BPSK phase modulation on each of the OFDM subcarriers to illustrate modulation principle using OFDM. The subcarriers can be modulated both in phase and amplitude.

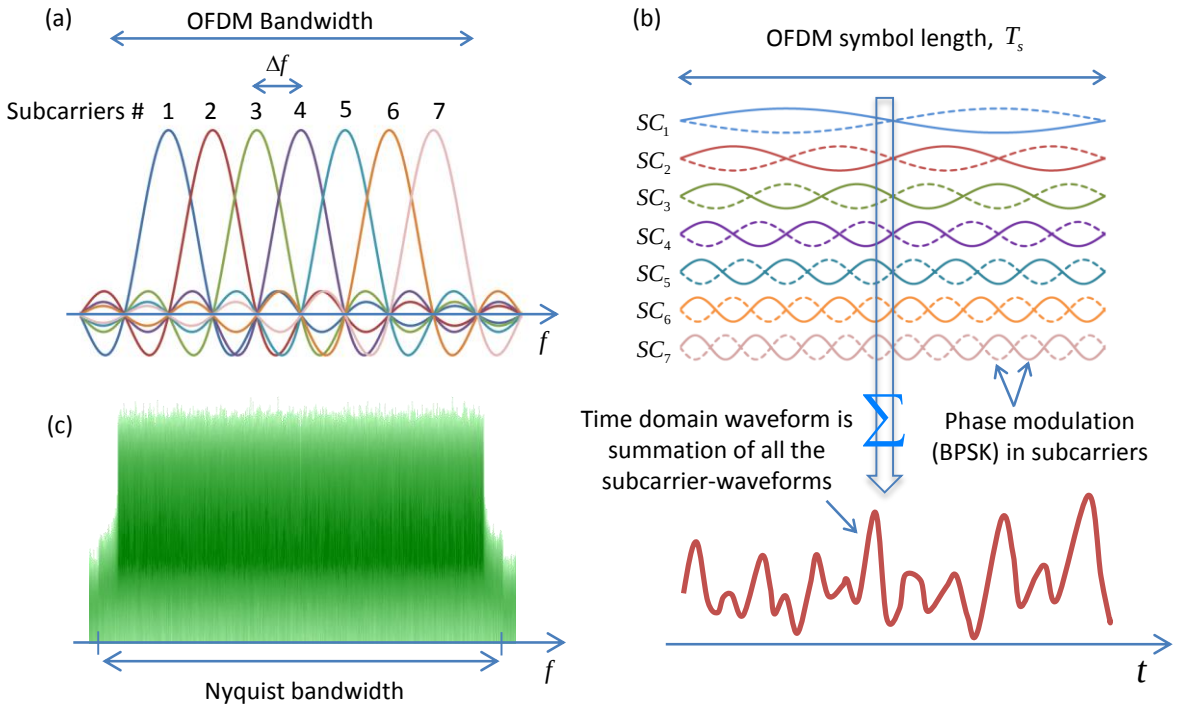

Figure 2-5: Principle of OFDM and its spectrum.

An OFDM signal spectrum can fill in available bandwidth close to the Nyquist bandwidth, thus improving the spectral efficiency. This is shown in Fig.2-5(c), for example, using an OFDM signal with 924 subcarriers, Δf of 125 MHz and OFDM symbol length of 105.6 ns. Demultiplexing at the receiver is usually performed by a fast Fourier transform (FFT).

In order to cope with dispersive channel effects such as chromatic dispersion and polarization mode dispersion, a cyclic prefix (CP) is used in most OFDM systems. In other words, a number of samples from the end of the symbol are appended to the beginning of the symbol. Figure 2-6 shows two OFDM subcarriers without CP upon the reception. The slow subcarrier is delayed by fiber group delay by amount t_d against the fast subcarrier. When a DFT window containing a complete OFDM symbol for the fast subcarrier for the *i*-th symbol, for example, is selected, it is apparent that a part of the slow subcarrier symbol has moved out of the DFT window boundary. This leads to so-called inter-symbol-interference (ISI).

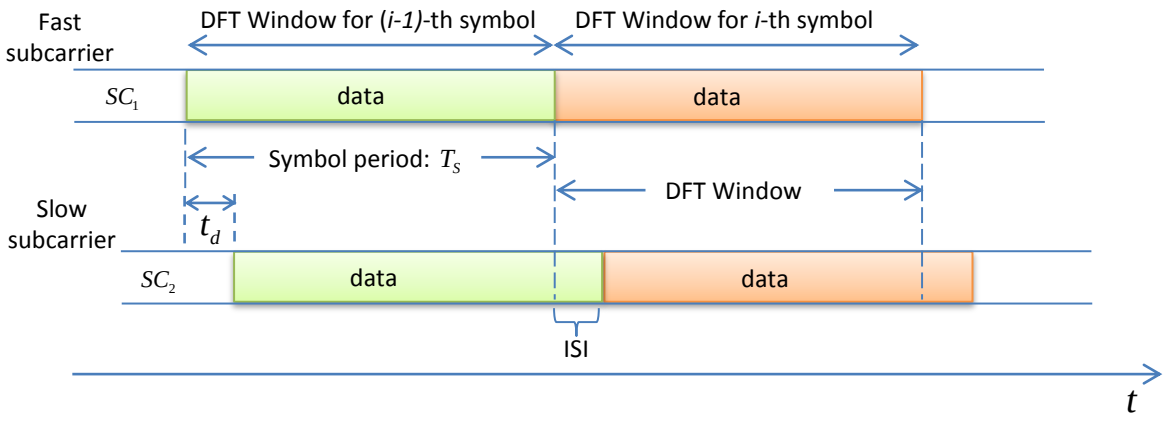

Figure 2-6: OFDM signals at the receiver without CP.

In contrast to that, when CP is used, it can be seen from Fig. 2-7 that a complete OFDM symbol for slow subcarrier is also maintained in the DFT window.

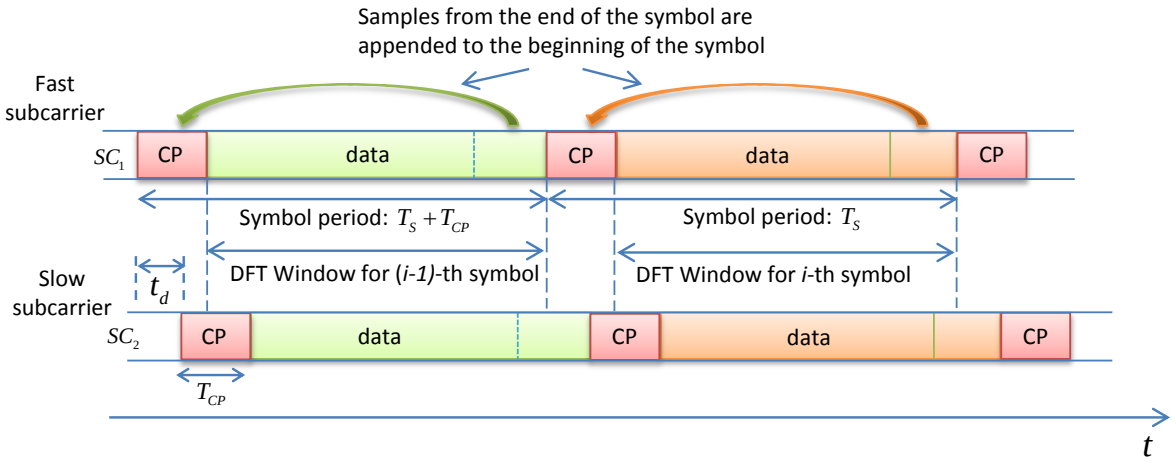

Figure 2-7: OFDM signals at the receiver with cyclic prefix.

This is because, a portion of the CP has moved into the DFT window to make up the identical part that has shifted out. Therefore, the OFDM symbol for slow subcarrier is an almost identical copy of the transmitted waveform with an additional phase shift. This phase shift is compensated through channel estimation and will be subsequently removed for symbol decision. The important criteria for ISI-free OFDM transmission is given by [43, 96]:

$$t_d < T_{CP} \tag{2.25}$$

Although the CP lengthens the OFDM symbol without transmitting additional data, so reduces the overall data rate, it is the key to simple equalization in OFDM [96].

2.2.1 Transmitter structure of CO-OFDM systems

The basic function blocks of a typical transmitter for CO-OFDM system are shown in Fig. 2-8 [97]. The receiver structure for CO-OFDM is shown in Fig. 2-9 [97]. In the transmitter, data are first serial-to-parallel (S/P) converted before being mapped into *M*-QAM modulation format. Each of the output of the *M*-QAM modulator block represents the data to be carried on the corresponding subcarrier. A training symbol which is a known OFDM symbol is then added periodically. The data in the training symbol is often chosen for the lowest PAPR, so it will not be distorted by clipping. The frequency domain data are then converted into time domain data by IFFT operation, which distinguish OFDM from single carrier systems. The data are then parallel-to-serial (P/S) converted before cyclic prefix (CP) is added. The *I* and *Q* tributaries of the data are then passed through DACs and LPFs before modulating a complex Mach-Zehnder modulator, which modulates the data onto an optical carrier coming from an external cavity laser (ECL).

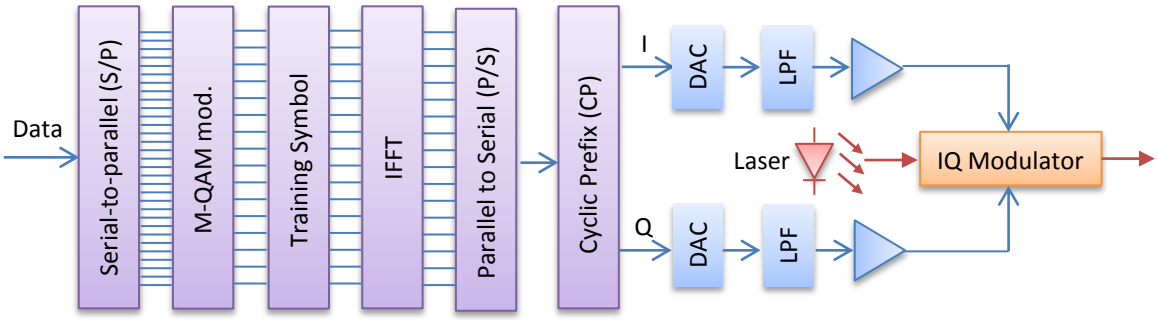

Figure 2-8: Schematic diagram of a CO-OFDM transmitter.

2.2.2 Receiver structure of CO-OFDM systems

At the receiver as shown in Fig. 2-9, the coherently detected *I* and *Q* data are sampled by ADCs and then combined to restore the complex amplitude of the received signal. This is then followed by symbol timing synchronization, removal of cyclic prefix and serial-to-parallel conversion. FFT is then performed to demultiplex the data into frequency domain subcarriers, which facilitates frequency domain CD compensation and channel estimation using simple 1-tap equalizer. In the case of MIMO processing, the zero-forcing 1-tap equalizer becomes an equalizer with a 2×2 matrix per subcarrier per OFDM symbol. Then carrier recovery, demodulation and BER estimation follows before parallel-to-serial conversion retrieves the data [96].

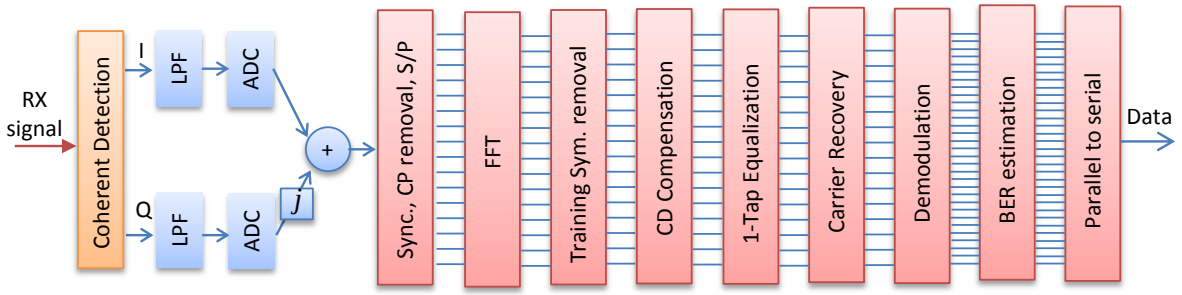

Figure 2-9: Schematic diagram of a CO-OFDM receiver.

2.3 Kerr effect

Optical fiber, made of silica glass (SiO_2) shows its nonlinearity for intense electromagnetic fields. The nonlinear optical response of a fiber to an optical wave is described by its electric-dipole induced polarization, $\hat{P}(t)$, as a power series expansion in the electric field, $E(t)$ [98]. This is expressed as:

$$\hat{P}(t) = \varepsilon_0 \left(\chi^{(1)} \cdot E(t) + \chi^{(2)} \cdot E^2(t) + \chi^{(2)} \cdot E^3(t) + \cdots \right) \tag{2.26}$$

where ε_0 is the permittivity of vacuum and $\chi^{(n)}$ is the n^{th} order susceptibility ($n = 1, 2, 3...$).

Susceptibilities higher than the 3rd order, in general, have small effects in transmission systems and can, therefore, be neglected. The linear susceptibility $\chi^{(1)}$ is the dominant contribution to $\hat{P}(t)$. It includes effects like fiber loss and material dispersion. For low optical powers, all higher order susceptibilities can be neglected. The second order susceptibility $\chi^{(2)}$ causes such nonlinear effects as second-harmonic generation (SHG) and sum-frequency generation (SFG). This effect is zero in media that have an inversion symmetry at the molecular level [98]. Since SiO_2 is a symmetric molecule, hence $\chi^{(2)}$ vanishes for optical fibers. As a result, optical fibers do not usually show second-order effects.

The lowest-order nonlinear effects in optical fibers arise from the third order susceptibility, $\chi^{(3)}$, commonly known as the Kerr effect. Due to the Kerr effect, the refractive index, n of a fiber becomes dependent on the optical power, P of the transmitted signal, and can be expressed as

$$n(\omega, P) = n_0(\omega) + n_2 \frac{P}{A_{eff}} = n_0(\omega) + n_2 I \tag{2.27}$$

where A_{eff} is the effective mode are of the fiber, $I = \frac{P}{A_{eff}}$ is the optical intensity and $n_0(\omega)$ and n_2 are the linear and nonlinear components of refractive index, respectively.

The linear Schrödinger Equation (LSE) [99] can describe the property light in optical fibers. Adding a term for the Kerr effect to the LSE [99], gives nonlinear Schrödinger Equation (NLSE) expressed as [99]:

$$\frac{\partial A}{\partial z} = -\frac{\alpha}{2} - \beta_1 \frac{\partial A}{\partial t} - \frac{j}{2}\beta_2 \frac{\partial^2 A}{\partial T^2} + \frac{1}{6}\beta_3 \frac{\partial^3 A}{\partial T^3} + j\gamma |A|^2 A \tag{2.28}$$

where A is slowly varying envelope of the field, and related to optical power by $P = |A|^2$. In Equation (2.28), β_1 in [ps/km] corresponds to the group-velocity as $\beta_1 = 1/v_g$. β_2 in [ps^2/km] and β_3 in [ps^3/km] represent the group velocity dispersion (GVD) and dispersion slope, respectively. The nonlinear coefficient, γ, is expressed in [W^{-1}.km^{-1}] and is defined as:

$$\gamma = \frac{n_2 \omega_0}{c A_{eff}} = k_0 \frac{n_2}{A_{eff}} \tag{2.29}$$

From Equation (2.28) it can be concluded that the impact of the Kerr effect is proportional to the optical signal power, $P = |A|^2$. As the signal power exponentially decreases along the fiber due to attenuation, the Kerr effect is the strongest in the first part of a fiber span. This part of the fiber span is referred to as effective length, L_{eff} [98]:

$$L_{eff} = \frac{1 - \exp(-\alpha L)}{\alpha} \tag{2.30}$$

For example, the effective length of an 80-km S-SMF with attenuation of 0.2 dB/km ($\alpha = 0.0461$ Np/km) is $L_{eff} = 21.15$ km.

Instead of the GVD, it is more common to use the dispersion parameter *D*, related to β_2 as

$$D = -\frac{2\pi c}{\lambda^2}\beta_2 \tag{2.31}$$

The dispersion parameter *D* is expressed in [ps/nm/km].

The Kerr effect manifests as self-phase modulation (SPM), cross-phase modulation (XPM) and four-wave mixing (FWM) depending on the transmission link, and channel properties. These are the most important nonlinear effects in optical communications today and will be discussed next.

2.3.1 Self-phase modulation (SPM)

The dependence of the refractive index on optical intensity, *I* (equal to the optical power per effective area in the fiber) as expressed by Equation (2.27), causes intensity dependent phase shift to the signal, which is referred to as self-phase modulation (SPM). The effect of SPM can be analysed by neglecting the effects of group velocity and chromatic dispersion ($\beta_1 = \beta_2 = \beta_3 = 0$) in the NLSE Equation (2.28) [98], which then becomes:

$$\frac{\partial A}{\partial z} = \left(-\frac{\alpha}{2} + j\gamma P \right) A \tag{2.32}$$

The solution can be obtained for the evolving field and is given as:

$$A(z,T) = A(0,T).\exp(-\alpha z/2).\exp(\, j(k+\gamma P)z - \omega t) \tag{2.33}$$

Where $A(0,T)$ represents the optical field amplitude at $z = 0$ and $k = n_0 k_0$ denotes wave number with $k_0 = \frac{\omega}{c}$ and $n_0 = n(\omega)$ as the linear, frequency dependent refractive index. The phase of the wave is the argument of the complex exponential function and is given by:

$$\begin{aligned} \varphi(z,t) &= \left(k + \gamma P\right) z - \omega t \\ &= \left(n_0 k_0 + k_0 \frac{n_2}{A_{eff}} P \right) z - \omega t \\ &= \left(n_0 + n_2 I\right) k_0 z - \omega t \end{aligned} \tag{2.34}$$

The phase alteration due to SPM is given by second term inside the bracket and is expressed by:

$$\varphi_{SPM}(z) = n_2 k_0 I L_{eff} = \gamma P L_{eff} \tag{2.35}$$

where L_{eff} the effective length as is defined in Equation (2.30).

The temporal change of the phase corresponds to the frequency of the wave. Therefore, the frequency of the wave is:

$$\omega(z) = -\frac{d\varphi(z,t)}{dt} = \omega_0 - \gamma L_{eff} \frac{dP}{dt} \tag{2.36}$$

Therefore, SPM induced frequency shift is given by [100] :

$$\Delta\omega_{SPM} = -\frac{d\varphi_{SPM}}{dt} = -\gamma L_{eff}\frac{dP}{dt} \tag{2.37}$$

The effect of GVD was not considered in the above equations. Together with GVD, this spectral broadening can lead to broadening or compression of an optical pulse. The longer-wavelength (redder) components travel faster than the shorter wavelength (bluer) ones in normal dispersion regime ($D<0$ or $\beta_1>0$). Therefore, the pulse shows the red components at the leading edge and the blue components at the trailing edge in such fibers. However, due to SPM, the leading edge is also shifted to longer wavelengths, while the trailing edge will be shifted to shorter wavelengths. Hence, both effects - SPM and GVD - act in the same direction and lead to a stronger temporal broadening of the pulse. Therefore, in the case of normal dispersion, SPM together with GVD leads to a reduction of the transmittable bit rate [100]. If the pulses spectrally-broadened by SPM are transmitted in the range of an anomalous dispersion range ($D>0$ or $\beta_2<0$) instead, the behaviour is opposite [100]. For example, the GVD of S-SMF is in the anomalous regime ($\beta_2<0$). Therefore, GVD induced temporal broadening is the inverse to that induced by the frequency broadening caused by SPM in SSMF. This results in a compression of the pulse in S-SMF [101].

Figure 2-10 shows the simulated SPM effect of a single non-return-to-zero (NRZ) 10 Gb/s channel transmitted through an 80 km of S-SMF. The figures in the left column (a, b, c and d) show the spectra, while those on the right column show time domain pulses. The input power in the fiber was 13 dBm, which was in the nonlinearity regime of the fiber so to clearly capture the SPM effect. Fiber attenuation (0.2 dB/km) is considered in all of these cases. Figure 2-10 (a), (a)' show the spectra and waveforms at the fiber input. The spikes at 10 GHz intervals are the clock within the NRZ signal at the bit rate. Clear and distinct pulses are visible in the fiber input. Figure 2-10(b), (b)' shows the fiber output with CD (16 ps/nm/km) but without fiber nonlinearity (γ =0 $W^{-1}.km^{-1}$). Due to CD, the waveform is distorted, with no change in its spectrum. Figure 2-10(c), (c)' shows the fiber output with fiber nonlinearity (γ =1.3 $W^{-1}.km^{-1}$), but without CD. Due to fiber nonlinearity, the spectrum is broadened. However, comparing Fig. 2-10 (a)' and (b)', it is understood that when CD is zero, the pulses do not show any pulse-broadening effects even with high SPM effect. The last row of the figure shows the fiber output when CD (16 ps/nm/km) is considered along with the fiber nonlinearity (γ =1.3 $W^{-1}.km^{-1}$). CD reduces spectral-broadening due to intra-channel walk-off. The waveforms show the neighbouring pulses overlap, which is mainly due to the fiber CD.

The temporal variation under GVD will convert the phase modulation (PM) induced by SPM into amplitude modulation (AM) of the received signal which in turn leads to a penalty in coherent transmission systems [102].

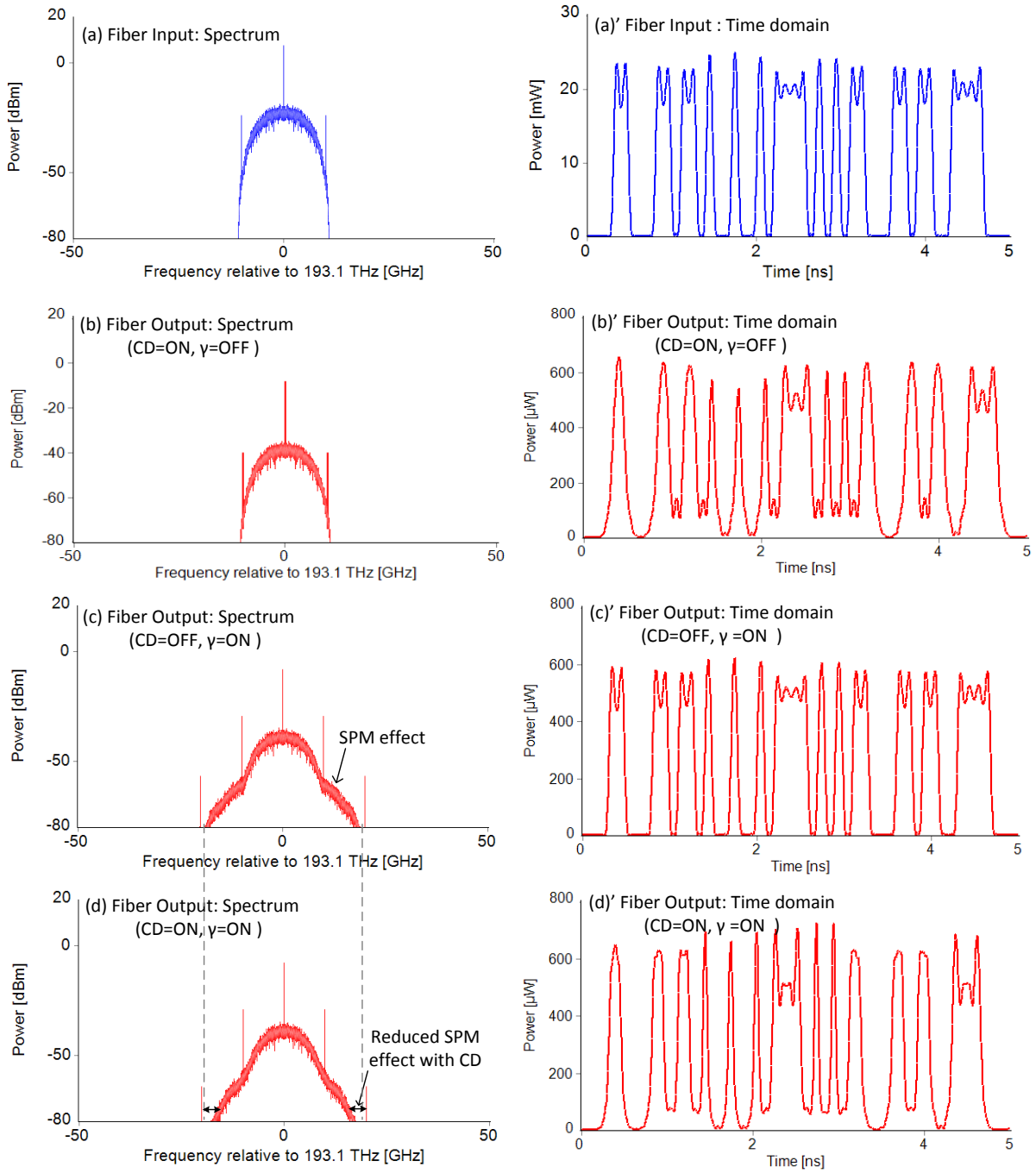

Figure 2-10: SPM effect in frequency and time domain in fiber input and output. (CD=16 ps/nm/km, nonlinear coefficient, γ =1.3 $W^{-1}.km^{-1}$).

2.3.2 Cross-phase modulation (XPM)

Cross-phase modulation (XPM) occurs in WDM systems and has a similar mechanism to SPM. In this case, optical power fluctuations in a WDM channel are converted to phase fluctuations in other co-propagating WDM channels [101]. In addition, since the refractive index seen by a particular

wavelength is affected by both the optical intensity of that channel itself and also by the optical power of neighbouring channels, SPM is always present when XPM occurs.

For a system consisting of *M* number of WDM channels, the SPM and XPM effect on Channel 1 is expressed by including the XPM term in the NLSE given by Equation (2.32):

$$\frac{\partial A_1}{\partial z} = j\gamma\left(P_1(z,t) + 2\sum_{i=2}^{M} P_i(z,t) \right) A_1 \qquad (2.38)$$

$$\text{SPM} \quad \overbrace{\qquad\qquad}^{\text{XPM}}$$

The first term in the parenthesis represents the SPM contribution and the second term shows the XPM effect. The factor 2 in the XPM expression shows the effect of XPM is twice than that of SPM for a given power. Fiber attenuation effect has been neglected in this Equation.

Since SPM is always present when XPM occurs, the total phase shift in the presence of XPM is given by:

$$\varphi_{XPM} = \gamma L_{eff}\left(P_1 + 2\sum_{i=2}^{M} P_i \right) \qquad (2.39)$$

The corresponding spectral broadening is expressed by:

$$\Delta\omega_{XPM} = -\gamma L_{eff}\left[\frac{dP_1}{dt} + 2\sum_{i=2}^{M} \frac{dP_j}{dt} \right] \qquad (2.40)$$

Again, the effect of chromatic dispersion is not considered here. With dispersion, XPM scales with the walk-off length which means two channels decorrelate under dispersion as they travel along. The walk-off length, L_W , is defined as the propagation length for which a faster moving pulse is shifted by one bit with respect to a slowly moving pulse of a co-propagating channel. L_W for two channels with group velocities v_{g1}, v_{g2} and bit period T_B is defined as:

$$L_W = \frac{T_B v_{g1} v_{g2}}{\left|(v_{g1} - v_{g2})\right|} \qquad (2.41)$$

As understood from the above equation, XPM is most severe when the difference in group velocities (or GVD) of the channels is small so that the neighbouring WDM channels propagate almost completely synchronous along the fiber. This occurs when the channel spacing between the WDM channels is small or when the dispersion coefficient of the fiber is low. When the difference in GVD

among the channels is large, the induced phase fluctuation of a pulse in a channel is spread over several pulses of the neighbouring channels and hence the XPM-induced impairments are small.

Figure 2-11 shows the simulation results of three co-propagating 10 Gb/s NRZ channels spaced 25 GHz apart transmitted through an 80 km S-SMF. Fiber input from each channel was 10 dBm.

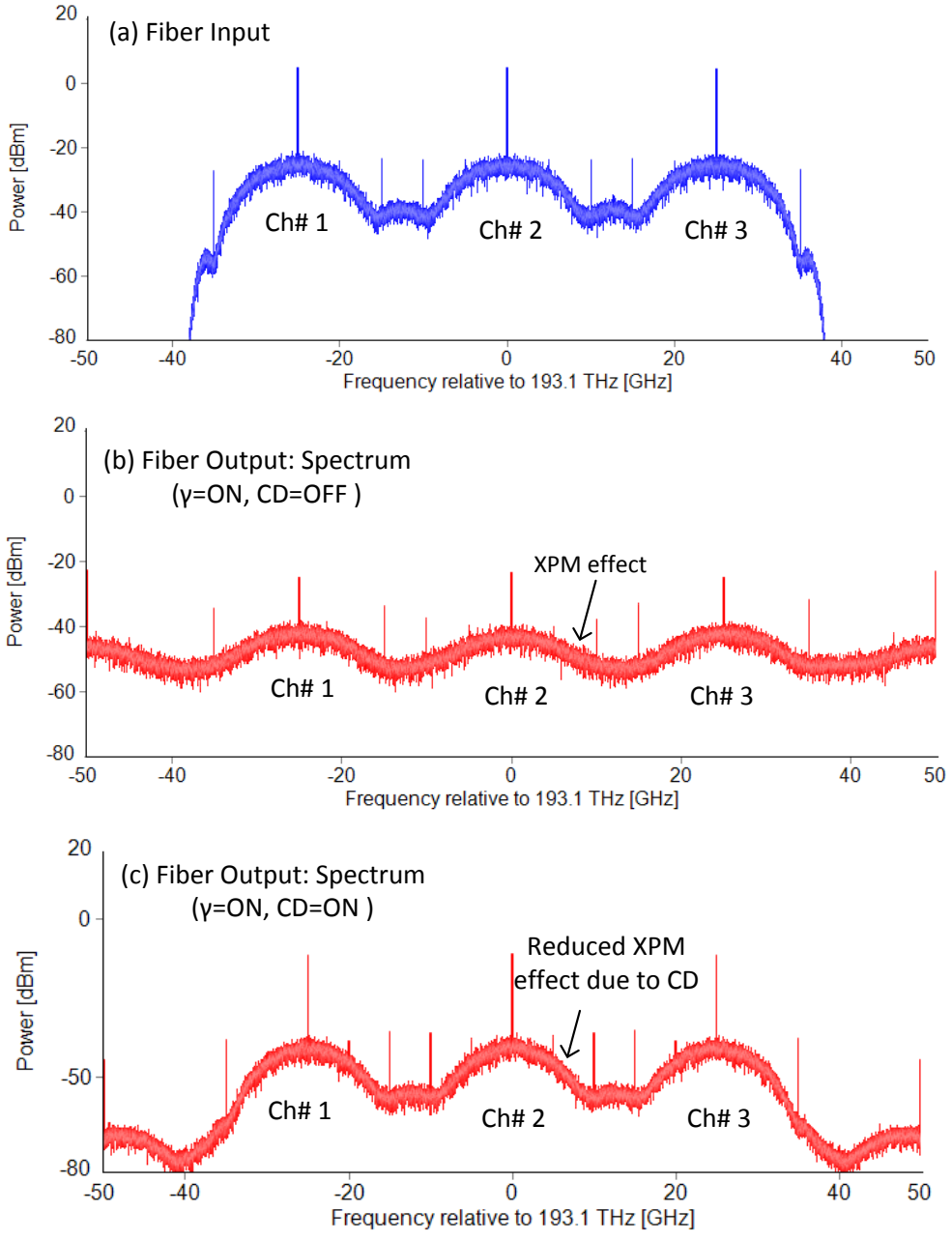

Figure 2-11: XPM effect with and without CD. (CD=16 ps/nm/km, nonlinear coefficient, γ =1.3 $W^{-1}.km^{-1}$).

Figure 2-11 (a) shows the spectrum at the fiber input, while (b) and (c) shows spectrum at the fiber output without and with CD (16 ps/nm/km) respectively. The fiber nonlinear coefficient is γ =1.3 $W^{-1}.km^{-1}$ and fiber attenuation is 0.2 dB/km. Due to the XPM effect, the two neighbouring channels

interact with the center channel and cause the spectrum-broadening as shown in Fig. 2-11 (b). Figure 2-11 (c) shows that XPM effect is reduced under CD, due to the channel walk-off effect.

As can be seen, the influence of XPM is much more important than the influence of SPM in WDM systems. Although this dominance can be effectively weaker if the effects of dispersion are included into the consideration, XPM is still the most important factor that determines the transmission capacity of optical fibers.

Finally, XPM is dependent on the polarization of the interacting channels. It has the strongest effect for co-polarized channels and the weakest effect for orthogonal or interleaved channels.

2.3.3 Four-wave mixing (FWM)

Four-wave mixing (FWM) is a manifestation of the Kerr effect at which three waves interact with each other to generate a fourth wave due to third-order nonlinearity. The new waves are generated with sum and difference frequencies. Similar to XPM, FWM is a multi-channel effect and dependent on the optical power, polarization and channel spacing of the WDM systems. While FWM is a way of describing the effect of Kerr nonlinearity in the frequency domain, XPM is a time-domain representation. FWM especially becomes major problem with OFDM systems or with DWDM systems having evenly spaced channels.

If three optical waves with frequencies f_i, f_j and f_k are co-propagating in the fiber, they can interact via third order nonlinearity and new waves with the frequencies $f_{i,j,k} = f_i + f_j - f_k$ can be generated by the FWM process, where i, j and k can have the values 1, 2 and 3. The waves with frequencies f_i and f_j are called pump waves, whereas the wave with frequency f_k is called the signal wave. $f_{i,j,k}$ is the so-called idler wave. If the signal frequency f_k equals either of the pump (f_i, f_j ,) frequencies, no new frequency is generated, resulting in f_i or f_j respectively ($f_i + f_j - f_i = f_j$). In fact, these cases give rise to either SPM ($n = k = i = j$) or XPM ($n = i, j = k$) [103]. Therefore, an additional condition for FWM process is $k \neq i, j$. Under this condition, for *N* original channels, the number of possible FWM products is

$$M = \frac{1}{2}\left(N^3 - N^2\right) \tag{2.42}$$

It is worth mentioning that, if the intensities of the newly generated FWM products are strong enough, they can interact again with each other or with the channels and will produce additional higher order mixing products.

Figure 2-12 shows the simulation results of three co-propagating CW lasers with linewidths of 10 MHz, spaced 200 MHz apart travelling an 80 km S-SMF. The power from each CW laser into the S-SMF was 10 dBm.

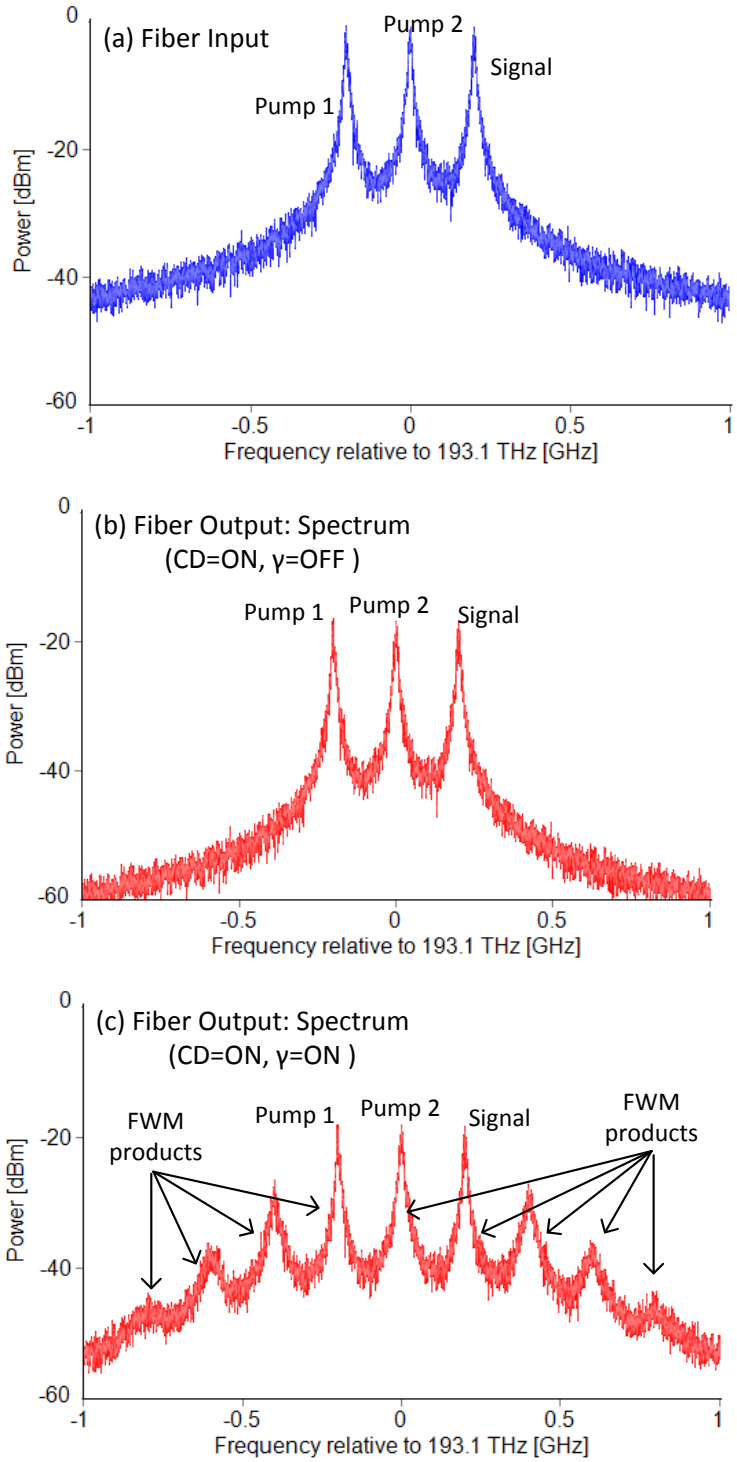

Figure 2-12: FWM generation for three equally spaced tones. (CD=16 ps/nm/km, nonlinear coefficient, γ =1.3 $W^{-1}.km^{-1}$).

Figure 2-12(a) shows the spectra at the input of the S-SMF. Figure 2-12(b) shows the output of the fiber with attenuation and chromatic dispersion but no Kerr effect. With no Kerr effect, the spectra of the CW lasers show no broadening effect or any new frequency components. However, due to the Kerr effect, as shown in Fig. 2-12(c), the overall spectra is broadened as predicted by SPM and XPM effect discussed earlier. Due to the FWM effect, nine frequency components are also generated. Three of these new components fall over the Pump 1, 2 and the signal, and three new components fall either side of the mixing signals, hence giving a total of six products at new frequencies.

FWM occurs strongly when the phases between the interacting signals are matched. However, due to chromatic dispersion, the group-velocity is not the same for all interacting signals. The smaller the difference in phase-velocity, the better the phase matching between different WDM channels is and hence the stronger the FWM generation. Therefore, FWM is stronger in transmission systems with low dispersive fibers and with narrow channel spacings.

For mathematical simplicity, only three interacting waves shown in Figure 2-12 (a) is considered. Although there are nine FWM products in this case, for the sake of simplicity, only one of them whose frequency is given by: $\omega_4 = \omega_1 + \omega_2 - \omega_3$ will be quantified. The NLSE Equation (2.38) in this case also includes the FWM effect. Therefore, the complex amplitude of an idler located at frequency, ω_4 is a solution of [100]:

$$\frac{\partial A_4}{\partial z} = j\gamma\left[\underbrace{\left(P_4 + 2\sum_{i\neq 4}^{M} P_i\right)}_{SPM\ \ XPM} A_4 + \underbrace{2A_1A_2A_3^* \exp(j\Delta k_{1,2,-3,-4}z)}_{FWM}\right] \tag{2.43}$$

where $i = 1,2,3,4$ and $\Delta k_{1,2,-3,-4}$ is called the wavenumber mismatch:

$$\Delta k_{1,2,-3,-4} = k_1 + k_2 - k_3 - k_4 \tag{2.44}$$

All other FWM components can be expressed in the same manner.

Neglecting the phase alteration by SPM and XPM, the following expression for the idler amplitude, A_4 is obtained:

$$\frac{\partial A_4}{\partial z} = 2j\gamma A_1A_2A_3^* \exp(j\Delta k_{1,2,-3,-4}z) \tag{2.45}$$

The power transfer from the pump waves to the signal and idler is described by Equation (2.44). If the equation becomes zero; *i.e*. the phases of the pump waves on one side and the signal and idler on the

other side are matched, the power transfer are maximum. If this phase-matching condition is not met, then the power transfer between these waves is decreases.

The power of the idler can be obtained from square of the idler field, A_4 obtained from the above equation and is expressed by [104]:

$$P_4 = \frac{1024\pi^6}{n^4\lambda^2c^2}\left(\frac{D\chi^{(3)}L_{eff}}{A_{eff}}\right)^2 P_1P_2P_3\exp(-\alpha L_{eff})\eta \tag{2.46}$$

where η is called the FWM efficiency, and is given by [104]:

$$\eta = \frac{\alpha^2}{\alpha^2+\Delta\beta^2}\left(1+\frac{4\exp(-\alpha L_{eff})\sin^2(\Delta\beta L_{eff}/2)}{\left(1-\exp(-\alpha L_{eff})\right)^2}\right) \tag{2.47}$$

where $\Delta\beta = \beta_1+\beta_2-\beta_3-\beta_4$ represents the phase mismatching.

Ellis *et al.* [105] and K. Inoue [106] has extended the FWM efficiency for multi-spans transmission and showed that phase-mismatching characteristic differs in transmission lines with and without optical amplifiers. This is called so-called phase-array (PA) effect [107]. The FWM efficiency, η in a multi-stage optical amplifier system can be expressed as [106]:

$$\eta = \frac{\alpha^2}{\alpha^2+\Delta\beta^2}\left(1+\frac{4\exp(-\alpha L_{eff})\sin^2(\Delta\beta L_{eff}/2)}{\left(1-\exp(-\alpha L_{eff})\right)^2}\right)\times\frac{\sin^2(N\Delta\beta L_{eff}/2)}{\sin^2(\Delta\beta L_{eff}/2)} \tag{2.48}$$

Figure 2-13 shows the FWM efficiency as a function of frequency separation between the interacting waves. The blue dotted curve shows FWM efficiency for single span using Equation (2.47). The red solid curve shows FWM efficiency using Equation (2.48) for 10 spans, each with 80 km of S-SMF. It shows that FWM efficiency decreases with frequency separation, due to the phase-array effect.

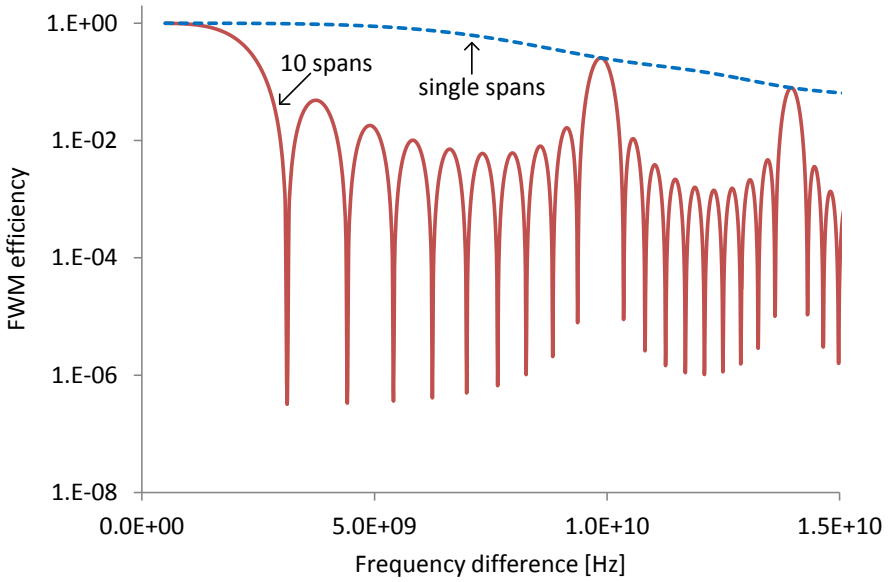

Figure 2-13: FWM efficiency as a function of frequency separation.

2.3.4 Analysis of fiber nonlinearities in CO-OFDM systems

The effect of FWM in CO-OFDM systems was of especially great interest because the subcarriers in the OFDM systems are closely spaced [108]. This means that FWM products could add coherently along the fiber's length rather than adding incoherently as the subcarriers will not walk-off. Lowery *et al.* developed a simple formula for estimating the signal quality for CO-OFDM systems in multi-span optical link [66], by calculating the power of each FWM product and number of FWM products that fall on each subcarrier. The results show that the degradation in nearly independent of the number of OFDM subcarriers, but is strongly dependent on the optical power and the fiber nonlinear coefficient, as given by:

$$q^2 \approx \frac{1}{2(\gamma L_{eff} P_{sig})} \tag{2.49}$$

where P_{sig} is the total OFDM signal power. By neglecting CD, the results provided a reasonable upper bound on the impact of FWM impairment in CO-OFDM systems.

Nazarathy *et al.* later developed a rigorous analytical closed-form expressions for the impact of FWM impairments in a CO-OFDM systems in a multiple spans dispersive link [107]. A new consequence of this analysis is that, even though OFDM subcarriers are closely spaced, the FWM contributions of the individual span do not add up in-phase. Similar to the presence of nulls in the radiation pattern of phased-array antennas, destructive interference may occur between the FWM products of the

individual fiber spans. As a result of this phased-array FWM effect, the overall FWM impact is greatly reduced in CO-OFDM systems.

The phase-array induced improvement is intuitively illustrated in Fig. 2-14. Fig. 2-14 (a) shows the phasor addition of the regularly dephased FWM products from each of the spans, forming a polygon tending to close onto itself [109]. This yields reduced overall FWM contributions. This remarkable FWM cancellation is made possible because the majority of the FWM products experience sufficient dispersive mismatch to place them in the sidelobes region shown in Fig. 2-14(b).

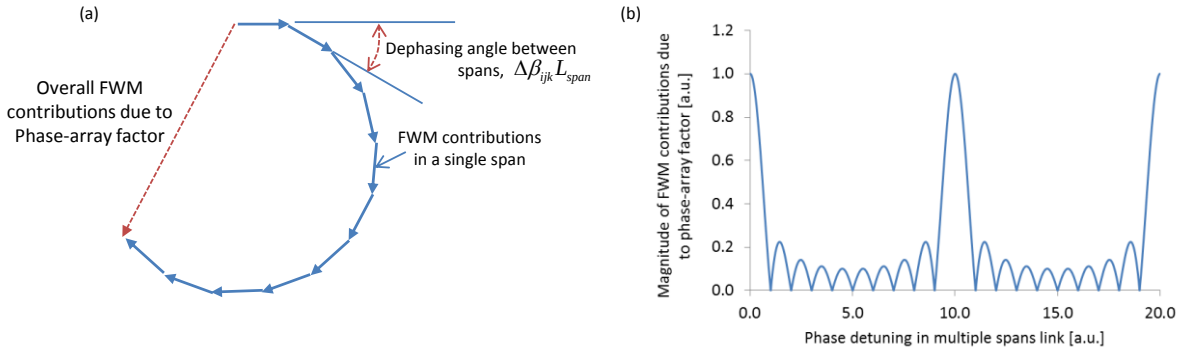

Figure 2-14: FWM contributions of the multiple spans for CO-OFDM systems (a): Phasor addition of FWM products in a multi-span dispersive link; (b) Phase-array factor versus phase detuning.

Chen *et al.* later derived simple closed-form expressions for nonlinear system performance of densely spaced CO-OFDM systems in multi-span dispersive links, identifying the dependence of system performance on key system parameters like fiber dispersion, number of spans, dispersion compensation ratio, and overall bandwidth [110]. The result showed that a total capacity of 25 Tb/s can be achieved for 10×100 S-SMF uncompensated EDFA-only single polarization 4-QAM CO-OFDM systems within the C-band alone [110]. Using combined *C+L* band and polarization division multiplexing, this shows the possibility transmitting 100 Tb/s in 10×100 S-SMF EDFA-only link using CO-OFDM systems.

2.3.5 Polarization dependence of nonlinear effects

Polarization division multiplexing (PDM), which transmits two channels with orthogonal states of polarization (SOPs) at an identical wavelength, is considered a standard option today for optical coherent systems as it doubles the spectral efficiency. PDM propagation with 2 WDM channels, for example, is schematically shown in Fig. 2-15.

Two important linear polarization effects are polarization-mode dispersion (PMD) and polarization-dependent loss (PDL) [111]. PMD arises from the random birefringence in fibers and optical

components, in which signals with different SOPs travel at different speeds. PDL occurs in optical components, such as isolators and couplers, whose insertion loss varies with the SOPs of input signals. The nonlinear polarization effect caused by fiber nonlinearity is manifested in cross polarization modulation (XPolM) between channels. When there are time-dependent amplitude and SOP variations in PDM channels, XPolM generates time-dependent nonlinear polarization scattering, which cause crosstalk between two polarizations for a PDM signal [111].

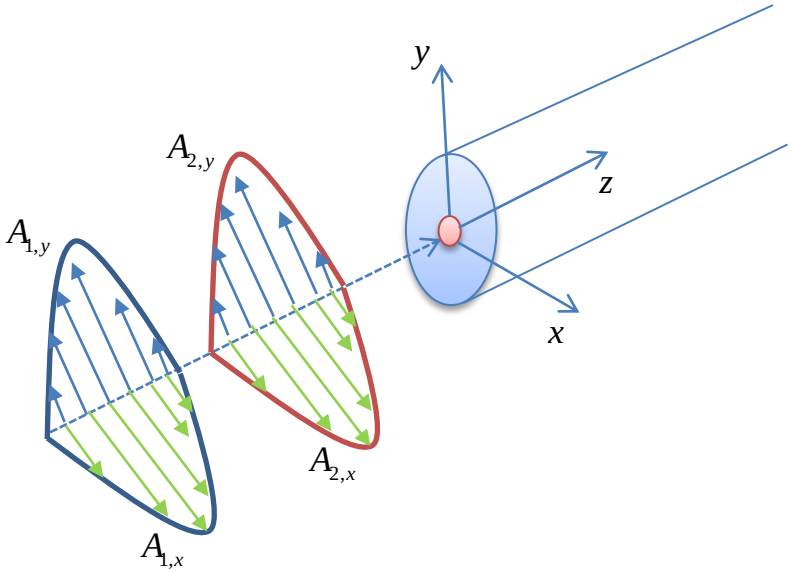

Figure 2-15: Propagation in a polarization division multiplexed (PDM) transmission system.

Consider a PDM WDM system with two channels ($i=1,2$) and the two channels have no overlapping spectra, as shown in Fig. 2-15. By neglecting four-wave mixing (FWM) between the two channels, signals propagation through the fiber can be expressed by coupled nonlinear Schrödinger equation (CNLSE) [100] :

$$\frac{\partial A_{1x}}{\partial z}+\beta_1\frac{\partial A_{1x}}{\partial t}+\frac{j}{2}\beta_2\frac{\partial^2 A_{1x}}{\partial t^2}=j\gamma\left[\left(\left|A_{1x}\right|^2+\left|A_{2x}\right|^2+\frac{2}{3}\sum_i\left|A_{iy}\right|^2\right)A_{1x}\right] \tag{2.50}$$

$$\frac{\partial A_{2x}}{\partial z}+\beta_1\frac{\partial A_{2x}}{\partial t}+\frac{j}{2}\beta_2\frac{\partial^2 A_{2x}}{\partial t^2}=j\gamma\left[\left(\left|A_{2x}\right|^2+\left|A_{1x}\right|^2+\frac{2}{3}\sum_i\left|A_{iy}\right|^2\right)A_{2x}\right] \tag{2.51}$$

$$\frac{\partial A_{1y}}{\partial z}+\beta_1\frac{\partial A_{1y}}{\partial t}+\frac{j}{2}\beta_2\frac{\partial^2 A_{1y}}{\partial t^2}=j\gamma\left[\left(\left|A_{1y}\right|^2+\left|A_{2y}\right|^2+\frac{2}{3}\sum_i\left|A_{ix}\right|^2\right)A_{1y}\right] \tag{2.52}$$

$$\frac{\partial A_{2y}}{\partial z}+\beta_1\frac{\partial A_{2y}}{\partial t}+\frac{j}{2}\beta_2\frac{\partial^2 A_{2y}}{\partial t^2}=j\gamma\left[\left(\left|A_{2y}\right|^2+\left|A_{1y}\right|^2+\frac{2}{3}\sum_i\left|A_{ix}\right|^2\right)A_{2y}\right] \tag{2.53}$$

$$\underbrace{\qquad}_{SPM}\quad\underbrace{\qquad}_{XPM}\quad\overbrace{\qquad}^{XPolM}$$

In the parenthesis of the Equations (2.52)-(2.53) above, the first term is SPM, the second term is polarization independent XPM and the third term is polarization dependent XPM or XPolM.

Similar to the derivation of the spectral broadening for SPM and XPM, the spectral broadening due to XPolM in Channel 1x is:

$$\varphi_{XPolM,1x}=\frac{2}{3}\gamma L_{eff}\sum_i\left|A_{iy}\right|^2 \tag{2.54}$$

2.4 Mitigating nonlinear effects

In the previous section, major fiber nonlinear impairments that degrade the system performance with increased launch power have been discussed. Therefore, it is not surprising that there has been considerable research interest in recent years that focus on mitigating the fiber nonlinear effects. In this section, various methods that are being investigated for mitigating fiber nonlinearities in CO-OFDM systems are discussed. However, it is worth mentioning that most of the methods proposed for CO-OFDM systems apply equally well to single-carrier coherent systems.

2.4.1 PAPR reduction

The high PAPR problem, which is proportional to the instantaneous signal power, increases the nonlinear effects in OFDM systems. However, conventional (single carrier per wavelength) systems also acquire high PAPR when propagating along dispersive fibers, especially if in-line dispersion compensation is not used.

An intuitive approach for reducing the detrimental effect of PAPR is to keep the instantaneous signal power close to its average at all times [103]. This is equivalent to minimizing the signal's PAPR, for which a several strategies have been suggested [112]. However, in a dispersion uncompensated link, the PAPR changes quickly depending on the accumulated chromatic dispersion (CD) and as a result the feasible improvement using this method is limited [113].

The most basic method to reduce the PAPR is to simply clip the OFDM signal [114]. However, this causes distortion which moves the constellation points from their original locations, and for most

cases, causes the symbols to move closer to other constellation points. This results in an increased bit-error-ratio (BER) [115], but can partially mitigated by changing the decision thresholds.

Another example of PAPR reduction scheme is the Selected Mapping Technique (SLM) [103] . SLM is based on the fact that the FWM effect is strongly dependent on the relation of the subcarriers' phases at the fiber input. Therefore, a set of vectors containing random complex phases is predefined in this scheme. Before sending an OFDM symbol, the OFDM vector in the frequency domain is weighted with the SLM vector that minimizes the PAPR [103]. However, this scheme comes at the price of a decreased data rate as the choice of the SLM phase vector has to be transmitted along with the data. It also comes with increased transmitter complexity, as an additional IFFT operation is necessary for every SLM phase vector [103].

Yet another scheme for reducing PAPR was using active constellation extension (ACE) [115]. The main idea of ACE is to reduce the PAPR by maintaining the minimum distance between constellation points and only allowing extension away from the maximum-likelihood decision boundaries [115]. However, the trade-off is increase in average power, in addition to the fact that this scheme is not suitable for higher order QAM, which is required for higher spectral efficiency.

2.4.2 Intensity-based SPM compensation:

It was first demonstrated by Liu *et al.* [116] and Xu *et al.* [117] that intensity of the received signal can be used to reduce phase jitter by compensating nonlinear phase noise for DPSK transmission with dispersion managed soliton (DMS) system. The schematic of the proposed method is shown in Fig. 2-16, where a phase modulator is used to modulate the phase of the data pulses in front of the receiver. The variable RF delay is used so that the optical and electrical signals of the same data pulse arrive at the phase modulator simultaneously. The magnitude of the phase modulation is directly proportional to the detected pulse intensity, and the sign is opposite the nonlinear phase shift due to SPM [117]. Numerical simulations showed that this method reduced the phase noise by about 5 dB in DMS-DPSK systems [117].

Later, Ho *et al.* performed the above compensation using electronic circuits at the receiver by using an optimum scaling factor [118]. The results showed that using optimum compensation, the standard deviation of residual phase noise is halved, doubling the transmission distance in DPSK systems limited by nonlinear phase noise [118].

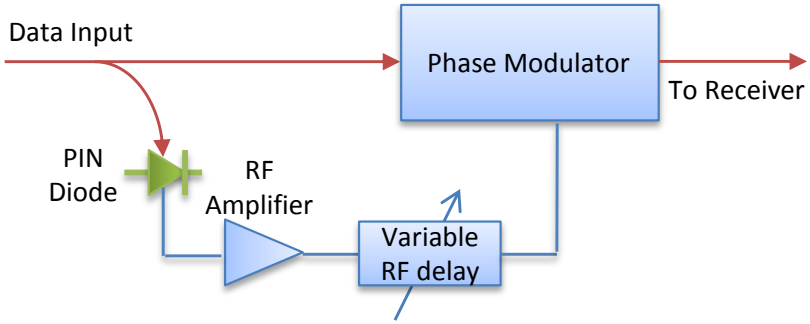

Figure 2-16: Schematic diagram of phase noise compensator using received intensity.

Lowery *et al.* proposed the similar technique using pre-compensation at the transmitter end for CO-OFDM systems [64]. This pre-compensation of nonlinearity uses a model of an 'inverse' fiber at the transmitter, so that the real transmission fiber undoes the effects of this 'virtual' inverse fiber [64]. In this method [64], a phase advance, $\theta(t)$ in proportion to the instantaneous optical power $P(t)$ is applied to the transmitted signal that is input to the first fiber span :

$$\theta(t) = 2\pi n_2 P(t) s L_{eff} / \left(\lambda_0 A_{eff}\right) \tag{2.55}$$

where S is the number of fiber spans. The advantage of this technique is that it can be applied either in the optical domain, where the optical power is proportional to the square of the sum of the fields of the subcarriers, as would be detected by a photodiode. More conveniently, it can be applied in the digital domain just after the inverse fast Fourier transform (IFFT) at the transmitter. The limiting side is that, the above expression of the phase neglects the CD effect completely. Therefore, although the method is highly promising where fiber dispersion is zero or low, its effectiveness is poor for real SSMF based systems where dispersion is large.

Receiver side post-compensation method of the above approach has also been experimentally demonstrated [70, 119-121], although with limited improvement. The pre-compensation is only accurate at the initial stages of the fiber link as it uses the transmitted power in its calculation, whereas the post-compensation is only effective at the final stages of the link as it uses the received power. An optimum combination of pre- and post-compensation gives far better results than the pre- or post-compensation alone [121]. The process is implemented both at the transmitter, following the IFFT, and at the receiver, prior to the FFT process [121, 122]. Figure 2-17 shows block diagram for such a method.

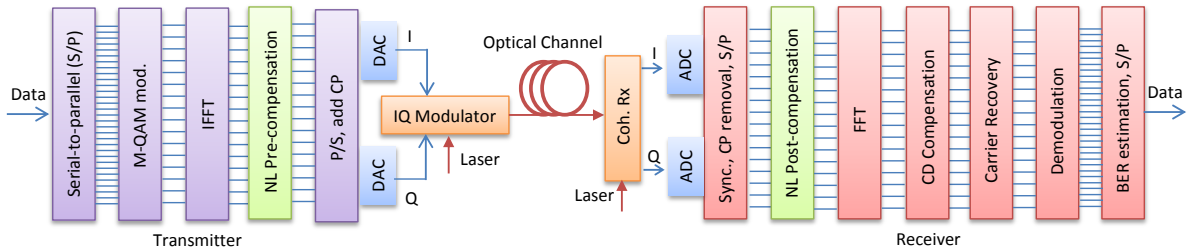

Figure 2-17: Block diagram for optical OFDM with nonlinear pre- and post-compensation.

Simulation results suggest that the combination of nonlinearity pre- and post-compensation allows a 2 dB increase in the nonlinear power limit for standard single mode fiber (SSMF) over 2000-km [121]. This is nearly double the benefit than pre- or post-compensation alone. However, it inherits the drawbacks of the earlier methods that it performs effectively when fiber dispersion is zero or low or dispersion map of the link is judiciously chosen so that signal waveform change during transmission is sufficiently small.

Du *et al.* proposed a XPM compensator, similar to the method shown in Fig. 2-16 using a low phase filter (LPF) [71]. This is because only low frequency components of the signal impose a significant amount of XPM on adjacent channels [71]. This greatly relaxed the requirements of the photodiode, which makes the method suitable for practical implementation. Simulation results showed that a combination of this XPM compensator with electrical post-compensation of SPM resulted in 1.3 dB increase in the *Q*-factor at the optimal power. This also resulted in about 5-dB increase in maximum allowable power. However, this was for a periodic dispersion map, where both SPM and XPM compensators work most effectively.

2.4.3 Dispersion mapping for nonlinearity mitigation

Most installed long-haul networks use a periodic inline dispersion map in order to compensate for chromatic dispersion. Fig, 2-18 shows two most commonly dispersion maps. In fully periodic map, DCF is used to fully compensate for dispersion after each span. The 10G optimal dispersion map, which consists of -510-ps/nm pre-compensation and each span is under-compensated by 85-ps/nm, is commonly used in commercial 10-Gb/s transmission systems [123]. However, it has been observed that for a system with periodically compensated dispersion map or with low dispersion fiber, the influence of both SPM and XPM is significantly larger than for a transmission link without inline compensation. The nonlinear performance of optical OFDM systems suffers more in such systems, as such this undermines the suitability for overlay of high data rate OFDM channels on the existing networks [124].

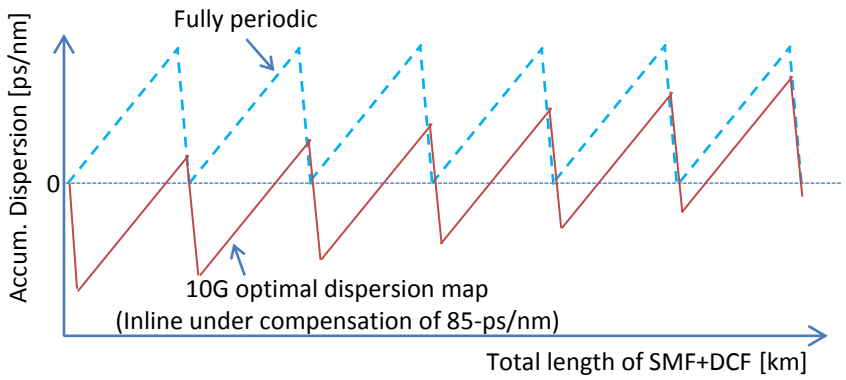

Figure 2-18: Inline periodic dispersion compensation maps.

Du *et al.* showed that using fiber nonlinearity pre-compensation is very effective for OFDM systems with such dispersion maps [125]. The method used intensity based nonlinearity pre-compensator as shown Fig. 2-19. Simulation results show that this offers about 1-dB *Q*-factor improvement at the optimal signal power, even in the presence of XPM from neighbouring channels [125].

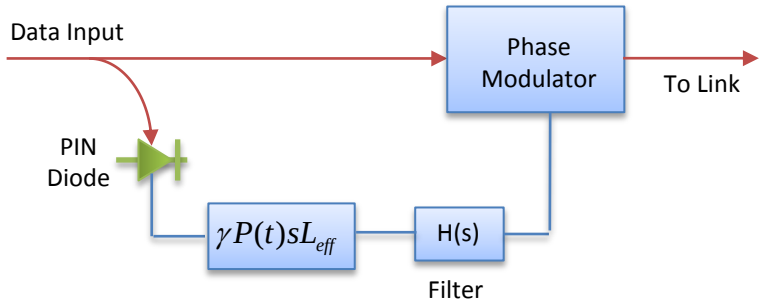

Figure 2-19: Intensity based optical pre-compensator.

2.4.4 Pilot-tone-based nonlinearity compensation

The use of RF-pilot-tone based phase noise compensation (RFP) for the compensation of both SPM and XPM has been proposed [126-128]. Although RFP has originally been proposed for the compensation of laser phase noise, it has been shown to be effective for increasing nonlinear tolerance as well. In this scheme, an RF-pilot or optical carrier is inserted in the middle of the OFDM spectrum. This is done by keeping several subcarriers around the RF-pilot unmodulated so that the RF-pilot and OFDM subcarriers do not spectrally overlap as shown in Fig. 2-20. At the receiver, a digital filter is applied around the pilot that is broadened in a similar fashion as the modulated subcarrier, due to laser phase noise and nonlinear effects such as SPM from the neighbouring subcarriers and XPM from neighbouring WDM channels. Therefore, the nonlinear impairments can be mitigated by inverting the pilot phase and by multiplying the OFDM symbol with it similar to phase noise compensation. The pilot-to-signal ratio (PSR) is an important parameter for the RFP method [128]. However, the

improvement using this technique is limited due to amplified spontaneous emission (ASE) corrupting the phase information in the RF-pilot tone. A nonlinearity limit improvement of only 0.5-dB in a 2000-km dispersion uncompensated link was observed.

Dual-stage nonlinearity compensation method has been proposed to increase the nonlinearity limit of the above RFP based method [129-131]. In this scheme, SPM compensator explained in Subsection 2.4.2 is applied prior to the XPM compensation. This dual stage nonlinearity compensator increased the nonlinear limit by 6 dB for 400-km dispersion managed link [130].

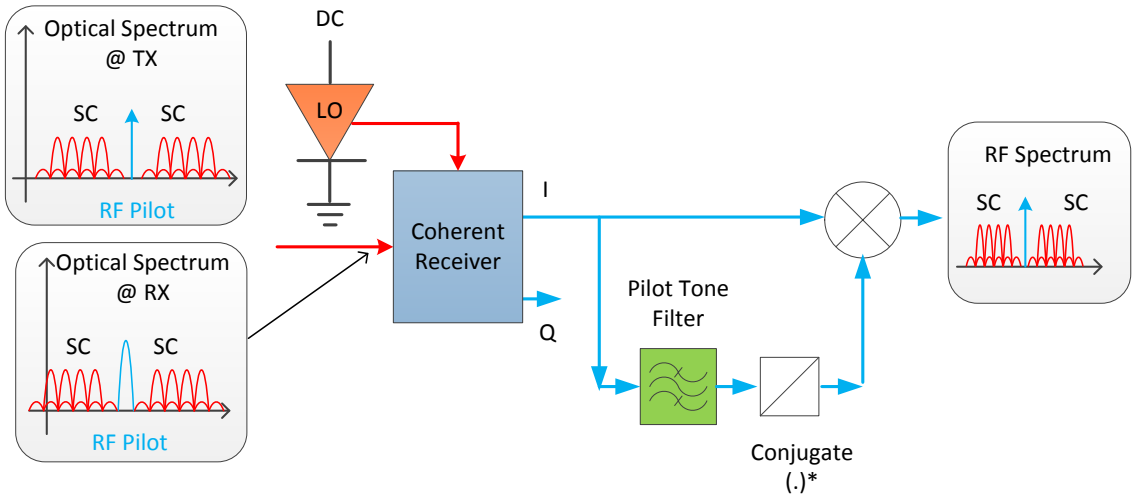

Figure 2-20: RFP-tone based nonlinearity compensation.

2.4.5 Symbol rate optimization

Recently, multiband discrete-Fourier-transform-spread OFDM (DFT-S OFDM) has been proposed to reduce PAPR in CO-OFDM systems [113]. DFT-S OFDM has been used in wireless communications to facilitate single-carrier frequency-domain equalization (SC-FDE), and has already been incorporated into next generation 4G mobile standard, known as long-term-evolution (LTE) [113, 132]. DFT-S OFDM works by reducing the PAPR of CO-OFDM signal for high-rate systems such as 400 Gb/s. For such high-rate systems, PAPR changes very quickly during transmission along a dispersive fiber, thereby rendering conventional PAPR reduction algorithm ineffective. In contrast, if PAPR mitigation approach is performed on a sub-band basis, then the signal within each sub-band can maintain its form for relatively large distance, due to slow walk-off between subcarriers. This results in PAPR reduction on sub-band basis more effective than that across the entire OFDM spectrum. Simulations show that the optimal sub-band bandwidth for DFT-S OFDM is about 3-12 GHz [113].

In DFT-S CO-OFDM systems, the original N data symbols first go through N-point DFT spreading, instead of directly applying the IFFT to convert it to time-domain symbol. Then the new frequency-

domain *N* symbols are mapped onto *M*-point DFT symbol vector, for instance, from the $(K_1+1)th$ to the $(K_1+N)th$ position, where K_1 is the starting position of band mapping. The entire M-point symbol is then converted to time-domain by applying an *M*-point IFFT, where $M = L \cdot N$ and L is the number of sub-bands. Figure 2-21 shows the conceptual diagram of multiband DFT-S OFDM generation.

The DFT-S scheme requires a set of extra DFTs for DFT spreading in the transmitter, and an extra IFFT at the receiver. Thus DFT-S reduces higher PAPR problems in CO-OFDM systems; however, it comes at the cost of larger computational complexity.

The concept of optimal sub-band bandwidth of CO-OFDM systems corresponds to the optimum granularity of Nyquist WDM (N-WDM) systems [133]. Du *et al.* shows that the baud rate has a significant effect on the nonlinearity-limited performance of coherent communication systems [133]. The optimum baud rate decreases as the length of the link is increased. The optimal baud rates for the 800-km and 3200-km link were 6.25-Gbaud/s and 3.125 Gbaud/s [133].

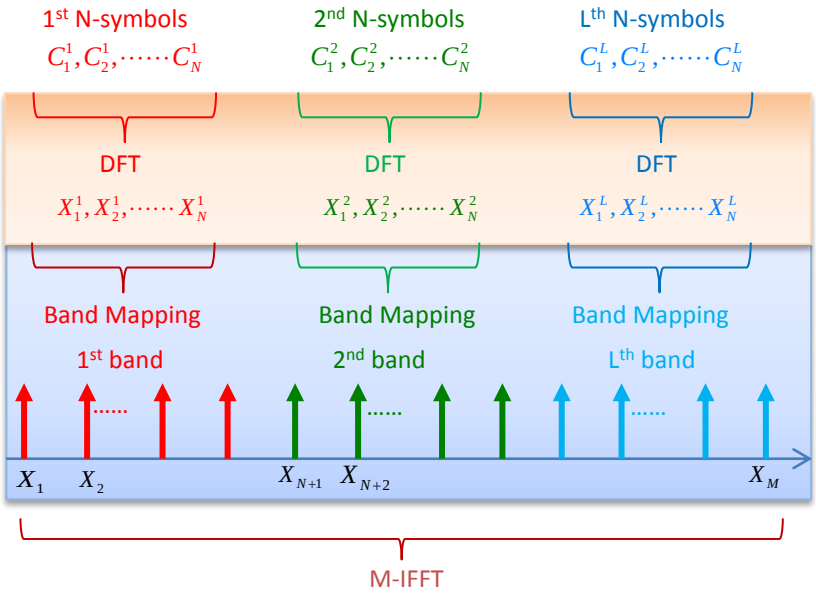

Figure 2-21: Conceptual diagram of DFT-S OFDM.

2.4.6 Digital back propagation

Recently, digital backpropagation (DBP) has been proposed as a universal technique for jointly compensating linear and nonlinear impairments [67, 68]. In BP, received signal is digitally propagated through an inverse fiber model. Therefore, it requires solving inverse nonlinear Schrödinger Equation (NLSE) through the fiber to estimate the transmitted signal, typically using the split-step Fourier method (SSFM). In SSFM the fiber is treated as a concatenation of nonlinear and linear sections as

shown in Fig. 2-22 (a). BP is explained in Fig. 2-22 (b), where the input-output relations of the nonlinear section, *N* and linear section, *D* are given by [68]:

$$y'(t, z+h) = y \times \exp(jh|y(t,z)|^2) \tag{2.56}$$

$$X(\omega) = Y'(\omega) \times \exp\left(-j\left(\frac{\alpha}{2} + \frac{\beta_2}{2}\omega^2\right)h\right) \tag{2.57}$$

where h is the step size. Nonlinear effects are strongest at the beginning of a fiber section where signal power is the highest. Therefore, nonlinear phase rotation is performed first before linear propagation. From Equations (2.56) and (2.57) it is observed that BP has two phases: CD is a phase multiplication in the frequency domain, whereas Kerr nonlinearity is a phase multiplication in the time domain.

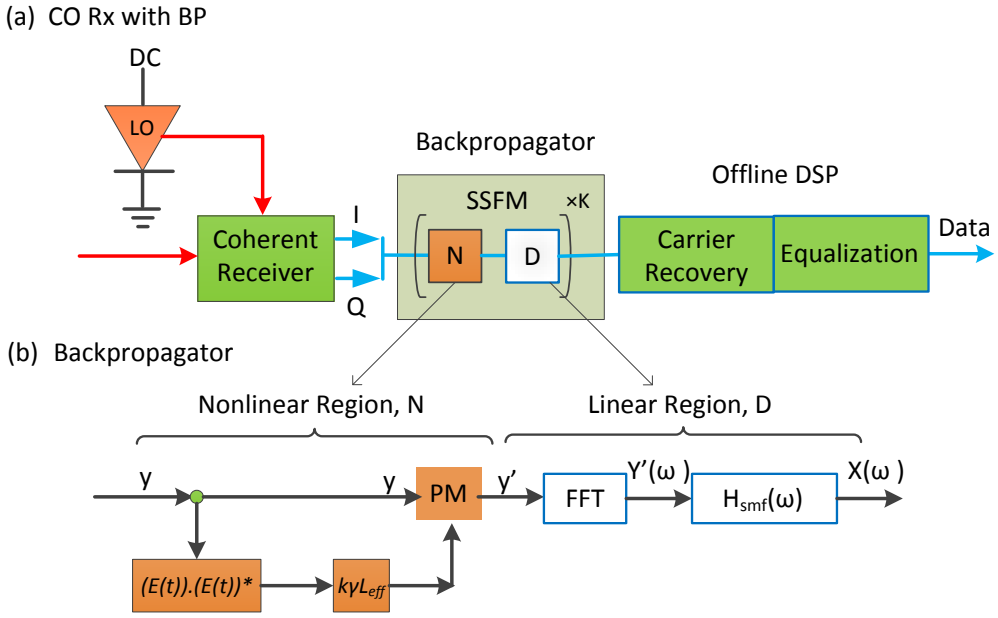

Figure 2-22: Block diagram of a coherent receiver with backpropagation (BP).

The main drawbacks of BP are its excessive computational requirement and the difficulty in applying it in the presence of PMD [68] and for WDM systems [69]. Less computationally intensive DBP for dual polarization CO-OFDM has been proposed [134], which offers 2-dB improvement in *Q*-factor at optimal launch power, and about 5-dB improvement in maximum allowable launch power. However, the extreme high computational complexity of DBP means that achieving ideal fiber nonlinearity compensation is impractical in WDM systems with present DSP capabilities.

2.5 Summary

In this chapter, relevant nonlinear fiber impairments arising from Kerr effect that limit the fiber-optic transmission capacity have been discussed. The Kerr effect originates from the dependence of the refractive index on the instantaneous optical signal power. Self-phase modulation (SPM) limits single channel systems, whereas cross-phase modulation (XPM or FWM) becomes the major limiting factor for WDM systems. Although chromatic dispersion (CD) reduces the nonlinear effects due to walk-off between co-propagating channels, XPM or FWM are still the major concerns to improve the fiber capacity.

Various methods that have been investigated for mitigating fiber nonlinearities have been reviewed: PAPR reduction method, intensity-based SPM and XPM mitigation, pilot-tone based nonlinearity compensation, symbol-rate optimization, digital backpropagation (BP) and optical phase conjugation (OPC). Figure 2-23 below summarizes the performance comparison of these methods. Fig. 2-23 (a) shows the increase in maximum allowable launch power and Fig. 2-23 (b) shows the improvement in the *Q*-factor at optimal launch power. Among all these methods, XPM+SPM compensator method and digital back propagation method show highest improvement in nonlinearity mitigation. However, the former method suffers from the limitation that its effectiveness becomes poor in a dispersive link, while the improvement in the latter was reported only in a single channel system. For a WDM system, digital back propagation is still unrealistic in terms of practical implementation.

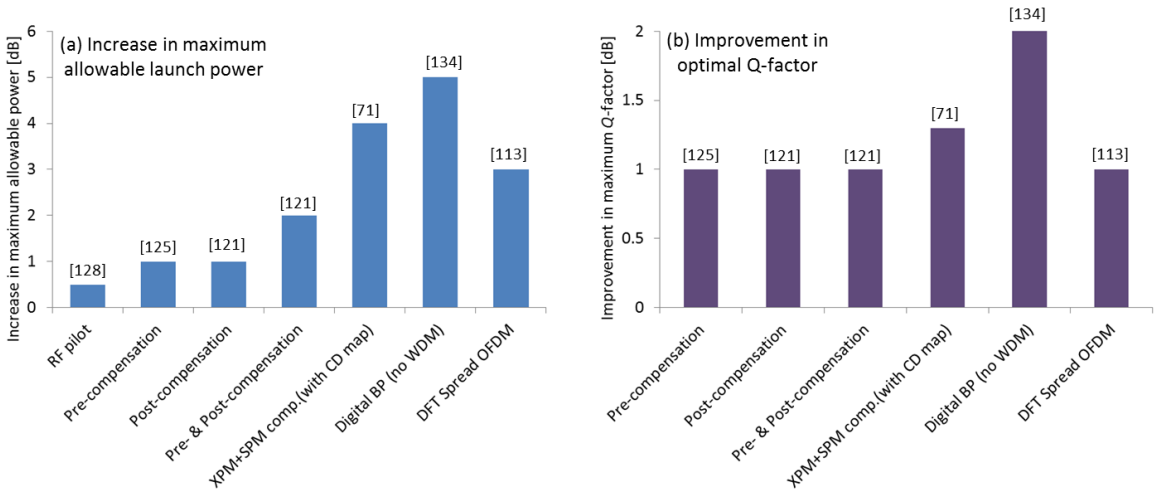

Figure 2-23: Performance comparison of various nonlinearity mitigation methods.

Mid-span spectral inversion (MSSI) which uses OPC in the middle of the link, has not been experimentally demonstrated yet for any coherent optical communication system. MSSI has great advantage that it is independent of number of WDM channels as well as modulation format. In this

PhD thesis, I have proposed using MSSI to mitigate fiber nonlinearity for coherent optical OFDM system.

The next chapter will discuss the concept of OPC for mitigating transmission impairments. Theoretical background of OPC and its application in mid-span spectral inversion (MSSI) for optical communication systems will be discussed.

3 MSSI for optical nonlinearity mitigation

Optical phase conjugation (OPC), which inverts the optical signal spectrum, is a useful application of nonlinear optical processing. In optical communication systems, OPC can be exploited in mid-span spectral inversion (MSSI) for the compensation of both linear; i.e. chromatic dispersion (CD) as well as nonlinear effects like, SPM or FWM. In this chapter, a discussion on how OPC mitigates these impairments will be presented. Limitations of OPC when using in practical systems will be discussed. Finally, some techniques for improving these limitations will be reviewed.

3.1 Optical phase conjugation

A commonly used medium for the implementation of OPC is periodically poled lithium-niobate (PPLN), which uses 2nd order nonlinear effects to generate sum and difference frequencies [76, 135]. Lithium niobate (LN) is a very promising material for optical applications, as it has high electro-optic and nonlinear coefficient. However, the main drawback that limits PPLN's widespread use is the presence of the photorefractive effect in the LN crystal; which is a change of crystal refractive indices when illuminated by a high-intensity beam. This may cause a modification of the phase modulation (PM) conditions and in severe case, significant distortion of the beam propagation [135]. The only way to avoid this effect is to keep the device at high temperature during the operation in the range between 90° C and 120° C. Several researches have been carried out in order to allow the realization of PPLN based OPC operating at near room temperature [136, 137].

Alternatively, optical phase conjugation can be implemented by FWM based on third order nonlinearity in a nonlinear medium like semiconductor optical amplifiers (SOA) [138], zero-dispersion single mode fiber (SMF) [139] and highly nonlinear fiber (HNLF). The use of HNLF based OPC is promising for its simplicity and low cost; moreover, having an all-fiber based OPC allows low coupling losses [135].

In this thesis, I use FWM process based on third-order nonlinearity in a highly nonlinear fiber (HNLF) to generate the OPC signal. The schematic configuration of OPC generation process in such a medium is shown in Fig. 3-1. Here, E_P is a CW-pump wave at frequency ω_P and E_S is the signal wave at frequency ω_S .

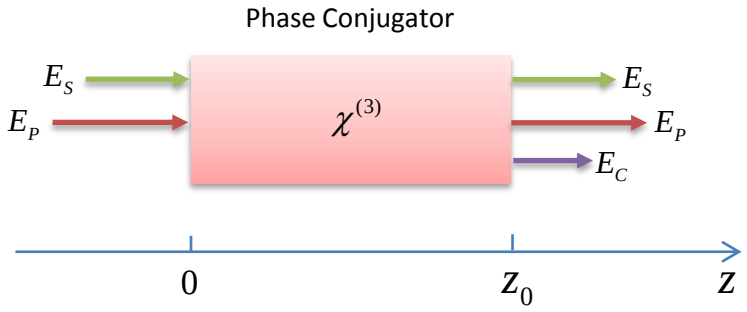

Figure 3-1: Generation of phase-conjugate wave, E_c, in a four-wave mixer.

As has been discussed in Section 2.3 of the previous chapter, a parametric mixing between the pump and signal wave will generate a new idler at frequency $\omega_C = 2\omega_P - \omega_S$, where the idler field can be obtained from Equation (2.45) as:

$$\frac{\partial E_C}{\partial z} \propto \gamma E_P E_P E_S^* \exp(j\Delta k_{P,P,-S,-C} z) \tag{3.1}$$

Since (E_P is constant (CW)) phase mismatch term $\Delta k_{P,P,-S,-C}$ becomes zero in a zero-dispersion fiber, the above expression is simplified as:

$$\frac{\partial E_C}{\partial z} \propto \gamma E_S^* \tag{3.2}$$

The idler field at point z_0 can be expressed as:

$$E_C(z_0) \propto \gamma E_S^*(t) z_0 \tag{3.3}$$

From Equation (3.3), it is noted that the idler wave is identical to the signal wave except that its phase is conjugated. Recalling from a Fourier transform property that, if $f(x) \overset{F.T.}{\Leftrightarrow} F(\omega)$ then $f^*(x) \overset{F.T.}{\Leftrightarrow} F^*(-\omega)$, the conjugated wave in time domain given at any given z_0 in Equation (3.3), will have its spectrum inverted and conjugated. This is schematically shown in Fig. 3-2 where OPC is used in the middle of a link in a transmission system. The figure shows that conjugation in time domain does not change the apparent shape of optical pulse, however it inverts the optical spectrum.

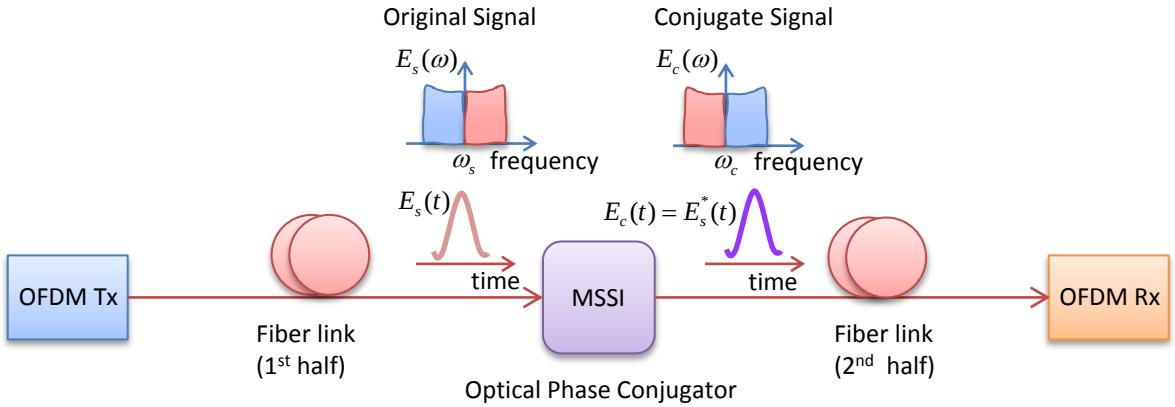

Figure 3-2: OPC in a MSSI system, showing optical pulse and spectral shape before and after the OPC.

3.2 Principle of transmission impairments compensation by OPC

In the previous section it has been shown that OPC inverts the spectrum of the signal by taking the conjugate of the signal in time domain. Therefore, the propagation of the conjugated signal in the second half of the link can be described by taking the complex conjugate of the NLSE which is mentioned in Equation (2.28). For the sake of simplicity a perfect medium with loss less condition ($\alpha = 0$) is considered here. NLSE and its conjugated form under this condition can be expressed as:

$$\frac{\partial A}{\partial z} = -\frac{j}{2}\beta_2 \frac{\partial^2 A}{\partial T^2} + \frac{1}{6}\beta_3 \frac{\partial^3 A}{\partial T^3} + j\lambda |A|^2 A \tag{3.4}$$

$$\frac{\partial A^*}{\partial z} = \frac{j}{2}\beta_2 \frac{\partial^2 A^*}{\partial T^2} + \frac{1}{6}\beta_3 \frac{\partial^3 A^*}{\partial T^3} - j\lambda |A|^2 A^* \tag{3.5}$$

A comparison between Equation (3.4) and (3.5) shows that the conjugated signal A^* propagates with the sign reversed for the GVD and nonlinear parameters. This suggests that if the optical field is phase conjugated in the middle of the link, as shown in Fig. 3-2, second-order dispersion (GVD) and the SPM-induced phase distortions acquired along the first part of the link will be exactly compensated in the second part. As the β_3 term does not change sign on phase conjugation, OPC cannot compensate for the third order dispersion (TOD). In fact, OPC compensates for all even-order dispersion terms, while leaving the odd-order terms unaffected.

Now, interestingly, A^* also satisfies Equation (3.4) when z is changed to $-z$. This suggests that propagation of A^* in forward direction is equivalent to sending the signal backwards, undoing distortions induced by GVD and Kerr effects simultaneously.

3.3 OPC effects in practical systems

Although OPC has excellent potential in cancelling nonlinear distortions in a system with ideal lossless fiber, in practice, however, fiber losses and subsequent amplifier gain greatly reduce its effectiveness. The reason can be understood by noting that the propagation of an OPC signal is equivalent to propagating a time-reversed signal. Thus, perfect Kerr nonlinearities compensation can occur only if the power variations are symmetric around the mid-span where the OPC is located. Fiber losses and optical amplifiers such as EDFA used to compensate the losses do not meet this property. For example, Fig. 3-3 shows the actual **(—)** and required **(- - -)** power profile for perfect compensation of the Kerr effect by OPC.

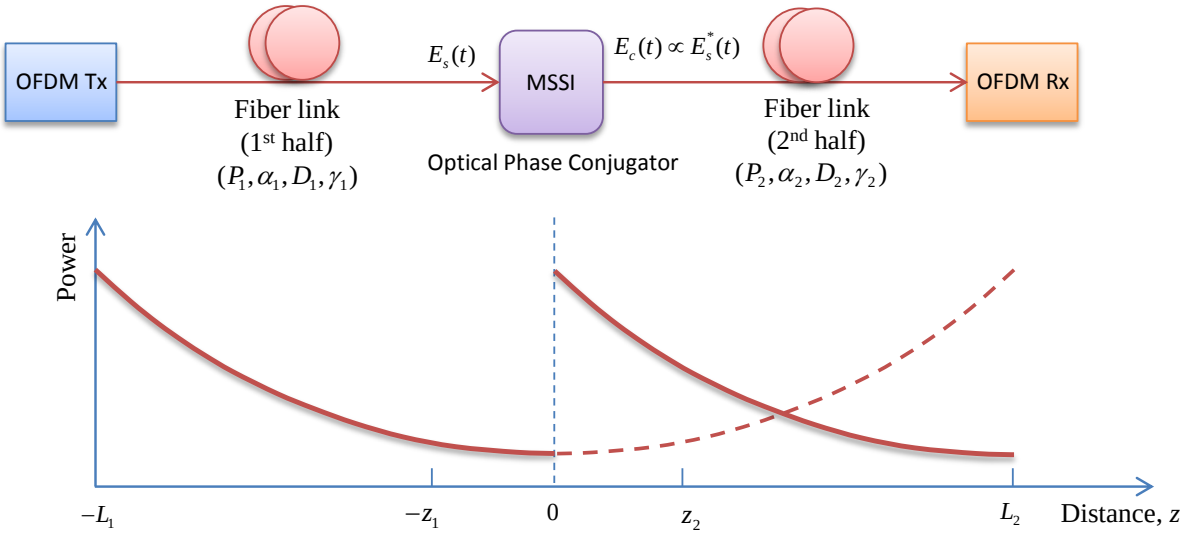

Figure 3-3: Actual (—) and required power profile (- - -) for perfect compensation of Kerr effect.

One way to get close to the ideal condition is to amplify the signal often enough so that the power does not vary by a large amount during each amplification stage [140]. However, this approach is not practical since it requires closely spaced amplifiers. Another way to improve the power profile symmetry is to use Raman amplification [141] with bidirectional pumping to maintain a nearly constant power.

3.3.1 Optimum link conditions for using OPC in practical systems

A practical and cost effective method to reduce the effect of power asymmetry in OPC was proposed using a path-averaged intensity approximation [142, 143]. Consider Fig. 3-3 again where the signal wave, E_S with power, P_1 is transmitted through the first fiber link, which has a loss, α_1, total nonlinear effective length, L_1, total dispersion, D_1 and an fiber nonlinear coefficient, γ_1. The complex conjugate wave, E_C propagates through the second half of the link where the corresponding parameters are

α_2, L_2, D_2 and γ_2 . Using the path-averaged intensity approximation method, the condition for compensation of both GVD and Kerr effect is approximately achieved when the total GVD and path-averaged Kerr-induced phase shift along both links are identical. These conditions are expressed as:

$$D_1 L_1 = D_2 L_2 \tag{3.6}$$

$$\gamma_1 P_1 L_1 = \gamma_2 P_2 L_2 \tag{3.7}$$

The limit is that this method is effective only when the intensity variation along the fiber is small. However, one significant derivative of this method is that if P_1 or γ_1 can be made significantly larger than P_2 or γ_2 , then the path-averaged approximation can even hold for when fiber Link 1 is significantly shorter than the fiber Link 2. This paved the way to more practically implementable systems using OPC with pre-compensation at the transmitter or post-compensation at the receiver [144].

Subsequently, a method for exact compensation of GVD and Kerr effect using OPC has been proposed by the same group [75]. In this method, the ratio of GVD to the strength of the Kerr effect is designed to be the same at two corresponding positions, $-z_1$ and z_2 , with respect to OPC. This condition is expressed as:

$$\frac{D_1(-z_1)}{\gamma_1(-z_1)P_1(-z_1)} = \frac{D_2(z_2)}{\gamma_2(z_2)P_2(z_2)} \tag{3.8}$$

This means that by providing the equal ratio of the dispersion and the nonlinearity at the corresponding positions, the condition for perfect compensation is satisfied. Equation (3.8) also indicates that we can substantially compensate for the fiber loss or amplifier gain by changing dispersion along the line. This is possible by decreasing the dispersion or increasing the optical Kerr effect, as power decreases along the fiber. The first experiment using OPC with decreasing dispersion fiber was demonstrated in [144] using two 10-Gb/s time-division multiplexed RZ signals. In this proof-of-concept experiment, OPC was used with pre-compensation in the transmitter. Five equal length sections of dispersion-compensation fiber (DCF) were spliced together, each with successively decreasing dispersion values. This approximated dispersion-decreasing DCF (DD-DCF), partially cancelling the effect of decreasing power profile along the fiber as indicated in Equation (3.8). The phase conjugated signal was transmitted through 3036-km, consisting of 46 DSF sections (0.21 dB/km loss) and 45 EDFAs with a noise figure of ~ 6 dB. Successful detection of signals at a BER of less than 10^{-9} after 3036 km with power penalty of 4.8 dB was achieved. The residual distortion was caused by an imperfect compensation condition. This was because the second link did not use

dispersion-decreasing fiber despite having each span length of 66 km, which is long enough to cause significant power change in each span.

3.3.2 OPC for deployed links

The above techniques for OPC system optimization have been designed for special types of link such as based on the use of close amplifier spacing [140], or special fibers [75] or high-power Raman distributed amplification [141]. Therefore, none of the above proposals are suitable for already deployed systems, which use standard single mode fiber (S-SMF) and EDFAs with wide amplifier spacing ($L_{amp} > 50$ km). For using OPC effectively in such embedded system, Minzioni *et al*. proposed nonlinearity cancellation with no other required equipment than an OPC, based on an optimized positioning of the OPC device [145]. It has been shown that the optimal OPC position is given by the following two Equations, depending on the number of fiber spans.

$$x_{OPC} = x_{msa} - \frac{1}{2}\left(L_{amp} - L_{eff}\right); \qquad \text{for even } N \tag{3.9}$$

$$x_{OPC} = x_{msa} + \frac{L_{eff}}{2}; \qquad \text{for odd } N \tag{3.10}$$

where x_{msa} is the position of the mid-span amplifier, L_{eff} is the effective nonlinear length, L_{amp} is amplifier spacing and N is the number of spans. The optimal position of OPC is shown in Fig. 3-4 (a) and (b) for even and odd number of spans.

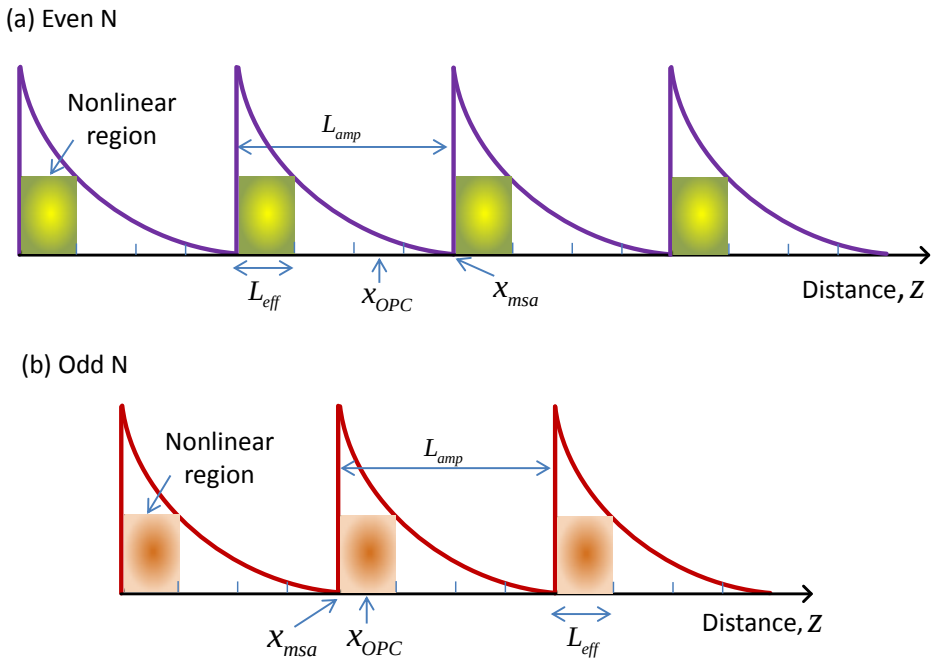

Figure 3-4: Optimum positioning of OPC in an embedded link.

Optimized positioning according to Equations (3.9) and (3.10) requires an OPC to be placed in a position other than an amplifier site. Therefore, this is not practical, yet the result is significant because it leverages the fact that when dealing with wide amplifier spacing, nonlinear effects play a significant role only in a part of the fiber much shorter than the span length. This region, shaded in Fig. 3-4, is referred as nonlinear effective length, L_{eff} . In rest of the region of a span, only attenuation and GVD play a significant role in signal transmission. Therefore, instead of making the power profile symmetrical over a complete link with respect to OPC, it is sufficient to create a symmetrical distribution of nonlinear regions only.

Minzioni *et al.* later proposed and demonstrated a modified distribution profile to satisfy both the link and implementation constraint [146]. They showed that if a certain length of fiber, properly modifying accumulated dispersion along the link, is added together with the OPC, then both of the above constraints can be satisfied. The scheme exploits a linear propagation regime in the added fiber to change the value of accumulated dispersion just before or after the OPC.

Consider an example of a four-span link with the OPC positioned according to MSSI; i.e. in the middle of the link. Fig. 3-5 (a) shows the superimposed evolution of optical power and accumulated dispersion. Fig. 3-5(b) shows optical power re-plotted against accumulated dispersion. Point A translates into point A′, and point B translates into point B′. The shaded areas show an absence of symmetry around zero dispersion point, thus nonlinearity compensation is not achieved.

If, now, an appropriate length of dispersion compensation fiber (DCF) or highly dispersive fiber (HDF) in which propagation can be considered linear, is added immediately before or after the OPC, then the distributions change as in Fig. 3-6, and symmetry condition is achieved with respect to zero-dispersion axis.

Moreover, since both the OPC and HDF/DCF are placed in an amplifier site, the implementation constraint in an embedded system is also satisfied. The optimal length of the added fiber (L_A) depends on its average dispersion coefficient (D_A) and must satisfy the following equation:

$$L_A = \pm \frac{D_0}{D_A}(L_{amp} - L_{eff}) \tag{3.11}$$

where D_0 is the dispersion value of the deployed fiber in the link and $\left(L_{amp} - L_{eff}\right)$ is the length of the linear region. When the sign in the above equation is positive, the added fiber is to be placed after the OPC; when the sign is negative, the added fiber has to be placed immediately before the OPC.

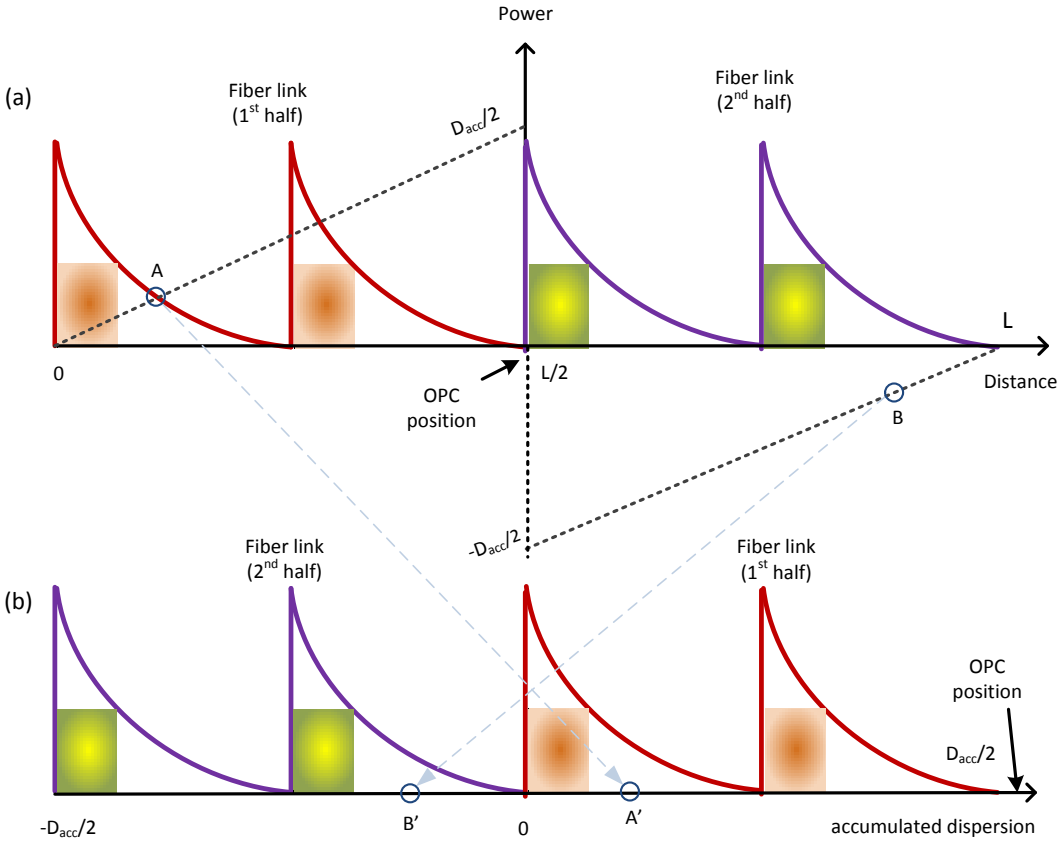

Figure 3-5: Power profile against distance and accumulated dispersion along the link.

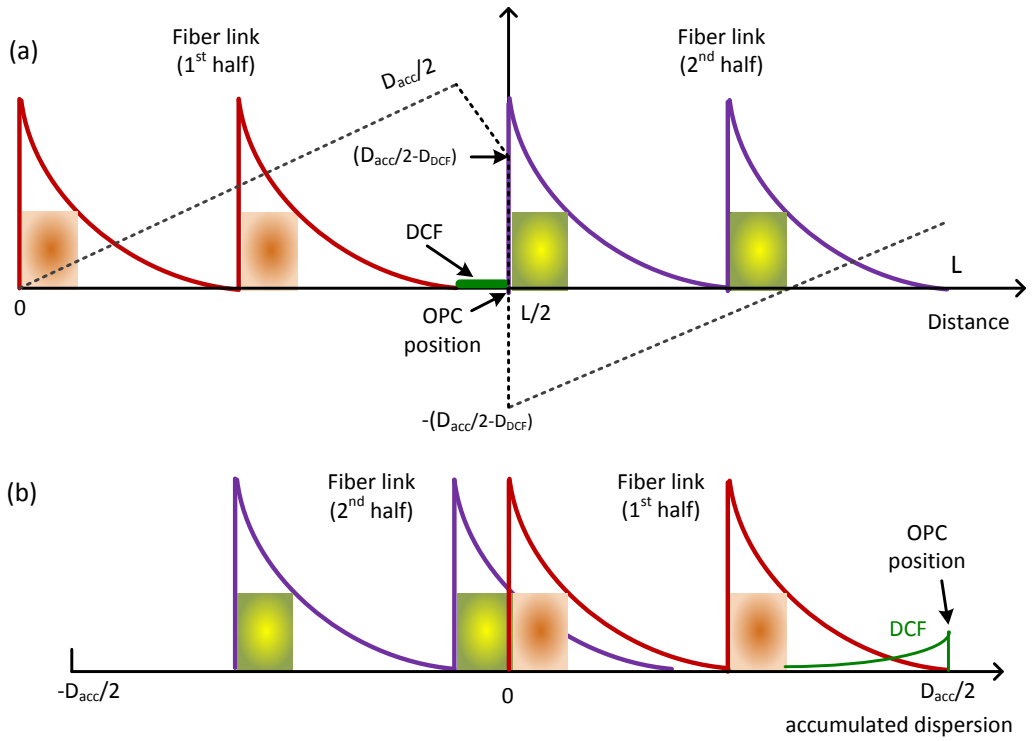

Figure 3-6: Modified power profile against distance and accumulated dispersion along the link.

3.4 FWM suppression ratio using OPC in CO-OFDM systems

In 2013, Pechenkin *et al.* analysed FWM suppression for CO-OFDM systems that use OPC for MSSI [82, 147]. The results use dispersion-free (DF) system as the reference system against which the phased-array (PA) and OPC systems are compared. In a highly dispersive link, FWM products generated in each span of a link adds incoherently resulting in destructive interference among a large number of FWM products. As a result, the overall FWM effect is much smaller than in an in-line dispersion compensated or a low dispersion link. This is so-called phase-array (PA) effect [107]. Pechenkin *et al.* showed that while the PA setup suppresses a major portion of large phase mismatched (large $\Delta\beta$) FWM processes remarkably well for sufficiently long dispersive links, well-matched (small $\Delta\beta$) FWM processes continue to accumulate power almost quadratically with propagation distance. On the other hand, OPC favourably changes the dynamics of FWM power accumulation to strongly suppress the well-matched FWM process. Therefore, the results conclude that if an OFDM system is designed in a phased-array fashion, the benefits of both approaches can be combined to achieve a remarkable degree of overall FWM suppression throughout the entire link. For the importance of this fact, the analysis has been summarized here briefly.

For the reference dispersion-free (DF) system, multi-span nonlinear effective length (NEL) is given by:

$$D_{DF} = NL_{eff} \tag{3.12}$$

where N is the number of spans, and L_{eff} is conventional effective fiber length per span.

For a PA system, with number of spans, N and span length, L_s , the same multi-span NEL becomes:

$$D_{klm-PA} = F_{klm} \cdot L_{klm} \tag{3.13}$$

where F_{klm} and L_{klm} are phase-array factor and single-span NEL respectively, and are given by [82]:

$$F_{klm} = e^{-j\Delta\beta_{klm}(NL_s - L_s)/2} \frac{\sin(\Delta\beta_{klm} NL_s / 2)}{\sin(\Delta\beta_{klm} L_s / 2)} \tag{3.14}$$

$$L_{klm} = \frac{1 - e^{-(\alpha + j\Delta\beta_{klm})L_s}}{\alpha + j\Delta\beta_{klm}} \tag{3.15}$$

where α is fiber attenuation coefficient.

For the MSSI system using OPC, the multi-span NEL is expressed by [82]:

$$D_{klm-OPC} = e^{-j\Delta\beta_{klm}NL_s/2}\frac{\sin(\Delta\beta_{klm}NL_s/2)}{\sin(\Delta\beta_{klm}L_s/2)}C_{klm} \tag{3.16}$$

where C_{klm} characterizes the impact of the OPC module, and is given by [82]:

$$C_{klm} = \frac{2i}{\alpha^2+(\Delta\beta_{klm})^2}\left[\alpha\left(1+e^{-\alpha NL_s}\right)\sin(\frac{\Delta\beta_{klm}NL_s}{2}) - \Delta\beta_{klm}\left(1-e^{-\alpha L_s}\right)\cos(\frac{\Delta\beta_{klm}L_s}{2})\right] \tag{3.17}$$

Now, the FWM suppression effects for PA and OPC systems compared to dispersion-free system are defined as: $|D_{klm-PA}|^2 / D_{DF}^2$ and $|D_{klm-OPC}|^2 / D_{DF}^2$ respectively. Fig. 3-7 shows the comparison. The blue curve (—) shows the FWM suppression factor for PA system and the red curve (—) is for the OPC system. For the calculation, the following values were used: $\alpha = 0.2$ [dB/km], $N = 20$ and $L_s = 80$ km.

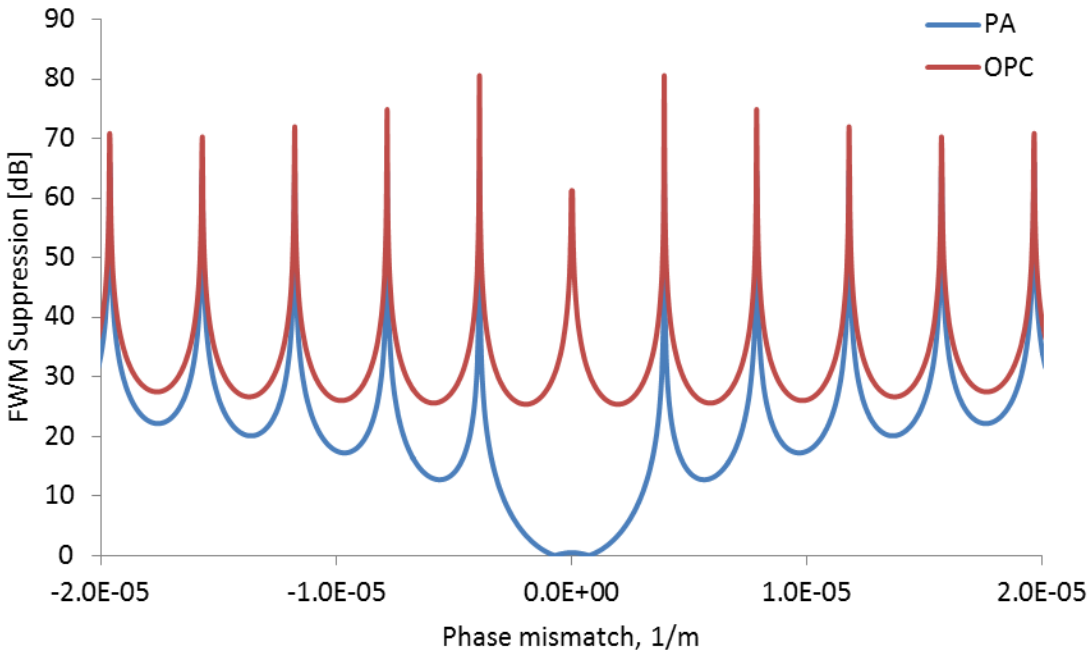

Figure 3-7: Relative FWM levels comparison between PA and OPC systems in reference with a dispersion-free system.

The result clearly demonstrates that the OPC technique achieves excellent performance in the critical region of the well-matched FWM processes, which are suppressed by more than 30 dB with respect to the PA setup. However, this analysis assumes the phase-conjugator is ideal and it generates a perfect phase-conjugated signal. Therefore, a practical system with MSSI is limited by a performance penalty, if any, due to MSSI [84, 85].

3.5 Recent growing interest in OPC for coherent communication systems

MSSI had fallen from favour for use in optical communication systems, although after significant research in the 1990s [74, 75, 138, 139, 141-144, 148]. Then in the mid-2000s, MSSI witnessed re-arrival of research interest for using in non-coherent phase-shift keying systems for ultra-long haul systems [76-79, 149, 150]. Interest in using MSSI for coherent communication systems started growing again after theoretical analysis [82, 147] and simulation results [83] showing its considerable benefit. Later, our group demonstrated the first experiment results using MSSI for fiber nonlinearity compensation in CO-OFDM systems [80, 81]. As part of thesis, I have demonstrated the first experimental results using MSSI in any dual-polarization coherent communication system [151, 152]. At Bell Labs, X. Liu *et al.* recently demonstrated phase-conjugated twin waves to cancel fiber nonlinearities [153]. In this experimental demonstration, phase-conjugated twin waves are co-transmitted in two orthogonal polarizations, which are then coherently superimposed at the receiver. Since the OPC twin-waves are anti-correlated, their coherent summation resulted in cancellation of signal-to-signal nonlinear interactions. This enabled nonlinear distortion reduction by >8.5 dB and helped in transmitting a 400 Gb/s super-channel over 12,800 km of fiber [153], although at the expense of halving the spectral efficiency. Subsequently, there have been demonstrations of Raman enhanced MSSI [91, 154] and multiple phase-conjugation [89] based coherent systems at the 2014 Optical Fiber Communications (OFC) conference.

3.6 Summary

In this chapter, a brief discussion on OPC fundamental based on NLSE followed by its principle for fiber impairments compensation have been discussed. It has been showed that theoretically perfect compensation using MSSI requires either lossless fiber or symmetric power distribution with respect to OPC position over the entire link. It also requires fiber with decreasing GVD (and all odd higher-order derivatives of propagation constant) and perfect phase-conjugation. However, none of these conditions are satisfied in a practical system. These limitations were followed by discussions on number of techniques to overcome these constraints, including symmetry over nonlinear regions only with respect to zero-dispersion axis by adding a special fiber. A recent analytical results showing considerable benefit of using MSSI for FWM suppression follows. Lastly, a brief introduction on recent growing interest in OPC for nonlinearity compensation has been reviewed.

All the techniques that have been discussed in this chapter for improving the performance of an OPC system were based on optimizing link design. On the other hand, the theoretical analysis by Pechenkin *et al*. discussed above assumes a perfect phase-conjugator. However, no study has been made so far that analyses the details of a practical MSSI system and its limitations, if any, from nonlinear distortion products within itself. The next chapter gives a detail analysis of a practical MSSI system. It

uses OPC based on third order nonlinear effect. The next chapter constitutes the beginning of original contributions derived from this PhD thesis.

4 Analysis of the fundamental performance limitations of OPC

Pechenkin and Fair [82] presented a detailed analysis showing effectiveness of OPC for suppressing the well-matched FWM products when used for CO-OFDM systems. However, they assumed an ideal MSSI with perfect OPC that only conjugates the incoming light to its output, and did not consider any other conjugation mechanisms that could degrade the OPC signal inside the module itself, for example, intermixing of the signal frequencies.

In this chapter, a detailed theoretical analysis of the performance limit of CO-OFDM systems that use MSSI based on third order nonlinearity is developed. In the next section, two different two-stage mixing mechanisms that limit the OPC signal quality at high powers are identified. The dominant limiting factor is the conjugated replica of the cross phase modulation (XPM) products between the pump and signal. The other significant limiting factor is the conjugated replica of the four-wave mixing (FWM) products of subcarriers. In Section 4.2, this theoretical analysis is verified with split-step Fourier method (SSFM) simulations, which show excellent agreement with the analysis. Experimental results are used to further confirm the theory.

The content of this chapter has been published in [84, 85].

4.1 System description

To identify the negative impact of an OPC module on signal quality, we consider a back-to-back system without fiber spans and dispersion compensating fiber (DCF) shown in Fig. 4-1(a). The OFDM signal is generated by digital processing, a serial to parallel converter (S/P) distributes the input data stream to a bank of QAM modulators, which provides amplitude and phase coefficients for the inverse fast Fourier transform (IFFT). The IFFT produces a waveform that is a superposition of the QAM-modulated subcarriers. A cyclic prefix (CP) is inserted and a parallel to serial converter (P/S) outputs the waveform samples sequentially, to two digital-to-analog converters (DACs), which feed a complex optical Mach-Zehnder modulator (MZM IQ MOD). The output of the optical modulator, at a power P_{TX} , is fed into the OPC module, without passing through any link in a back-to-back system.

The details of OPC module are shown in Fig. 4-1(b). The input amplifier boosts the transmitter power, P_{TX} to input signal level, P_{sig}. This input signal to the MSSI is then filtered with a band-pass filter

(BPF) and is combined with the output of a CW laser pump. In our simulation and theoretical analysis, the pump (P_{pump}) and the signal (P_{sig}) powers are defined at the input to nonlinear element. The output of the nonlinear element is passed through a filter to remove the pump and the original signal, but leave the optical phase conjugated (OPC) signal. The OPC signal is then amplified before passing to a CO-OFDM coherent receiver. The coherent receiver feeds a digital processor that removes the CP, performs a Fourier transform to separate the subcarriers, equalizes the phases of the channels and them demodulates the subcarriers to recover the data in each subcarrier.

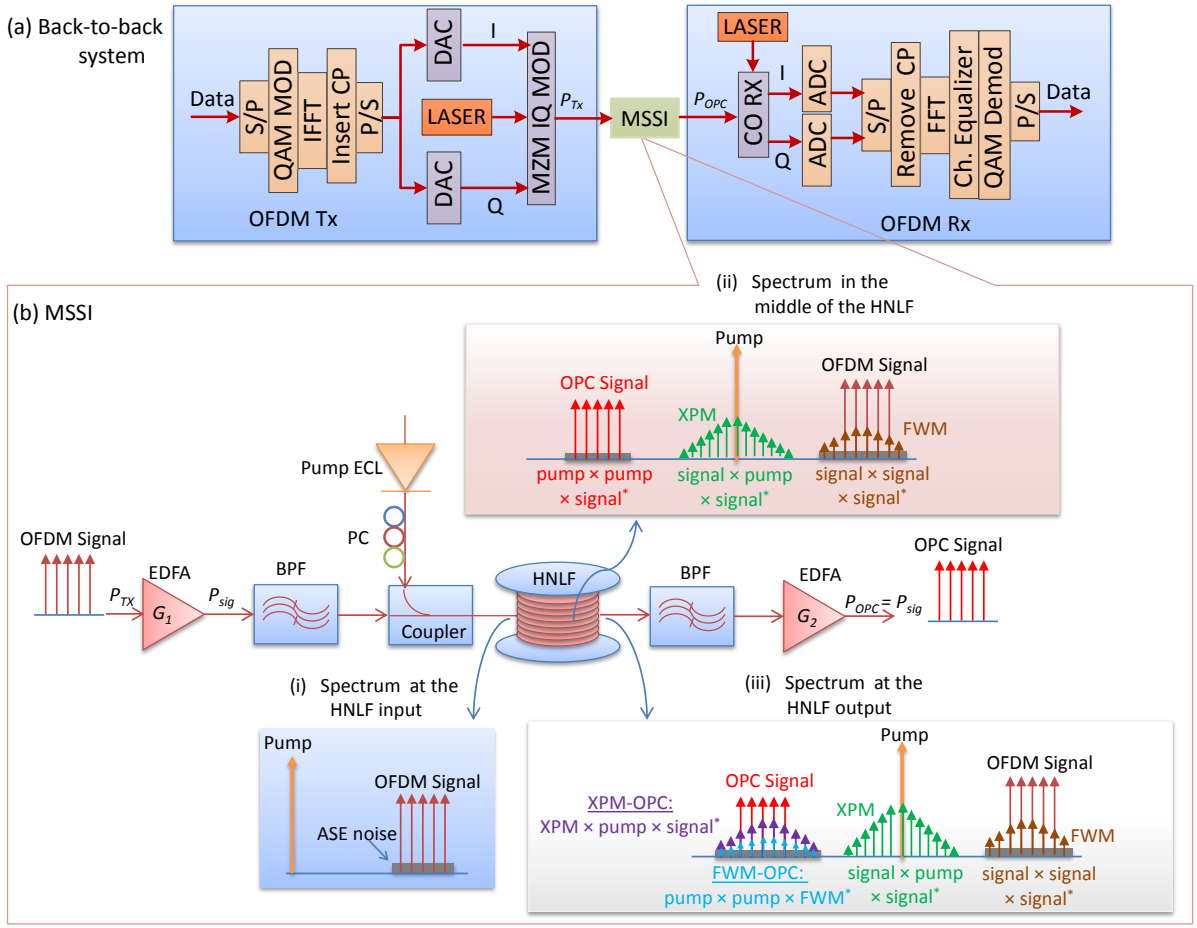

Figure 4-1: System schematic of a back-to-back MSSI system and spectrum at the input (i), middle (ii) and output (iii) of the HNLF.

The insets in Fig. 4-1(b) show the spectra at three different points along the nonlinear element, which is a highly nonlinear fiber (HNLF). The first inset (i) shows the spectrum at the input. Only Amplified Spontaneous Emission, ASE, (gray color) generated by the input amplifier is present at this point. The second inset (ii) shows the spectrum at the middle of the HNLF. It shows the subcarrier intermodulation products (brown) that are generated by four-wave mixing (FWM) between the OFDM subcarriers. The input signal, P_{sig}, has been phase-conjugated into the opposite side of the

pump signal, which we call the OPC signal (red). Cross Phase Modulation (XPM) products (green), due to *signal* × *pump* × *(signal)** mixing, fall around the pump, where * denotes conjugation. As the two signals in the XPM mixing come from the same light source, these tones (green) are non-degenerate FWM products. However, to distinguish these tones from the FWM products that fall upon the signal's bandwidth (brown), we prefer to call these tones XPM. The third inset (iii) shows the spectrum at the output. It shows two additional features other than the ASE, which we call XPM-OPC products (purple) and FWM-OPC products (blue) falling over the conjugated signal. The XPM-OPC products are generated by non-degenerate FWM between *XPM tones* × *Pump* × *(Signal)**. The FWM-OPC products are generated due to degenerate FWM between *Pump* × *Pump* × *(FWM tones)**. The XPM-OPC and FWM-OPC products fall partially on the conjugated signal's band (red), so cannot be filtered out by the second BPF. Together we call these two new features "OPC distortions". Strictly, these are deterministic distortions, though, due to the large numbers of modulated subcarriers, these will have noise-like properties. In the following sub-sections, we calculate the power of the OPC signal and all the above relevant distortions separately to determine the system's *Q*. The analysis has been done for a single-polarization case, where all interacting wavelengths (signal and pump) are co-polarized. The effect of cross-polarization modulation effect is not considered.

4.2 Calculation of OPC distortion power

The derivation of OPC distortion power follows that of [66], which gives a simple method of counting the numbers of distortion products and calculating their powers. It relies on each product growing coherently along the fiber; if their fields increase linearly, their powers will grow quadratically. At the receiver, the products falling on a particular subcarrier signal are mostly incoherent, so the error they cause is proportional to the sum of their powers. However, in the nonlinear element the OPC products are generated by a two-stage process: (1) the FWM or XPM products are generated; (2) they are phase conjugated to fall on the conjugated signal band. The analysis of [66] only accounted for products formed by the first stage; therefore, it must be extended to calculate the power of the two-stage mixing products.

Reference [66] provides a simple equation describing the output power of a nonlinear product, P_{ijk}, due to three tones, powers P_i, P_j, P_k, propagating through a lossless and dispersionless nonlinear element of length Δz. This is

$$P_{ijk} = \left(\frac{D_a}{3} \gamma \Delta z \right)^2 P_i P_j P_k \tag{4.1}$$

where: D_a is the degeneracy factor which equals 6 for non-degenerate (NDG) products and 3 for degenerate (DG) products, and γ is the nonlinear coefficient.

4.2.1 Calculation for FWM-OPC products

Analysis of the FWM-OPC products will be made first; the process by which they are generated is illustrated in Fig. 4-2. The calculations assume P_{pump} is not depleted by the nonlinear process.

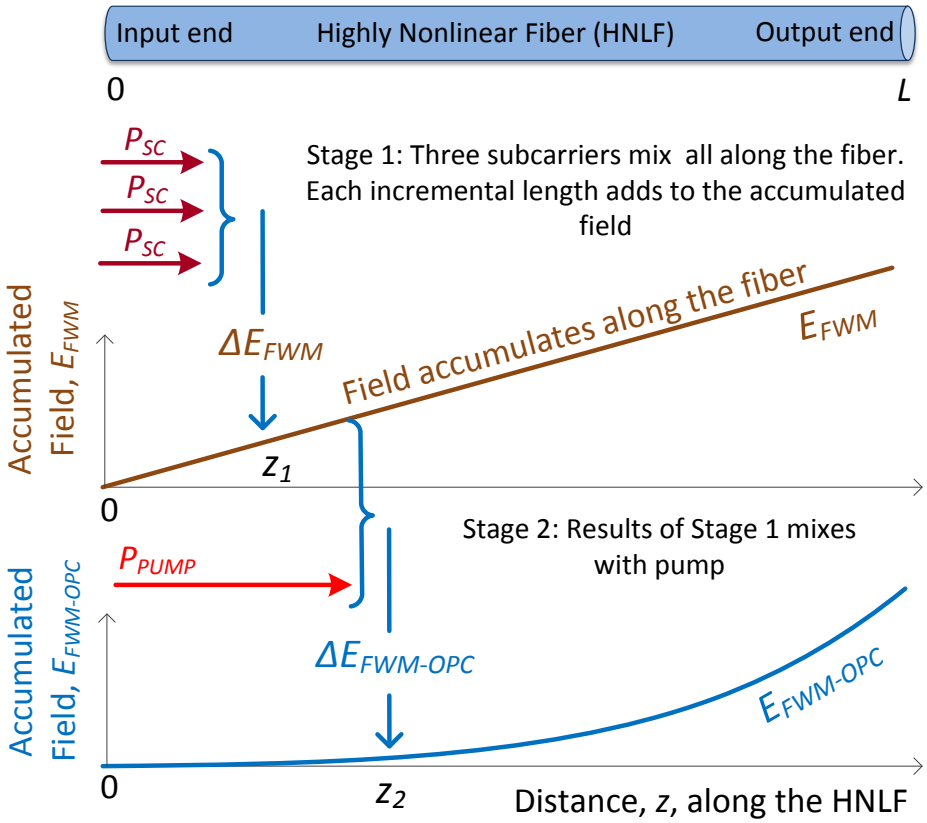

Figure 4-2: Two-stage calculation process of a single FWM-OPC product's field.

The first stage is that one of many FWM products is generated by three input subcarriers (indices i, j, k), each of power P_{SC}, undergoing four-wave mixing (two in the degenerate case). This process occurs from the input of the HNLF to its output. Using Equation (4.1), in each incremental length, Δz, of the fiber, at position z_1 along the fiber, the magnitude of the FWM field generated (watts$^{0.5}$) is

$$\left|\Delta E_{FWM}(z_1)\right| = \frac{D_a}{3}\gamma\Delta z\sqrt{P_{SC}(z_1)P_{SC}(z_1)P_{SC}(z_1)} \quad . \tag{4.2}$$

If we assume that the nonlinear element is lossless then $P_{SC}(z_1)$ becomes the input power of each subcarrier, $P_{SC}(0)$, which we shorten to P_{SC}. In the limit of $\Delta z \rightarrow 0$, the growth rate of the field is

$$\frac{d\left|E_{FWM}(z_1)\right|}{dz} = \frac{D_a}{3}\gamma\sqrt{P_{SC}^3} \quad . \tag{4.3}$$

The field at distance z_1 along the nonlinear element is found by integrating Equation (4.3), which gives

$$\left|E_{FWM}(z_1)\right| = \frac{D_a}{3}\gamma z_1\sqrt{P_{SC}^3} \ . \tag{4.4}$$

Thus the magnitude of the field associated with one FWM product (one combination of *i*, *j* and *k*) grows linearly with distance along the fiber, as shown in the brown trace in Fig. 4-2.

Stage 2 of the process for FWM-OPC mixes the accumulated product $E_{FWM}(z_1)$ with the *pump* × *pump*, at every point along the HNLF. We again assume the HNLF is lossless, so the pump power is constant along its length. At z_2, a new field is created, and is given by

$$\left|\Delta E_{FWM-OPC}(z_2)\right| = \frac{D_b}{3}\gamma\Delta z\left|E_{FWM}(z_2)\right|P_{pump} \ . \tag{4.5}$$

D_b is the degenerate factor in this case. If we substitute in from Equation (4.5), we find that the incremental contributions to the product's field are dependent upon the distance along the fiber, as

$$\left|\Delta E_{FWM-OPC}(z_2)\right| = \frac{D_a D_b}{9}\left(\gamma z_2\right)\left(\gamma\Delta z\right)\sqrt{P_{SC}^3}P_{pump} \ . \tag{4.6}$$

We can find the growth rate of this field at any point, *z*, using the limit $\Delta z \to 0$

$$\frac{d\left|E_{FWM-OPC}(z)\right|}{dz} = \frac{D_a D_b}{9}\left(\gamma z\right)\gamma\sqrt{P_{SC}^3}P_{pump} \ . \tag{4.7}$$

By integration over the length of the HNLF we find that the field at the output of the HNLF is

$$\left|E_{FWM-OPC}(L)\right| = \frac{D_a D_b}{9}\frac{\left(\gamma L\right)^2}{2}\sqrt{P_{SC}^3}P_{pump} \ . \tag{4.8}$$

The factor of ½ that comes from the integration is physically due to the second process being vanishingly small at the start of the fiber, because the first process has yet to begin. This factor is given the name as *two-stage effective length factor* in this thesis.

This calculation has provided the field strength of a single FWM-OPC product. There will be in the order of N_{SC}-cubed of these products, due to the various combinations of subcarriers (*i* ,*j*, *k*) contributing to the mixing process. Many of these products will fall on the same conjugated subcarrier, so we will define that $N_{FWM\text{-}OPC}(k')$ fall on conjugated subcarrier *k*'. Because the original subcarriers

are phase modulated, the products falling on a particular subcarrier will be incoherent, so their powers will add. Also, in the majority of cases, D_a = 6. Thus the total power of the FWM-OPC products falling on a single conjugated subcarrier k' will be

$$P_{FWM-OPC}(k') = N_{FWM-OPC}(k')(\gamma L)^4 P_{SC}^3 P_{pump}^2 \ . \tag{4.9}$$

4.2.2 Calculation for XPM-OPC products

A similar calculation can be performed for the XPM-OPC products, as shown in Fig. 4-3:

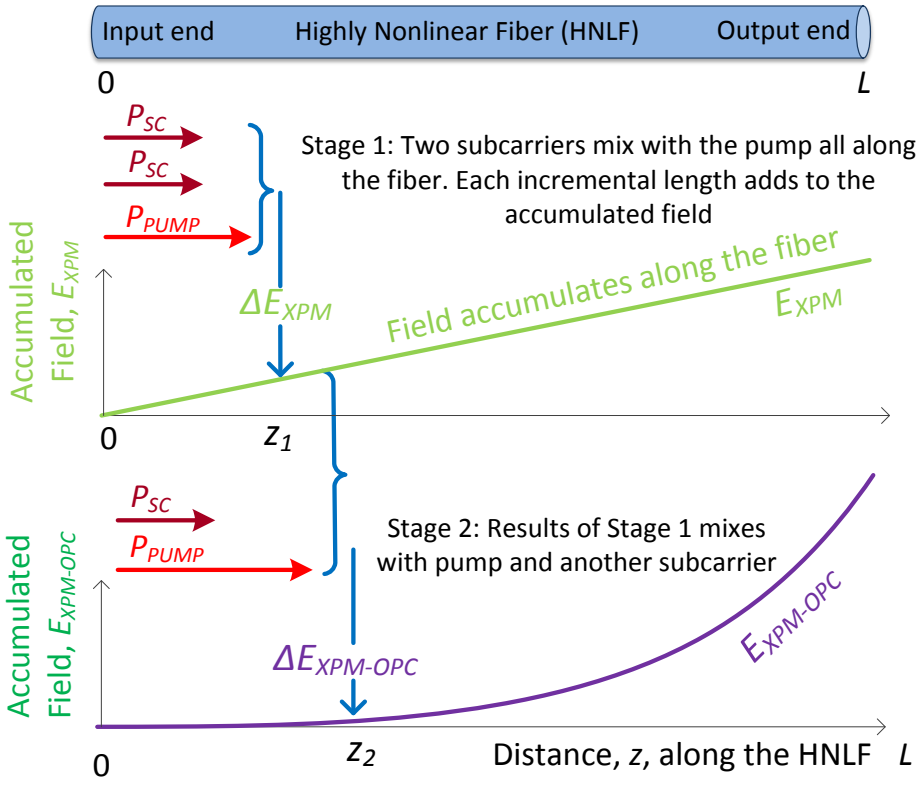

Figure 4-3: Two-stage calculation process of a single XPM-OPC product's field.

At Stage 1, the incremental field is

$$\left|\Delta E_{XPM}(z)\right| = \frac{D_c}{3}\gamma \Delta z \sqrt{P_{SC} P_{SC} P_{pump}} \ . \tag{4.10}$$

D_c is non-degenerate factor in this case and its value is 6. The field of a single XPM product grows linearly along the fiber and at distance z_1 is

$$\left|E_{XPM}(z_1)\right| = \frac{D_c}{3}\gamma z_1 \sqrt{P_{SC} P_{SC} P_{pump}} \ . \tag{4.11}$$

Stage 2 mixes the above field with an original subcarrier and the pump at every point along the fiber. The rate of growth of the resultant XPM-OPC product is

$$\frac{d\left|E_{XPM-OPC}(z)\right|}{dz} = \frac{D_c D_d}{9}(\gamma z)\gamma\sqrt{P_{SC}^3 P_{pump}} \ . \tag{4.12}$$

Both D_c and D_d are non-degenerate factors with value of 6. Integrating along the whole length, L, of the HNLF gives

$$\left|E_{XPM-OPC}(L)\right| = \frac{D_c D_d}{9}\frac{(\gamma L)^2}{2}\sqrt{P_{SC}^3 P_{pump}} \ . \tag{4.13}$$

Again, because the products from many combinations of input subcarrier are incoherent, the power of the tones that all fall on the same conjugated subcarrier, index k', is

$$P_{XPM-OPC}(k') = 4N_{XPM-OPC}(k')(\gamma L)^4 P_{SC}^3 P_{pump}^2 \tag{4.14}$$

where $N_{XPM\text{-}OPC}(k')$ is the number of the XPM-OPC products falling on conjugated subcarrier k'. Note how $P_{XPM\text{-}OPC}$ is 4-times stronger than $P_{FWM\text{-}OPC}$ because the pump was degenerate in Stage 2 of the calculation of $P_{FWM\text{-}OPC}$.

4.2.3 Calculation of the numbers of products falling on a conjugated subcarrier k'

The exact number of FWM-OPC products falling on a subcarrier will be considered now. Reference [66] provided equations for the numbers of non-degenerate and degenerate products due to FWM of three (or two) subcarriers. As illustrated in Fig. 4-1(*ii*) (brown), a proportion of these fall outside the bandwidth of the OFDM signal spectrum (dark red). These equations can be used for Stage 1 of the FWM-OPC process. The number of non-degenerate products is [66]

$$N_{FWM-NDG}(k) = \frac{\left(3N_{SC}^2 - 10N_{SC} - 4k(k-1)\right)}{8} + 1 \tag{4.15}$$

where k is the index of the input subcarrier, over a range $-N_{SC}/2$ +1 to $N_{SC}/2$. The number of degenerate products falling on a single subcarrier is

$$N_{FWM-DG}(k) = (N_{SC} - 2)/2 \ . \tag{4.16}$$

$N_{FWM\text{-}DG}$ is a small number compared with the number of non-degenerate products subcarriers. Stage 2 simply mirrors these products around the pump, so there are the same numbers of products falling on the conjugated signals. In the simulations an average signal quality across the conjugated signals band

will be calculated. So the average number of products over the OPC signal band is used. Ignoring the degenerate products, this gives the average number of products per subcarrier as approximately [66]

$$\overline{N_{FWM-OPC}} \approx 0.335 N_{SC}^2 \ . \tag{4.17}$$

This result can be used with Equation (4.9) to find the average power of the FWM-OPC products falling on a conjugated subcarrier, which is approximately

$$\overline{P_{FWM-OPC}} \approx 0.335 N_{SC}^2 \left(\gamma L\right)^4 P_{pump}^2 P_{SC}^3 \, . \tag{4.18}$$

A similar calculation can be performed for the XPM-OPC power falling on a subcarrier; however, in Stage 1, there are N_{SC}^2 XPM products, as the pump frequency is fixed. Stage 2 mixes each of these products with the pump and N_{SC} of input subcarriers, so the number of possible combinations will be multiplied by N_{SC}, giving a total of N_{SC}^3 XPM-OPC products. Again, many of these products fall outside the band of the OPC signal. MATLAB has been used to calculate the frequencies of all possible XPM-OPC products. Figure 4-4 plots the number of XPM-OPC products falling on a particular subcarrier, $N_{XPM\text{-}OPC}(k')$. The number of subcarriers is 100, which we used in simulation described in Section 4.3.

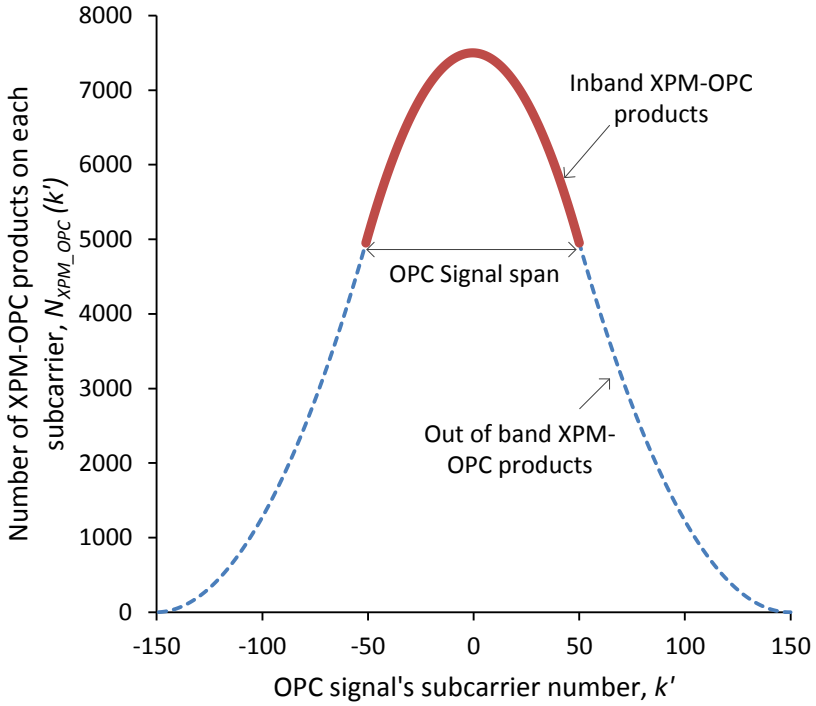

Figure 4-4: Number of XPM-OPC products falling on and around the conjugated (OPC) signal bandwidth for 100 subcarriers.

The ratio of the number of in-band XPM-OPC products to the total number of products was found to be 2/3, so the average power of an in-band XPM-OPC product is found by multiplying Equation (4.14) with factor of 2/3:

$$\overline{P_{XPM-OPC}} \approx 2.667 N_{SC}^2 (\gamma L)^4 P_{pump}^2 P_{SC}^3 . \tag{4.19}$$

The average power of both types of in-band OPC products that fall on a conjugated subcarrier is the sum of Equations (4.18) and (4.19), which gives

$$P_{NL-OPC} = P_{XPM-OPC} + P_{FWM-OPC} = 3 N_{SC}^2 (\gamma L)^4 P_{pump}^2 P_{SC}^3 . \tag{4.20}$$

4.2.4 Power of conjugated subcarrier

Using Equation (1) in [66], the power of a single optical phase-conjugated subcarrier, $P_{SC\text{-}OPC}$, is

$$P_{SC-OPC} = \frac{D_{DG}^2}{9} (\gamma L)^2 P_{pump}^2 P_{SC} = (\gamma L)^2 P_{pump}^2 P_{SC} . \tag{4.21}$$

4.2.5 Calculation of FWM distortion power

Another type of distortion is caused by intermodulation between the subcarriers after they have been phase conjugated, which is caused by non-degenerate FWM. Again, this process occurs once a subcarrier has been phase-conjugated. Using the previously derived *two-stage effective length factor* of 0.5 to calculate the power of these distortions and a factor to account for some of these products falling out of band [66] , the FWM power is estimated as:

$$P_{FWM} = 0.335 N_{SC}^2 (\gamma L)^2 P_{SC-OPC}^3 . \tag{4.22}$$

4.2.6 Calculation of ASE

The ASE noise generated in the input amplifier is conjugated to fall upon the conjugated signal bandwidth. Added to this is the ASE noise from the second amplifier. If the gain factors of the amplifiers are G_1 and G_2, the ASE at the output of the second amplifier in a single polarization, within the bandwidth of OPC signal, B_{sig}, is

$$P_{ASE} = 0.5 F \times B_{sig} \times hf \times \left((G_1 - 1)(\gamma L P_{pump})^2 G_2 L_{HNLF} + (G_2 - 1) \right) \tag{4.23}$$

where: F is the noise figure of the amplifiers, hf is the energy of a photon, and G_1 and G_2 are the gain factors of the first and second amplifiers, respectively. In the simulations, G_1 is set to give the

required P_{sig} assuming a modulator output, P_{TX} of -20 dBm, and G_2 is set to compensate for the loss in signal power during conjugation and the intrinsic loss factor of the HNLF, L_{HNLF}, found from Equation. (4.24), so

$$G_2 = \left(\left(\gamma L P_{pump} \right)^2 L_{HNLF} \right)^{-1} \tag{4.24}$$

where $L_{HNLF} = 10^{-(\alpha_{HNLF} L)/10}$.

4.2.7 Calculation of system *Q*

The average *Q*-value over all of the received subcarriers is calculated and compared with the simulation results. The average signal quality, *q*, over all subcarriers, where *Q* (dB) = 20.log$_{10}$(*q*), is the ratio of subcarrier power to all of the noise and distortions in the bandwidth of a subcarrier, and can be expressed as :

$$q^2 = \frac{G_2 P_{SC-OPC}}{G_2 P_{NL-OPC} + G_2 P_{FWM} + P_{ASE}}. \tag{4.25}$$

In the above equation, the OPC signal, FWM-OPC and FWM-OPC terms have been multiplied by G_2 to make the output of the second EDFA as the reference point for *Q*-value calculation.

The effect of attenuation in the nonlinear process can be approximately accounted for by using L_{eff} instead of L [66] in Equations (4.20), (4.21) and (4.22). However, there will be a small error because the *two-stage effective length factor* is ½ only for the lossless case; loss slightly increases this as shown later in Fig. 4.9. A perfect model for a fiber with loss can be achieved by integrating along *z* for the true power map.

4.2.8 System performance

Consider a hypothetical case with parameters for back-to-back system as given in Table I.

Table 4-1: Parameters Value for a hypothetical system.

Quantity	Value
Noise figure, NF	6 dB
Optical frequency, f	193.1 THz
Optical bandwidth, B_{sig}	7.8125 GHz
Transmitter output, T_x	-20 dBm
HNLF loss, α_{HNLF}	0.97 dB/km
HNLF CD	0 ps/nm/km
HNLF length, L	1000 m
HNLF nonlinear coefficient, γ	11.5 $W^{-1}km^{-1}$
Pump power, P_{pump}	7.8 dBm

Figure 4-5 shows the average powers of the unwanted products falling within the signal band and noise versus the input signal subcarrier power. The results show that ASE is the limiting factor below a subcarrier power of -17 dBm; XPM-OPC is the most severe limitation at powers above -17 dBm. The power of FWM-OPC, which is 9-dB lower than the XPM-OPC, is also significant. The FWM products due to the OPC signal subcarriers are insignificant, being 60-dB below the OPC distortions. This is because the conjugated signals are about 20-dB below the input subcarriers.

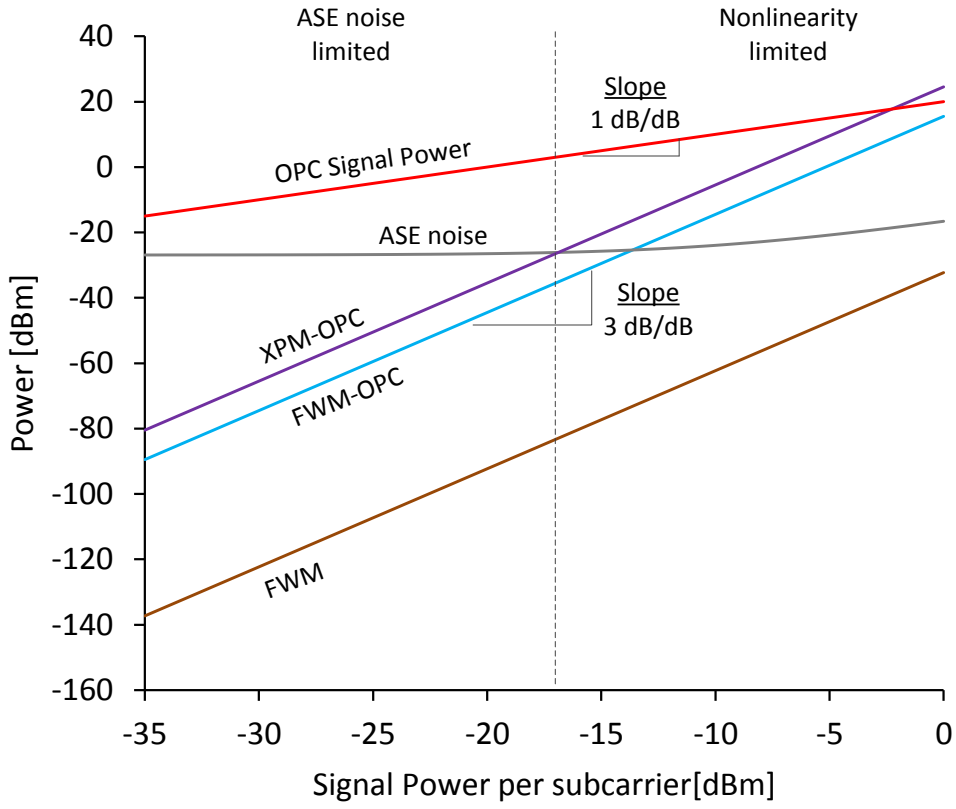

Figure 4-5: OPC signal and NL distortion power versus input signal subcarrier power after the output EDFA. The powers are summed over the bandwidth of the conjugated OFDM spectrum.

Figure 4-5 also shows that at an input subcarrier power of -3.0 dBm, XPM-OPC added to FWM-OPC becomes stronger than the OPC signal. This is because these terms increase with the cube of the signal power, whereas the OPC signal power only increases linearly with the signal power. Therefore, the usable signal power into the HNLF is limited by this effect. On the other hand, an EDFA is required to amplify the OPC signal after the nonlinear element, which produces ASE. These counteracting features imply that there is an optimal input signal power that maximizes back-to-back OPC performance.

Figure 4-6 plots the calculated OPC signal power (—), total unwanted products ($P_{NL\text{-}OPC}$ and ASE) (—) and the Q-value (●) against input signal subcarrier power. It shows that the optimum signal subcarrier power is -18 dBm. An important conclusion from Fig. 4-6 is that an OPC module can limit the maximum achievable performance of the system, even if the transmission fiber's nonlinearity is completely canceled by MSSI. For higher-order modulation schemes, where a good Q-value is crucial, care should be taken to raise this limit by optimizing the OPC module, by using high P_{pump} and γL, and also by operating with optimum signal power into the $\chi^{(3)}$ nonlinear element for the specific pump power.

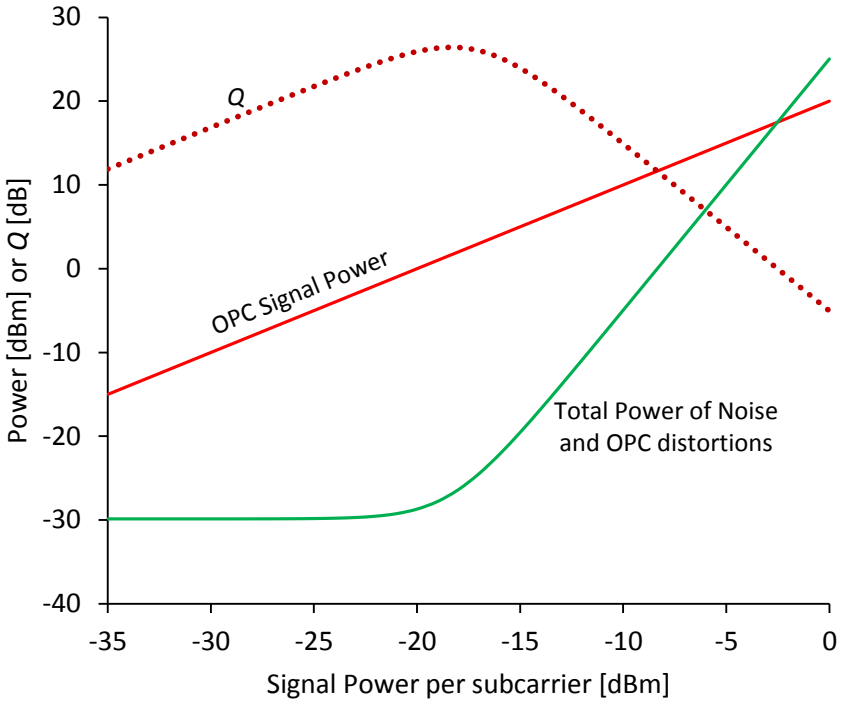

Figure 4-6: Theoretical back-to-back performance with OPC module versus input signal power per subcarrier.

4.3 Verification with simulation and experimental results

In this section, the analytical results in Section 2 are compared with simulation and experimental results. The numerical simulations were conducted using VPItransmissionMaker v8.7. The OFDM

signal was generated using MATLAB for the simulations and experiments, using a 128-point inverse fast Fourier transform (IFFT). 100 subcarriers were modulated with 4-QAM and 8-point cyclic prefix (CP) was inserted.

The schematic of the experimental setup is shown in Fig. 4-1(a). For the experiment, a Tektronix AWG 7102 10-GSamples/s 2-port arbitrary waveform generator (AWG) is used in the transmitter. The in-phase (I) and quadrature (Q) components of the AWG drove a Sumitomo complex optical Mach-Zehnder modulator (C-MZM) to create a 14.7-Gb/s OFDM signal. A single-polarization coherent receiver, consisting of a Kylia optical hybrid and U^2T balanced photodiodes, was used to down-convert the optical signal. A polarization controller was used to maximize the detected electrical power. A Photonetics Tunics ECL was used as the local oscillator (LO). An Agilent Infiniium DSO-X 92804A 80-GSample/s 28-GHz real-time sampling oscilloscope was used as the analog to digital converter (ADC). The digital signal was then equalized using a typical single-tap OFDM equalizer [46].

Figure 4-7 shows the theoretical, simulated and experimental *Q*-values for back-to-back system when the input signal subcarrier power is varied.

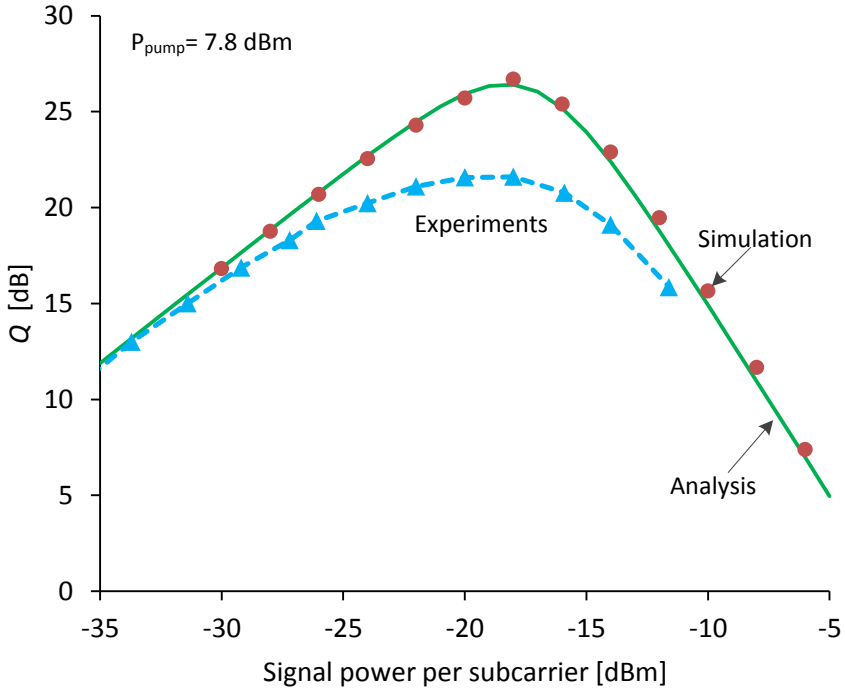

Figure 4-7: Analytical (—), simulated (●) and experimental (▲) *Q* values versus input signal subcarrier power for a back-back system.

The simulation results match very well with the results obtained from the analytical calculation. The experimental results show a ceiling in the peak performance. This could be due to system imperfections such as the quantization noise of the DAC and ADC, imbalances in the I and Q signal paths and laser phase noise.

Next, back-to-back system performance dependence on three design parameters is investigated. These parameters are: pump power, the length of the nonlinear element and the total bandwidth of the optical signal.

4.3.1 Influence of pump power

Figure 4-8 shows theoretical and simulated Q value for three different pump powers, P_{pump}. It shows that the Q-value in the ASE region increases by 2 dB for every 1-dB increase in the pump power. This agrees with Equation (4.23), since the OPC signal is proportional to $P_{pump} \times P_{pump} \times P_{SC}$. At nonlinearity-limited input subcarrier powers, the Q value does not increase by using higher pump powers. This is because the main limiting factor, the OPC distortion power, given by Equation (4.20), is also proportional to $P_{pump} \times P_{pump}$, This causes both the OPC signal and the OPC distortion to increase with the square of P_{pump}; thus the performance in the nonlinear region does not improve when P_{pump} is increased.

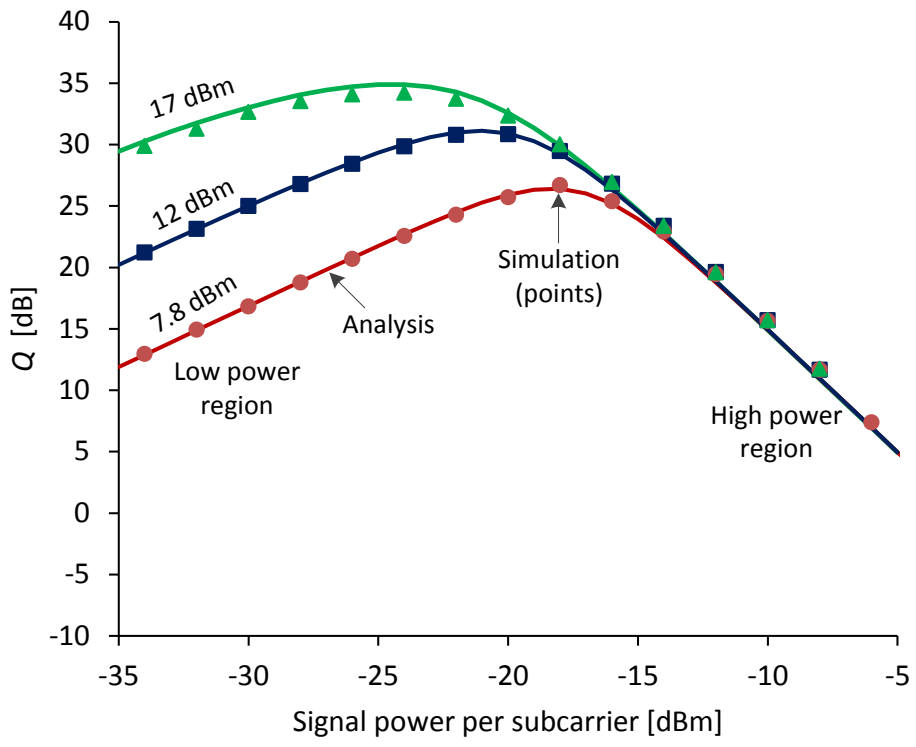

Figure 4-8: Theoretical (solid lines) and simulated (symbols) Q-value versus signal subcarrier power for three pump powers.

Importantly, the optimum input signal subcarrier power at which the Q peaks shifts towards lower powers when P_{pump} is increased. Additionally, a simple geometrical calculation predicts that the Q_{max} is improved by $2\sqrt{3}/(1+\sqrt{3}) = 1.26$ dB for every 1-dB increase of P_{pump}.

4.3.2 Influence of the length of the HNLF

Figure 4-9 shows the effect of the length of the HNLF on optimal signal quality, and the input power used to obtain each optimum. As the length is increased, the optimum signal quality increases; however, beyond 1000 m the quality begins to reduce in the simulation, but not in the theory. This shows that simply substituting L_{eff} for the total HNLF length, to account for attenuation, is inaccurate for long HNLF when two-stage processes are present, but is sufficient for most situations.

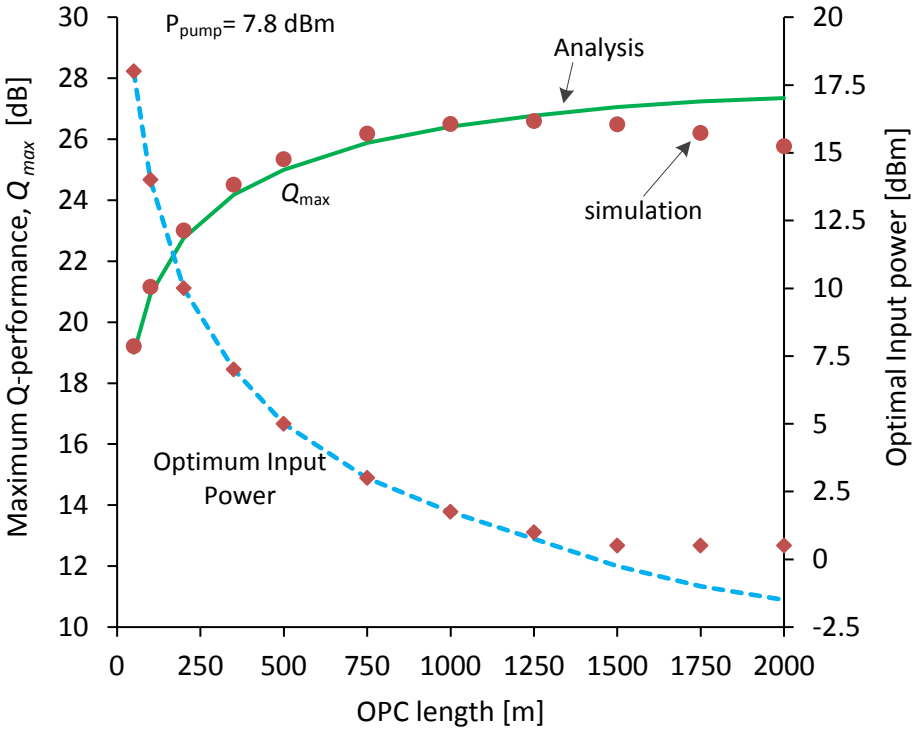

Figure 4-9: Maximum Q performance and optimal input power versus HNLF length.

4.3.3 Influence of the signal bandwidth

Figure 4-10 shows the simulation and analytical prediction of maximum Q-value for different optical OFDM signal bandwidths. The pump power was increased to 17 dBm to accommodate the broad band OPC. The theoretical results agree very well with the simulation results irrespective of the OFDM signal bandwidth when CD is ignored; OPC could span the C and L bands (λ=1530-1625 nm, $\Delta f \approx 10$ THz), provided the HNLF is dispersionless across the span or its dispersion is managed

appropriately. However, simulation results using the parameters from our OFS HNLF (CD = 0.01 ps/nm/km) show some penalty when the bandwidth is more than one terahertz.

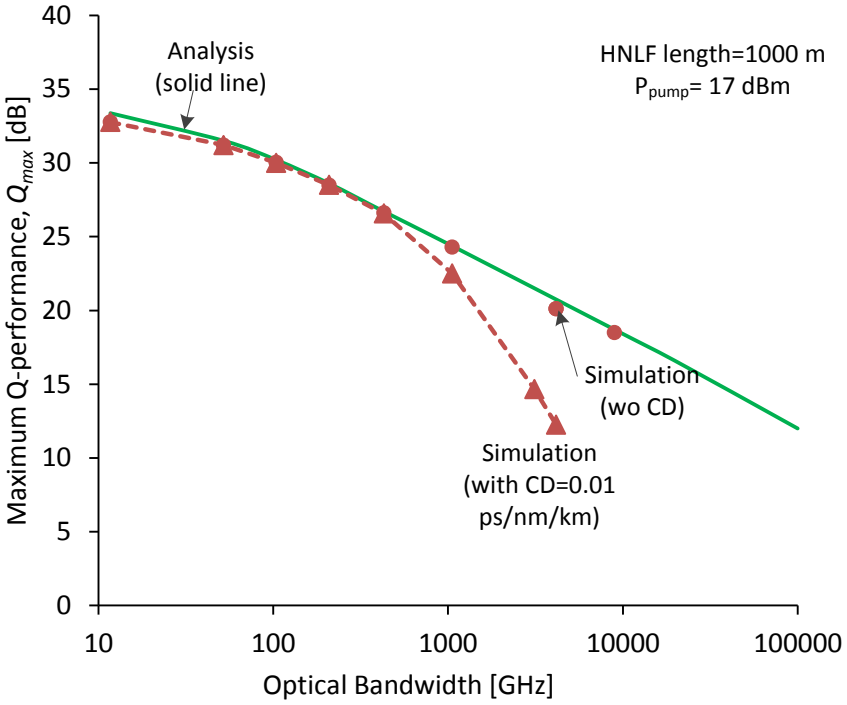

Figure 4-10: Optimal signal quality and corresponding input power versus signal bandwidth.

4.4 Conclusion

In this chapter, analytical expressions for the performance limiting factors in CO-OFDM systems with mid-span spectral inversion using optical phase conjugation has been presented. It has been identified for the first time that two different two-stage mixing products, XPM-OPC and FWM-OPC, are the major nonlinear limiting factors in the high power region for CO-OFDM systems using OPC, with XPM-OPC dominating. The analytical results agree well with our split-step Fourier method (SSFM) simulations and experiments. The results show that OPC could support signals with over 10-THz bandwidths, though the dispersion of the nonlinear element would have to be carefully managed.

In the next chapter, the first experimental demonstration of nonlinearity compensation using MSSI in a dual polarization CO-OFDM system will be presented.

5 Experimental demonstrations of MSSI in dual polarization CO-OFDM systems

In the previous chapter, major nonlinear limiting factors were identified for an OPC module relying on third order nonlinearity. Therefore, it is of great interest and concern to quantify practical benefit achieved in a real world system which uses MSSI for nonlinearity compensation. Our group has previously reported the first experimental results for MSSI in a single-polarization CO-OFDM systems [80, 81], which to the best of our knowledge represents the first use of MSSI for coherent communication systems.

At the Opto-Electronics and Communications Conference 2013 (OECC 2013) [86, 152], an experimental demonstration of MSSI for fiber nonlinearity compensation in a dual-polarization (DP) CO-OFDM system was presented for the first time. The demonstration was at a rate of 1.2 Tb/s. This demonstration is, to the best of knowledge, again the first demonstration of polarization-diversity MSSI for any type of coherent communication system. Subsequently, interest in broadband phase-conjugation based techniques for nonlinearity mitigation in coherent communication systems has led to demonstrations of Raman-enhanced MSSI [91, 154] and multiple phase-conjugation based-systems [89] at the 2014 conference of Optical Fiber Communications (OFC).

In this chapter, a detailed discussion of the above experimental demonstration and its benefit for 121-Gb/s and 1.2-Tb/s DP CO-OFDM MSSI systems for fiber nonlinearity compensation are presented. An overview of important design considerations is also discussed for improving the performance of the OPC module itself.

The content of this chapter has been published in [86, 152, 155].

5.1 System carrying 121 Gb/s

5.1.1 Experimental setup

Figure 5-1 shows the transmitter configuration for 121-Gb/s system. It comprises of three sections: Optical modulation and comb generator, Frequency Shifter and Pol. Mux. Emulator. An external cavity laser (ECL, 193.1 THz) provides the optical carrier. The external cavity lasers used throughout this chapter are specified to have a linewidth less than 100 kHz. A 30.3-Gb/s OFDM signal band is created using 194-point inverse fast Fourier transforms (IFFT) with 154 16-QAM modulated subcarriers and a 9-point cyclic prefix (CP). A 10-GS/s arbitrary waveform generator (AWG) is used for digital to analog conversion, producing 20.3-ns long, 7.94-GHz bandwidth OFDM symbols.

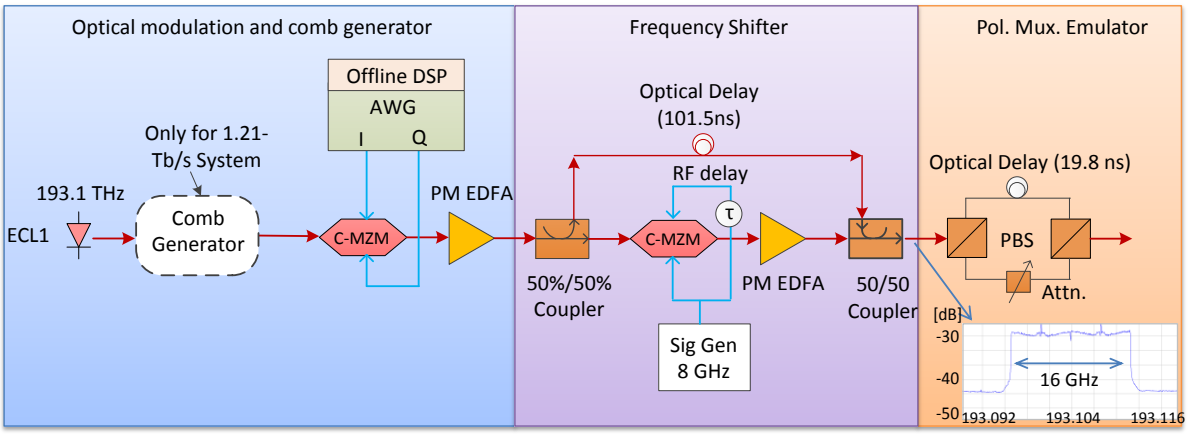

Figure 5-1: System diagram showing experimental setup for Transmitter.

A 20-GHz optical bandwidth complex Mach-Zehnder modulator (C-MZM) modulates the electrical OFDM signal onto the output of the ECL. The optical signal is then divided into two paths; one path is frequency shifted by 8 GHz using another C-MZM as a serrodyne modulator, then the shifted and un-shifted signals are combined to form a continuous 16-GHz wide channel, as shown in inset of Fig. 5-1. The spectrum also shows the optical carrier at the center of each band. In order to maintain the optical carrier at the center, the two central subcarriers of the electrical OFDM signal were nulled. A delay of exactly 5 OFDM symbols (101.5 ns) produces an integer-OFDM-symbol delay between the shifted and un-shifted signals. The channel is then passed through a POLMUX emulator (Kylia PDME-00019), with a 19.8-ns delay between the two orthogonal polarizations to de-correlate them, to create a 121-Gb/s DP signal.

Figure 5-2 shows the receiver configuration, which is the same for the 121-Gb/s and 1.21-Tb/s systems.

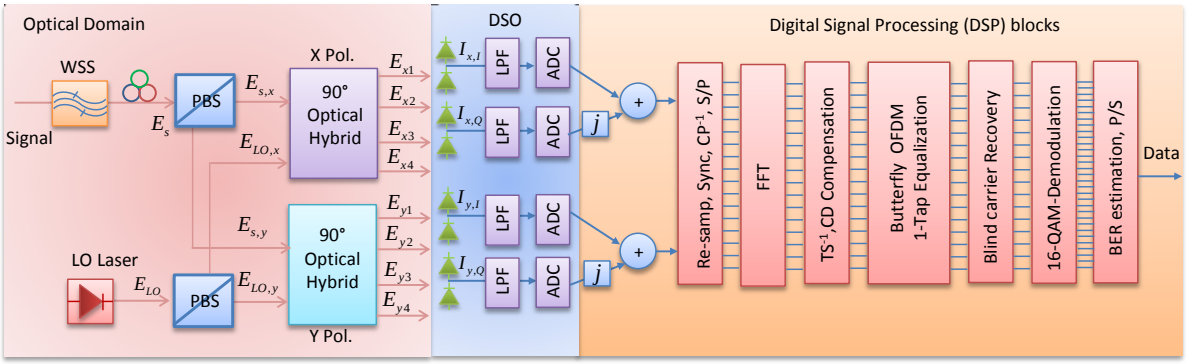

Figure 5-2: Schematic diagram showing experimental setup for dual polarization coherent receiver.

In the optical front end, a wavelength selective switch (WSS, Finisar Waveshaper) is used to remove the out-of-band noise. The filtered signal is fed into the signal port of a coherent receiver, consisting of an optical hybrid (Kylia MINT-2×8) and 25-GHz bandwidth balanced photodiodes. A second ECL, tuned to match the frequency of either the original signal for reference system without MSSI (193.1 THz) or the conjugate idler for the MSSI system (193.5 THz), is used as the local oscillator. A 40-GSample/s, 16-GHz bandwidth real-time sampling oscilloscope (Agilent DSO-X 92804A) digitizes the photo-detected signals. The signal is processed offline, with the equalizer comprising [81]: a resampler; a frequency offset compensator; a butterfly OFDM 1-tap equalizer [156]; and a blind symbol phase estimator [157, 158]. In the system without MSSI, digital chromatic dispersion (CD) compensation precedes the 1-tap equalizer.

Figure 5-3 shows the details of the optical link with OPC module.

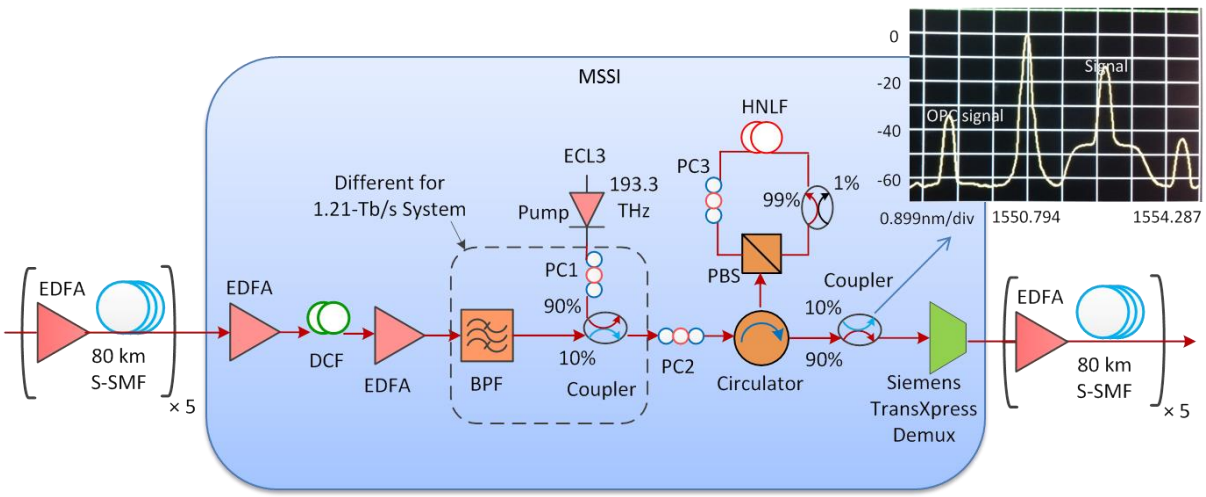

Figure 5-3: Schematic diagram of the experimental link and OPC module.

The link comprises 10×80-km standard single-mode fiber (S-SMF) spans with variable output power erbium doped fiber amplifiers (EDFA) to compensate for the loss of each span. The OPC module is

placed after the fifth span. The launch power into each span is set by adjusting the output power of the EDFAs. The EDFAs have specified maximum noise figures of 7 dB. A dispersion compensation fiber (DCF, Siemens BDCM-60, 1011 ps/nm, 12 dB loss), placed after the fifth span, is used to improve the fiber nonlinearity compensation [159]. The input power into the DCF was -4 dBm for 121-Gb/s system and 0 dBm for 1.21-Tb/s system, to ensure the linear propagation through the DCF. The role of DCF and how it helps improve the nonlinear mitigation have been discussed in detail in Section 3.3.2.

After the DCF, another EDFA amplifies the signal to 18 dBm. Then the signal is filtered by a band pass filter (BPF, 5 nm bandwidth) before being fed into the 10%-port of a 90%/10% coupler. The pump from a third ECL (193.3 THz), set to 16 dBm output power, is input to the 90% port of the coupler. The pump power is kept at 16 dBm, because when the MSSI unit was pumped with higher powers the system's stability was found to degrade, indicating significant stimulated Brillouin scattering (SBS). To achieve efficient generation of the OPC signal, the wavelength of the pump is tuned slightly above the zero dispersion wavelength (ZDW) of the HNLF, to minimize the phase mismatch between the interacting waves [160].

The combined signal and pump wave is passed to a polarization-diversity OPC module [161], as recently used to demonstrate pre-compensation of fiber nonlinear effect in 80-Gb/s RZ-DPSK dual polarization signals [162]. Note that this polarization diverse configuration is insensitive to the polarization state of the input signal [161, 162]. The combined waves feed Port 1 of an optical circulator. Port 2 of the circulator connects to the common port of a polarization beam splitter (PBS). The two polarized (X Pol. and Y Pol.) ports of the PBS are interconnected via a polarization controller (PC), 1 km of highly nonlinear fiber (HNLF) and a 99%/1% coupler for power monitoring. After the insertion losses of the circulator, PBS and polarization controller, the pump and signal powers launched into the HNLF module from each direction are 12 dBm and 4 dBm respectively. The HNLF has a nonlinear coefficient, γ, of 11.5 W-1km-1, CD of 0.01 ps/nm/km at 1550 nm, CD slope of 0.02 ps/nm^2/km, zero-dispersion-wavelength (ZDW) of 1549.120 nm and loss coefficient of 0.81 dB/km. Port 3 of the circulator connects to a 90%/10% coupler; the 10% Port connects to an optical spectrum analyzer (OSA): the 90% Port connects to a 200-GHz channel spacing demultiplexer (Siemens TransXpress), which selects the conjugated signal and removes the original signal, the pump and the out of band amplified spontaneous emission (ASE). The output of the demultiplexer is transmitted through the second half of the link.

The function of the three polarization controllers is as follows. PC3 is used to adjust the polarization of the travelling waves to be linearly polarized upon launch into the HNLF to maximize conversion efficiency (CE), which is continuously monitored at the OSA connected at Port 3 of the circulator, using a 90%/10% coupler. PC1 and PC2 can then be adjusted to reduce the pump power as measured

at the 1% coupler output within the polarization diversity loop by 3dB, which corresponds to an equal power split of the pump to both the clockwise ('x') and anti-clockwise ('y') arms of the polarization diverse OPC module. Once set, the polarization of the pump wave in the polarization diversity loop was stable enough to gather consistent performance measurements.

By splitting the pump wave equally into the two branches of the loop, the CE of the orthogonally polarized counter-clock- and clockwise travelling signals should be similar [163]. This is because CE is given by $\left(\gamma P_{pump} L_{eff}\right)^2$, where P_{pump} is pump power, γ is nonlinear coefficient of HNLF, and L_{eff} is its effective length. Therefore, in a counter propagating fiber loop scheme where both signals experience very similar loss and dispersion, almost equal CE between the two counter propagating signals is expected.

It is worth noting that the polarization controllers can be avoided entirely by using polarization maintaining fiber and components in the OPC module. This will then ensure alignment of the pump wave to be 45^o to the reference polarization axis of the polarization beam splitter and linear polarization states at input to the HNLF.

Inset of Fig. 5-3 shows an optical spectrum analyzer (OSA) trace (sensitivity: -75 dBm, resolution bandwidth: 0.1 nm) containing the original signal, pump and the OPC signal. This trace is taken after the circulator and before the demultiplexer filter in an 800-km MSSI system. The CE, defined here as the ratio of conjugate power to signal input power at circulator Port 3, was about -20 dB.

Even if the CEs of the counter propagating signals are slightly different in practice, the true performance of the OPC module is best revealed through rigorous testing through measuring the quality of the received signal at the end of the link.

5.1.2 Results for the 121-Gb/s system

Figure 5-4 shows the *Q* in a back-to-back system with our fiber spans for both X polarization (●) and Y polarization (○) versus signal input power measured at the output of the EDFA placed after the DCF. The *Q* was calculated from the counted bit error ratio (BER), using $Q[dB] = 20 \times \log_{10}\left(\sqrt{2} erfc^{-1}\left(2BER\right)\right)$ [99, 164].

The result shows that the X and Y polarizations have very similar performance, demonstrating that the performance of MSSI in our system is polarization independent, able to effectively handle dual-polarization, coherent signals. It also shows that the optimum signal input power is 18 dBm, which gives the maximum back-to-back *Q* of 12.5 dB. For the transmission results shown in Fig. 5-5, the output power of the EDFA after the DCF was fixed at 18 dBm to maximize the transmission performance. The *Q* in a back-to-back configuration without MSSI is 15.2 dB. The 2.7-dB decrease in

measured *Q* after the OPC module, shown in Fig. 5-4, is likely to be due to nonlinear mixing products generated within the MSSI and ASE from the EDFA that is used to compensate for the low four-wave mixing conversion efficiency within the HNLF [84, 85].

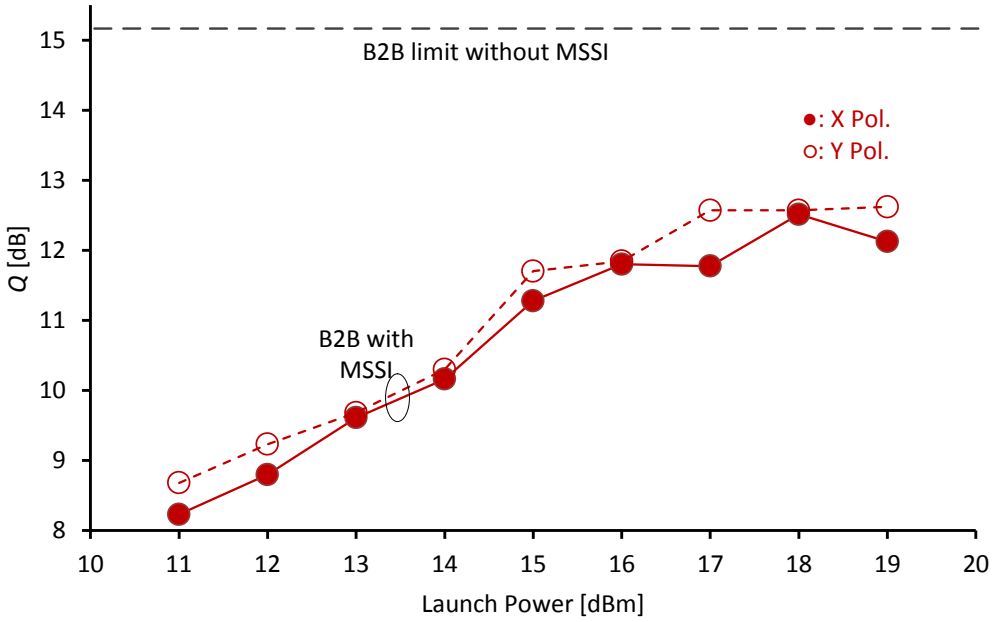

Figure 5-4: Back-to-back performance of the MSSI system for 121-Gb/s system. Launch power is measured at the output of the EDFA after the DCF.

Figure 5-5 shows the transmission performance in a 10×80-km link against the launch power into the S-SMF spans for two systems: one with MSSI (X Pol.: ●, Y Pol.: ○) and one without MSSI (X Pol.:▲, Y Pol.:Δ). Although the MSSI system has 2.7-dB less back-to-back *Q* than the system without MSSI, MSSI increases the maximum launch power measured at 7%-overhead hard-decision FEC limit by about 6.4 dB, from 3 dBm to 9.4 dBm. This shows that MSSI is effective in reducing the impact of fiber nonlinearity in DP CO-OFDM systems. The peak *Q* is not improved with MSSI. This is due to back-to-back performance penalty [84, 85] introduced by the OPC module, which we investigate in Section 5.3.

The MSSI system performance shows a plateau which is mainly due to sub optimal operation for the MSSI systems around the launch powers where the system was supposed to show peak performance. During measurement, I adjusted the signal and local oscillator polarizations, polarization of the signal and pump inside the OPC loop at the lowest launch power for each channel. But at the time when I reached the optimum power region, the adjusted condition was slightly off from the optimum condition, which resulted about 0.5 dB penalty for the MSSI system. Adjusting those measurement

conditions at the optimum launch power region for every channel is the better solution to avoid such kind of measurement penalty.

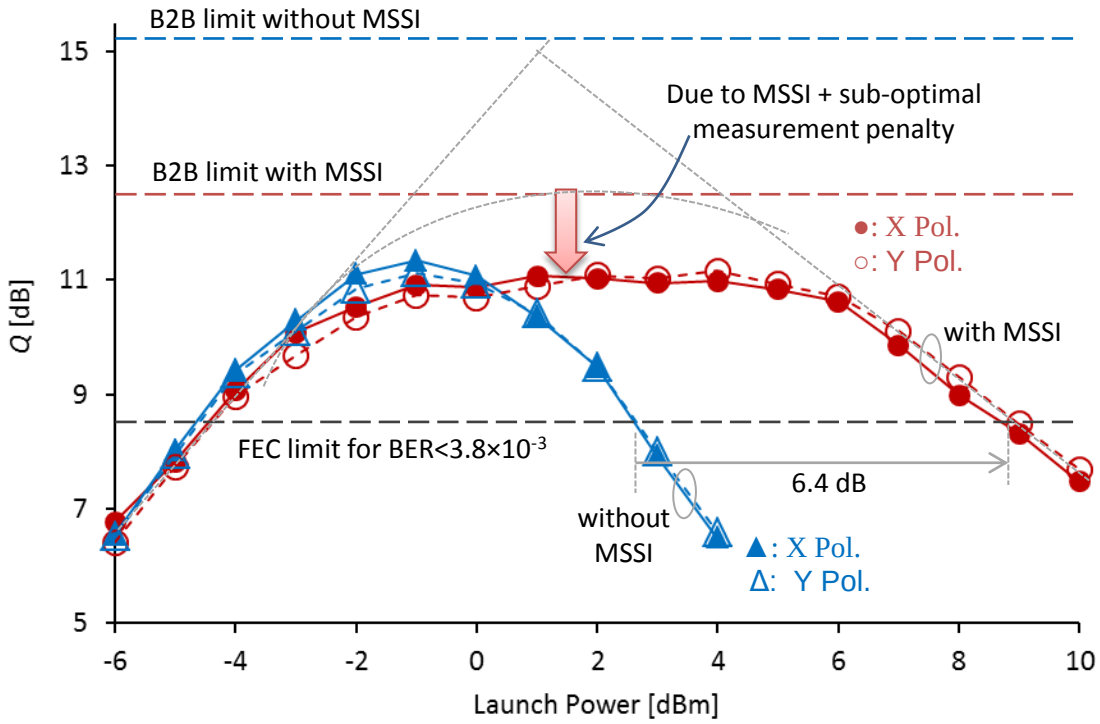

Figure 5-5: *Q* versus launch power after 800 km with and without MSSI for 121-Gb/s system.

5.2 System carrying 1.21-Tb/s

5.2.1 Experimental setup

The majority of the experimental setup for the 1.21-Tb/s system is the same as for the 121-Gb/s system as shown in Fig. 5-1. Only difference was using an optical frequency comb generator for the 1.21-Tb/s transmitter, which is discussed below.

The output of a 193.7-THz ECL is fed into the frequency comb generator module [165], which is shown in Fig. 5-6. Two 40-GHz bandwidth phase modulators are used to generate 10 comb lines. The modulators have $V_{\pi} = 6$ V, and are driven by a 16-GHz RF signal, that is split into two paths before amplification by SHF amplifiers to give peak-to-peak voltages of 7.10 V.

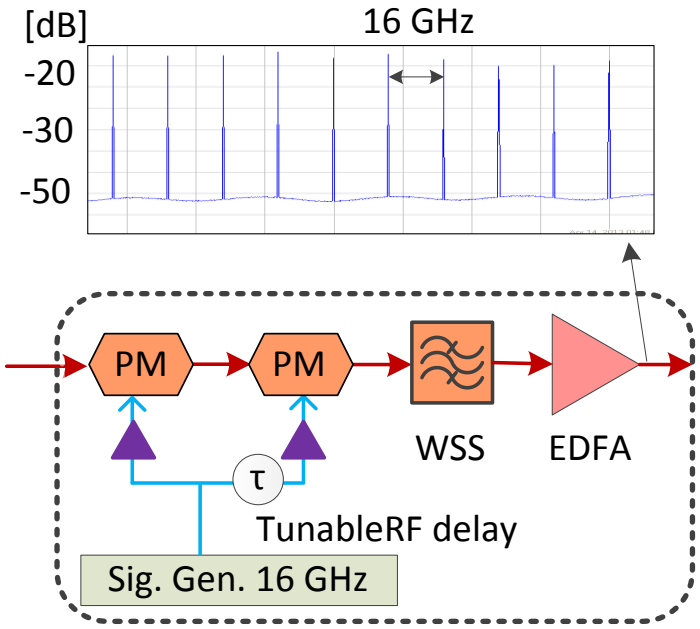

Figure 5-6: Schematic diagram of optical frequency comb generation module used in the 1.2-Tb/s Transmitter.

These RF signals are fed into the modulators, to generate peak phase shifts of about 0.6π. In order to flatten the output comb lines from the second modulator, the phase difference between the two RF paths is adjusted by a tunable RF delay. The 10 selected comb lines used for the OFDM super-channel have a 6-dB variation between the edge and center lines. These lines are selected and equalized in power by a WSS, as shown in inset of Fig. 5-6. The tones are then amplified and fed through the C-MZM to modulate OFDM signal onto these tones. The modulated signal is then divided into two paths; one path is frequency shifted by 8 GHz and then combined with through paths to form a 20-band 160-GHz wide super-channel as shown in Fig. 5-8(a).

Some modifications were made to OPC module also for the 1.2-Tb/s system, to increase the back-to-back performance with MSSI. Figure 5-7 shows the module that combines the signal and pump.

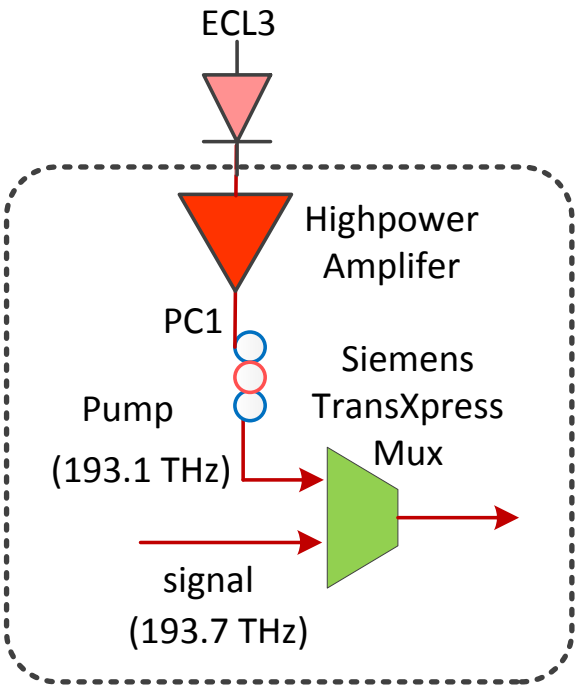

Figure 5-7: Schematic diagram of combining the signal and pump for Tb/s MSSI system.

The pump (ECL3, 193.1 THz) is amplified from 16 dBm to 33 dBm using a high power EDFA (Amonics AEDFA -33-B-FA) run at maximum power. The signal is amplified to 19 dBm using another variable gain EDFA. A multiplexer with a 200-GHz channel spacing simultaneously combines the signal and pump, while reducing out-of-band ASE in each of these wavebands. The HNLF in the OPC module is shortened to 45 m, to reduce the long-scale fluctuations of the ZDW which become significant in longer HNLFs. Such variations along the fiber occur in an unpredictable manner, which degrades the OPC gain and bandwidth [160]. Thus, a short HNLF is more suitable for broad band OPC [160]. However, the pump power needs to be increased in order to get reasonable conversion efficiency, and this is possible due to the higher SBS threshold of shorter HNLFs [166].

The HNLF has a nonlinear coefficient, γ, of 11.5 $W^{-1}km^{-1}$, CD of −0.05 ps/nm/km at 1550 nm, CD slope of 0.02 $ps/nm^2/km$, zero-dispersion-wavelength (ZDW) of 1552.82 nm and loss coefficient of 0.97 dB/km. Note that, the wavelength of the pump is adjusted to match with the ZDW of this HNLF. The pump and signal powers launched into the HNLF from each direction are 29 dBm and 15 dBm respectively.

Figure 5-8(a) shows the spectrum of 160-GHz OFDM super-channel comprising 20 OFDM bands each 8-GHz wide, measured with a high-resolution spectrophotometer (resolution 20 MHz) after the 50%/50% coupler and before the POLMUX emulator. Fig. 5-8(b) is the spectrum after the circulator, measured with an optical spectrum analyzer (OSA) with a sensitivity of -80 dBm and resolution bandwidth of 0.1 nm.

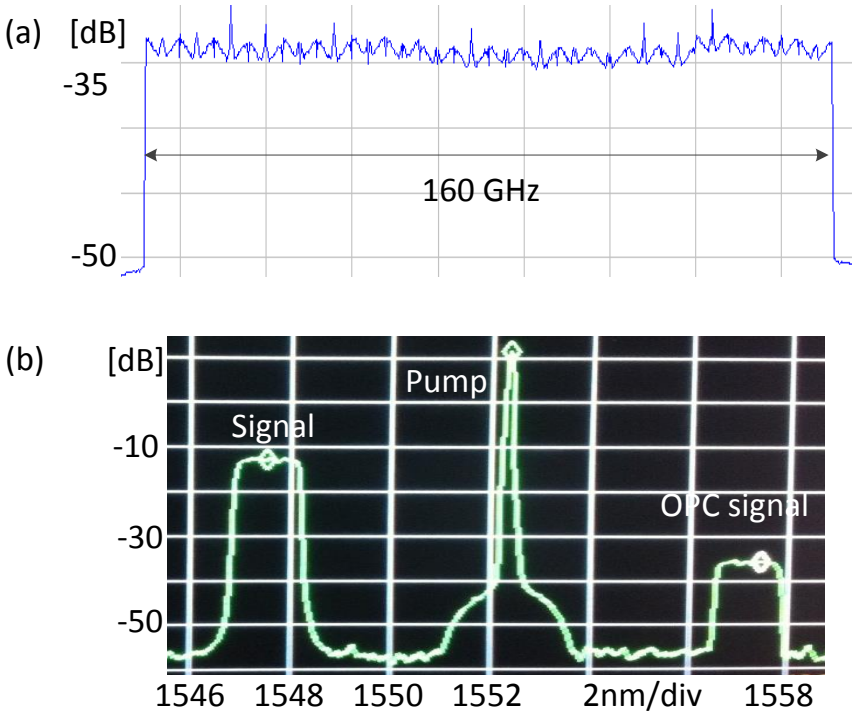

Figure 5-8: Spectra at the output of the frequency shifter, and before the output filter of the OPC module.

The conversion efficiency was -24 dB. Although the conversion efficiency was 4-dB lower than the previous OPC module, due to the shorter HNLF, the OPC signals from the 121-Gb/s and 1.21-Tb/s systems had similar optical signal-to-noise ratio (OSNR), as shown by the OSA in Fig. 5-3 and Fig. 5-8(b). This is because of higher signal power and higher pump to signal ratio (121-Gb/s system: 8 dB, 1.21-Tb/s system: 14 dB) fed into the OPC module in the 1.21-Tb/s system. Again, the OSA is placed after the circulator and before the demultiplexer filter in the 800-km link.

5.2.2 Results for the 1.21-Tb/s system

Figure 5-9 shows the *Q*, derived from the average BER of the center OFDM band at different launch powers. The back-to-back penalty for MSSI is 2.5 dB, comparable to the penalty measured for the 121-Gb/s system. The performance with MSSI for two orthogonal polarization (X Pol: ●, Y Pol: ○) and without MSSI (X Pol:▲, Y Pol:Δ) are very similar at low powers, where ASE from the link dominates. However, at higher powers, the MSSI mitigates fiber nonlinearity; the maximum launch power (measured at the FEC limit) is increased by 2.8 dB, to 10.0 dBm. This benefit is reduced compared with the 121-Gb/s system, partially due to the lower back-to-back performance for the 1.21-Tb/s system with MSSI (*Q* = 10.3 dB for the 1.21-Tb/s signal versus 12.6 dB for the 121-Gb/s system).

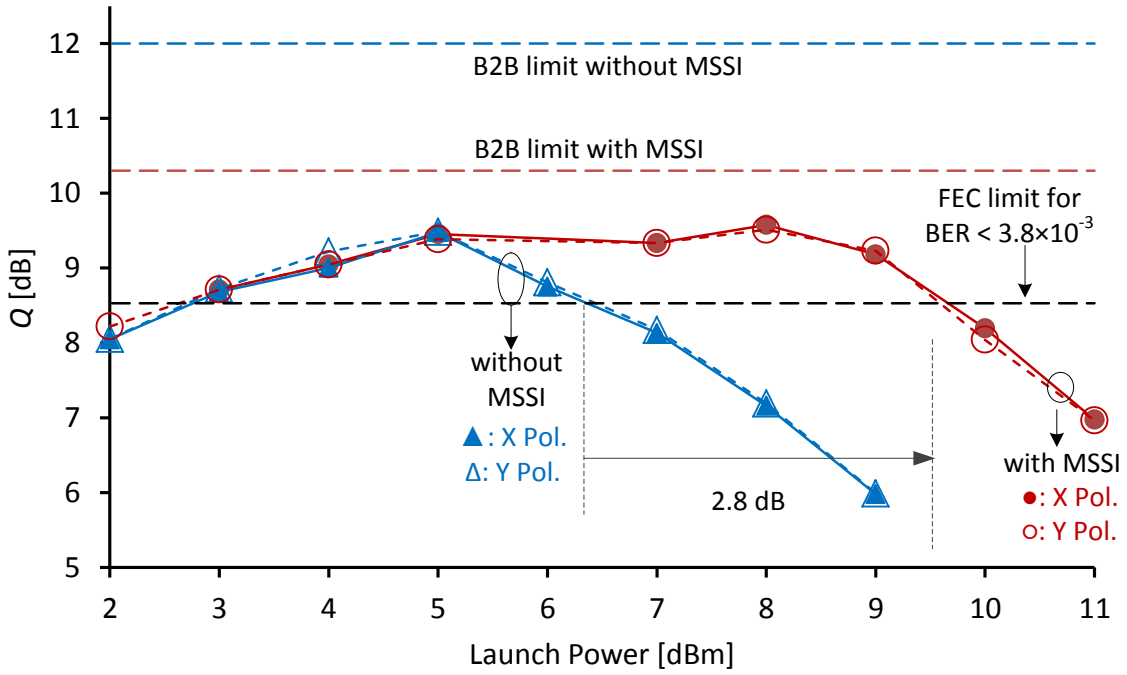

Figure 5-9: Q versus launch power after 10×80-km with and without MSSI for the 1.21-Tb/s system.

This performance could be improved by using lower-loss filters (to reduce the added ASE in the MSSI stage) as discussed in Section 4, and by using two-stage OPC (to reduce spurious nonlinear mixing products) as discussed in [87, 88]. Additionally, the benefit of MSSI decreases with higher bandwidth signals [82]. This is because MSSI decreases the benefit of the phased-array effect [107], which reduces inter-channel nonlinear cross-talk in high bandwidth systems. This phased array effect is decreased as MSSI effectively reverses the effect of dispersion in the second half of the link.

Figure 5-10(a) shows the BERs for all of the OFDM bands at a 5-dBm launch power, which is the optimal power for the system without MSSI. The channels in the middle of the band have similar BERs; however, the roll-off of the 200-GHz multiplexers attenuates the edges of the MSSI signal, increasing the error rates. This could be avoided by using an optical filter with a wider passband.

Figure 5-10(b) shows the BER of the OFDM bands at a power of 8 dBm, where nonlinearity dominates the system's performance. All but three of the edge subcarriers of the MSSI system have BERs better than the 7%-overhead hard-decision FEC limit of 3.8×10^{-3}. When the BER is averaged over all of the subcarriers, the MSSI beneficially decreases the BER from 1.0×10^{-2} to 3.0×10^{-3}. Pairwise coding or similar techniques could be used to balance the error rates across the channels [167].

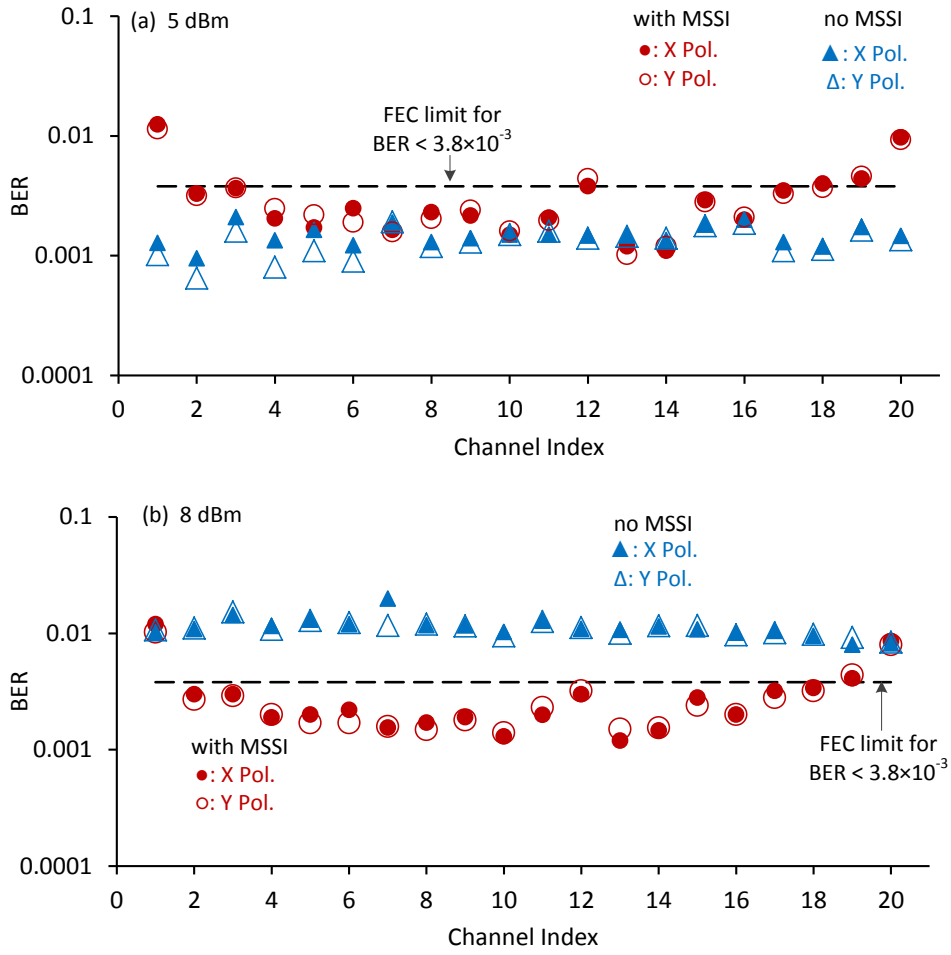

Figure 5-10: BER for 20 channels after 800 km at two launch powers, with and without MSSI for the 1.21-Tb/s system.

5.3 Simulation results

From the experimental results presented in the previous section, it is observed that although MSSI did not improve the maximum *Q*, it improved the maximum launch power of 1.21-Tb/s dual polarization 80×10-km transmission system by 2.8 dB. The system would be able to benefit from this increase in permissible launch power to overall transmission distance by having longer spans. In order to demonstrate this benefit with MSSI, a 20-band 160-GHz wide OFDM super-channel is simulated using VPItransmissionMaker™ for different span lengths and numbers of spans.

For sake of simplicity, the simulated system is a single polarization system. However, in a system that is limited by fiber nonlinear impairment rather than cross polarization nonlinear effects, this is able to demonstrate the practical benefit of using MSSI with a 160-GHz wide dual polarization 16-QAM OFDM super channel. In the simulations, the combined insertion loss inside OPC module is used as a simulation parameter, which comprises losses of a Siemens TransXpress Mux, Circulator, 99%/1%

coupler, 90%/10% coupler and Siemens TransXpress Demux. The peak *Q*'s in the simulation and experiment were made similar by tuning the simulated total combined insertion loss (IL) between 9-12 dB. Figure 5-11 shows the simulation model used for MSSI, showing optical attenuator, that incorporates the total insertion loss.

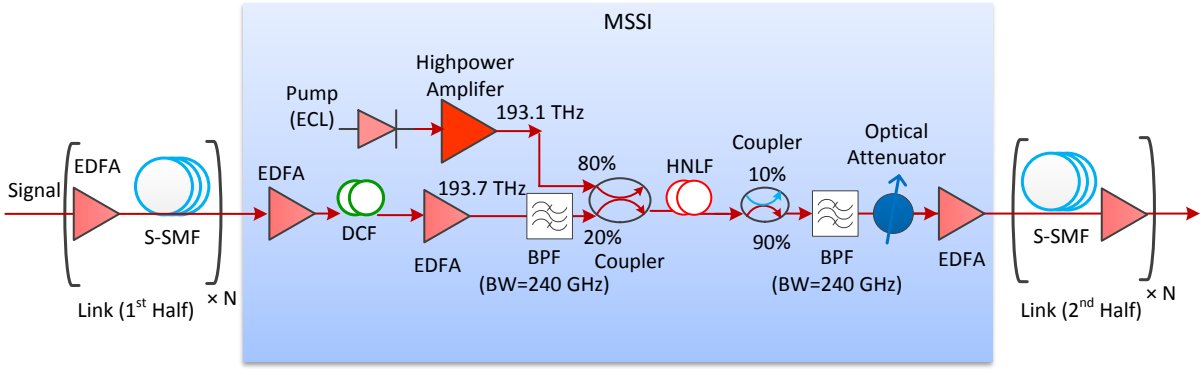

Figure 5-11: Simulation model for OPC module, showing optical attenuator to include total insertion loss due to BPFs and couplers.

5.3.1 Benefit of MSSI with increased span lengths

Figure 5-12(a) shows the simulation results for reference system (▲) and system with MSSI (■) with 12-dB IL after 10×80-km transmission. Compared with the results shown in Fig. 5-9, a similar relation in peak *Q* between experiment and simulation was obtained. All other parameters in the simulation were set as described in the experimental setup in Section 5.1.

Figure 5-12(a) also shows the simulation results of *Q* versus launch power with increased span lengths (10×90-km: ▲; and 10×110-km: ▲) in a 160-GHz OFDM super-channel for the reference system without MSSI. The purple curve with squares (■) shows the 10×110-km results with MSSI. The gray dashed line (--) shows the FEC limit for BER < 3.8×10^{-3}. The results show that maximum span length of the reference system is about 90 km, beyond which performance degrades below the FEC limit. On the other hand, the MSSI system sustains its performance over the FEC limit up to span lengths of 110 km. At launch powers of 8 dBm, the MSSI system clears the FEC limit, while the 10×110-km system without MSSI is well below this limit for all launch powers. Therefore, the overall transmission distance could be increased from 10×90 km to 10×110 km; a reach improvement of nearly 22% without increasing the number of inline amplifiers. Figure 5-12(b) shows the maximum *Q* value for different span lengths from 80 km to 110 km for both systems (Reference system: —; MSSI system: —) and the corresponding improvement with MSSI (▲). This shows that effect of nonlinearity mitigation due to MSSI increases with longer spans. This is due to the increased maximum launch power with MSSI. Another reason for increased benefit of using MSSI for increased span lengths is

that the OSNR penalty decreases sharply with increased transmission distance. On the other hand, the reference link performance degrades sharply for increased distance due to stronger nonlinearities at the required higher power. Therefore, the benefit of MSSI mitigating the fiber nonlinearity becomes more significant for systems with longer spans.

With span lengths of 90 km, MSSI shows about 1.2 dB improvement compared to the reference system.

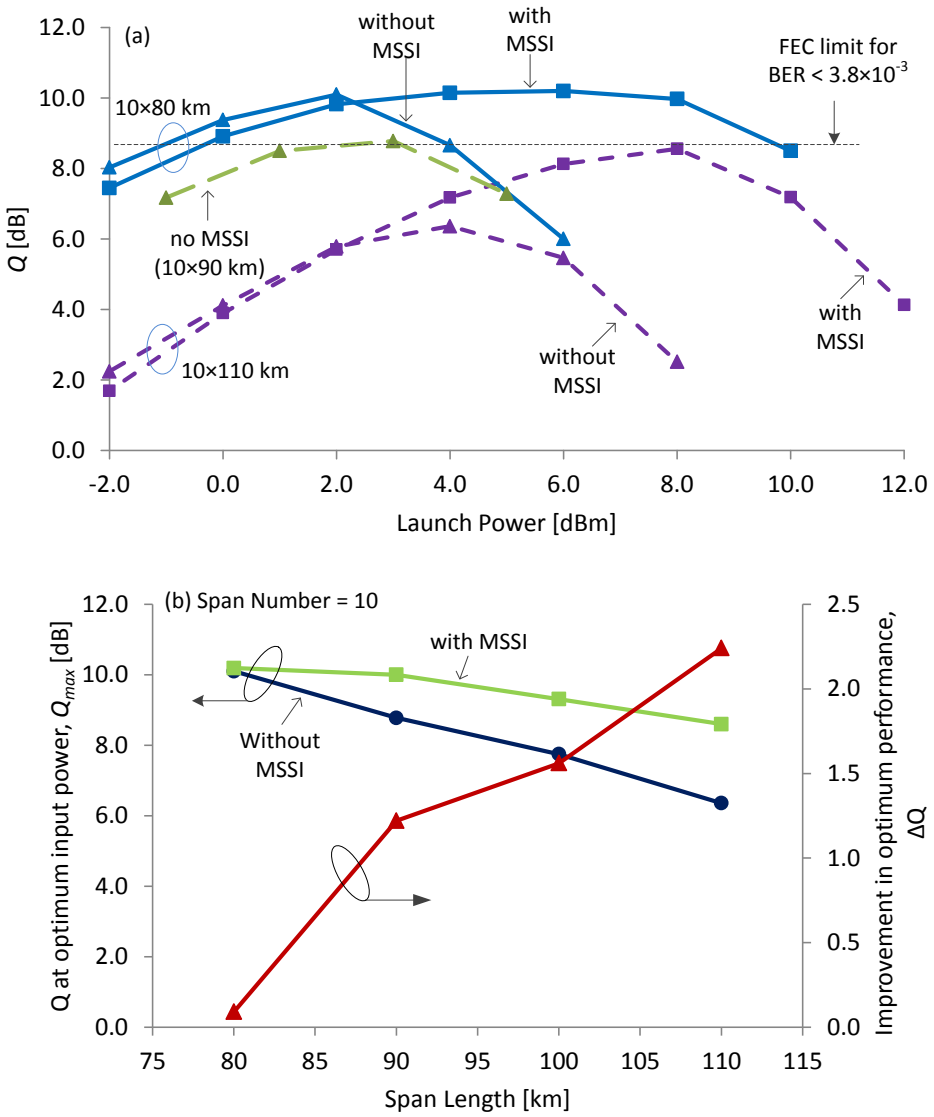

Figure 5-12: Performance comparison with different span lengths between two systems. (a) *Q* versus launch power for single polarization 160-GHz OFDM super channel. (b) Optimum performance and improvement versus span length. HLNF length, *L*=45m, OPC conversion efficiency, *CE*=-24 dB, and number of spans=10.

5.3.2 Benefit of MSSI for increased transmission distance with fixed span length

Next, the performance improvement due to MSSI for longer transmission distances when the span length is kept fixed at 80 km is investigated. Fig. 5-13(a) shows *Q* versus launch power for three different transmission distances (10×80km, 12×80km, 14×80km), for both the reference system and MSSI.

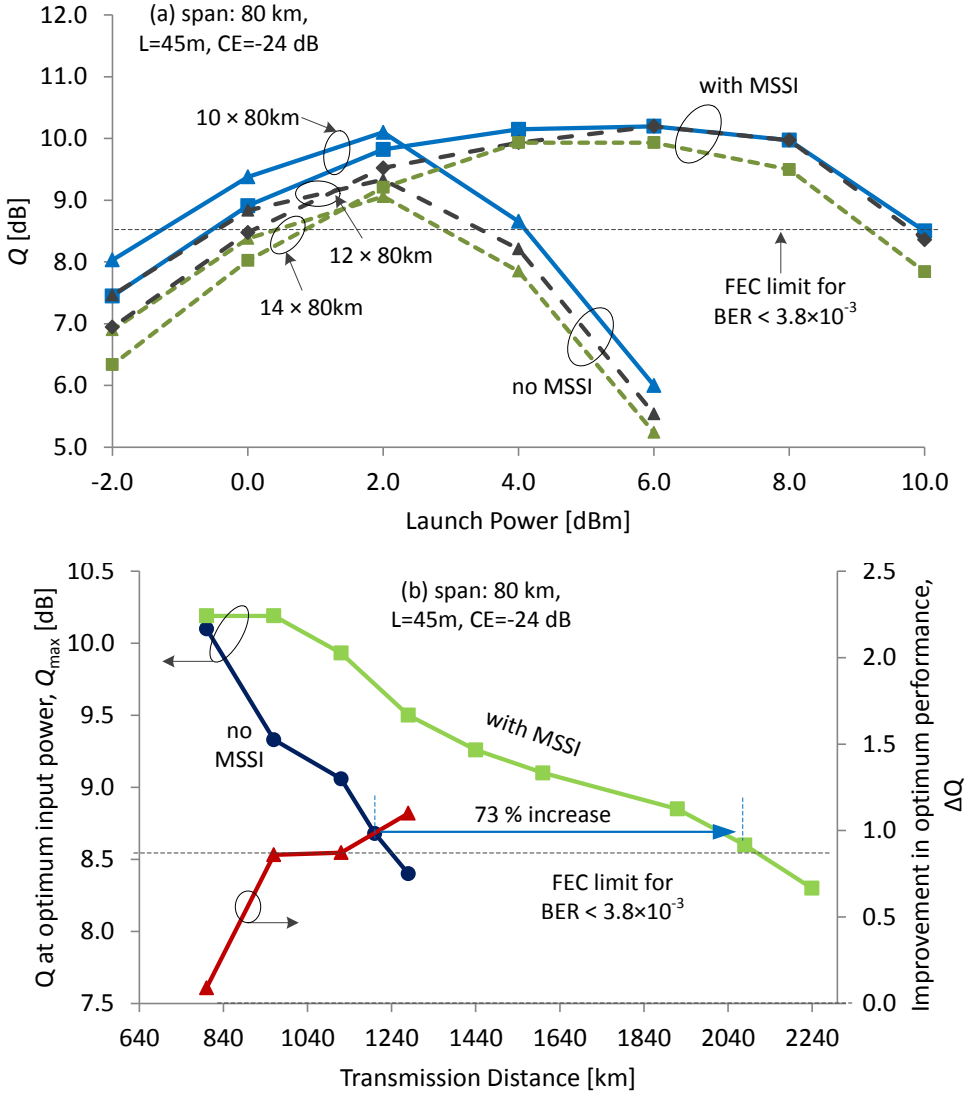

Figure 5-13: Performance comparison with different transmission distance.(a) *Q* versus launch power with and without MSSI for single polarization 160-GHz OFDM super channel (for three transmission distance: 10×80 km, 12×80 km, 14×80 km). (b) *Q* at optimum power, and *Q* improvement versus transmission distance. HLNF length, *L*=45 m, OPC conversion efficiency, *CE*=-24 dB, and Span length=80 km.

While the optimum *Q* of the reference system falls rather sharply, the system with MSSI shows less degradation in performance with increasing transmission distance. This is due to the increased maximum launch power with MSSI for a given nonlinear penalty. Another reason for increased

benefit of using MSSI for increased transmission distance is that the ASE from the OPC module becomes less significant when more or longer spans are used. On the other hand, the reference link (no OPC) performance degrades sharply for increased distance due to stronger nonlinearities at the required higher power. Therefore, the benefit of MSSI mitigating the fiber nonlinearity becomes more significant for increased transmission distance.

The analysis of OSNR penalty has been shown in Appendix A. Appendix B shows the OSNR evolution for the reference and MSSI link. These simple analyses show that OSNR penalty decreases with increasing distances or number of spans. Therefore, the benefit of using MSSI is expected to be more significant for longer transmission distances or longer spans.

Figure 5-13(b) shows the *Q* at optimum input power versus transmission distance for both systems. The reference system peak *Q* falls below the FEC limit with links longer than 15×80km. On the other hand, the MSSI system performs above the FEC limit up to 26×80 km. This shows that MSSI has the potential to increase the transmission distance by more than 70% when 80-km spans are used. The red curve in Fig. 5-13(b) shows about 1-dB peak performance improvement at 1240 km when MSSI is used.

5.3.3 Maximizing OPC performance

Next, the investigation is made on improving the maximum performance of the OPC module itself by changing the parameters of components within the OPC module. Three parameters were considered here: the total combined insertion loss (*IL*) inside the OPC module, the OPC conversion efficiency (*CE*) and HNLF length (*L*).

The three curves overlapping with the left arrow in Fig. 5-14 show the back-to-back system performance for increasing conversion efficiency (*CE*) with fixed HNLF length (*L*=45m). The curves overlapping with the right arrow show the back-to-back performance shorter HNLF length, with fixed *CE* of -24 dB. In all cases, insertion loss of the OPC module was fixed at -12 dB. *Q* was calculated from mean and standard deviation of a constellation [66].

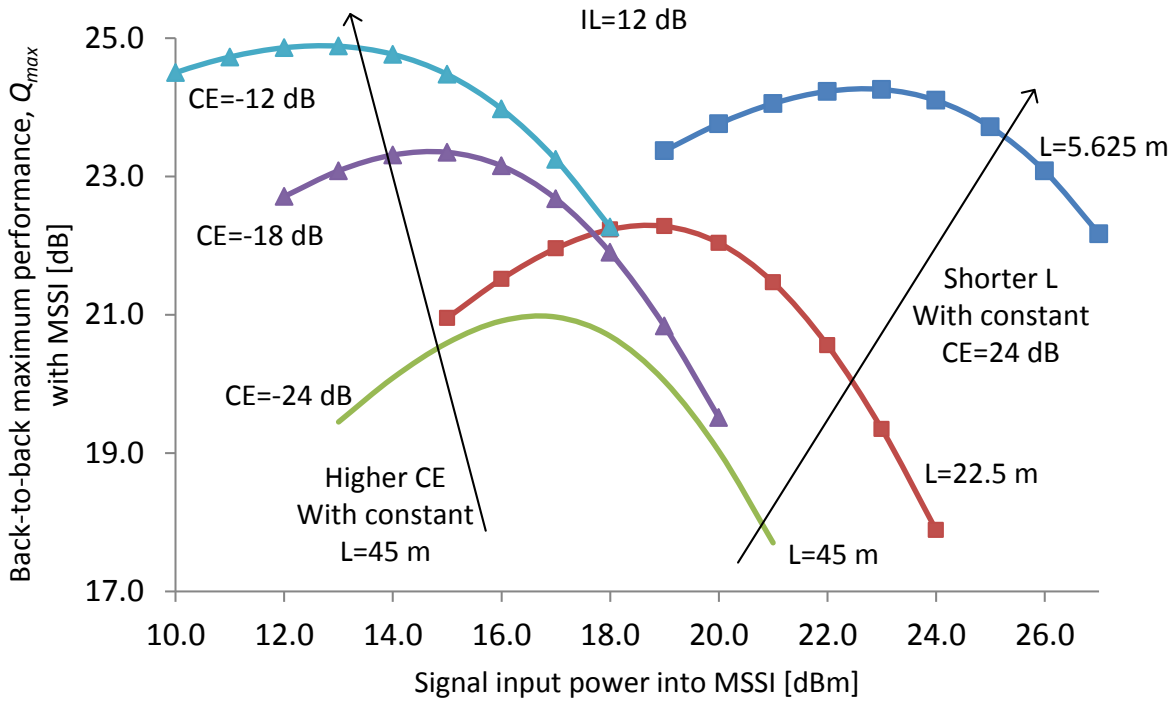

Figure 5-14: Back-to-back performance dependence on conversion efficiency and HNLF length.

The light green curve in Fig. 5-14 shows the reference MSSI system with *L*=45, *IL*=12 dB and *CE*=24 dB. The left two curves with triangles (▲,▲) show that with a constant HNLF length, back-to-back performance increases with higher conversion efficiency due to reduction in ASE generated by the output EDFA of MSSI. The right two curves with squares (■,■) show that with constant conversion efficiency, back-to-back performance increases with shorter HNLF length due to reduction in nonlinear distortions expressed by Equation (4.20) in Chapter Four.

Figure 5-15 shows *Q* improvement for two different lengths of HNLF, 45 m (Δ) and 22.5 m, (■) versus *CE*. The insertion loss in both of these cases is 12 dB. The HNLF nonlinear coefficient was kept as in Section 3.1. The result shows that maximum *Q* performance could be improved by about 0.7 dB by improving the *CE* from -24 dB to -18 dB using a shorter HNLF. Numerical results shows better performance with shorter HNLF at the same conversion efficiency, which agrees with the analytical prediction of [85]. Shorter HNLF is also preferable to minimize the effect of the variation in zero dispersion wavelength along the HNLF. This helps maintain a uniform gain over a wide OPC bandwidth and a higher threshold for SBS.

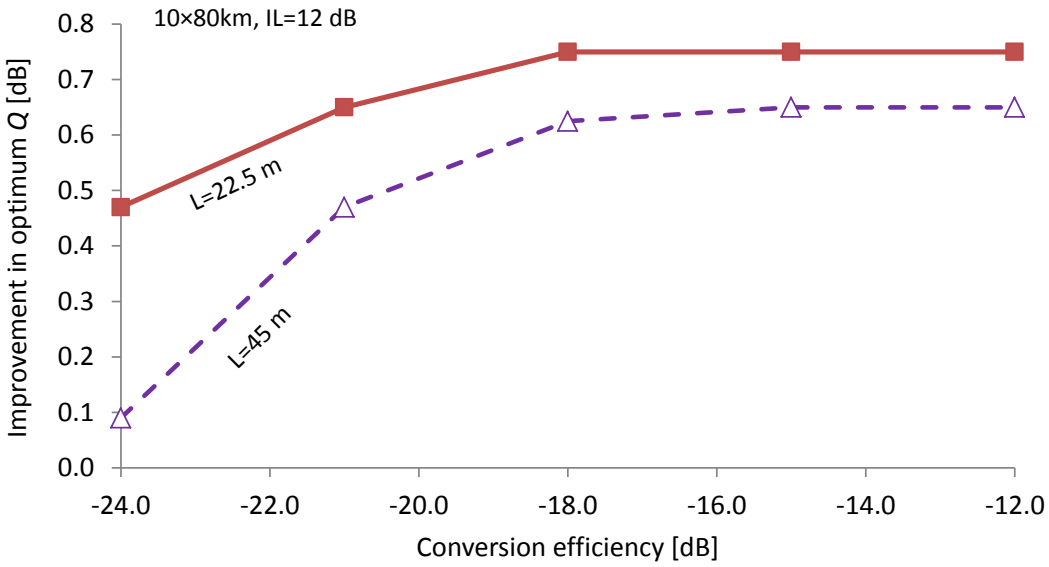

Figure 5-15: Improvement in maximum Q performance versus OPC conversion efficiency and HNLF length.

Next, the effect of insertion loss is investigated.

Figure 5-16(a) shows the *Q* versus launch power for the reference system and MSSI system with different total insertion losses. The transmission distance is 10×80 km. Figure 5-12(b) shows the improvement in maximum *Q* performance, comparing systems with and without MSSI, versus total insertion loss. These results show that reducing total insertion loss inside MSSI is critical in increasing maximum *Q*. With the ideal case of no insertion loss, the MSSI system could improve the maximum *Q* by about 1 dB.

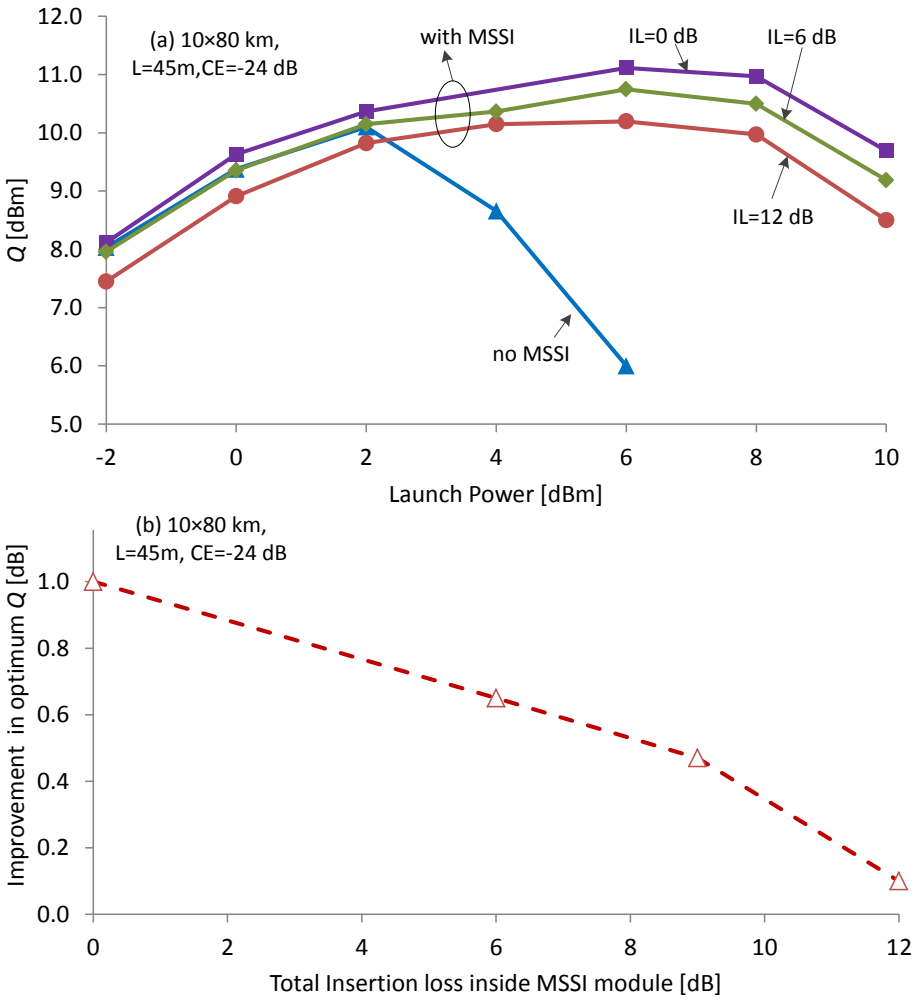

Figure 5-16: Tuning of the MSSI performance by adjusting total insertion loss inside the OPC module.

5.3.4 Performance improvement by an ideal OPC

In this section, simulation results including ideal OPC without penalty (—) are presented in order to estimate the maximum achievable performance improvement using OPC for a EDFA-only based transmission system. Simulation results show that an ideal OPC can improve the performance of the present system by about 3 dB ((a) in Fig. 5-17) compared to a reference system without OPC (—). Fig. 5-17 also shows the simulation results of transmission system using a hypothetical OPC with ASE noise but without nonlinear distortions (—) and the experimental OPC (—) with both ASE and nonlinear distortions. From these graphs, it is clear that, a practical OPC shows about 2 dB performance penalty due to combined effects of ASE and nonlinear distortions. About 2/3 of this penalty arises due to ASE noise generated within the OPC module when compensating for the conversion loss (-24 dB) and insertion loss due to filters (-6 to -8 dB). Using our particular OPC (HNLF 45m, Conversion efficiency: -24 dB) a penalty of about 0.7 dB arises from the nonlinear mixing products, which is about 1/3 of the total penalty. It is assumed from the analytical results of

Chapter 4 that the longer the HNLF, the higher the nonlinear penalty. Therefore, a short HNLF of 45 m has been used in our experimental demonstrations.

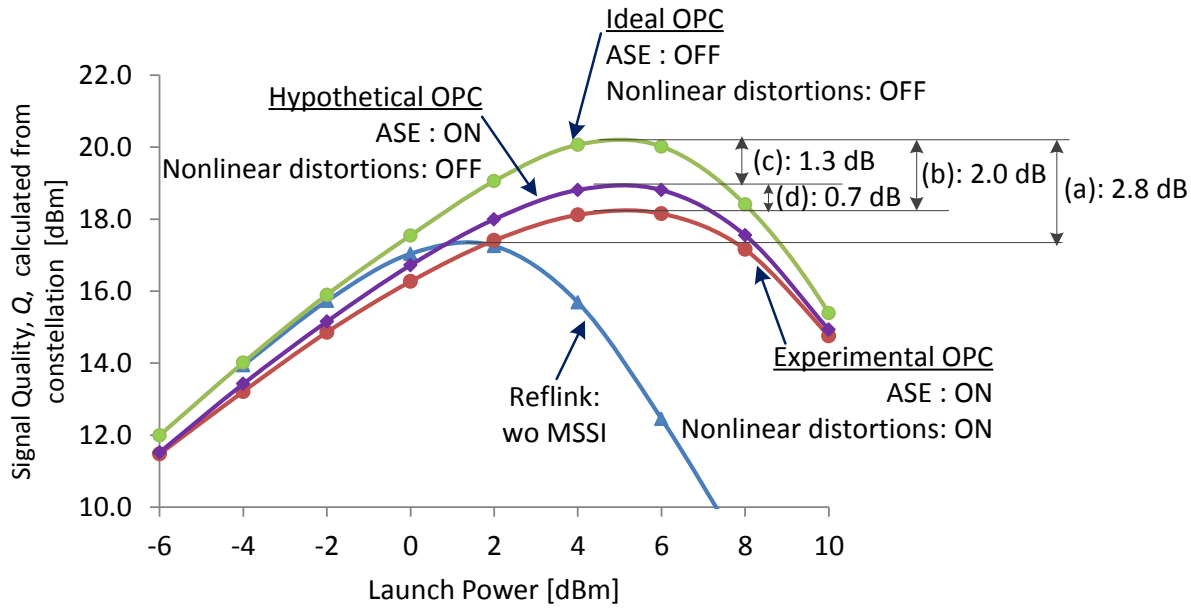

Fig. 5-17: System performance comparisons for different OPC limitations.

The ASE penalties can be minimized by increasing the conversion efficiency. Several methods have been proposed to achieve higher CE [168-170]. Stimulated Brillouin scattering (SBS) limits the maximum allowable launch power into HNLF resulting in relatively low CE FWM process. To suppress the SBS [168], phase/frequency dithering has been demonstrated [170]. However, the phase of the dithered pump transfers to the idler by a factor of two through the degenerate FWM process, thereby degrading the signal quality of any phase-modulated signals [170]. To overcome this phase dithering effect on the idler signals, a two-stage counter dithering scheme where two pumps are phase modulated 180° out of phase has been demonstrated [168]. This method has almost zero penalty. On the other hand, it requires a large frequency guard band, and also generates many undesired idlers. Recently, a modified two-stage counter dithering scheme was proposed using a single pump [169]. This method eliminates the need for large frequency guard band, at the expense of precise control of the phases between the pumps in two stages.

5.4 Conclusion

In this chapter, the first experimental demonstration of the use of MSSI for fiber nonlinearity compensation for DP CO-OFDM systems has been presented. The polarization independence of the OPC module was confirmed by observing very similar performance between counter-propagating X and Y polarization signals. MSSI increases the maximum permissible launch power by 2.8 dB for a 1.21-Tb/s 16-QAM DP CO-OFDM system and 6.4 dB at 121 Gb/s. Simulations show that this

increase in maximum viable launch power could support about a 22% increase in total transmission distance without increasing the number of inline amplifiers, by extending each fiber span from 90 km to 110 km, for 1.21-Tb/s system. For a fixed length of span, the MSSI system shows less degradation in optimum performance with increasing number of spans (i.e. increased transmission distances), and supports more than 70% increase in overall transmission distance when 80-km spans are used. As for optimization of the OPC module itself, simulations show that reducing total insertion loss inside OPC module is very important in achieving higher maximum *Q* performance as is using shorter HNLF and increasing the OPC conversion efficiency.

I have also separated the penalties due to ASE noise and nonlinear distortions. With more sophisticated OPC with no CE loss and nonlinear distortions, it is expected that the optimum Q performance can improve by further 2.0 dB using MSSI.

In the next two chapters, two different novel methods will be presented to reduce the fundamental limitations due to MSSI in order to achievement further improvement for nonlinearity compensation.

6 Performance Improvement: Two-stage OPC with notch filter

In the previous chapter, an experimental demonstration of using MSSI in a dual polarization (DP) CO-OFDM super-channel was presented. An improvement of 2.8 dB in the maximum allowable launch power at FEC threshold (BER < 3.8×10^{-3}) for a 10 × 80-km 1.21-Tb/s 16-QAM CO-OFDM super channel was achieved. However, the performance at the operating power for maximal signal quality did not improve compared with a system without MSSI. This was because the OPC module itself introduces a performance penalty in the system. Chapter Four contained a detailed theoretical analysis [84, 85] showing that two two-stage nonlinear processes and amplified spontaneous emission (ASE) are the causes of this performance penalty.

In this chapter, a novel method of reducing the intrinsic performance penalty due to MSSI that uses third-order nonlinearity based optical phase conjugation (OPC) is presented. The method is evaluated by simulating the back-to-back performance penalty of a CO-OFDM system. The method splits the nonlinear element into two parts, and then inserts a band-stop filter (BSF) centered on the pump between them to remove the XPM products and the pump. The pump is then reinserted into the second part. This method reduces the performance penalty that is due to a two-stage nonlinear process. Numerical simulations using the split-step Fourier method (SSFM) show that this two-part OPC module has a 3-dB better back-to-back maximum Q performance compared with a conventional OPC module. Simulation results also show that this better back-to-back performance results in an improvement of the maximum signal quality, Q_{max}, by 1 dB in a 10 × 80-km 4-QAM 224-Gb/s CO-OFDM system.

This content of this chapter has been published in [87, 88].

6.1 MSSI with a mid-way filter

6.1.1 Conventional OPC

Figure 6-1(a) shows the block diagram of a conventional system using MSSI near the middle of the link. Figure 6-1(b) shows the details of a conventional OPC module. The output of the first half of the link is fed into the OPC module. The input amplifier of the OPC module boosts the input power. The input signal is then filtered with a band-pass filter (BPF) and is combined with a CW pump. The output of the nonlinear element is passed through another BPF to remove the pump and the original signal, leaving the wanted phase-conjugated signal. The output signal is then amplified before passing to the second half of the link. The details of the coherent transmitter and receiver are discussed in [81].

Inset (*i*) in Fig. 6-1(b) shows the spectrum at the output of the $\chi^{(3)}$ nonlinear element, which is a Highly Non-Linear Fiber (HNLF) in this thesis. Inset (*ii*) shows the simulated spectrum at the output of the OPC module. Two types of nonlinear products, XPM-OPC (dark green: —) and FWM-OPC (dark blue: —) [84, 85], fall within the band of the wanted OPC signal, so cannot be filtered out by the BPF. Thus, these two nonlinear products, along with ASE from the erbium doped fiber amplifiers (EDFA), cause a fundamental back-to-back performance penalty in conventional MSSI. As the insets show, XPM-OPC dominates over FWM-OPC [84, 85].

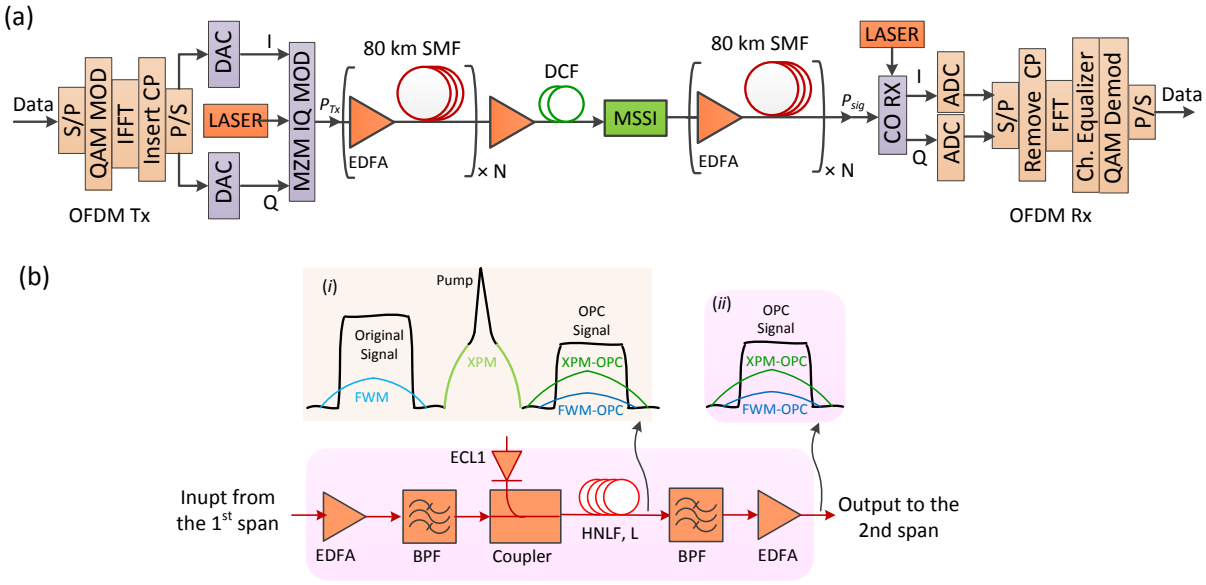

Figure 6-1: System schematic of (a) the transmission system; (b) single-stage OPC module.

At IPC 2012, a theoretical analysis of the back-to-back performance limitation of CO-OFDM systems using an OPC modelled with all nonlinear mixing terms [84] was presented. An in-depth analysis shows that nonlinear products generated by two-stage mixing processes impose a fundamental

performance limit [85]. This has been discussed in Chapter Four of this thesis. In the first stage, XPM products (light green: —) are generated by mixing between *signal* × *pump* × (*signal*)* tones and FWM products (light blue: —) are generated due to *signal* × *signal* × (*signal*)* mixing. In the second stage, XPM-OPC (dark green) products are generated by *XPM products* × *pump* × (*signal*)* and the FWM-OPC (dark blue) products are generated by *pump* × *pump* × (*FWM tones*)*. Here, $(x)^*$ denotes the conjugate of the term x. In conventional OPC, the first stage of these processes generates nonlinear products whose fields grow linearly along the whole length of the HNLF; because the second stage products require the first stage products as an input, they grow quadratically over the length for the HNLF. Thus the output end of the HNLF is responsible for the generation of most of the power in the unwanted products.

6.1.2 Two-part OPC with mid-way filter

The novel idea is to suppress the first-stage products at one or more places along the HNLF, so the input to the second-stage process is suppressed. This is possible because the first-stage products fall outside the band of the wanted OPC signal. Figure 6-2 shows the block diagram implementing this idea. The HNLF, length L, has been divided in half, to form two OPC sub-modules. The output of the first OPC sub-module is passed through a band-stop filter to remove the XPM products generated within it. Unfortunately, the pump is also removed. The frequency response of the BSF is shown by the red dashed curve in inset (*i*) and its output in inset (*ii*). The pump is reintroduced after the filter. This must be coherent with the original pump to ensure that the new conjugate products generated in this second half add in phase with those created in the first half. The combined signal then travels along the second half (HNLF2), a BPF and an output EDFA. Inset (*iii*) shows the spectrum at the output of HNLF2, which shows that both the XPM and the XPM-OPC products have been considerably suppressed. Inset (*iv*) shows the spectrum at the output of the second OPC module. The XPM-OPC products are several times smaller than those produced by a single stage OPC module. Thus, the system performance should also improve significantly, since the dominant nonlinear limiting factor, XPM-OPC, has been suppressed. Obviously, XPM-OPC generated entirely within the first half cannot be suppressed, as it already falls upon the conjugated signal's spectrum. The same argument holds for XPM generated in the second half and converted to XPM-OPC in the second half. This implies that additional filters could be placed along the HNLF for even better performance, if their losses are sufficiently small.

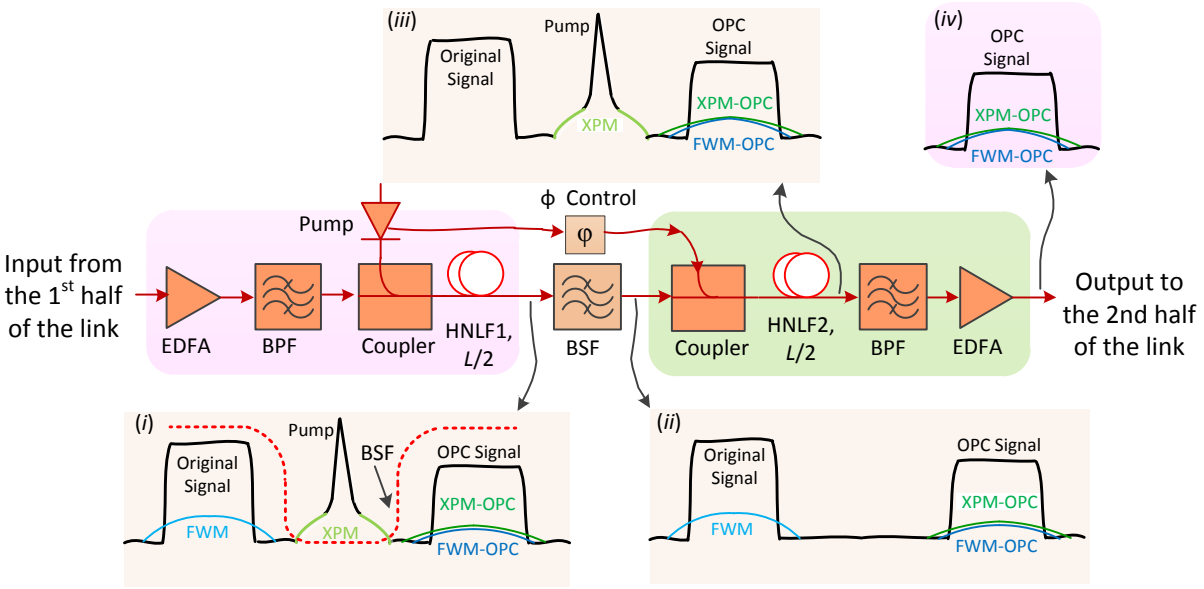

Figure 6-2: Block diagram of the two-part OPC module using a notch filter, with illustrative spectra.

6.2 Back-to-back performance

To quantify the maximum possible benefit of splitting the nonlinear element into two parts, first a back-to-back system, that is, without a transmission fiber, as shown in Fig. 6-1(a) was considered. The numerical simulations were conducted using VPItransmissionMaker v8.7. Table 6-1 gives the simulation parameters.

Table 6-1: Simulation parameters.

Parameters	Value	Unit
Pump Power	10	dBm
EDFA Noise Figure	6	dB
OFDM Signal Bandwidth	112	GHz
Length of the HNLF, *L*	1000	m
HNLF Loss coefficient	0.97	dB/km
Nonlinear Coefficient	11.5	$W^{-1}km^{-1}$
Chromatic Dispersion of HNLF, CD	0.0	ps/nm/km

The OFDM signal was generated using MATLAB, using a 1024-point inverse fast Fourier transform (IFFT); 920 subcarriers were modulated with 4-QAM and a 32-point cyclic prefix (CP) was inserted before each OFDM symbol. The total bit rate was 224-Gb/s, resulting in a net data rate of 200-Gb/s after 12% overhead for FEC and training. At the receiver, a coherent OFDM receiver feeds a digital processor that removes the CP, performs a Fourier transform to separate the subcarriers, equalizes the phases of the subcarriers and then demodulates the subcarriers to recover the data in each subcarrier.

6.2.1 Improvement in back-to-back performance

Figure 6-3 shows the back-to-back *Q* versus input signal power into the HNLF. The signal quality, *Q* has been calculated from the error vector magnitude (EVM) [66].

The blue curve with circles (●) shows the performance of the system with conventional MSSI and the red curve with squares (■) shows the performance with the proposed two-part OPC module. The orange line (—) shows the back-to-back performance without OPC (35 dB), which is limited due to DSP limitations. Splitting the OPC module into two parts with a mid-way filter improves the *Q* by 3 dB at the optimum signal power. The performance in the nonlinear threshold increases by 6 dB. Unfortunately, there still remains a 7-dB performance penalty because the XPM-OPC products generated within each part via XPM cannot be separated from the desired OPC signal. Also FWM-OPC products and amplified spontaneous emission (ASE) of the input and output EDFAs add to this penalty and cannot be removed by filtering. Further suppression of XPM-OPC products could be achieved using more than one filter, with the associated increase in complexity.

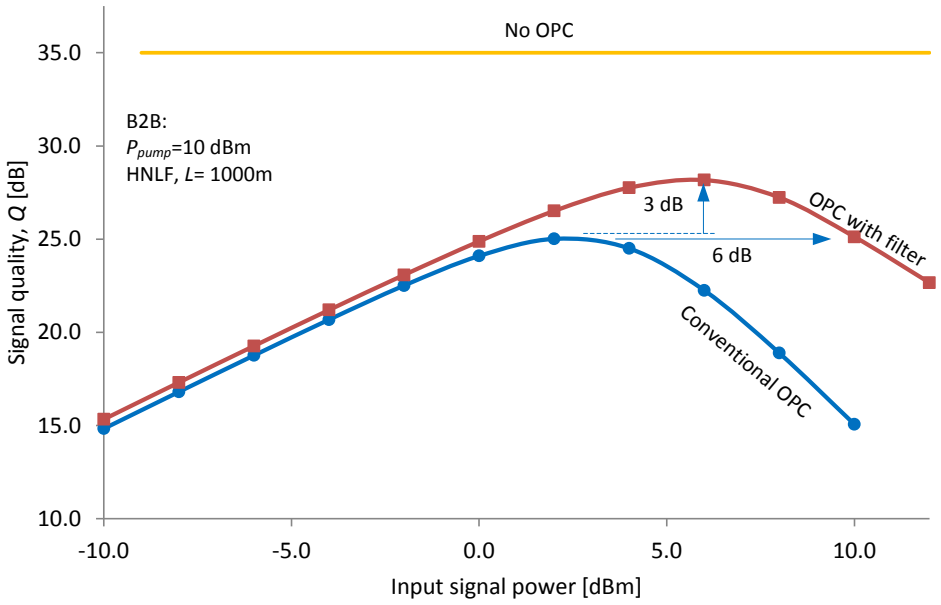

Figure 6-3: Back-to-back performance comparison between the conventional OPC module and the two-part OPC module with mid-way filtering.

6.2.2 Dependence on pump power and HNLF length

In a practical OPC module, the product of the nonlinear coefficient of the HNLF and its length, γL, and the pump power are important parameters. Therefore, the dependence of the performance improvement on pump power and HNLF length are investigated. The nonlinear coefficient, γ, has been kept constant at 11.5 $W^{-1}.km^{-1}$. The length of the HNLF, *L*, is 500 m (Fig.6- 4(a)), 1000 m (Fig. 6-4(b)) or 1500 m (Fig. 6-4(c)).

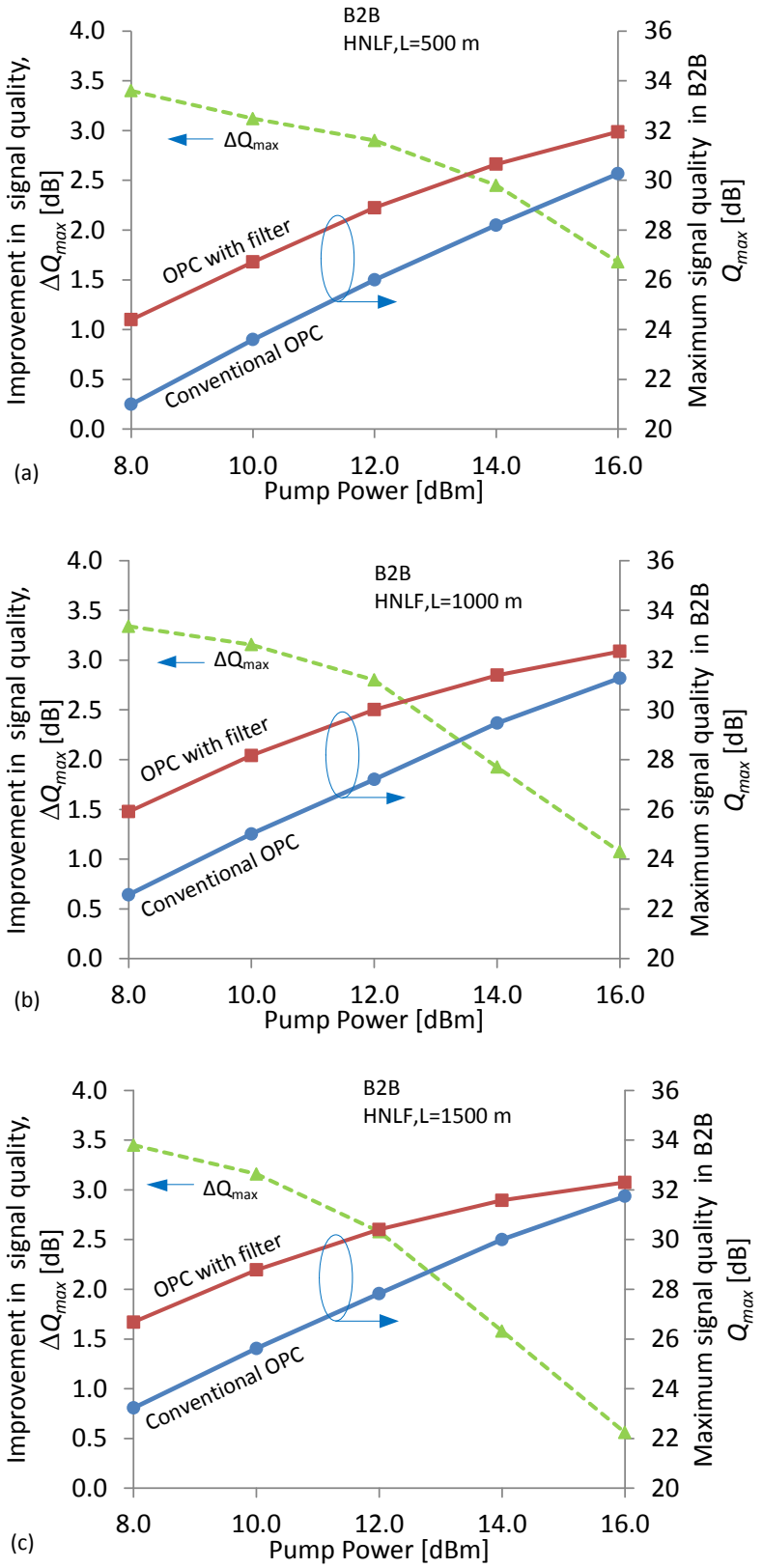

Figure 6-4: Pump power and HNLF length dependence of performance improvement for three fiber lengths. All results are back-to-back.

The optimum signal input power is always used for each point on each graph. The results show that for higher pump powers and longer HNLF, the improvement due to the suppression of the XPM products decreases. With a higher pump power and/or longer HNLF, the maximum signal quality is improved, which makes Q_{max} of the conventional OPC modules approach the DSP limit of 35 dB. Thus the improvement using a two-part module is limited in these circumstances. However, as Fig. 6-4 shows, using a two-part module is more beneficial for higher conversion losses, *i.e.*, for lower γL products and/or for lower pump powers. This may be helpful when designing OPC modules implemented with photonic integrated circuits (PICs) [171, 172], where the γL product term is about 20 times smaller (9900 $W^{-1}km^{-1} \times 6$ cm) [172] than the value we have employed to represent a typical MSSI using HNLF (11.5 W^{-1} $km^{-1} \times 1000$ m) when stimulated Brillouin scattering (SBS) limits pump power.

6.2.3 Bandwidth dependence

Figure 6-5 shows the dependence of the back-to-back performance improvement on the signal bandwidth. The blue curve with circles (●) shows the maximum signal quality, Q_{max}, using the conventional OPC module. The red curve with squares (■) shows Q_{max} with two-part OPC.

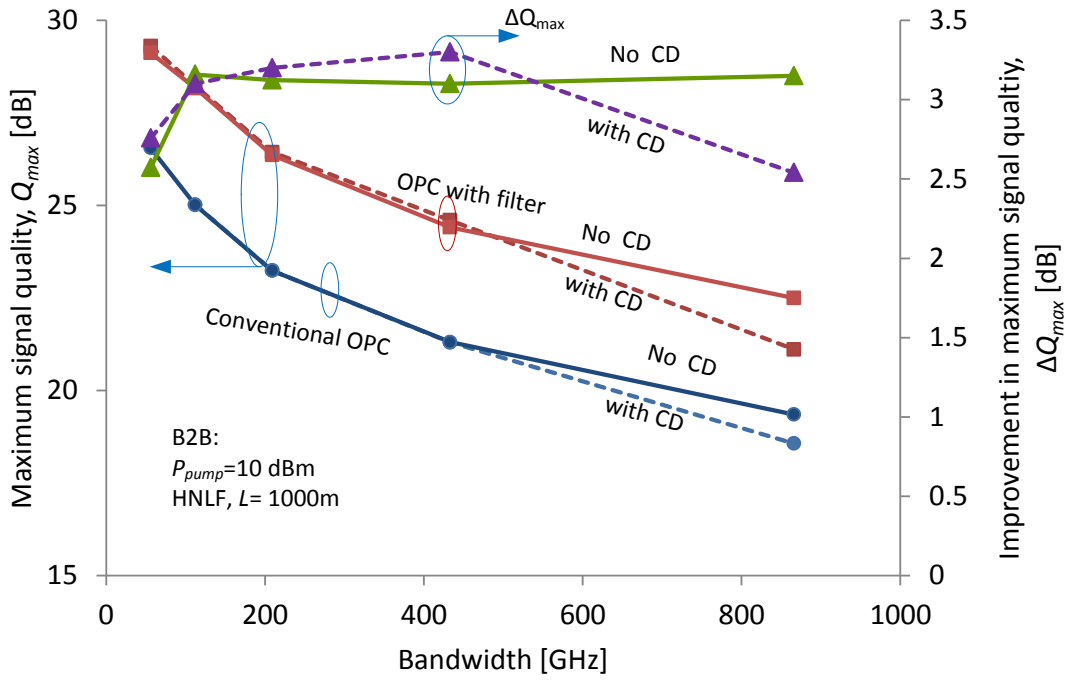

Figure 6-5: Bandwidth dependence of performance improvement. All results are back-to-back.

It is interesting to note that, in the region below 100 GHz, higher signal bandwidths give larger performance improvements. This is because, at bandwidths ≤ 100 GHz, the back-to-back performance using conventional OPC is already very high; that is, there is no significant performance penalty.

Therefore, the improvement in this region with mid-way filtering is not significant. At higher bandwidths, the improvement saturates at 3 dB, shown by green curve with triangles (▲). These results show that the novel two-part OPC is more suitable for high bandwidth devices such as PICs [171, 172].

The effect of chromatic dispersion is shown by the dashed lines in Fig. 6-5. The CD value for this simulation is 0.01 ps/nm/km, which is typical for an OFS HNLF. For signal bandwidths narrower than 400 GHz, CD has almost no effect in the conjugated signal quality. However, for signal bandwidths wider than 400 GHz, the effect of CD degrades the signal quality for a conventional OPC, and reduces the improvement achieved by the two-part OPC. This is because conversion efficiency for the conjugated signal decreases for broad band OPC due to phase mismatch (walk off) caused by CD.

6.3 Performance improvement in a transmission system

To demonstrate that the back-to-back performance improvement translates to an end-to-end performance improvement in a CO-OFDM transmission system of Fig. 6-1(a), a series of simulations has been performed. The optical link comprised 10×80-km spans of standard single mode fiber (S-SMF) with EDFAs to compensate the span loss. A 60-km dispersion compensation fiber (DCF) has been used just before the OPC module to achieve nonlinear symmetry in terms of chromatic dispersion, to maximize the benefit of OPC [146]. However, it is clearly impossible to achieve perfect power symmetry with lumped amplifiers. The OPC module is placed after the fifth span. The input power into the OPC module is the optimum power from the back-to-back simulations as shown in Fig. 6-3, which are 2 dBm for the conventional OPC system and 6 dBm for the two-part OPC system. The input power into the DCF was set to be 4-dB less than the OPC input power.

6.3.1 Improvement in signal quality with transmission system

Figure 6-6 shows the comparison of transmission performance between systems with conventional OPC (●) and with two-part OPC (■). Results without OPC are also plotted (○) to show the benefit of using OPC. The system with conventional OPC shows 1-dB better peak *Q* performance than the system without OPC. It also shows a 4.5-dB improvement in the nonlinear threshold (NLT) power. The system with two-part OPC module has an additional 1-dB *Q* improvement at the optimal signal power. Two-part OPC (■) does not change the optimum input signal power compared with conventional OPC (●). This is because both of the systems are affected by the same link impairments.

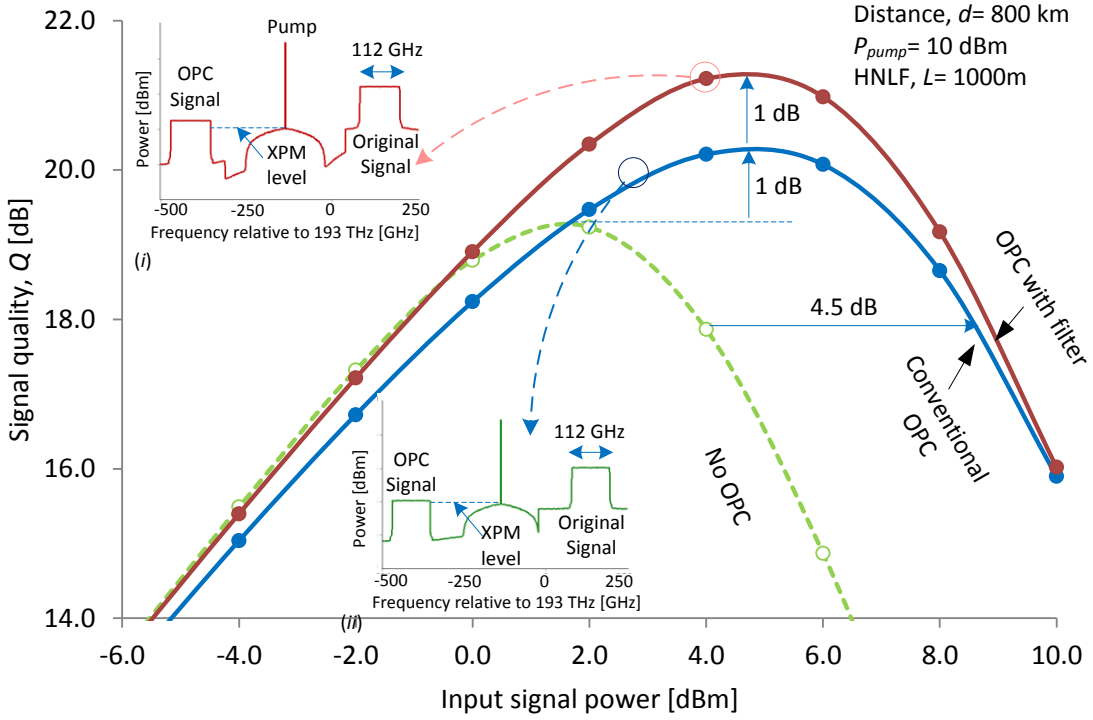

Figure 6-6: Performance comparison between 10×80 km systems using the conventional OPC and two-part OPC. Inset spectra: (i) two-part OPC; (ii) conventional OPC.

6.3.2 Transmission distance dependence

Figure 6-7 shows the dependence of performance improvement on the transmission distance. Using a pump power of 10 dBm, an improvement of 1.4 dB is obtained at 480 km. This improvement decreases to 0.5 dB for a transmission distance of 2400 km. This is because the increasing amount of ASE and nonlinearity generated in the longer links overshadows the back-to-back performance improvement gained by using the two-part OPC module.

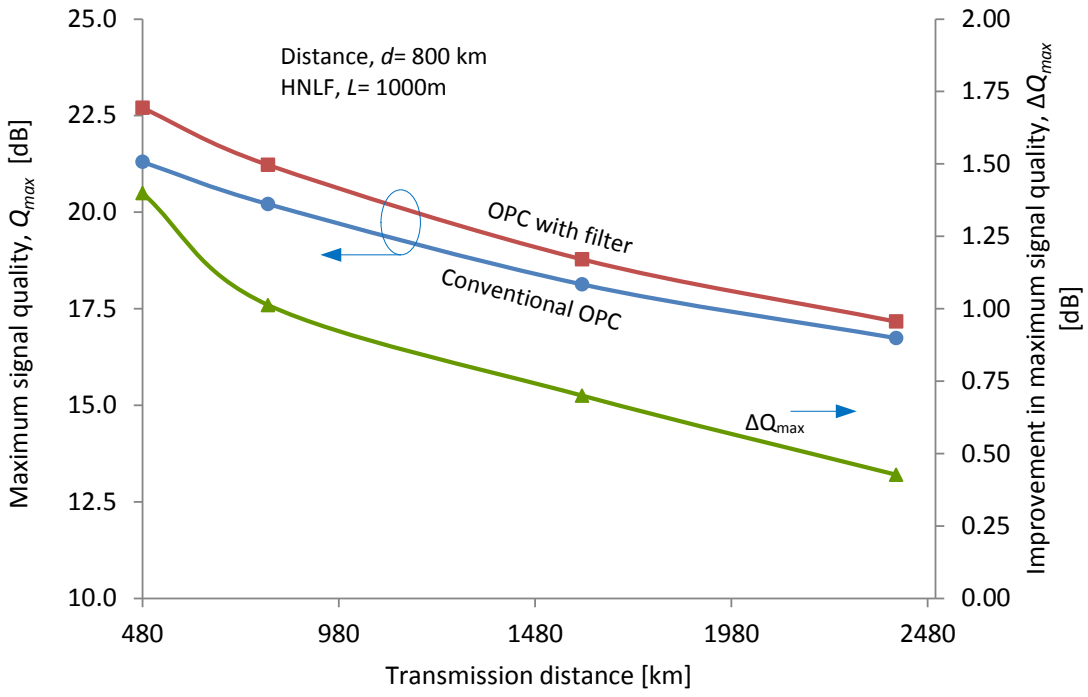

Figure 6-7: Transmission distance and pump power dependence of performance improvement due to the mid-stage filter.

6.3.3 Signal bandwidth dependence in transmission system

Figure 6-8 shows the signal bandwidth dependence of the performance improvement for the 10×80-km transmission system. Again, the blue curve with circles (●) shows the maximum signal quality, Q_{max}, from the system with a conventional OPC module and the red curve with squares (■) is for the system with a two-part OPC. The green curve with triangles (▲) shows the improvement in Q_{max}. The improvement increases with increasing bandwidth and reaches to about 2.0 dB with a signal bandwidth of 866 GHz. In contrast to the back-to-back case (Section 6.2), where the improvement saturated at 3 dB, the improvement in a transmission system increases gradually with signal bandwidth. In a transmission system using OFDM super channel which covers several hundred GHz of signal bandwidth, this method of OPC could become attractive for fiber nonlinearity compensation. Systems with wider bandwidths could be converted in parts, perhaps using an integrated device to save space.

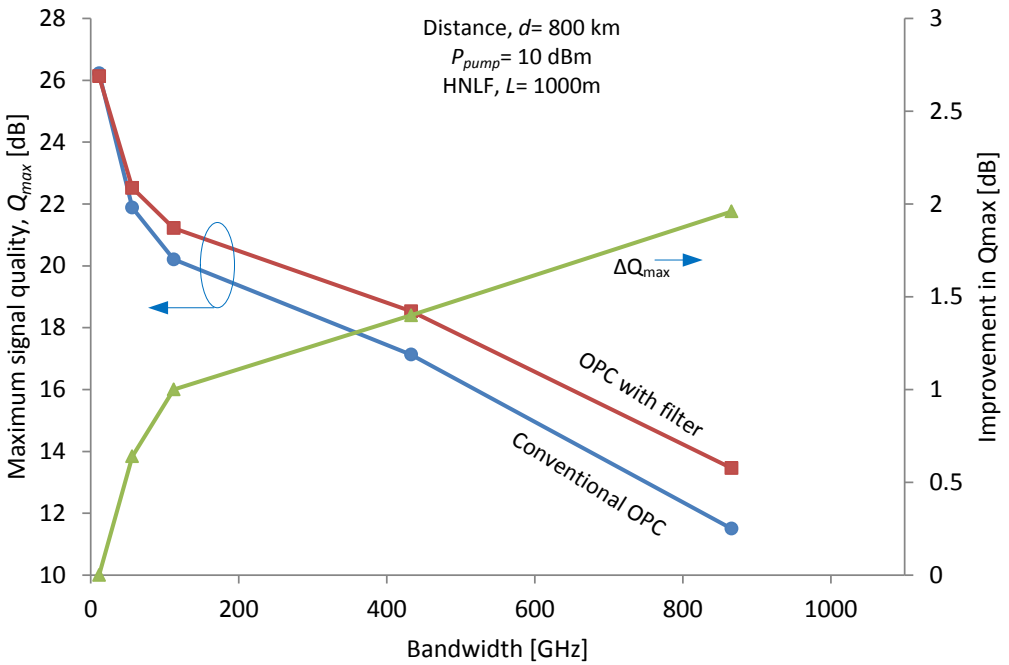

Figure 6-8: Signal bandwidth dependence of performance improvement in transmission system.

6.3.4 Effect of pump phase difference

An open question is how the new OPC module will perform in a real implementation, where there could be some phase difference between the two pumps used in the first and second parts of the module. In this regard, the performance penalty due to phase mismatches between the two pumps was evaluated by simulation. The phase of the second pump was swept from 0 to 360 degrees relative to the first pump. The simulation results are plotted in Fig. 6-9. For an absolute phase difference less than 20°, as shown in the shaded region in Fig. 6-9, the penalty is less than 0.05 dB. However, the penalty increases sharply for larger phase differences. Therefore, the new method of OPC can be implemented practically in a real system, provided that the pump phases can be controlled adequately, perhaps by integrating the system upon a photonic chip

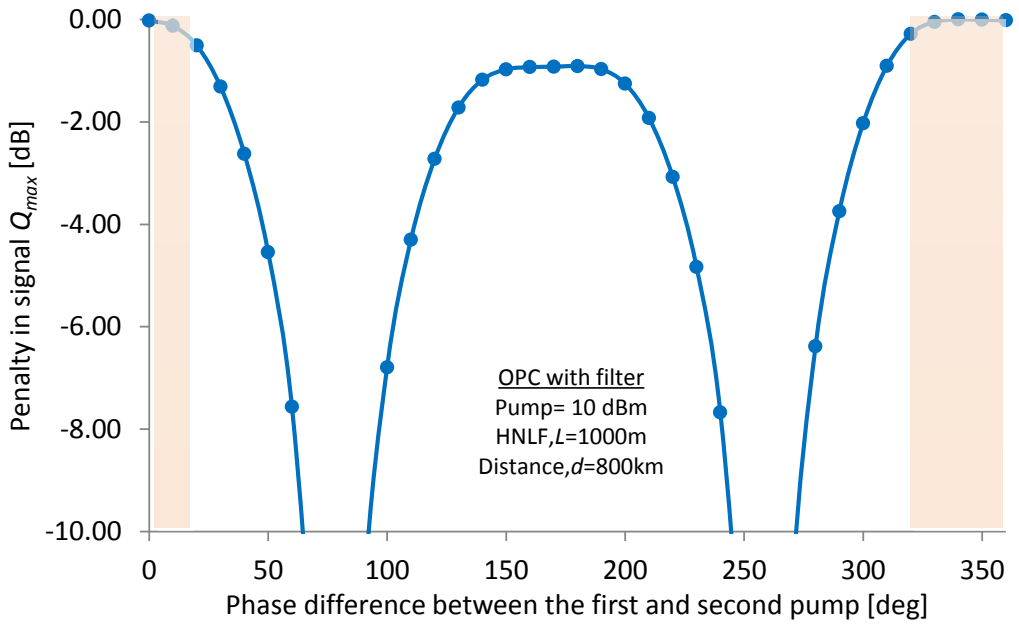

Figure 6-9: Effect of phase difference between the pumps injected into the first and second part of the HNLF on performance improvement.

6.4 Discussion

An alternative method of implementing optical phase conjugation, by using second-order optical nonlinear process with periodically poled $LiNbO_3$ (PPLN) waveguide has been reported for RZ-DPSK and RZ-DQPSK systems [78, 79, 150]. Two cascaded second-order nonlinear processes take place inside a PPLN waveguide to generate the conjugated signal: (*i*) second harmonic generation (SHG) of the pump from a frequency ω_p to $2\omega_p$; (*ii*) difference frequency generation (DFG) of the SHG by mixing with the input signal ω_s, giving a conjugated signal at $2\omega_p - \omega_s$.

One advantage of using PPLN is that no third-order nonlinear impairments such as self-phase modulation (SPM) and cross-phase modulation (XPM) occur in the phase conjugation process [150]. Using PPLN for OPC gave a 1.5-dB improvement in signal quality for a 3200-km 40-Gb/s RZ-DPSK system [173]. Similarly, Jansen *et al*. gained an improvement of 0.5 dB for a 5000-km system [79].

A possible disadvantage of using PPLN is that it requires a relatively high pump powers to increase the efficiency of SHG, typically 20-27 dBm [78, 79, 150, 173]. These high powers cause photorefractive damage, unless the PPLN is heated above 100°C [174]. In addition, the pump frequency is strictly determined by the period of the poling. OPC using third-order nonlinearity does not have these issues; therefore, with the improvements presented in this chapter, it is a viable alternate to PPLN devices. A common analysis framework, including SBS, would need to be developed to quantify the relative performance of these methods.

6.5 Conclusion

A new design of an OPC to improve the back-to-back performance of CO-OFDM systems using MSSI has been proposed and its performance has been evaluated. The new design reduces the performance penalty introduced by a conventional OPC module by 3 dB. It has been shown that this back-to-back performance improvement results in a 1-dB improvement in a 10 × 80-km 4-QAM 224-Gb/s CO-OFDM system. The improvement increases gradually with higher signal bandwidths, which is useful for ultrahigh bandwidth transmission. Finally, it has been shown that the new system would have almost no degradation due to the phase difference between the injected pumps, provided that this is controlled to within +/- 20 degrees.

In the next chapter, a modified novel two-part OPC module that performs better than the OPC module, yet with more robustness in terms of practical implementation is presented.

7 Performance Improvement: Two-stage OPC with phase shift filter

In the previous chapter, a novel method for improving the fundamental performance of third-order optical nonlinearity based OPC systems was proposed [87, 88]. The method involved splitting the nonlinear element into two sections, suppressing the cross-phase modulation (XPM) products from the first element with a notch-filter before the second section, and then re-inserting the pump into the second section. Using numerical simulations, we showed that this method reduced the fundamental degradation introduced by OPC by 3 dB, giving an improvement in the maximum signal quality, Q_{max}, by 1 dB in a 10 × 80-km 4-QAM 224-Gb/s CO-OFDM system [87, 88].

In this chapter, a modified two-part OPC method that gives a better performance improvement than the notch-filter OPC, yet with more robustness in terms of practical implementation is proposed. The method uses an in-line phase-shifting filter (PSF) between the two nonlinear sections of the OPC. Numerical simulations show that this phase-shifting filter OPC module has a 3.6 dB higher back-to-back signal quality, Q_{max} [66], compared with a conventional OPC module. This better back-to-back performance results in an improvement of the maximum Q_{max} by 1.2 dB in a 10 × 80-km 4-QAM 224-Gb/s CO-OFDM system.

A part of this work has been presented in Optical Fiber Communication Conference 2014 [175].

7.1 OPC with phase-shifting filter

Figure 7-1(a) shows the details of the novel OPC module using a two-part OPC with phase-shifting filter in between them. It has been found through simulations that the performance of the systems is optimum when the PSF also has 6-dB attenuation in the phase-shifted region, shown by the purple line (—). The reason behind this 6 dB attenuation is discussed in Section 7.3.

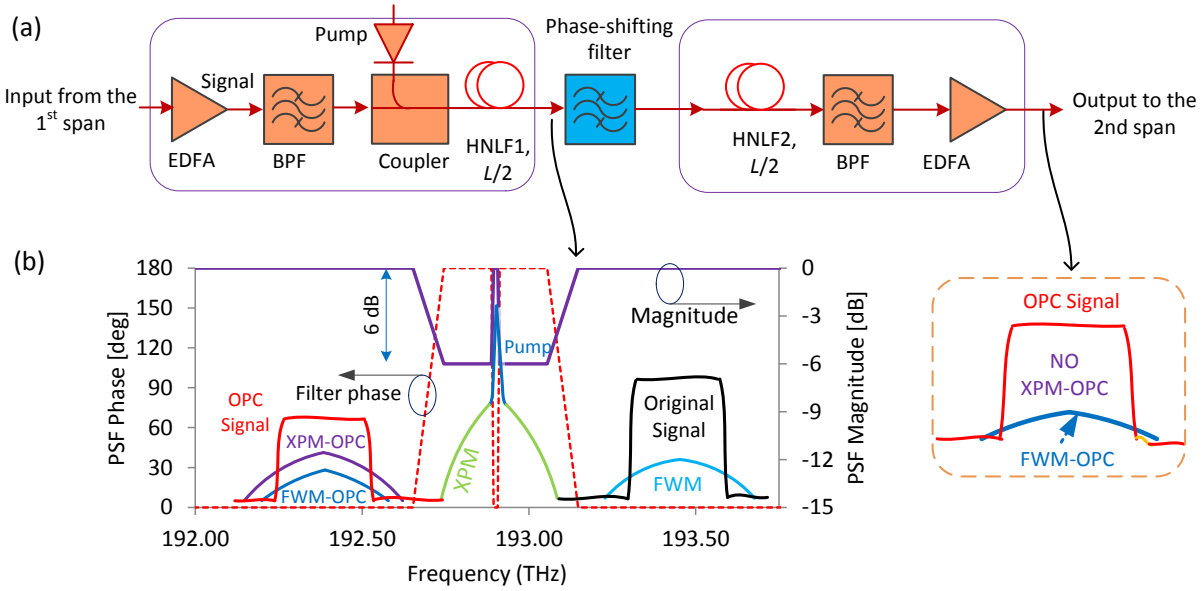

Figure 7-1: Schematic of OPC module with phase shift filter (PSF).

The proposed phase shifting filter (PSF) has a frequency-dependent phase characteristic as shown by the red dotted line (▪▪▪) in Fig. 7-1(b). The simulated filter had the bandwidth of 12 GHz for the phase-shifting region. It is expected that if the filter bandwidth is large than 20 GHz, then there will be penalty. However, a filter with 10-12 GHz bandwidth is practically available in a standard WaveShaper.

Figure 7-1(b) also shows representative spectra of: the original signal, pump, OPC signal, XPM distortions around the pump, four-wave mixing (FWM) distortions, XPM-OPC (—) and FWM-OPC distortions (—) [84, 85]. XPM-OPC falls on the OPC signal band and is the dominant degradation. Fortunately, the XPM-OPC distortion is generated in a two-stage process, via XPM. Thus, if we can suppress XPM, we can suppress XPM-OPC. To achieve this, the PSF's phase response must be zero for all the above spectral components except for the XPM distortions (—) around the pump; the XPM products should be phase shifted by 180 degrees. Note that the phase of the pump is not shifted. After the PSF, all the spectral components shown in Fig. 7-1(b) are fed into the second highly nonlinear fiber (HNLF2), followed by a band-pass filter (BPF) and an output EDFA.

7.1.1 Working principle of phase-shift filter OPC

The improvement in performance by considering the effect of the phase shift on the generation of XPM-OPC is explained in this section. Figure 7-2(a) illustrates the accumulated field of XPM products, E_{XPM} (—), and its conjugate, $E_{XPM\text{-}OPC}$ (—), along the HNLF when conventional OPC is used. E_{XPM} grows linearly along the fiber and $E_{XPM\text{-}OPC}$ grows quadratically, and can be expressed as [84, 85]:

$$E_{XPM}(z) = 2\gamma z\sqrt{P_{pump}}P_{sig} \tag{7.1}$$

$$E_{XPM-OPC}(z) = 2(\gamma z)^2 P_{pump}\sqrt{P_{sig}^3} \tag{7.2}$$

Figure 7-2(b) shows the corresponding fields when a 180° phase shift is used in the PSF in the spectral range of XPM products. Applying this phase shift inverts the E_{XPM} vector. New contributions to E_{XPM} generated in HNLF2 are anti-phase with the E_{XPM} at the output of HNLF1; so the accumulated E_{XPM} reduces along HNLF2. As an additional benefit, the new $E_{XPM\text{-}OPC}$ field generated at any point in HNLF2 is anti- phase with the $E_{XPM\text{-}OPC}$ field at the output of HNLF1 due to the inverted E_{XPM} field. The accumulated $E_{XPM\text{-}OPC}$ field (▪▪▪) becomes zero at the end of the HNLF2. As for the desired OPC signal, since the pump remains in phase with the input in the second part of the OPC module, HNLF2 generates OPC signals in phase with those generated by the first part. Thus, this PSF is expected to significantly improve system performance. Note, however, that we found that the filter should also have additional loss at the frequencies of the phase-shifted region for optimum cancellation, due to higher-order mixing processes.

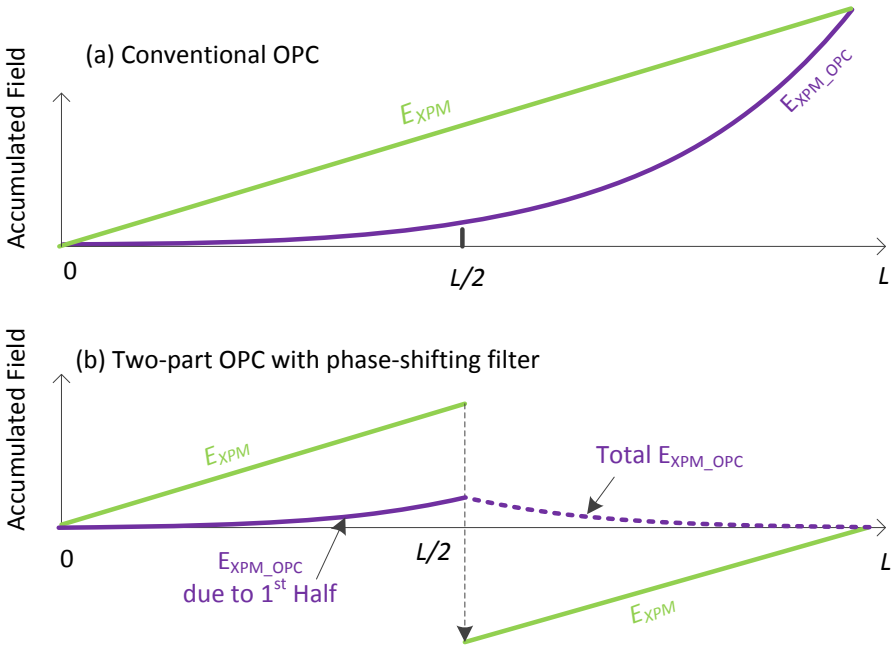

Figure 7-2: One-stage (EXPM) and two-stage (EXPM-OPC) mixing of nonlinear products inside the OPC: (a) conventional OPC; (b) PSF OPC with PSF.

7.2 System performance using simulation

The back-to-back performance of PSF OPC in a CO-OFDM system (Fig. 7-3) is quantified using VPItransmissionMaker v8.7. The OFDM signal used a 1024-point inverse fast Fourier transform (IFFT); 920 subcarriers were modulated with 4-QAM and a 32-point cyclic prefix (CP) was inserted before each OFDM symbol. The total bit rate was 224-Gb/s, resulting in a net data rate of 200 Gb/s with 12% overhead for FEC and training. The optical link comprised 10×80-km spans of standard 0.2-dB.km^{-1} loss single mode fiber (S-SMF) with EDFAs to compensate the span losses. The OPC module is placed after the fifth span. A 60-km dispersion compensation fiber (DCF) was used just before the OPC module [145]. The detail of the OPC module is shown in Fig. 1(a). The nonlinear coefficient of the HNLF, γ is 11.5 W^{-1}.km^{-1}, its loss coefficient is 0.97 dB/km, and chromatic dispersion, CD is zero. The pump power into the HNLF is 10 dBm.

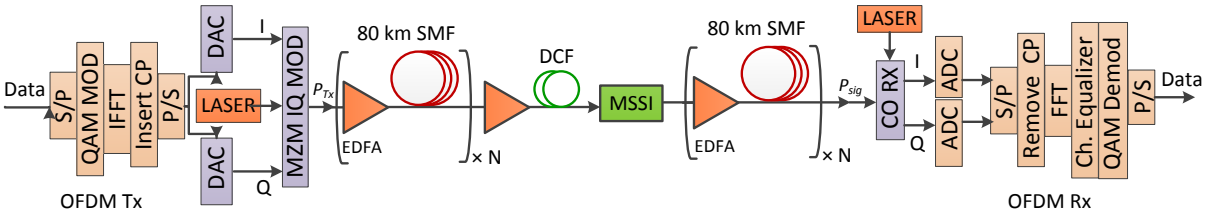

Figure 7-3: Schematic of CO-OFDM transmission system. The detail of MSSI has been shown in Fig. 7-1(a).

7.2.1 Back-to-back performance

First, the effect of the phase-shift filter on the spectrum at the output of the HNLF, before the output band-pass filter (BPF) is shown in Fig. 7-4. The spectrum (—) for conventional OPC is shown in Fig. 7-4(a), and that for the PSF OPC is shown in Fig. 7-4(b) (—).

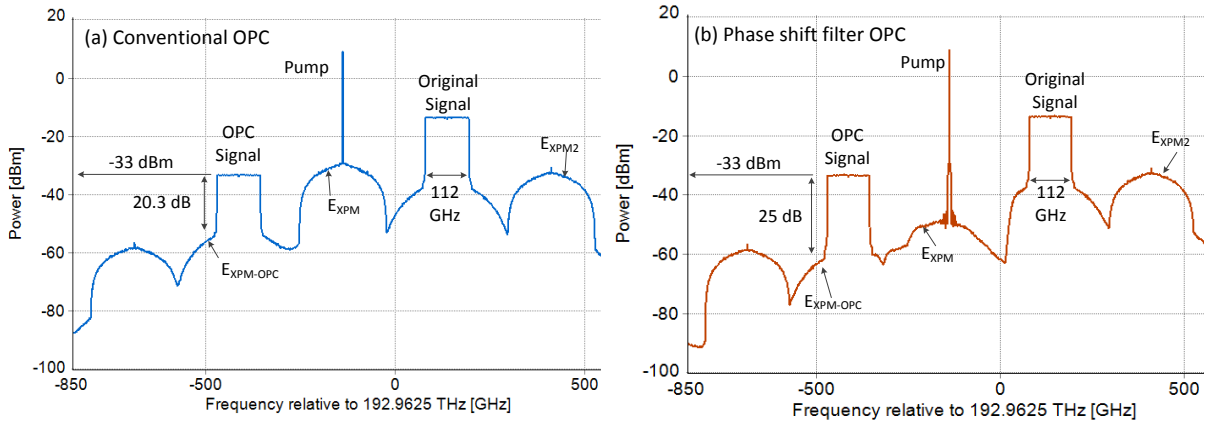

Figure 7-4: Spectrum after the HNLF; (a): for Conventional OPC; (b) for PSF OPC.

The OPC signal levels in both of the cases were about -33 dBm, before the output BPF. However, both the E_{XPM} and $E_{XPM\text{-}OPC}$ were significantly smaller when phase shift filter OPC is used. Therefore, a performance improvement is expected using this method.

Figure 7-5 shows the back-to-back Q versus input signal power into the HNLF. The signal quality, Q, has been calculated from error vector magnitude (EVM) [66]. The blue curve with circles (●) shows the system performance with conventional OPC and the red curve with squares (■) shows the system performance with PSF OPC. The dotted black line (---) shows back-to-back performance when OPC is not used. The PSF improves the back-to-back signal quality, Q_{max}, by 3.6 dB at the optimum signal power.

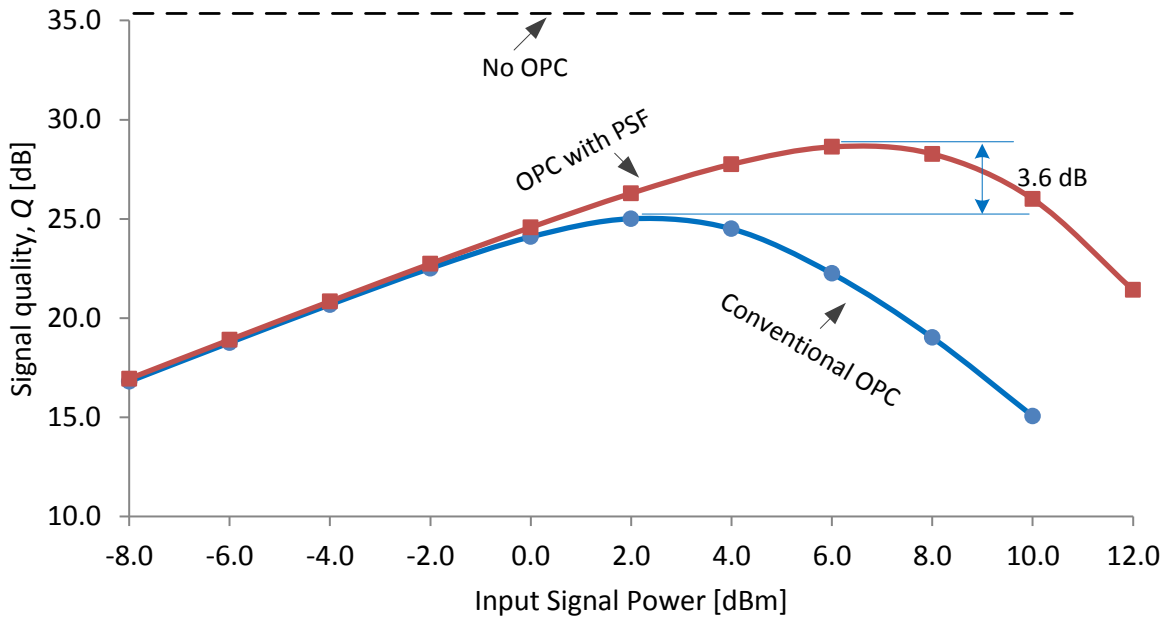

Figure 7-5: Performance comparisons between the conventional OPC module and the two-part OPC module with PSF in a back-to-back system.

7.2.2 Transmission performance

Figure 7-6 shows the comparison of transmission performance between systems with conventional OPC (●) and phase-shifting filter OPC (■). The input power into the OPC module is the optimum power from the back-to-back simulations shown in Fig. 7-5, which are 2 dBm for conventional OPC system and 6 dBm for PSF OPC. The input power into the DCF was 4-dB less than the OPC input power. Results without OPC (▪▪▪) show the benefit of OPC. The system with conventional OPC shows 1-dB better Q_{max} than the system without OPC. The system with the phase-shifting filter has an additional 1.2-dB Q_{max} improvement at the optimal signal power.

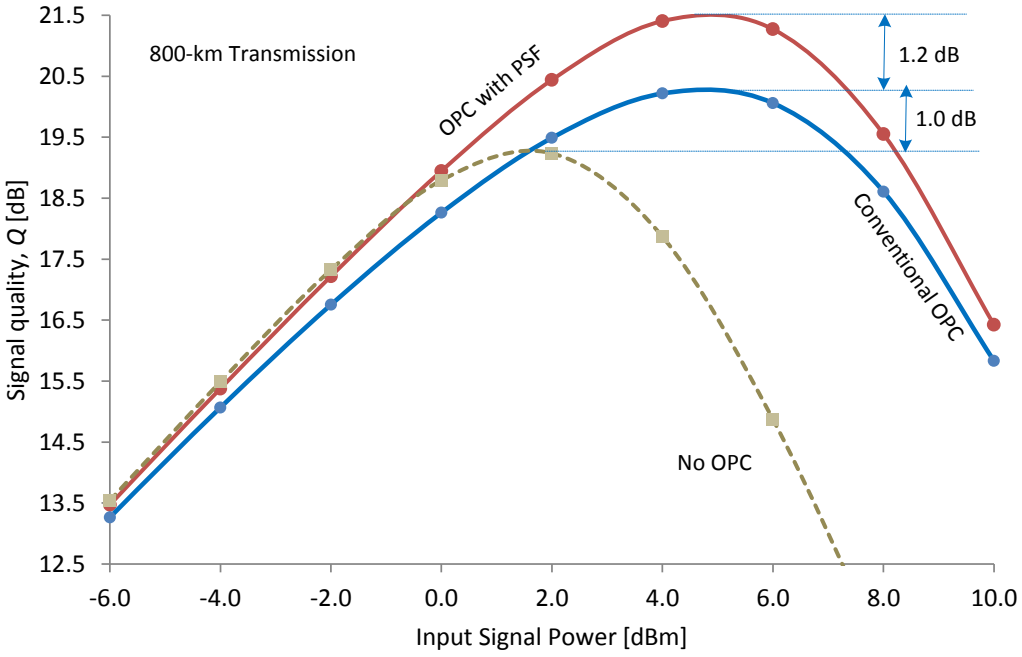

Figure 7-6: Performance comparisons between the conventional OPC module and the two-part OPC module with PSF in an 800-km transmission system.

7.3 Discussion

7.3.1 Effect of higher order mixing on XPM products

In the above simulations, XPM products generated around the pump were not only phase shifted by 180 degrees using the phase shift filter; these products were also attenuated by 6 dB, using the filter profile shown in Fig. 7-1(b). Figure 7-7 shows the XPM attenuation versus back-to-back performance improvement using phase shift filter OPC compared to conventional OPC. The result shows that when the XPM products have attenuation range from 3-9 dB, performance shows highest signal quality.

The reason for this optimum XPM attenuation can be explained when the effect of higher order mixings on XPM products is considered. At the input of the 1st HNLF, only the original signal and pump interact to generate XPM products around the pump, whereas, the input of the 2nd HNLF includes, in addition to original signal and pump, other newly generated side modes as well as OPC signal itself that can also contribute to the XPM products in the 2nd HNLF. The fields of the XPM products generated by these second order mixings add constructively with the fields of the XPM products that are phase inverted by the all pass filter. This makes the two-stage OPC asymmetric with regard to nonlinear mixing mechanisms. Figure 7-8 shows the spectra at the input of the 2nd HNLF, showing at least four other sources that can make additional contributions to XPM products other than regular mixing mechanism; the OPC signal itself and the three ‘side modes’ as indicated. Therefore, it

is highly likely that when these higher order mixings take place, the XPM products newly generated in the 2nd HNLF will be slightly stronger than those generated in the 1st HNLF. Thus it necessitates certain amount of attenuation of the XPM products in the beginning of the 2nd HNLF, so that the total XPM products in the two HNLFs become similar in order to maximize the cancellation of XPM-OPC products.

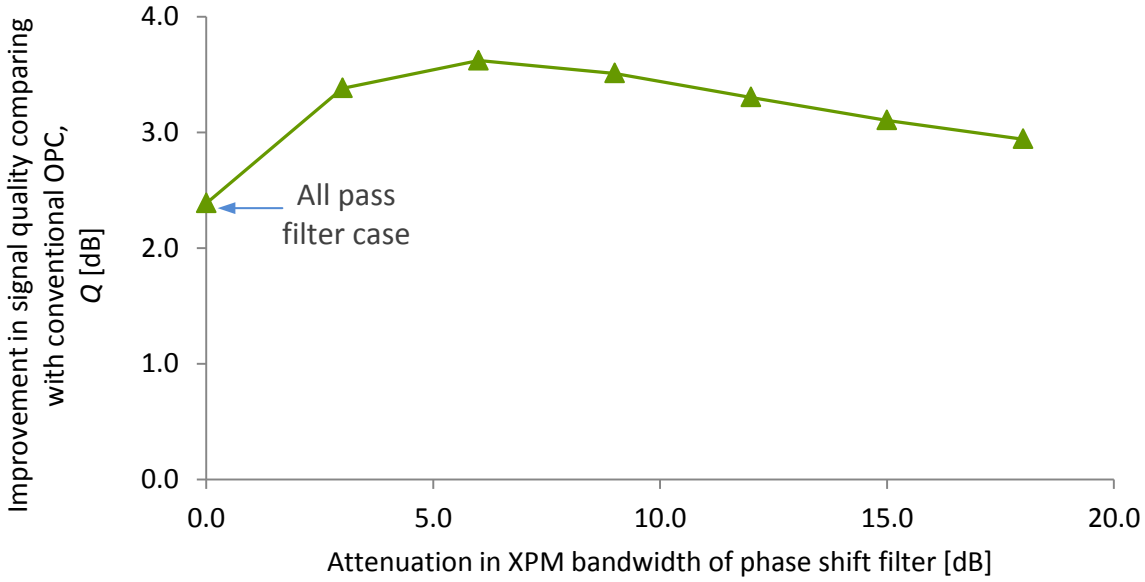

Figure 7-7: Back-to-back performance versus XPM attenuation by PSF.

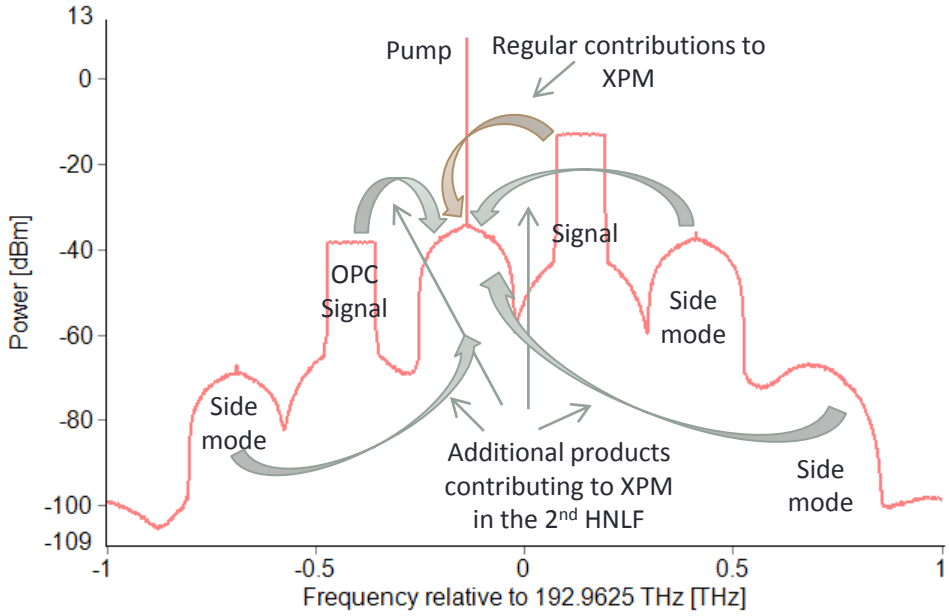

Figure 7-8: Spectra at the input of the 2nd HNLF showing additional sources other than original signal and pump that contribute on XPM in the 2nd HNLF.

7.3.2 PSF insertion loss and EDFA noise figure dependence

In the reality, the phase shift filter will have insertion loss, which will need to be compensated by an additional EDFA before the PSF as shown in Fig. 7-13. Therefore, it is of practical interest to investigate the effect of the PSF insertion loss and noise figure of the associated EDFAs to compensate this loss.

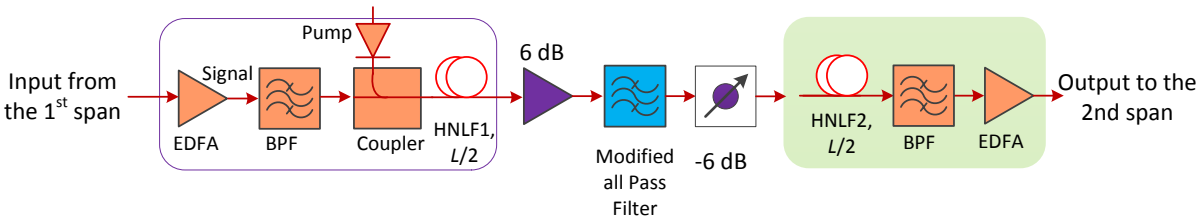

Figure 7-9: Phase shift filter insertion loss and its compensation using an EDFA.

The red curve (—) of Fig. 7-14 shows signal quality of the back-to-back system versus phase shift filter insertion loss. The noise figures of all the EDFAs used in the OPC module were set to 6 dB in this case. The results show that for insertion loss less than 6 dB, the performance does not show strong dependence on insertion loss. For insertion loss greater than 6 dB, performance degrades considerably.

The blue curve (—) of Fig. 7-14 shows signal quality of the same back-to-back system versus EDFA noise figure. The insertion loss of the filter was fixed at 6 dB in this case. The performance shows strong dependence on the noise figure of the EDFAs used in the OPC module. Therefore, low-noise EDFAs inside the OPC module are required for better performance.

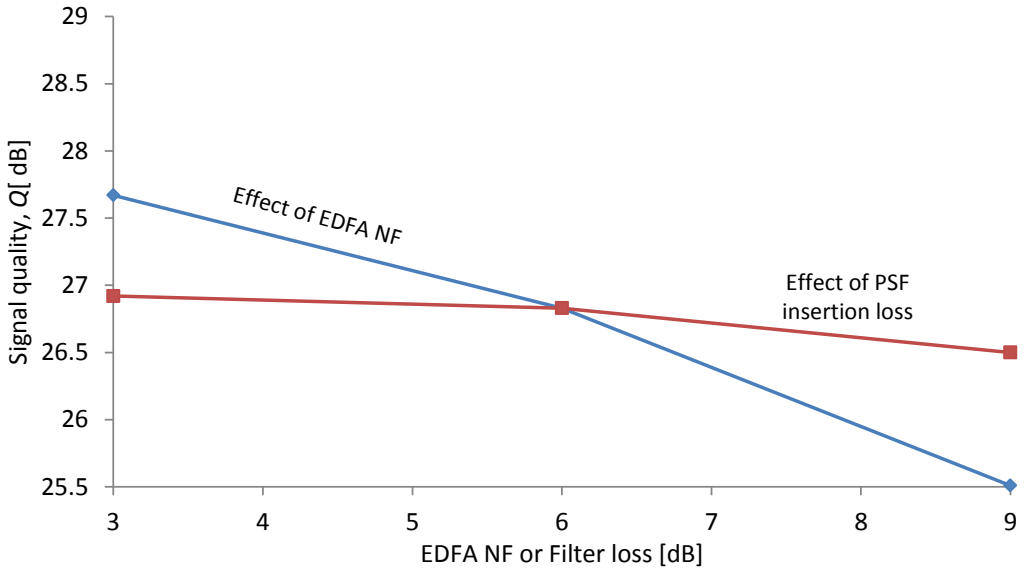

Figure 7-10: Back-to-back performance versus EDFA noise figure, filter insertion loss.

Figure 7-15 shows the transmission performance with 0 dB filter insertion loss (—) and 6 dB insertion loss (—). For reference, performance with conventional OPC (—) and no OPC (···) are also shown. The EDFA noise figure for all of these cases was fixed at 6 dB. The performance with 6 dB insertion loss (—) shows 0.4 dB penalty compared with ideal lossless PSF case due to ASE noise generated by the EDFA to compensate the loss. However, the results show that, using practical value of 6 dB insertion loss and an EDFA with, 6-dB Noise Figure still gives more than 0.8-dB performance improvement compared to conventional OPC system. Therefore, the new method promises novel OPC which gives considerable performance improvement with prospect of more robustness than the previous notch-filter method for practical implementation.

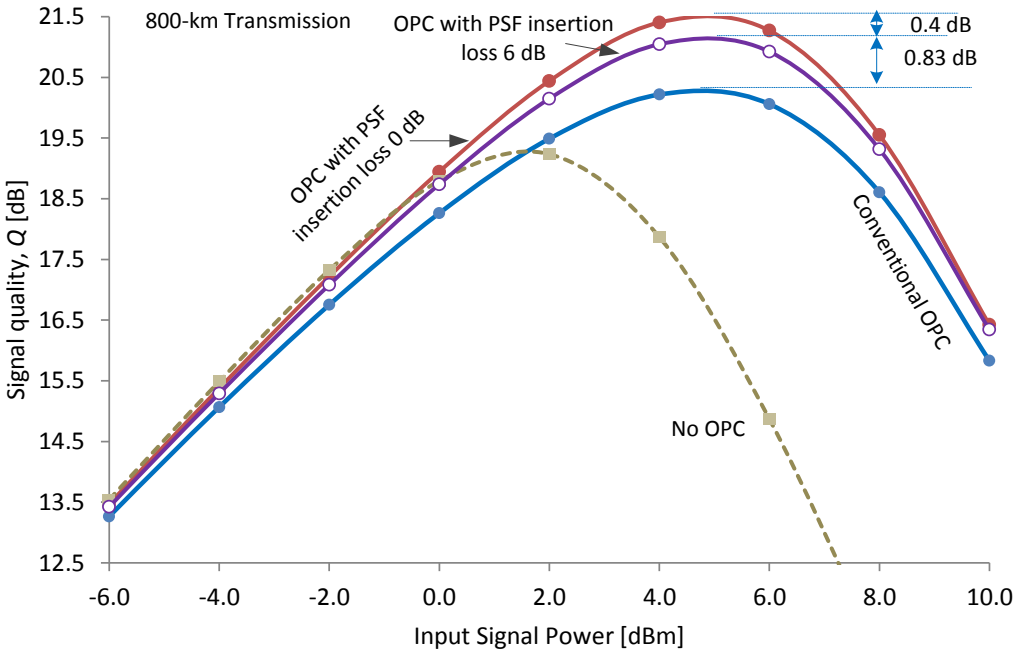

Figure 7-11: Transmission performance improvement using phase shift filter OPC with filter insertion loss 6 dB and EDFA noise figure 6 dB.

7.4 Conclusion

A modified design of two-part OPC using third-order nonlinearity to improve the back-to-back performance of CO-OFDM systems using MSSI has been presented. The proposed design improves the back-to-back performance by 3.6 dB and the transmission performance at optimum power by 1.2 dB in a 10 × 80-km 4-QAM 224-Gb/s CO-OFDM system. This is because the filter reverses the phase of the XPM generated around the pump in the first half, so that similarly-generated XPM in the second half cancels that in the first half. Performance of the new method has been verified using real life system parameters. The result shows that the new method promises better performance as well as improved robustness for practical implementation than the notch-filter OPC.

8 Conclusions

In this thesis, fiber nonlinearity compensation using mid-span spectral inversion (MSSI) in coherent optical orthogonal frequency division multiplexing (CO-OFDM) systems has been investigated. The motivation of the work was derived from the capacity of the present optical networks being approached to its fundamental limits. With the internet traffic increasing at an astounding 75% per year, and new video-centric applications emerging, the research for the fiber capacity growth is actively being pursued today in order to meet long-term needs and challenges.

The fundamental limits of present capacity limits arise due to signal-to-noise ratio and distributed nonlinearity of conventional standard single mode fiber (S-SMF), which becomes a prominent issue especially in high bandwidth long haul optical fiber transmission.

In attempts to increase the capacity limits for high bandwidth long haul optical fiber transmission, mitigating the fiber nonlinearity with advanced modulation format like coherent optical OFDM systems (CO-OFDM) is being studied. The thesis proposed using mid-span spectral inversion (MSSI) with CO-OFDM systems in order to achieve this purpose.

8.1 Fulfilling the goal of the thesis

In the beginning of the thesis, the following generalized goals were set to achieve the desired capacity improvement in high bandwidth long haul CO-OFDM transmission systems using MSSI:

- Survey the current state-of-the art in optical fiber communications and existing methods for mitigating fiber nonlinearities.
- Develop analytical formalisms to quantify the performance penalty and limitations due to undesired FWM products falling over the conjugated signal.
- Analyse the OSNR penalty introduced due to MSSI, and thus outline the system requirements that can benefit from using MSSI for nonlinearity mitigation.
- Experimentally demonstrate using MSSI with CO-OFDM systems for fiber nonlinearity mitigation.
- Outline the design considerations for CO-OFDM systems that use MSSI for fiber nonlinearity mitigation.
- Investigate novel OPC methods to improve system performance that uses MSSI of third order nonlinearity.

The following section will discuss how these goals were fulfilled as described in corresponding chapters of the thesis.

The thesis started with an overview of optical fiber communication systems, explaining its history from its beginning until present time. The pioneering experimental demonstrations that formulated the course of history for optical fiber communication have been reviewed.

The next chapter discussed the three major nonlinear effects in optical fiber; these are: self-phase modulation (SPM), cross-phase modulation (XPM) and four-wave mixing (FWM) and form the main limiting factor today. A detailed literature review of the methods being studied to mitigate nonlinear effects was discussed in this chapter and optical phase conjugation (OPC) used in MSSI for nonlinearity mitigation was introduced.

The third chapter reviewed the optical phase conjugation (OPC) and MSSI in detail. The theoretical background, benefits and limits of MSSI in ideal and practical links were discussed. Several methods that have been introduced to improve the benefit in practical systems were reviewed.

The key original contributions of the thesis started from Chapter Four. In this chapter, analytical formalisms to describe the performance limitations due to practical MSSI were developed. It was found that two major two-stage nonlinear mixing products cause performance penalty; these have been called XPM-OPC and FWM-OPC products, with XPM-OPC dominating. Analytical expressions of these nonlinear products along with back-to-back system performance were presented. This is one of the major original contributions of this thesis.

An experimental demonstration of using MSSI with CO-OFDM was presented in Chapter Five. It was shown, for the first time, that using MSSI allows higher launch powers in dual polarization CO-OFDM systems. Simulations showed that this increase in maximum viable launch power could support about a 22% increase in total transmission distance with fixed number of inline amplifiers, by extending each fiber span from 90 km to 110 km, for 1.21-Tb/s system. For a fixed length of span, the MSSI system showed less degradation in optimum performance with increasing number of spans (i.e. increased transmission distances), and supported more than 70% increase in overall transmission distance when 80-km spans are used. As for optimization of the OPC module itself, simulations showed that reducing total insertion loss inside OPC module is very important in achieving higher maximum *Q* performance as is using shorter HNLF and increasing the OPC conversion efficiency.

Although MSSI increased the maximum launch power, the maximum signal quality at optimum launch power did not improve, which was mainly due to the performance limitations discussed in

Chapter Four. Using the insight from the theoretical formalisms, two novel methods to reduce this performance penalty were proposed. The first of the two methods is discussed in Chapter Six. The method includes a new design of an OPC to improve the back-to-back performance of CO-OFDM systems that use MSSI. The new design reduced the performance penalty introduced by a conventional OPC module by 3 dB. It was shown that this back-to-back performance improvement results in a 1-dB improvement in a 10 × 80-km 4-QAM 224-Gb/s CO-OFDM system. The improvement increases gradually with higher signal bandwidths, which is useful for ultrahigh bandwidth transmission. It has been shown that the new system would have almost no degradation due to the phase difference between the injected pumps, provided that this is controlled to within +/- 20 degrees.

The second method for improving the performance of OPC module for fiber nonlinearity mitigation was introduced in Chapter Seven. A modified two-part OPC method that gives a better performance improvement than the notch-filter OPC, yet with more robustness in terms of practical implementation was proposed. The method uses an in-line phase-shift filter (PSF) between the two nonlinear sections of the OPC. Numerical simulations showed that this phase-shift filter OPC module has a 3.6 dB higher back-to-back signal quality, Q_{max}, compared with a conventional OPC module. This better back-to-back performance resulted in an improvement of the maximum Q_{max} by 1.2 dB in a 10 × 80-km 4-QAM 224-Gb/s CO-OFDM system.

Figure 8-1 below summarizes the performance of nonlinearity mitigation of the existing methods discussed in Chapter Two along with this work that used MSSI. Fig. 8-1 (a) shows the increase in maximum allowable launch power and Fig. 8-1 (b) shows the improvement in the *Q*-factor at optimal launch power. The blue bars ( ) in Fig. 8-1 (a) represent the increase in maximum allowed launch powers for the existing methods. The purple bars ( ) in Fig. 8-1(b) represent the improvement in optimal *Q*-factors for the same. For both Fig. 8-1(a) and Fig. 8-1(b), the red bar ( ) shows the performance improvement with a one-stage OPC, the green bar ( ) with two-stage OPC using notch filter, and orange bar ( ) with two-stage OPC using a phase shift filter. Considering that MSSI can process multiple WDM channels simultaneously, while the DBP result shown here is for a single channel system, Fig. 8-1 reveals that MSSI offers highest degree of nonlinearity mitigation benefit for a WDM system in a highly dispersive system that uses no in-line dispersion compensation mapping in the link. Additionally, the proposed two novel methods shown in green ( ) and orange bars ( ) further improve the performance by more than 1 dB, making the overall benefit using MSSI about 5 dB and 2 dB for maximum allowable launch power and optimal *Q*-factor, respectively.

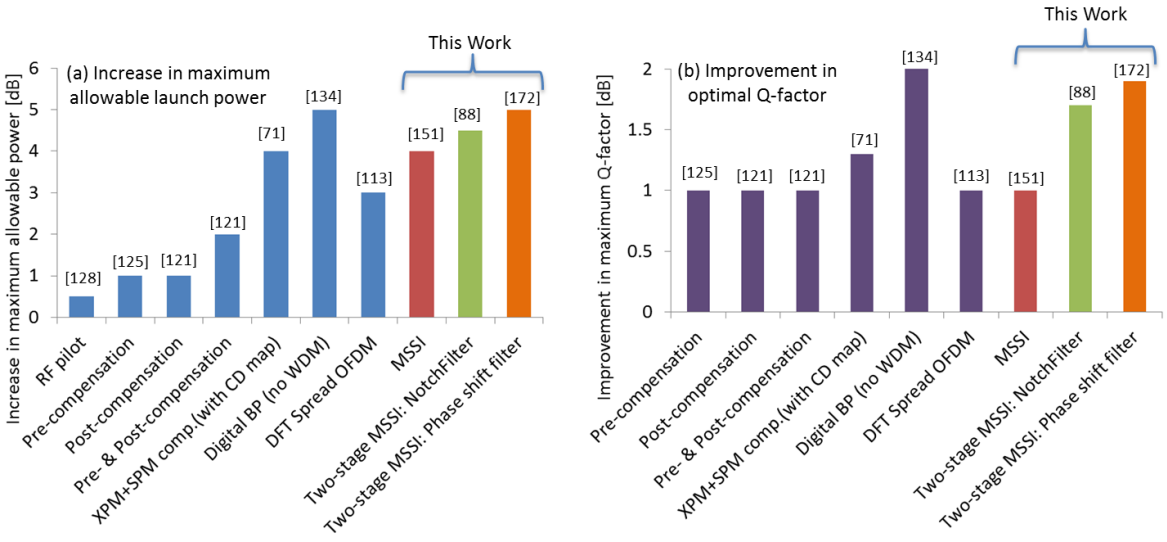

Figure 8-1: Achievements of this thesis work comparing with existing methods.

8.2 Limitations and recommendations when using MSSI

The limit of using MSSI arises from two aspects. Firstly, MSSI is more effective for point-to-point links, as the OPC module needs to be placed around the mid-link for maximize the benefit. Therefore, any link using MSSI may suffer the flexibility required for next generation flexible optical networks employing ROADMs. In ROADM based networks, a particular node can flexibly add/drop from either the 'East' or 'West' bound traffic. Therefore, point-to-point link is not suitable for such networks. However, this limitation can be overcome by using technique to make the dispersion map symmetric by adding DCF, or using pre/post distortion techniques. Also, end-span OPC could be a solution for any kind of network connections such as bypass or add/drop.

Secondly, another source of penalty comes from nonlinear distortions generated within the OPC module itself by FWM when using MSSI that relies on third order nonlinearity. This has been analysed in detail in Chapter Four. The analysis revealed that these nonlinear distortions increase with the 4^{th} power of HNLF length and the 2^{nd} power of the pump power (Equation (4.20) in Chapter Four). This implies that using shorter HNLF and lower pump power generates less nonlinear distortion. However, the OPC conversion efficiency, expressed in Equation (4.21) in Chapter Four, is proportional to the 2^{nd} power of both the HNLF length and the pump power. Reconciling these two constraints implies that for target conversion efficiency, opting for shorter HNLF with increased pump power offers less nonlinear distortion. On the other hand, the maximum usable pump power is ultimately limited by stimulated Brillouin scattering (SBS) for a given HNLF. Therefore, a trade-off between higher conversion efficiency, lower nonlinear distortion and SBS limit of usable pump power in a given HNLF governs the overall design criteria for optimum OPC choice.

For the point-to-point link, MSSI is suitable only for long haul transmission, because of the associated penalty due to OPC module. The penalty includes OSNR penalty arising from ASEs in the EDFAs to compensate the loss due to OPC conversion and other insertion losses. A simple analysis, shown in Appendix A, shows that for a small number of spans (< 8), the OSNR penalty increases sharply even with low loss OPC module. However, the OSNR penalty decreases with increasing number of spans because the ASE of the span amplifiers becomes dominant. If the total loss inside the OPC module is comparable to one span-loss, which is practically achievable, a penalty of less than 1 dB can be achieved when 10 or more spans are used. In this scenario, a realistically implementable MSSI will not cause any considerable penalty for long haul transmission.

If the OPC module can be implemented with higher conversion efficiency and no nonlinear distortions, then it could be used for both long and short-reach transmission systems.

One way for achieving higher conversion efficiency with a shorter HNLF is using an HNLF with an increased nonlinear coefficient. However, as Equation (4.20) shows, nonlinear distortion again scales with the 4^{th}-power of the HNLF nonlinear coefficient. Therefore, using a high pump power within the SBS limit with a shorter HNLF and a lower nonlinear coefficient is desirable for optimum OPC performance.

Other methods like phase dithering of the pump [170], two-stage counter phase dithering [168] where two pumps are phase modulated 180° out of phase and recently demonstrated modified two-stage counter dithering scheme [169] were proposed to achieve conversion efficiency as close to 0 dB. In order to get rid of the nonlinear distortions, PPLN based OPC can be used as it is based on 2^{nd} order nonlinear effects. Therefore, an OPC with higher conversion efficiency based on PPLN could be an ideal candidate for both long and short-reach transmission systems.

MSSI will show its best performance when the transmission is well designed in terms of dispersion map, and power level. The present thesis demonstrated using MSSI for currently deployed systems which uses EDFA only amplifications. This is too far from the desirable scenario for MSSI taking into effect. Using Raman assisted hybrid amplifications; the power profile through link could be made almost symmetrical with respect to MSSI. In such scenario, the benefit of using MSSI could be significant [91]. Since the benefit MSSI could bring to the systems could be significant, setting up a new fiber link based on MSSI could be a solution in many high-capacity applications in the future which need to overcome the nonlinear Shannon limit.

The two filter-based methods proposed in this thesis to reduce the nonlinear distortion products generated within the OPC module itself can improve the OPC performance by more than 1 dB. However, these come at the expense of increased complexity of the OPC module.

8.3 Recommendations for future research and open issues

Following the research undertaken in this thesis, certain issues and challenges require further research and development. These are:

- Incorporating the back-to-back system performance derived in this thesis into a set of design rules for any end-to-end transmission system.
- Implementing OPC module using two-part OPC, as outlined in Chapters Six and Seven. In the first method, the phase of the pump inserted in the second part of MSSI should be actively controlled using a complex optical phase locked loop (OPLL). Therefore, from a practical point of view, the second method where an all pass filter is used with controlled phase shifting characteristics seems more practical for implementation.
- Finally, for improving the flexibility, the first half of the link can be replaced by a highly nonlinear, dispersive grating, so that the OPC module can be located at the transmitter [176, 177]. This will improve the practicality of using OPC in a next generation flexible ROADM networks.

Appendix A

Analysis of OSNR penalty due to MSSI

A simple analysis has been made to estimate the impact of the noise of the MSSI on the OSNR at the end of the link. The model used in the calculation is shown in Fig. A-1. It is assumed that ASE is the dominant noise source of the link. It is also assumed that each amplifier gain, G compensates for the previous span loss, αL, where α is the attenuation coefficient of the fiber in Nepers/km and L is the span length in km.

After the 1st half of the link, the input signal power is boosted to P_T before put into the OPC module. At the input of the OPC module, the signal attenuates due to insertion loss or due to attenuation in the DCF module that may be used to maximize the MSSI performance. The insertion loss and/or DCF loss is compensated by the input EDFA. For simplification, it is assumed that the total insertion loss and/or DCF attenuation amounts to one span loss, *i.e.* $G_{in} = G = \alpha L$. On the other hand, the output EDFA's gain is G_{out}, which compensates the loss due to HNLF attenuation and OPC conversion loss; i.e. $G_{out} = \alpha_{mssi} = \alpha_{hnlf} \times \alpha_{OPC}$, where α_{hnlf} is the attenuation inside the HNLF and α_{OPC} is the OPC conversion loss.

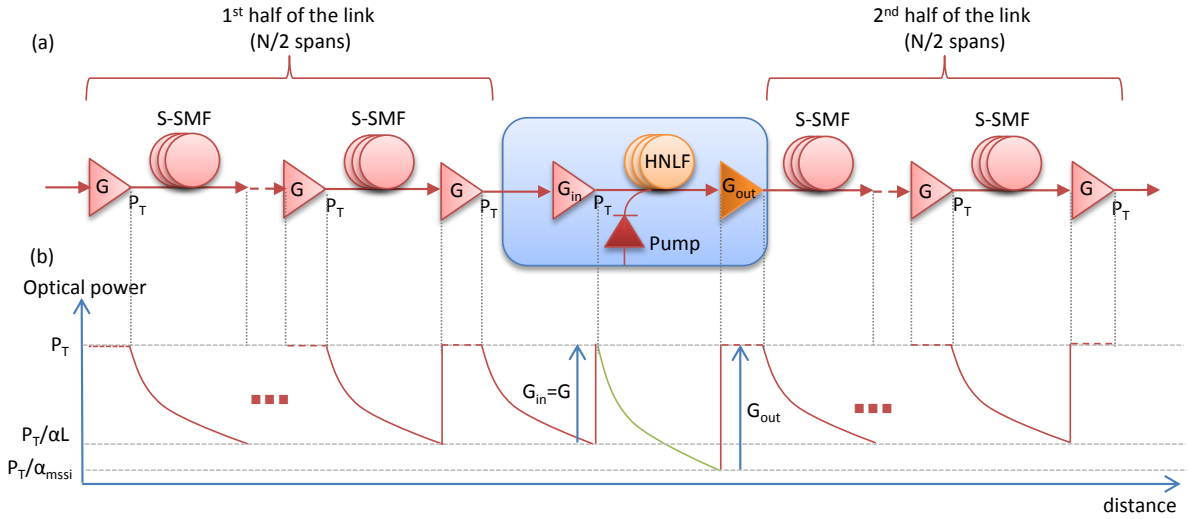

Figure A-1: Schematic diagram to calculate OSNR penalty due to MSSI.

The power of the ASE generated in bandwidth B_0 at the output of each inline amplifier can be given by:

$$P_{ASE} = F.(G-1).hf.B_0 \qquad \text{(A.1)}$$

$$P_{ASE} = F.(G-1).hf.B_0 \tag{A.2}$$

where, F is the noise factor of the amplifier, h is Planck's constant (6.626069 x 10^{-34} Js), f is the optical signal center frequency (193.0 THz) and B_o is the optical channel bandwidth in Hz.

The total ASE power due to all inline amplifiers is given by:

$$P_{ASE,N} = N\,P_{ASE} \tag{A.3}$$

Therefore, optical signal to noise ratio (OSNR) of a reference system consisting only N inline amplifiers without MSSI is given by:

$$\begin{aligned} OSNR_{ref} &= 10\log_{10}\left(\frac{P_T}{P_{ASE,N}}\right) \\ &= 10\log_{10}\left(\frac{P_T}{N\,P_{ASE}}\right) \\ &= 10\log_{10}\left(\frac{P_T}{N.F\,(G-1).hf.B_0}\right) \end{aligned} \tag{A.4}$$

On the other hand, noise generated inside the OPC module can be calculated by:

$$\begin{aligned} P_{ASE,MSSI} &= P_{ASE,in} + P_{ASE,out} \\ &= F.(G-1).hf.B_0 + F.(G_{out}-1).hf.B_0 \\ &= F.(G-1).hf.B_0\left(1+\frac{(G_{out}-1)}{(G-1)}\right) \\ &= P_{ASE}\left(1+\frac{(G_{out}-1)}{(G-1)}\right) \\ &= P_{ASE}\left(1+\frac{(bG-1)}{(G-1)}\right) \end{aligned} \tag{A.5}$$

where b is the ratio of MSSI loss consisting of HNLF attenuation and OPC conversion loss to the loss of one span, *i.e.*:

$$b = \frac{G_{out}}{G} \tag{A.6}$$

The OSNR of the transmission system consisting of N spans and a OPC module is given by:

$$OSNR_{MSSI} = 10\log_{10}\left(\frac{P_T}{P_{ASE,N} + P_{ASE,MSSI}}\right)$$
$$= 10\log_{10}\left[\frac{P_T}{P_{ASE}\left(N + 1 + \frac{bG-1}{G-1}\right)}\right] \quad \text{(A.7)}$$

The OSNR penalty in calculated by subtracting Equation (A.6) from (A.3), and is given by:

$$\delta_{(dB)} = 10\log_{10}\left(1 + \frac{1 + \frac{bG-1}{G-1}}{N}\right) \quad \text{(A.8)}$$

Figure A-2 shows the OSNR penalty as a function of number of spans, *N*, for various *b* factors. It shows that for a small number of spans (< 8), the penalty increases sharply even for MSSI with a low total loss. However, it decreases with increasing number of spans because the ASE of the span amplifiers becomes dominant. With $b \approx 1$ which is practically achievable, a penalty of less than 1 dB can be achieved when 10 spans or more are used. This is desirable, as realistically implementable MSSI will not cause any considerable penalty for long haul transmission.

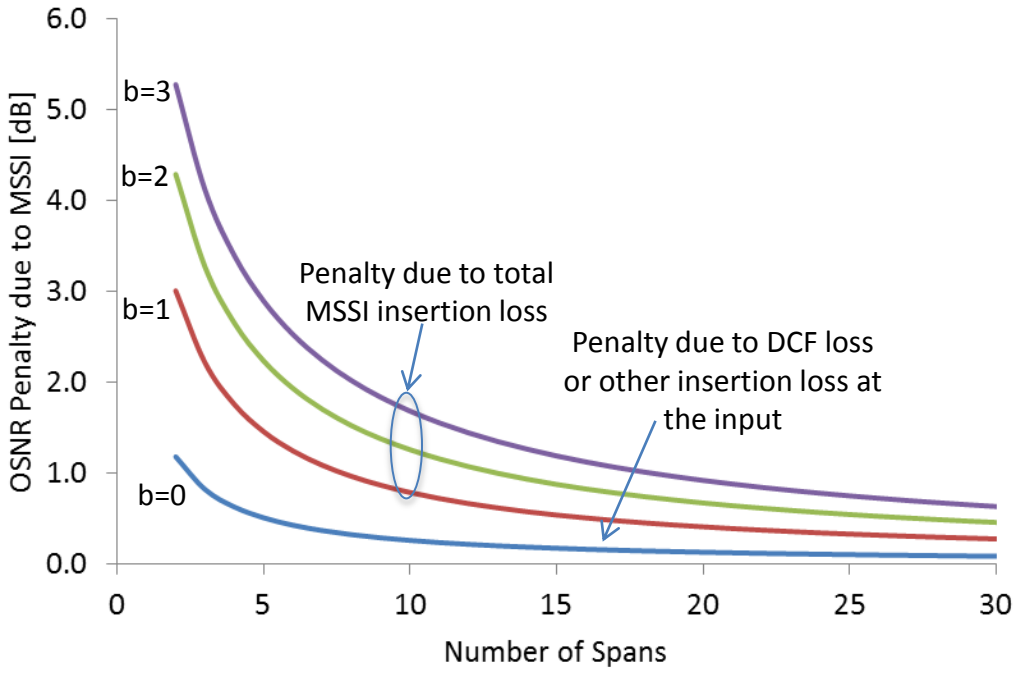

Figure A-2: OSNR penalty due to MSSI.

Appendix B

Calculation of an OSNR evolution

The following two equations have been used to calculate the OSNR evolution for both the reference link and MSSI link:

$$OSNR = \frac{GP_{in}}{F.(G-1).hf.B_0} \qquad \text{(B.1)}$$

$$\frac{1}{OSNR_F} = \frac{1}{OSNR_1} + \frac{1}{OSNR_2} + ... + \frac{1}{OSNR_N} \qquad \text{(B.2)}$$

Where

$OSNR_F$=final OSNR seen at the receiver

$OSNR_N$=OSNR of individual optical amplifiers up to N

And F, G, h, f and B_0 have the same meaning as mentioned in Appendix A.

Table B-1 uses the above two equations to determine the final OSNR for one or two EDFA links. For a link with more than two EDFAs, the successive of the same formant of table is added to the bottom of this table using the output OSNR of the previous EDFA calculation as the input to the next EDFA OSNR.

Table B-1: Calculation of an OSNR evolution throughout the link.

		Equation	Input Data	Calculation	Unit
First EDFA					dB
Input OSNR	OSNRindB		57		
Input OSNR	OSNRin	=10^(OSNRindB/10)		501187.234	
Input Signal Power	PindB		-16		dBm
Input Signal Power	Pin	=10^(PindB/10)/1000		2.5119E-05	Watt
Noise Figure	NF		6		dB
Noise Factor	F	=10^(NF/10)		3.98107171	
Channel Bandwidth	Br		1.25E+10	1.25E+10	Hz
Frequency	f		1.93E+14	1.93E+14	Hz
Plank Const	h		6.63E-34	6.63E-34	Js
Pase/G	FhfBr	=F× h × f ×B0		6.38E-09	
Output OSNR	OSNRout	=1/(1/OSNRin+FhfBr/Pin)		3.91E+03	
Output OSNR	OSNRoutdB	=10×log10(OSNRout)		**35.92**	**dB**

		Equation	Input Data	Calculation	Unit
2nd EDFA					
Input OSNR	OSNRindB		35.92		dB
Input OSNR	OSNRin	=10^(OSNRindB/10)		3908.20773	
Input Signal Power	PindB		-16		dBm
Input Signal Power	Pin	=10^(PindB/10)/1000		2.5119E-05	Watt
Noise Figure	NF		6		dB
Noise Factor	F	=10^(NF/10)		3.98107171	
Channel Bandwidth	Br		1.25E+10	1.25E+10	Hz
Frequency	f		1.93E+14	1.93E+14	Hz
Plank Const	h		6.63E-34	6.63E-34	Js
Pase/G	FhfBr	=F× h × f ×B0		6.38E-09	
Output OSNR	OSNRout	=1/(1/OSNRin+FhfBr/Pin)		1.96E+03	
Output OSNR	OSNRoutdB	=10×log10(OSNRout)		**32.93**	**dB**

The final result of OSNR evolution for both the reference link and the MSSI link is shown in Fig. B-1. For the calculation of the OSNR evolution of the MSSI link, DCF loss of 12 dB, total CE + Insertion loss of 30 dB is used. This gives the OSNR penalty at the end of the 10th EDFA to be about 1.6 dB. This matches well with the result of Appendix A, which also predicts OSNR penalty of about 1.6 dB for total CE+ Insertion loss amounting to 2-3 span loss.

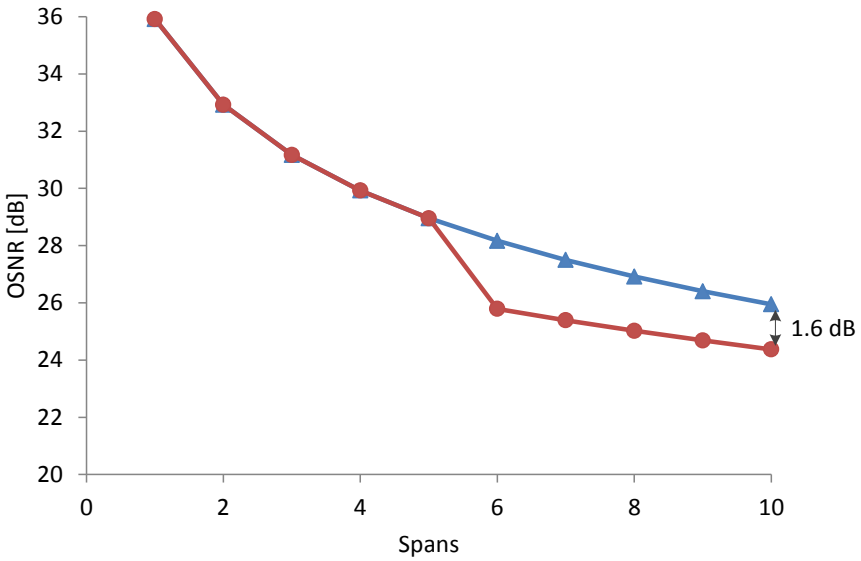

Fig. B-1: Evolution of OSNR for reference link and MSSI link.

Appendix C

Glossary

ADC	Analog to Digital Converter
AM	Amplitude Modulation
ASE	Amplified Spontaneous Emission
AWG	Arbitrary Waveform Generator
BER	Bit Error Rate
BSF	Band Stop Filter
BP	Back Propagation
BPF	Band Pass Filter
CD	Chromatic Dispersion
CE	Conversion Efficiency
CO-OFDM	Coherent Optical Orthogonal Frequency Division Multiplexing
CP	Cyclic Prefix
CW	Continuous Wave
DAB	Digital Audio Broadcasting
DAC	Digital to Analog Converter
DCF	Dispersion Compensation Fiber
DD-DCF	Dispersion Decreasing DCF
DCM	Dispersion Compensation Module
DD	Direct Detection
DDO-OFDM	Direct Detection Optical OFDM
DFT-S	Discrete Fourier Transform Spread
DP	Dual Polarization
DSO	Digital Sampling Oscilloscope
DSP	Digital Signal Processing
DVB	Digital Video Broadcasting
ECL	External Cavity Laser
ECOC	European Conference on Optical Communication
EDFA	Erbium Doped Fiber Amplifier
EVM	Error Vector Magnitude
FDE	Frequency Domain Equalization
FEC	Forward Error Correction
FTTH	Fiber-to-the-Home
FWM	Four Wave Mixing
FWM-OPC	Four Wave Mixing Optical Phase Conjugation
GVD	Group Velocity Dispersion
HDF	Highly Dispersive Fiber
HNLF	Highly Nonlinear Fiber
ISI	Inter-Symbol Interference
IMDD	Intensity Modulation Direct Detection

ITU	International Telecommunication Union
LEAF	Large Effective Area Fiber
LSE	Linear Schrödinger Equation
LTE	Long Term Evolution
LO	Local Oscillator
MAN	Metropolitan Area Network
MIMO	Multiple Input Multiple Output
MSSI	Mid-span Spectral Inversion
MZM	Mach-Zehnder Modulator
NLT	Nonlinear Threshold
NLSE	Nonlinear Schrödinger Equation
NRZ	Non-Return to Zero
OCG	Optical Comb Generator
OFC	Optical Fiber Communication Conference
OSA	Optical Spectrum Analyzer
OSNR	Optical Signal to Noise Ratio
OPC	Optical Phase Conjugation
OPLL	Optical Phase Locked Loop
PA	Phased Array
PAPR	Peak-to-Average Power Ratio
PBS	Polarization Beam Splitter
PC	Polarization Controller
PD	Photo Diode
PM	Phase Modulation
Pol-Mux	Polarization Multiplexing
PMD	Polarization Mode Dispersion
PPLN	Periodically Poled Lithium-Neobate
PSF	Phase Shift Filter
QAM	Quadrature Amplitude Modulation
ROADM	Reconfigurable Add/Drop Multiplexer
RZ-D(Q)PSK	Return-to-Zero Differential (Quadrature) Phase Shift Keying
RFP	Radio Frequency Pilot
RFS	Recirculating Frequency Shifter
SC	Sub-carrier
SC-FDE	Single Carrier Frequency Domain Equalization
SHG	Second Harmonic Generation
SFG	Sum-Frequency Generation
SLM	Selective Mapping
SOP	State of Polarization
SSFM	Split-step Fourier Method
SSMF	Standard Single Mode Fiber
SPM	Self-Phase Modulation
TOD	Third Order Dispersion
UWB	Ultra Wide Band

WAN	Wide Area Network
WDM	Wavelength Division Multiplexing
WSS	Wavelength Selective Switch
XPM	Cross-Phase Modulation
XPM-OPC	Cross-Phase Modulation Optical Phase Conjugation
ZDW	Zero Dispersion Wavelength

References

1. J. M. Kahn, and K.-P. Ho, "Communications technology: A bottleneck for optical fibres," Nature **411**, 1007-1010 (2001).
2. J. Goell, "A repeater with high input impedance for optical-fiber transmission systems," Quantum Electronics, IEEE Journal of **9**, 641-642 (1973).
3. R. D. Maurer, "Glass fibers for optical communications," Proceedings of the IEEE **61**, 452 (1973).
4. G. White, and G. Chin, "A 100-Mbp.s^{-1} fiber-optic communication channel," Proceedings of the IEEE **61**, 683-684 (1973).
5. T. J. Xia, "Optical channel capacity – From Mb/s to Tb/s and beyond," Optical Fiber Technology **17**, 328-334 (2011).
6. D. Qian, M.-F. Huang, E. Ip, Y.-K. Huang, Y. Shao, J. Hu, and T. Wang, "101.7-Tb/s (370×294-Gb/s) PDM-128QAM-OFDM Transmission over 3×55-km SSMF using Pilot-based Phase Noise Mitigation," in *Optical Fiber Communication Conference/National Fiber Optic Engineers Conference 2011*(Optical Society of America, Los Angeles, California, 2011), p. PDPB5.
7. A. Sano, T. Kobayashi, S. Yamanaka, A. Matsuura, H. Kawakami, Y. Miyamoto, K. Ishihara, and H. Masuda, "102.3-Tb/s (224 x 548-Gb/s) C- and Extended L-band All-Raman Transmission over 240 km Using PDM-64QAM Single Carrier FDM with Digital Pilot Tone," in *Optical Fiber Communication Conference*(Optical Society of America, Los Angeles, California, 2012), p. PDP5C.3.
8. E. B. Desurvire, "Capacity Demand and Technology Challenges for Lightwave Systems in the Next Two Decades," Lightwave Technology, Journal of **24**, 4697-4710 (2006).
9. M. G. Taylor, "Coherent detection method using DSP for demodulation of signal and subsequent equalization of propagation impairments," Photonics Technology Letters, IEEE **16**, 674-676 (2004).
10. I. P. Kaminov, T. Li, and A. E. Willner, *Optical Fiber Telecommunications V B : Systems and Networks* (Academic Press, Boston, 2008).
11. S. Saito, Y. Yamamoto, and T. Kimura, "Optical heterodyne detection of directly frequency modulated semiconductor laser signals," Electronics Letters **16**, 826-827 (1980).
12. Y. Yamamoto, and T. Kimura, "Coherent optical fiber transmission systems," Quantum Electronics, IEEE Journal of **17**, 919-935 (1981).
13. F. Favre, L. Jeunhomme, I. Joindot, M. Monerie, and J. Simon, "Progress towards heterodyne-type single-mode fiber communication systems," Quantum Electronics, IEEE Journal of **17**, 897-906 (1981).
14. R. Hooper, J. E. Midwinter, D. W. Smith, and I. Stanley, "Progress in monomode transmission techniques in the United Kingdom," Lightwave Technology, Journal of **1**, 596-611 (1983).
15. T. Okoshi, "Recent progress in heterodyne/coherent optical-fiber communications," Lightwave Technology, Journal of **2**, 341-346 (1984).
16. L. G. Kazovsky, "Decision-driven phase-locked loop for optical homodyne receivers: Performance analysis and laser linewidth requirements," Lightwave Technology, Journal of **3**, 1238-1247 (1985).
17. L. G. Kazovsky, and D. A. Atlas, "A 1320-nm experimental optical phase-locked loop: performance investigation and PSK homodyne experiments at 140 Mb/s and 2 Gb/s," Lightwave Technology, Journal of **8**, 1414-1425 (1990).
18. T. Pfau, "Carrier Recovery Algorithms and Real-time DSP Implementation for Coherent Receivers," in *Optical Fiber Communication Conference*(Optical Society of America, San Francisco, California, 2014), p. W4K.1.

19. R. Wyatt, "Techniques and results of linewidth narrowing of semiconductor lasers for coherent system applications," in *Optical Fiber Communication*(Optical Society of America, Atlanta, Georgia, 1986), p. MI2.
20. R. I. Killey, P. M. Watts, V. Mikhailov, M. Glick, and P. Bayvel, "Electronic dispersion compensation by signal predistortion using digital Processing and a dual-drive Mach-Zehnder Modulator," IEEE Photonics Technology Letters **17**, 714-716 (2005).
21. R. I. Killey, P. M. Watts, V. Mikhailov, M. Glick, and P. Bayvel, "Electronic dispersion compensation by signal predistortion using a dual-drive Mach-Zehnder modulator," (2005), p. 3 pp. Vol. 4.
22. D. McGhan, "Electronic dispersion compensation," in *Conference on Optical Fiber Communication, OFC*(Anaheim, CA, 2006), p. OWK1.
23. G. Vareille, F. Pitel, and J. F. Marcerou, "3Tbit/s (300x11.6Gbit/s) Transmission Over 7380 km Using C+L Band with 25GHz Channel Spacing and NRZ Format," in *Optical Fiber Communication Conference and International Conference on Quantum Information*(Optical Society of America, Anaheim, California, 2001), p. PD22.
24. G. Charlet, J. C. Antona, S. Lanne, P. Tran, W. Idler, M. Gorlier, S. Borne, A. Klekamp, C. Simonneau, L. Pierre, Y. Frignac, M. Molina, F. Beaumont, J. P. Hamaide, and S. Bigo, "6.4Tb/s (159 x 42.7Gb/s) Capacity Over 21 x 100 km Using Bandwidth-Limited Phase-Shaped Binary Transmission," (2002), pp. 1-2.
25. B. Zhu, L. E. Nelson, S. Stulz, A. H. Gnauck, C. Doerr, J. Leuthold, L. Gruner-Nielsen, M. O. Pedersen, J. Kim, R. Lingle, Y. Emori, Y. Ohki, N. Tsukiji, A. Oguri, and S. Namiki, "6.4-Tb/s (160 x 42.7 Gb/s) transmission with 0.8 bit/s/Hz spectral efficiency over 32 x 100 km of fiber using CSRZ-DPSK format," in *Optical Fiber Communication Conference*(Optical Society of America, Atlanta, Georgia, 2003), p. PD19.
26. G. Charlet, J. C. Antona, S. Lanne, and S. Bigo, "From 2,100 km to 2,700 km distance using phase-shaped binary transmission at 6.3 Tbit/s capacity," in *Optical Fiber Communications Conference, 2003. OFC 2003*(2003), pp. 329-330 vol.321.
27. G. Charlet, E. Corbel, J. Lazaro, A. Klekamp, R. Dischler, P. Tran, W. Idler, H. Mardoyan, A. Konczykowska, F. Jorge, and S. Bigo, "WDM transmission at 6 Tbit/s capacity over transatlantic distance, using 42.7Gb/s Differential Phase-Shift Keying without pulse carver," in *Optical Fiber Communication Conference*(Optical Society of America, Los Angeles, California, 2004), p. PD36.
28. G. Charlet, P. Tran, H. Mardoyan, M. Lefrancois, T. Fauconnier, F. Jorge, and S. Bigo, "151× 43 Gb/s transmission over 4080 km based on return-to-zero-differential quadrature phase-shift keying," (2005).
29. A. Sano, H. Masuda, E. Yoshida, Y. Miyamoto, T. Yamada, T. Furuta, and H. Fukuyama, "55 × 86 Gb/s CSRZ-DQPSK transmission over 375 km Using Extended L-band Erbium-Doped Fiber Amplifiers," in *European Conference on Optical Communications, 2006. ECOC 2006.* (2006), pp. 1-2.
30. A. Gnauck, P. Winzer, L. Buhl, T. Kawanishi, T. Sakamoto, M. Izutsu, and K. Higuma, "12.3-Tb/s C-band DQPSK transmission at 3.2 b/s/Hz spectral efficiency," in *European Conference on Optical Communicaiton, 2006. (ECOC 2006)*(Cannes, France, 2006), p. PD Th4.1.2.
31. H. Masuda, A. Sano, T. Kobayashi, E. Yoshida, Y. Miyamoto, Y. Hibino, K. Hagimoto, T. Yamada, T. Furuta, and H. Fukuyama, "20.4-Tb/s (204× 111 Gb/s) transmission over 240 km using bandwidth-maximized hybrid Raman/EDFAs," in *Optical Fiber Communication Conference*(Optical Society of America, 2007), p. PDP20.
32. A. H. Gnauck, G. Charlet, P. Tran, P. Winzer, C. Doerr, J. Centanni, E. Burrows, T. Kawanishi, T. Sakamoto, and K. Higuma, "25.6-Tb/s C+L-Band Transmission of Polarization-Multiplexed RZ-DQPSK Signals," in *Optical Fiber Communication Conference and Exposition and The National Fiber Optic Engineers Conference*(Optical Society of America, Anaheim, California, 2007), p. PDP19.

33. A. Sano, E. Yamada, H. Masuda, E. Yamazaki, T. Kobayashi, E. Yoshida, Y. Miyamoto, S. Matsuoka, R. Kudo, K. Ishihara, Y. Takatori, M. Mizoguchi, K. Okada, K. Hagimoto, H. Yamazaki, S. Kamei, and H. Ishii, "13.4-Tb/s (134 x 111-Gb/s/ch) no-guard-interval coherent OFDM transmission over 3,600 km of SMF with 19-ps average PMD," in *34th European Conference on Optical Communication, 2008. ECOC 2008.* (2008), pp. 1-2.
34. Y. Jianjun, Z. Xiang, H. Ming-Fang, S. Yin, Q. Dayou, W. Ting, M. Cvijetic, P. Magill, L. Nelson, M. Birk, S. Ten, H. B. Matthew, and S. K. Mishra, "17 Tb/s (161 × 114 Gb/s) PolMux-RZ-8PSK transmission over 662 km of ultra-low loss fiber using C-band EDFA amplification and digital coherent detection," in *34th European Conference on Optical Communication, 2008. (ECOC 2008).* (2008), pp. 1-2.
35. G. Charlet, J. Renaudier, H. Mardoyan, P. Tran, O. Bertran Pardo, F. Verluise, M. Achouche, A. Boutin, F. Blache, J.-y. Dupuy, and S. Bigo, "Transmission of 16.4Tbit/s Capacity over 2,550km Using PDM QPSK Modulation Format and Coherent Receiver," in *Optical Fiber Communication Conference/National Fiber Optic Engineers Conference*(Optical Society of America, San Diego, California, 2008), p. PDP3.
36. Z. Xiang, Y. Jianjun, H. Ming-Fang, S. Yin, W. Ting, P. Magill, M. Cvijetic, L. Nelson, M. Birk, Z. Guodong, S. Ten, H. B. Matthew, and S. K. Mishra, "32Tb/s (320 × 114Gb/s) PDM-RZ-8QAM transmission over 580km of SMF-28 ultra-low-loss fiber," in *Optical Fiber Communication Conference , 2009. OFC 2009.* (2009), p. PDPB4.
37. A. Sano, H. Masuda, T. Kobayashi, M. Fujiwara, K. Horikoshi, E. Yoshida, Y. Miyamoto, M. Matsui, M. Mizoguchi, H. Yamazaki, Y. Sakamaki, and H. Ishii, "69.1-Tb/s (432 x 171-Gb/s) C- and Extended L-Band Transmission over 240 Km Using PDM-16-QAM Modulation and Digital Coherent Detection," in *Optical Fiber Communication Conference*(Optical Society of America, San Diego, California, 2010), p. PDPB7.
38. X. Zhou, J. Yu, M.-F. Huang, Y. Shao, T. Wang, L. Nelson, P. Magill, M. Birk, P. I. Borel, D. W. Peckham, and R. Lingle, "64-Tb/s (640x107-Gb/s) PDM-36QAM Transmission over 320km Using Both Pre- and Post-Transmission Digital Equalization," in *Optical Fiber Communication Conference*(Optical Society of America, San Diego, California, 2010), p. PDPB9.
39. T. J. Xia, G. Wellbrock, A. Tanaka, M.-F. Huang, E. Ip, D. Qian, Y.-K. Huang, S. Zhang, Y. Zhang, P. Ji, Y. Aono, S. Murakami, and T. Tajima, "High Capacity Field Trials of 40.5 Tb/s for LH Distance of 1,822 km and 54.2 Tb/s for Regional Distance of 634 km," in *Optical Fiber Communication Conference/National Fiber Optic Engineers Conference 2013*(Optical Society of America, Anaheim, California, 2013), p. PDP5A.4.
40. A. H. Gnauck, G. Raybon, S. Chandrasekhar, J. Leuthold, C. Doerr, L. Stulz, A. Agarwal, S. Banerjee, D. Grosz, S. Hunsche, A. Kung, A. Marhelyuk, D. Maywar, M. Movassaghi, X. Liu, C. Xu, X. Wei, and D. M. Gill, "2.5 Tb/s (64 × 42.7 Gb/s) Transmission Over 40x100 km NZDSF Using RZ-DPSK Formatand All-Raman-Amplified Spans," in *Optical Fiber Communications Conference*(Optical Society of America, Anaheim, California, 2002), p. FC2.
41. R. Schmogrow, D. Hillerkuss, S. Wolf, B. Bäuerle, M. Winter, P. Kleinow, B. Nebendahl, T. Dippon, P. C. Schindler, C. Koos, W. Freude, and J. Leuthold, "512QAM Nyquist sinc-pulse transmission at 54 Gbit/s in an optical bandwidth of 3 GHz," Optics Express **20**, 6439-6447 (2012).
42. S. Hara, and R. Prasad, *Multicarrier Techniques for 4G Mobiler Communications* (Artech House, Boston, 2003).
43. W. Shieh, H. Bao, and Y. Tang, "Coherent optical OFDM: theory and design," Opt. Express **16**, 841-859 (2008).
44. W. Shieh, and I. Djordjevic, *OFDM for Optical Communications* (ELSEVIER Inc., San Diego, California, USA, 2010).
45. A. J. Lowery, L. Du, and J. Armstrong, "Orthogonal frequency division multiplexing for adaptive dispersion compensation in long haul WDM systems," in *Conference on Optical Fiber Communication, OFC*(Anaheim, CA, 2006), p. PDP39.

46. W. Shieh, and C. Athaudage, "Coherent optical orthogonal frequency division multiplexing," Electronics Letters **42**, 587-588 (2006).
47. W. Shieh, X. Yi, and Y. Tang, "Transmission experiment of multi-gigabit coherent optical OFDM systems over 1000km SSMF fibre," Electronics Letters **43**, 183-184 (2007).
48. B. J. Schmidt, A. J. Lowery, and J. Armstrong, "Experimental Demonstrations of 20 Gbit/s Direct-Detection Optical OFDM and 12 Gbit/s with a Colorless Transmitter," in *Optical Fiber Communication Conference and Exposition and The National Fiber Optic Engineers Conference*(Optical Society of America, Anaheim, California, 2007), p. PDP18.
49. S. Chandrasekhar, X. Liu, P. J. Winzer, T. Lotz, C.-J. Youn, Y.-H. Kwon, and E.-S. Nam, "Field Demonstration of 3x341-Gb/s PDM-OFDM-256 Iterative Polar Modulation Signals with a Record 11.0-b/s/Hz Intrachannel Spectral Efficiency," in *Optical Fiber Communication Conference 2014, OFC 2014*(Optical Society of America, San Francisco, California, 2014), p. Th5A.8.
50. I. B. Djordjevic, and B. Vasic, "Orthogonal frequency division multiplexing for high-speed optical transmission," Optics Express **14**, 3767-3775 (2006).
51. Q. Yang, Y. Ma, and W. Shieh, "107 Gb/s Coherent Optical OFDM Reception Using Orthogonal Band Multiplexing," in *Optical Fiber Communication Conference/National Fiber Optic Engineers Conference*(Optical Society of America, San Diego, California, 2008), p. PDP7.
52. S. L. Jansen, I. Morita, and H. Tanaka, "10x121.9-Gb/s PDM-OFDM transmission with 2-b/s/Hz spectral efficiency over 1,000 km of SSMF," in *Conference on Optical Fiber Communication, OFC*(San Diego, 2008), p. PDP2.
53. E. Yamada, A. Sano, H. Masuda, E. Yamazaki, T. Kobayashi, E. Yoshida, K. Yonenaga, Y. Miyamoto, K. Ishihara, Y. Takatori, T. Yamada, and H. Yamazaki, "1 Tbit/s (111 Gbit/s/ch X 10 ch) no-guard-interval CO-OFDM transmission over 2100 km DSF," Electronics Letts. **44**, 1417-1418 (2008).
54. Y. Ma, Q. Yang, Y. Tang, S. Chen, and W. Shieh, "1-Tb/s single-channel coherent optical OFDM transmission over 600-km SSMF fiber with subwavelength bandwidth access," Opt. Express **17**, 9421-9427 (2009).
55. R. Dischler, and F. Buchali, "Transmission of 1.2 Tb/s continuous waveband PDM-OFDM-FDM signal with spectral efficiency of 3.3 bit/s/Hz over 400 km of SSMF," in *Optical Fiber Communications Conference , 2009. OFC 2009.* (2009), p. PDPC2.
56. S. Chandrasekhar, L. Xiang, B. Zhu, and D. W. Peckham, "Transmission of a 1.2-Tb/s 24-carrier no-guard-interval coherent OFDM superchannel over 7200-km of ultra-large-area fiber," in *35th European Conference on Optical Communication, 2009. ECOC '09.* (2009), pp. 1-2.
57. D. Hillerkuss, T. Schellinger, R. Schmogrow, M. Winter, T. Vallaitis, R. Bonk, A. Marculescu, J. Li, M. Dreschmann, J. Meyer, S. Ben Ezra, N. Narkiss, B. Nebendahl, F. Parmigiani, P. Petropoulos, B. Resan, K. Weingarten, T. Ellermeyer, J. Lutz, M. Möller, M. Hübner, J. Becker, C. Koos, W. Freude, and J. Leuthold, "Single Source Optical OFDM Transmitter and Optical FFT Receiver Demonstrated at Line Rates of 5.4 and 10.8 Tbit/s," in *Optical Fiber Communication Conference*(Optical Society of America, San Diego, California, 2010), p. PDPC1.
58. D. Hillerkuss, R. Schmogrow, T. Schellinger, M. Jordan, M. Winter, G. Huber, T. Vallaitis, R. Bonk, P. Kleinow, F. Frey, M. Roeger, S. Koenig, A. Ludwig, A. Marculescu, J. Li, M. Hoh, M. Dreschmann, J. Meyer, S. Ben Ezra, N. Narkiss, B. Nebendahl, F. Parmigiani, P. Petropoulos, B. Resan, A. Oehler, K. Weingarten, T. Ellermeyer, J. Lutz, M. Moeller, M. Huebner, J. Becker, C. Koos, W. Freude, and J. Leuthold, "26 Tbit s-1 line-rate super-channel transmission utilizing all-optical fast Fourier transform processing," *Nat. Photon.* **5**, 364-371 (2011).
59. X. Liu, S. Chandrasekhar, T. Lotz, P. Winzer, H. Haunstein, S. Randel, S. Corteselli, B. Zhu, and D. Peckham, "Generation and FEC-Decoding of a 231.5-Gb/s PDM-OFDM Signal with 256-Iterative-Polar-Modulation Achieving 11.15-b/s/Hz Intrachannel Spectral Efficiency and 800-

km Reach," in *National Fiber Optic Engineers Conference*(Optical Society of America, Los Angeles, California, 2012), p. PDP5B.3.

60. L. B. Du, J. Schroeder, M. M. Morshed, B. Eggleton, and A. J. Lowery, "Optical Inverse Fourier Transform Generated 11.2-Tbit/s No-Guard-Interval All-Optical OFDM Transmission," in *Optical Fiber Communication Conference/National Fiber Optic Engineers Conference 2013*(Optical Society of America, Anaheim, California, 2013), p. OW3B.5.
61. P. P. Mitra, and J. B. Stark, "Nonlinear limits to the information capacity of optical fibre communications," Nature **411**, 1027-1030 (2001).
62. R.-J. Essiambre, "Exploring capacity limits of fibre-optic communication systems," in *34th European Conference on Optical Communication, ECOC*(2008), p. We.1.E.1.
63. A. D. Ellis, Z. Jian, and D. Cotter, "Approaching the non-linear Shannon limit," J. Lightwave Technol. **28**, 423-433 (2010).
64. A. J. Lowery, "Fiber Nonlinearity Mitigation in Optical Links That Use OFDM for Dispersion Compensation," Photonics Technology Letters, IEEE **19**, 1556-1558 (2007).
65. J. Armstrong, B. J. C. Schmidt, D. Kalra, H. A. Suraweera, and A. J. Lowery, "Performance of asymmetrically clipped optical OFDM in AWGN for an intensity modulated direct detection system," in *IEEE Globecom 2006 Proceedings*(IEEE, 2006), p. 5.
66. A. J. Lowery, S. Wang, and M. Premaratne, "Calculation of power limit due to fiber nonlinearity in optical OFDM systems," Opt. Express **15**, 13282-13287 (2007).
67. X. Li, X. Chen, G. Goldfarb, E. Mateo, I. Kim, F. Yaman, and G. Li, "Electronic post-compensation of WDM transmission impairments using coherent detection and digital signal processing," Optics Express **16**, 880-888 (2008).
68. E. Ip, and J. M. Kahn, "Compensation of dispersion and nonlinear impairments using digital backpropagation," J. Lightwave Technol. **26**, 3416-3425 (2008).
69. E. Ip, "Nonlinear compensation using backpropagation for polarization-multiplexed transmission," J. Lightwave Technol. **28**, 939-951 (2010).
70. K. Kikuchi, M. Fukase, and K. Sang-Yuep, "Electronic post-compensation for nonlinear phase noise in a 1000-km 20-Gbit/s optical QPSK transmission system using the homodyne receiver with digital signal processing," in *Optical Fiber Communication and the National Fiber Optic Engineers Conference, 2007. OFC/NFOEC 2007*(2007), pp. 1-3.
71. L. B. Du, and A. J. Lowery, "Practical XPM compensation method for coherent optical OFDM systems," IEEE Photon. Technol. Letts. **22**, 3 (2010).
72. A. Yariv, D. Fekete, and D. M. Pepper, "Compensation for channel dispersion by nonlinear optical phase conjugation," Opt. Lett. **4**, 52-54 (1979).
73. D. M. Pepper, and A. Yariv, "Compensation for phase distortions in nonlinear media by phase conjugation," Opt. Lett. **5**, 59-60 (1980).
74. S. Watanabe, "Cancellation of four-wave mixing in a single-mode fiber by midway optical phase conjugation," Opt. Lett. **19**, 1308-1310 (1994).
75. S. Watanabe, and M. Shirasaki, "Exact compensation for both chromatic dispersion and Kerr effect in a transmission fiber using optical phase conjugation," Lightwave Technology, Journal of **14**, 243-248 (1996).
76. S. L. Jansen, S. Spalter, G. D. Khoe, H. de Waardt, H. E. Escobar, L. Marshall, and M. Sher, "16×40 gb/s over 800 km of SSMF using mid-link spectral inversion," IEEE Photon. Technol. Lett. **16**, 1763-1765 (2004).
77. S. L. Jansen, D. v. d. Borne, A. Schöpflin, E. Gottwald, P. M. Krummrich, G. D. Khoe, and H. d. Waardt, "26x42.8-Gbit/s DQPSK transmission with 0.8-bits/Hz spectral efficiency over 4,500-km SSMF using optical phase conjugation," in *Proceedings of the 31st European Conference on Optical Communication (ECOC 2005)*(Institution of Electrical Engineers, 25 - 29 September 2005, Glasgow, Scotland, 2005), p. p. TH 4.1.5.
78. S. L. Jansen, D. van den Borne, C. Climent, M. Serbay, C. J. Weiske, H. Suche, P. M. Krummrich, S. Spalter, S. Calabro, N. Hecker-Denschlag, P. Leisching, W. Rosenkranz, W.

Sohler, G. D. Khoe, T. Koonen, and H. de Waardt, "10,200 km 22×2×10 Gbit/s RZ-DQPSK dense WDM transmission without inline dispersion compensation through optical phase conjugation," in *Optical Fiber Communication Conference (OFC/NFOEC)*(2005), p. PDP 28.

79. S. L. Jansen, D. van den Borne, B. Spinnler, S. Calabrò, H. Suche, P. M. Krummrich, W. Sohler, G. D. Khoe, and H. de Waardt, "Optical phase conjugation for ultra long-haul phase-shift-keyed transmission," *J. Lightwave Technol.* **24**, 54 (2006).
80. L. B. Du, M. M. Morshed, and A. J. Lowery, "604-Gb/s coherent optical OFDM over 800 km of S-SMF with mid-span spectral inversion," in *Opto-Electronics and Communications Conference* (Busan, 2012), pp. 3B2-3.
81. L. B. Du, M. M. Morshed, and A. J. Lowery, "Fiber nonlinearity compensation for OFDM super-channels using optical phase conjugation," Opt. Express **20**, 19921-19927 (2012).
82. V. Pechenkin, and I. J. Fair, "Analysis of four-wave mixing suppression in fiber-optic OFDM transmission systems with an optical phase conjugation module," Optical Communications and Networking, IEEE/OSA Journal of **2**, 701-710 (2010).
83. X. Liu, Y. Qiao, and Y. Ji, "Reduction of the fiber nonlinearity impairment using optical phase conjugation in 40Gb/s CO-OFDM systems," Opt. Commun. **283**, 2749-2753 (2010).
84. M. Morshed, L. B. Du, and A. J. Lowery, "Performance limitation of coherent optical OFDM systems with non-ideal optical phase conjugation," in *IEEE Photonics Conference (IPC)*(Burlingame, CA, 2012), pp. 394-395, TuU.
85. M. Morshed, L. B. Du, and A. J. Lowery, "Mid-span spectral inversion for coherent optical OFDM systems: Fundamental limits to performance," J. Lightwave Technol. **31**, 58-66 (2013).
86. M. Morshed, L. B. Du, B. Foo, M. D. Pelusi, and A. J. Lowery, "Optical phase conjugation for nonlinearity compensation of 1.21-Tb/s pol-mux coherent optical OFDM," in *18th Opto-Electronics and Communications Conference*(Kyoto, Japan, 2013), pp. PD 3-4.
87. M. Morshed, L. B. Du, and A. J. Lowery, "Improving the performance of optical phase conjugator using a mid-way filter," in *CLEO-PR & OECC/PS*(Kyoto, Japan, 2013), pp. TuR4-3.
88. M. Morshed, A. J. Lowery, and L. B. Du, "Improving performance of optical phase conjugation by splitting the nonlinear element," Opt. Express **21**, 4567-4577 (2013).
89. H. Hu, R. M. Jopson, A. Gnauck, M. Dinu, S. Chandrasekhar, X. Liu, C. Xie, M. Montoliu, S. Randel, and C. McKinstrie, "Fiber Nonlinearity Compensation of an 8-channel WDM PDM-QPSK Signal using Multiple Phase Conjugations," in *Optical Fiber Communication Conference*(Optical Society of America, San Francisco, California, 2014), p. M3C.2.
90. D. Rafique, T. Rahman, A. Napoli, and B. Spinnler, "Dynamics of Intra Super-channel Fiber Nonlinearity Compensation in Flex-grid Optical Networks," in *Optical Fiber Communication Conference*(Optical Society of America, San Francisco, California, 2014), p. Tu3A.4.
91. I. Phillips, M. Tan, M. F. Stephens, M. McCarthy, E. Giacoumidis, S. Sygletos, P. Rosa, S. Fabbri, S. T. Le, T. Kanesan, S. K. Turitsyn, N. J. Doran, P. Harper, and A. D. Ellis, "Exceeding the Nonlinear-Shannon Limit using Raman Laser Based Amplification and Optical Phase Conjugation," in *Optical Fiber Communication Conference*(Optical Society of America, San Francisco, California, 2014), p. M3C.1.
92. M. Salsi, C. Koebele, P. Tran, H. Mardoyan, E. Dutisseuil, J. Renaudier, M. Bigot-Astruc, L. Provost, S. Richard, P. Sillard, S. Bigo, and G. Charlet, "Transmission of 96×100Gb/s with 23% Super-FEC Overhead over 11,680km, using Optical Spectral Engineering," in *Optical Fiber Communication Conference/National Fiber Optic Engineers Conference 2011*(Optical Society of America, Los Angeles, California, 2011), p. OMR2.
93. D. G. Foursa, H. G. Batshon, H. Zhang, M. Mazurczyk, J. X. Cai, O. Sinkin, A. Pilipetskii, G. Mohs, and N. S. Bergano, "44.1 Tb/s transmission over 9,100 km using coded modulation based on 16QAM signals at 4.9 bits/s/Hz spectral efficiency," in *39th European Conference on Optical Communication (ECOC 2013),* (2013), pp. 1-3.
94. Y. Koizumi, K. Toyoda, M. Yoshida, and M. Nakazawa, "1024 QAM (60 Gbit/s) single-carrier coherent optical transmission over 150 km," Optics Express **20**, 12508-12514 (2012).

95. S. J. Savory, "Digital Coherent Optical Receivers: Algorithms and Subsystems," Selected Topics in Quantum Electronics, IEEE Journal of **16**, 1164-1179 (2010).
96. J. Armstrong, "OFDM for Optical Communications," Lightwave Technology, Journal of **27**, 189-204 (2009).
97. A. Lowery, and J. Armstrong, "Orthogonal-frequency-divison multiplexing for optical dispersion compensation," in *Proc. of Otpcial Fiber Communication and the National Fiber Optic Engineers Conference 2007 (OFC/NFOEC 2007).*(IEEE, 2007), p. 3.
98. G. P. Agrawal, *Nonlinear Fiber Optics* (Academic Press, 1995).
99. G. P. Agrawal, *Fiber-optic Communication Systems* (Wiley and Sons, New York, 2010).
100. T. Schneider, *Nonlinear Optics in Telecommunications* (Springer, Berlin,Heidelberg,New York, Hong Kong, London, Milan, Paris, Tokyo, 2004).
101. G. Keiser, *Optical Fiber Communications* (McGrawHill, New York, 2011).
102. A. R. Charaplyvy, R. W. Tkach, L. L. Buhl, and R. C. Alferness, "Phase modulation to amplitude modulation conversion of CW laser light in optical fibres," Electronics Letters **22**, 409-411 (1986).
103. B. Goebel, B. Fesl, L. D. Coelho, and N. Hanik, "On the effect of FWM in coherent optical OFDM systems," in *Conference on Optical Fiber Communication, OFC*(2008), pp. 1-3.
104. R. W. Tkach, A. R. Chraplyvy, F. Forghieri, A. H. Gnauck, and R. M. Derosier, "Four-photon mixing and high-speed WDM systems," Lightwave Technology, Journal of **13**, 841-849 (1995).
105. A. D. Ellis, and W. A. Stallard, "Four wave mixing in ultra long transmission systems incorporating linear amplifiers," in *Non-Linear Effects in Fibre Communications, IEE Colloquium on*(1990), pp. 6/1-6/4.
106. K. Inoue, "Phase-mismatching characteristic of four-wave mixing in fiber lines with multistage optical amplifiers," Optics Letters **17**, 801-803 (1992).
107. M. Nazarathy, J. Khurgin, R. Weidenfeld, Y. Meiman, P. Cho, R. Noe, I. Shpantzer, and V. Karagodsky, "Phased-array cancellation of nonlinear FWM in coherent OFDM dispersive multi-span links," Opt. Express **16**, 15777-15810 (2008).
108. A. J. Lowery, L. B. Du, and J. Armstrong, "Performance of optical OFDM in ultralong-haul WDM lightwave systems," J. Lightwave Technology **25**, 131-138 (2007).
109. M. Nazarathy, J. Khurgin, R. Weidenfeld, Y. Meiman, P. Cho, R. Noe, and I. Shpantzer, "The FWM Impairment in Coherent OFDM Compounds on a Phased-Array Basis over Dispersive Multi-Span Links," in *Coherent Optical Technologies and Applications*(Optical Society of America, Boston, Massachusetts, 2008), p. CWA4.
110. X. Chen, and W. Shieh, "Closed-form expressions for nonlinear transmission performance of densely spaced coherent optical OFDM systems," Opt. Express **18**, 19039-19054 (2010).
111. S. Kumar, *Impact of Nonlinearities on Fiber Optic Communications* (Springer, 2011).
112. B. S. Krongold, T. Yan, and W. Shieh, "Fiber nonlinearity mitigation by PAPR reduction in coherent optical OFDM systems via active constellation extension," in *Optical Communication, 2008. ECOC 2008. 34th European Conference on*(2008), pp. 1-2.
113. Y. Tang, W. Shieh, and B. S. Krongold, "Fiber Nonlinearity Mitigation in 428-Gb/s Multiband Coherent Optical OFDM Systems," in *Optical Fiber Communication Conference*(Optical Society of America, San Diego, California, 2010), p. JThA6.
114. J. Armstrong, B. Schmidt, D. Kalra, H. A. Suraweera, and A. J. Lowery, "SPC07-4: Performance of Asymmetrically Clipped Optical OFDM in AWGN for an Intensity Modulated Direct Detection System," in *Global Telecommunications Conference, 2006. GLOBECOM '06. IEEE*(2006), pp. 1-5.
115. B. S. Krongold, T. Yan, and W. Shieh, "Fiber nonlinearity mitigation by PAPR reduction in coherent optical OFDM systems via active constellation extension," in *34th European Conference on Optical Communication, 2008 (ECOC 2008).*(2008), pp. 1-2.

116. X. Liu, X. Wei, R. E. Slusher, and C. J. McKinstrie, "Improving transmission performance in differential phase-shift-keyed systems by use of lumped nonlinear phase-shift compensation," Optics Letters **27**, 1616-1618 (2002).
117. C. Xu, and X. Liu, "Postnonlinearity compensation with data-driven phase modulators in phase-shift keying transmission," Optics Letters **27**, 1619-1621 (2002).
118. K.-P. Ho, and J. M. Kahn, "Electronic Compensation Technique to Mitigate Nonlinear Phase Noise," Journal of Lightwave Technology **22**, 779 (2004).
119. H. Keang-Po, and J. M. Kahn, "Electronic compensation technique to mitigate nonlinear phase noise," J. Lightwave Technology **22**, 779-783 (2004).
120. W. Shieh, X. Yi, Y. Ma, and Y. Tang, "Theoretical and experimental study on PMD-supported transmission using polarization diversity in coherent optical OFDM systems," Opt. Express **15**, 9936-9947 (2007).
121. A. J. Lowery, "Fiber nonlinearity pre- and post-compensation for long-haul optical links using OFDM," Optics Express **15**, 12965-12970 (2007).
122. X. Liu, F. Buchali, and R. W. Tkach, "Improving the Nonlinear Tolerance of Polarization-Division-Multiplexed CO-OFDM in Long-Haul Fiber Transmission," Journal of Lightwave Technology **27**, 3632-3640 (2009).
123. C. Fürst, C. Scheerer, G. Mohs, J. P. Elbers, and C. Glingener, "Influence of the dispersion map on limitations due to cross-phase modulation in WDM multispan transmission systems," in *Optical Fiber Communication Conference and International Conference on Quantum Information*(Optical Society of America, Anaheim, California, 2001), p. MF4.
124. K. Forozesh, S. L. Jansen, S. Randel, I. Morita, and H. Tanaka, "The influence of the dispersion map in coherent optical OFDM transmission systems," in *IEEE/LEOS Summer Topical Meetings, 2008 Digest of the*(2008), pp. 135-136.
125. L. B. Du, and A. J. Lowery, "Fiber Nonlinearity Compensation for CO-OFDM Systems with Periodic Dispersion Maps," in *OFC/NFOEC 2009*(IEEE, 2009), p. 3.
126. S. L. Jansen, I. Morita, N. Tadeka, and H. Tanaka, "20-Gb/s OFDM transmission over 4,160-km SSMF enabled by RF-pilot tone phase noise compensation," in *Conference on Optical Fiber Communication, OFC*(Anaheim, CA., 2007), p. PDP15.
127. S. L. Jansen, I. Morita, T. C. W. Schenk, N. Takeda, and H. Tanaka, "Coherent Optical 25.8-Gb/s OFDM Transmission Over 4160-km SSMF," Lightwave Technology, Journal of **26**, 6-15 (2008).
128. B. Inan, S. Randel, S. L. Jansen, A. Lobato, S. Adhikari, and N. Hanik, "Pilot-tone-based nonlinearity compensation for optical OFDM systems," in *36th European Conference and Exhibition on Optical Communication (ECOC), 2010* (2010), pp. 1-3.
129. L. B. Du, and A. Lowery, "Experimental demonstration of pilot-based XPM nonlinearity compensator for CO-OFDM systems," in *37th European Conference and Exposition on Optical Communications*(Optical Society of America, Geneva, 2011), p. Th.11.B.14.
130. L. B. Y. Du, and A. J. Lowery, "Pilot-based XPM nonlinearity compensator for CO-OFDM systems," Optics Express **19**, B862-B867 (2011).
131. L. B. Du, and A. J. Lowery, "Pilot-based cross-phase modulation compensation for coherent optical orthogonal frequency division multiplexing long-haul optical communications systems," Optics Letters **36**, 1647-1649 (2011).
132. H. Ekstrom, A. Furuskar, J. Karlsson, M. Meyer, S. Parkvall, J. Torsner, and M. Wahlqvist, "Technical solutions for the 3G long-term evolution," Communications Magazine, IEEE **44**, 38-45 (2006).
133. L. B. Du, and A. J. Lowery, "Optimizing the subcarrier granularity of coherent optical communications systems," Optics Express **19**, 8079-8084 (2011).
134. L. B. Du, B. Schmidt, and A. J. Lowery, "Efficient digital backpropagation for PDM-CO-OFDM optical transmission systems," in *Proceedings of the 2010 (OFC/NFOEC) Optical Fiber*

Communications Conference and Exposition and the National Fiber Optic Engineers Conference(Optical Society of America, 2010), p. 3.

135. P. Minzioni, "Nonlinearity Compensation in a Fiber Optic Link by Optical Phase Conjugation," Fiber and Integrated Optics **28:3**, 179-209 (2009).
136. M. Asobe, O. Tadanaga, T. Yanagawa, H. Itoh, and H. Suzuki, "Reducing photorefractive effect in periodically poled ZnO- and MgO-doped LiNbO3 wavelength converters," Applied Physics Letters **78**, 3163-3165 (2001).
137. I. Cristiani, L. Razzari, P. Minzioni, V. Degiorgio, and E. P. Kokanyan, "Photorefractivity of hafnium-doped congruent lithium-niobate crystals," in *Lasers and Electro-Optics Europe, 2005. CLEO/Europe. 2005 Conference on*(2005), p. 208.
138. S. Watanabe, "Compensation of the phase fluctuation in a transmission line by optical phase conjugation," Optics letters **17**, 1355-1357 (1992).
139. A. H. Gnauck, R. M. Jopson, and R. M. Derosier, "10-Gb/s 360-km transmission over dispersive fiber using midsystem spectral inversion," Photonics Technology Letters, IEEE **5**, 663-666 (1993).
140. W. Pieper, C. Kurtzke, R. Schnabel, D. Breuer, R. Ludwig, K. Petermann, and H. G. Weber, "Nonlinearity-insensitive standard-fibre transmission based on optical-phase conjugation in a semiconductor-laser amplifier," Electronics Letters **30**, 724-726 (1994).
141. I. Brener, B. Mikkelsen, K. Rottwitt, W. Burkett, G. Raybon, J. B. Stark, K. Parameswaran, M. H. Chou, M. M. Fejer, E. E. Chaban, R. Harel, D. L. Philen, and S. Kosinski, "Cancellation of all Kerr nonlinearities in long fiber spans using a LiNbo3 phase conjugator and Raman amplification," in *Optical Fiber Communication Conference*(Optical Society of America, Baltimore, Maryland, 2000), p. PD33.
142. K. Kikuchi, and C. Lorattanasane, "Compensation for pulse waveform distortion in ultra-long distance optical communication systems by using nonlinear optical phase conjugator," (1993).
143. S. Watanabe, T. Chikama, G. Ishikawa, T. Terahara, and H. Kuwahara, "Compensation of pulse shape distortion due to chromatic dispersion and Kerr effect by optical phase conjugation," Photonics Technology Letters, IEEE **5**, 1241-1243 (1993).
144. S. Watanabe, S. Kaneko, and T. Chikama, "Long-Haul Fiber Transmission Using Optical Phase Conjugation," Optical Fiber Technology **2**, 169-178 (1996).
145. P. Minzioni, F. Alberti, and A. Schiffini, "Optimized link design for nonlinearity cancellation by optical phase conjugation," IEEE Photon. Technol. Lett. **16**, 813-815 (2004).
146. P. Minzioni, F. Alberti, and A. Schiffini, "Techniques for nonlinearity cancellation into embedded links by optical phase conjugation," J. Lightwave Technol. **23**, 2364-2370 (2005).
147. V. Pechenkin, and I. J. Fair, "On four-wave mixing suppression in dispersion-managed fiber-optic OFDM systems with an optical phase conjugation module," J. Lightwave Technol. **29**, 1677-1690 (2011).
148. A. H. Gnauck, R. M. Jopson, and R. M. Derosier, "Compensating the compensator: a demonstration of nonlinearity cancellation in a WDM system," Photonics Technology Letters, IEEE **7**, 582-584 (1995).
149. S. L. Jansen, D. van den Borne, P. M. Krummrich, S. Spalter, G. D. Khoe, and H. de Waardt, "Long-haul DWDM transmission systems employing optical phase conjugation," IEEE J. Sel. Top. Quantum Electron. **12**, 505-520 (2006).
150. S. L. Jansen, D. van den Borne, P. M. Krummrich, S. Spälter, H. Suche, W. Sohler, G. D. Khoe, H. de Waardt, I. Morita, and H. Tanaka, "Applications of optical phase conjugation in robust optical transmission systems," Proc. of SPIE, Optical Transmission, Switching and Subsystems **V. 6783**, 67830P (2007).
151. M. Morshed, L. B. Du, B. Foo, M. D. Pelusi, and A. J. Lowery, "Optical phase conjugation for nonlinearity compensation of 1.21-Tb/s pol-mux coherent optical OFDM," in *CLEO-PR & OECC/PS*(Kyoto, Japan, 2013), pp. PD3-4.

152. M. Morshed, L. B. Du, B. Foo, M. D. Pelusi, B. Corcoran, and A. J. Lowery, "Experimental demonstrations of dual polarization CO-OFDM using mid-span spectral inversion for nonlinearity compensation," Optics Express **22**, 10455-10466 (2014).
153. X. Liu, A. R. Chraplyvy, P. J. Winzer, R. W. Tkach, and ChandrasekharS, "Phase-conjugated twin waves for communication beyond the Kerr nonlinearity limit," Nat Photon **7**, 560-568 (2013).
154. K. Solis-Trapala, T. Inoue, and S. Namiki, "Nearly-Ideal Optical Phase Conjugation based Nonlinear Compensation System," in *Optical Fiber Communication Conference*(Optical Society of America, San Francisco, California, 2014), p. W3F.8.
155. M. Morshed, B. Corcoran, and A. J. Lowery, "Mid-span Spectral Inversion in Broad Band CO-OFDM Systems for Increased Transmission Distance," in *Optoelectronics and Communications Conference/ Australian Conference on Optical Fibre Technology (OECC/ACOFT)*(Melbourne, AUS, 2014).
156. S. L. Jansen, I. Morita, T. C. Schenk, and H. Tanaka, "Long-haul transmission of16×52.5 Gbits/s polarization-division-multiplexed OFDM enabled by MIMO processing (Invited)," J. Opt. Netw. **7**, 173-182 (2008).
157. I. Fatadin, D. Ives, and S. J. Savory, "Blind equalization and carrier phase recovery in a 16-QAM optical coherent system," J. Lightwave Technol. **27**, 3042-3049 (2009).
158. Y. Xingwen, W. Shieh, and T. Yan, "Phase estimation for coherent optical OFDM," IEEE Photon. Technol. Lett. **19**, 919-921 (2007).
159. P. Minzioni, I. Cristiani, V. Degiorgio, L. Marazzi, M. Martinelli, C. Langrock, and M. M. Fejer, "Experimental demonstration of nonlinearity and dispersion compensation in an embedded link by optical phase conjugation," IEEE Photonics Technology Letters **18**, 995-997 (2006).
160. M. Karlsson, "Four-wave mixing in fibers with randomly varying zero-dispersion wavelength," J. Opt. Soc. Am. B **15**, 2269-2275 (1998).
161. T. Hasegawa, K. Inoue, and K. Oda, "Polarization independent frequency conversion by fiber four-wave mixing with a polarization diversity technique," IEEE Photon. Technol. Lett. **5**, 947-949 (1993).
162. M. D. Pelusi, "Fiber looped phase conjugation of polarization multiplexed signals for pre-compensation of fiber nonlinearity effect," Opt. Express **21**, 21423-21432 (2013).
163. M. E. Marhic, G. Kalogerakis, and L. G. Kazovsky, "Gain reciprocity in fibre optical parametric amplifiers," Electronics Letters **42**, 519-520 (2006).
164. W.-R. Peng, T. Tsuritani, and I. Morita, "Transmission of high-baud PDM-64QAM signals," J. Lightwave Technol. **31**, 2146-2162 (2013).
165. S. Ozharar, F. Quinlan, I. Ozdur, S. Gee, and P. J. Delfyett, "Ultraflat Optical Comb Generation by Phase-Only Modulation of Continuous-Wave Light," Photonics Technology Letters, IEEE **20**, 36-38 (2008).
166. S. Le Floch, and P. Cambon, "Theoretical evaluation of the Brillouin threshold and the steady-state Brillouin equations in standard single-mode optical fibers," J. Opt. Soc. Am. A **20**, 1132-1137 (2003).
167. Y. Hong, A. Lowery, and E. Viterbo, "Sensitivity improvement and carrier power reduction in direct-detection optical OFDM systems by subcarrier pairing."
168. K. K. Y. Wong, M. E. Marhic, and L. G. Kazovsky, "Phase-conjugate pump dithering for high-quality idler generation in a fiber optical parametric amplifier," Photonics Technology Letters, IEEE **15**, 33-35 (2003).
169. H. Nguyen Tan, T. Inoue, K. Tanizawa, S. Petit, Y. Oikawa, S. Takasaka, T. Yagi, and S. Namiki, "Counter-Dithering Pump Scheme for Cascaded Degenerate FWM Based Wavelength Converter," in *Optical Fiber Communication Conference*(Optical Society of America, San Francisco, California, 2014), p. W3F.4.
170. F. S. Yang, M. E. Marhic, and L. G. Kazovsky, "CW fibre optical parametric amplifier with net gain and wavelength conversion efficiency >1," Electronics Letters **32**, 2336-2338 (1996).

171. B. J. Eggleton, T. D. Vo, R. Pant, J. Schroeder, M. D. Pelusi, D. Y. Choi, S. J. Madden, and B. Luther-Davies, "Photonic chip based ultrafast optical processing based on high nonlinearity dispersion engineered chalcogenide waveguides," Laser Photonics Reviews **6**, 97-114 (2012).
172. M. D. Pelusi, F. Luan, D. Y. Choi, S. J. Madden, D. A. P. Bulla, B. Luther-Davies, and B. J. Eggleton, "Optical phase conjugation by an As_2S_3 glass planar waveguide for dispersion-free transmission of WDM-DPSK signals over fiber," Opt. Express **18**, 26686-26694 (2010).
173. A. Chowdhury, G. Raybon, R. J. Essiambre, J. H. Sinsky, A. Adamiecki, J. Leuthold, C. R. Doerr, and S. Chandrasekhar, "Compensation of intrachannel nonlinearities in 40-Gb/s pseudolinear systems using optical-phase conjugation," J. Lightwave Technol. **23**, 172-177 (2005).
174. P. Martelli, P. Boffi, M. Ferrario, L. Marazzi, P. Parolari, R. Siano, V. Pusino, P. Minzioni, I. Cristiani, C. Langrock, M. M. Fejer, M. Martinelli, and V. Degiorgio, "All-Optical Wavelength Conversion of a 100-Gb/s Polarization-Multiplexed Signal," Opt. Express **17**, 17758-17763 (2009).
175. M. M. Morshed, A. J. Lowery, and L. B. Du, "Reducing Nonlinear Distortion in Optical Phase Conjugation using a Midway Phase-Shifting Filter," in *Optical Fiber Communication Conference*(Optical Society of America, San Francisco, California, 2014), p. W2A.56.
176. M. D. Pelusi, and B. J. Eggleton, "Optically tunable compensation of nonlinear signal distortion in optical fiber by end-span optical phase conjugation," Opt. Express **20**, 8015-8023 (2012).
177. M. D. Pelusi, "Fiber looped phase conjugation of polarization multiplexed signals for pre-compensation of fiber nonlinearity effect," Optics Express **21**, 21423-21432 (2013).